CONTROL OF COHERENT STRUCTURE IN COAXIAL SWIRLING TURBULENT JETS

BY

WONJOONG LEE

Submitted to the graduate degree program in Aerospace Engineering
and the Graduate Faculty of the University of Kansas
in partial fulfillment of the requirements for the degree of
Doctor of Philosophy

_____

Chairperson

Committee Members   _____

_____

_____

_____

Date Defended: November 10, 2008

The Dissertation Committee for WONJOONG LEE certifies
that this is the approved version of the following dissertation:

CONTROL OF COHERENT STRUCTURE IN

COAXIAL SWIRLING TURBULENT JETS

Committee:

_____

Chairperson

_____

_____

_____

_____

Date Approved: November 10, 2008

ABSTRACT

The purpose of this investigation is to explore the swirl jet characteristics and the possibility of using artificial means for excitation of shear layers with the application as swirl jet control. For this purpose, a subsonic jet facility and a mechanical excitation device are designed and fabricated for the low speed and plain perturbations. The major system components consist of concentric subsonic nozzles, swirl generators, and the excitation devices with straight lobes. The experiments are carried out at various swirl flow conditions and excitation modes. Three components of mean velocity and turbulence fluctuation measurements are carried out with wave excitation using a stereoscopic particle image velocimetry. The acquired data are presented in cubic plots and two-dimensional contour plots. Furthermore, the numerical analysis is performed to investigate the helical excitation effects on a relatively high speed region. The computed data are presented in two-dimensional contour pictures and the trace plots of particles. Including extracted vorticity, both the experimental and computational results are compared with the baseline at various conditions, and with the values reported in the existing literature.

In general, axisymmetric swirling jets are unstable in the near field to all the excitation modes examined. It is shown that the overall response of the swirling jet to excitation is not only dependent on the wave mode number, but also strongly on its sign; meaning the spiral direction of the convex lobes with respect to the swirling jet. This confirms the previous theoretical results. Excitation at both plain and helical perturbations simultaneously affects the flow property distributions in the vortex core and the shear layer at the jet periphery. Especially negative helical wave excitation is considered as the effective way of mixing enhancement for swirling jets compared to the straight lobe perturbation. The preferred mode is the second negative helical excitation in the present work.

Consequently, the knowledge gained from this research could benefit the fluid dynamic community by increasing the fundamental understanding of turbulent swirling flows and their effective control for the formation and breakdown of coherent structure.

ACKNOWLEDGEMENTS

TABLE OF CONTENTS

LIST OF FIGURES

LIST OF TABLES

NOMENCLATURE

Symbol	Description	Unit
D	Jet diameter, Defined in Figure 5.1	m
D_h	Hydraulic jet diameter	m
f	Excitation frequency	s^{-1}
G	Degree of swirl, Defined in Equation (2.4)	-
G_θ	Jet torque, Defined in Equation (2.2)	N·m
G_x	Axial thrust, Defined in Equation (2.3)	N
h	Helical disturbance azimuthal wave number or mode	-
m	Disturbance azimuthal wave number or mode	-
$\dot{m}$	Mass flow rate	kg/s
q	Ratio of maximum tangential to axial velocity	-
r	Radial coordinate	m
R	Nozzle exit radius	m
Re	Reynolds number	-
S	Jet swirl number, Defined in Equation (2.5)	-
St	Strouhal number, Defined in Equation (2.10)	-
T	Temperature	K
T_o	Total Temperature	K
T_s	Static Temperature	K
U	Mass averaged axial velocity	m/s
u	Turbulent function, Defined in Equation (5.1)	-
u	Axial velocity	m/s
V	Mass averaged radial velocity	m/s
v	Radial velocity	m/s
W	Mass averaged tangential velocity	m/s
w	Tangential velocity	m/s
x	Axial coordinate	m
y	Lateral coordinate	m
z	Longitudinal coordinate	m

Greek Symbols

Γ	Constant circulation parameter outside the jet core
θ	Momentum thickness
Ω	Angular velocity inside the jet core
ϕ	Angle of the guide vane

Subscripts

m_o	Local maximum at $x/D=0$
o	Quantity at jet exit

Abbreviations

BL	Boundary Layer
CCD	Charge Coupled Device
CFD	Computational Fluid Dynamics
CPU	Central Processing Unit
CRZ	Corner Recirculation Zone
CTRZ	Central Toroidal Recirculation Zone
DAP	Data Acquisition Program
DAS	Data Acquisition System
DC	Direct Current
HWA	Hot Wire Anemometry
IA	Interrogation Area
LDV	Laser Doppler Velocimetry
LES	Large Eddy Simulation
LSV	Laser Speckle Velocimetry
MFC	Mass Flow Controller
PIV	Particle Image Velocimetry
RANS	Reynolds Average Navier-Stokes
RMS	Root Mean Square
RSM	Reynolds Stress Model
SKO	Standard K-Omega

1. INTRODUCTION

The pervasiveness of vortical flows in nature makes their description and control an important issue in fluid dynamics. The dynamics and mixing characteristics of jet flows have been studied quite extensively over a number of decades[1]. Advanced designs for combustors, quiet jet engines, and other technological applications, depend on the identification of strategies for effectively modifying the spreading rate of shear layers formed at the exit of a jet. The ability to control natural evolution, and consequently enhance mixing characteristics of turbulent jets, has only been made possible by the discovery of coherent structures.

The evolution of this coherent structure in jets and wakes is known to be very sensitive to the nature of the underlying basic flow field[2]. Controlling the coherent structures and vortex interaction can be quite helpful in several technical applications, such as combustion, chemical processes, diffusion flames, and ejectors. The existence of large-scale coherent structures in shear flows has been confirmed by a number of experimental observations. Due to the fact that coherent structures in turbulence have been shown to play an important role in the dynamic relationship

with turbulent flow, the flow control group has focused on these coherent structures[3]. Development of robust, effective and flight-worthy excitation devices has posed a serious challenge to bridging the gap between the laboratory discoveries and flight-prototype hardware. Theoretical hydrodynamic stability analysis of swirling jets has been conducted by several researchers. From these studies, it was concluded that instability waves that counter-spin to the swirling jet (turning in the opposite direction from the swirling jet itself) posses the highest spatial amplification factors[4]. These waves are known to be responsible for the formation of large-scale coherent structures and mixing enhancement. Basically, controlling the flow is characterized by enhancing the turbulence mixing rate or increasing the energy entrainment from the outside of the boundary layer into the inside, especially retarding, preventing flow separation, or reducing drag.

Turbulent flow control can generally be divided into two parts, active or passive, according to the existence or absence of continuous or intermittent dynamic energy input. In the case of the active control, the fundamental approach begins with the generating of an artificial turbulence or the supplying of momentum and energy into the flow using an additional device. On the other hand, the passive control

approach has major advantages over the active one due to the following factors:

- It involves a simple mechanism

- It achieves volume and weight reduction

- It prevents flow separation or drag from the excitation device itself

- It is free from the thermal deformation (e.g., speakers for acoustic excitation)

Generation of pure and controllable helical waves to excite the natural fast-growing instability waves has always been a difficult task. Among many attempts, an array of loud speakers have been placed surrounding the jet. The impracticalities of such excitation generators, among other problems, have prevented a realistic and practical application of this important physical phenomenon to date. Motivated by the above arguments, the following research activities were carried out:

- To generate coaxial dual swirl flows, a device that is capable of supplying co- and counter-swirl was designed, fabricated, and applied.

3

- To incorporate a novel, robust mechanical excitation device that is capable of producing disturbances, mechanically and passively, rather than acoustically and actively, which has traditionally been done, such a novel device was designed and built. It facilitates future hardware design for practical applications.

- To reveal the controlled characteristics of the coherent structure from the excitation at different swirl jet conditions, various jet flow properties were measured by a stereoscopic particle image velocimetry (PIV), and their results are presented.

- To analyze the excitation effects from helical disturbances, the computational models were generated, and their results are simulated numerically.

The above unique facility is used to excite the instabilities of various swirl jet combinations (i.e., inner and outer jet independently) at different modes (i.e., m=0, m=1, m=2, m=3, and m=4, where 'm' is the azimuthal wave number for experimental analysis). For the numerical analysis, the effects of growth of helical

instability waves of different modes (i.e., h=0, h=-1, h=-2, h=-3, and h=-4, where 'h'

is the helical wave number for computational simulation) on swirl flow

characteristics are demonstrated and analyzed.

2. REVIEW OF LITERATURE

A turbulent jet with swirl exhibits distinctive characteristics which are absent in their non-rotating counterparts[5]. For example, a subsonic swirl-free jet experiences, theoretically, no static pressure gradient in the radial or axial direction. Therefore, in this case, the mechanism for jet spread is dominated by the turbulent mixing at the mean characteristic boundary between the jet and the ambient fluid. At low degree of swirl the adverse pressure gradient is not enough to cause axial recirculation. However, a turbulent jet with strong swirl is primarily driven in the near field by the static pressure gradients in both radial and axial directions. It results in axial recirculation in the formation of a central toroidal recirculation zone (CTRZ), which is not observed at a weaker degree of swirl.

2.1. Turbulent Jets with Swirl
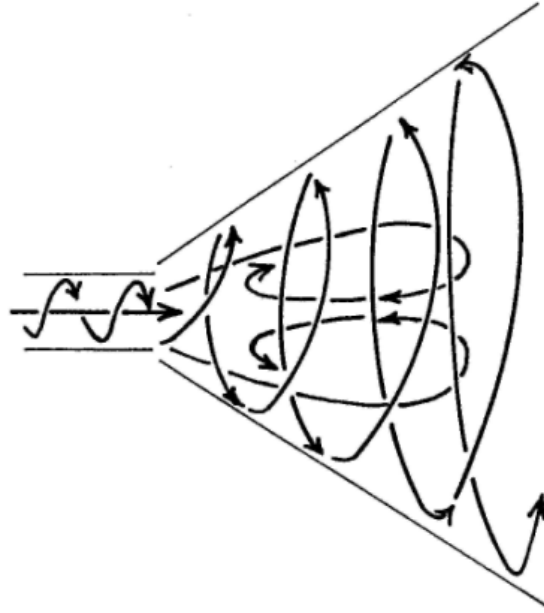
Figure 2.1 Typical jet flow with high degree of swirl

Figure 2.1[6] illustrates the recirculation bubble produced. Of course, the precise effect is found to depend on many factors as well as the swirl number; for example, nozzle geometry, size of enclosure, if any, and the particular exit velocity profiles[6]. Then, turbulent mixing becomes a major factor only when the strong pressure gradients are weakened through rapid initial jet spread. The occurrence of flow reversal in the jet, or what is known as vortex breakdown, is a fascinating phenomenon observed in high-intensity swirling flows.

S is essentially the ratio of jet mean torque to jet thrust, non-dimensionalized, with the nozzle radius after Gupta, Lilley, and Syred[6].

$$S = \frac{G_\theta}{G_x R} \qquad (2.1)$$

where the jet torque is

$$G_\theta = 2\pi \int_0^\infty \rho U W r^2 dr \qquad (2.2)$$

the jet axial thrust is

$$G_x = 2\pi \int_0^\infty [\rho U^2 + (p - p_\infty)] r dr \qquad (2.3)$$

and R is the nozzle exit radius. Originally, the degree of swirl in the experiment of Chigier and Chervinsky[7][8] was defined as:

$$G = \frac{W_{m0}}{U_{m0}} \qquad (2.4)$$

which is the ratio of maximum mean tangential-to-axial velocity at the nozzle exit. The realistic relationship between S and G can be expressed as[6]:

$$S = \frac{G/2}{1 - G/2} \tag{2.5}$$

To introduce a new correlation for the swirl number of a radial-type swirl generator, an investigation[9] (Sheen et al., 1996) was undertaken under various Reynolds' numbers and vane angle conditions. Based on the experimental results, a modified swirl number S is derived as:

$$S = \frac{\dot{M}^2}{4\pi^2 \rho BR \int\limits_0^\infty \rho U^2 r dr} \sigma(\phi) \tag{2.6}$$

where $\dot{M}$ is the mass flow rate, B is the axial width of the annular channel, and σ is the ratio of the mean tangential and radial velocity components at the swirler exit.

The vane angle ϕ is the angle of the guide vane with respect to the radial direction, and the value of σ can be obtained as:

$$\sigma(\phi) = \frac{1}{1 - \psi} \left(\frac{\tan \phi}{1 + \tan \phi \tan(\pi/z)} \right) \tag{2.7}$$

where $\psi = zs/2\pi R \cos \phi$ is a blockage factor that comes from the finite thickness of the guide vanes, z is the number of vanes, and s is the thickness of the vanes.

In 2003, experimental investigation (Ivanic et al.)[10] of the near-field structure of coaxial flows was presented for different configurations: coaxial jets without rotation (reference case), outer flow rotating only, inner-jet rotating only and co-rotating jets. The effects of azimuthal velocity and axial velocity ratio variations on flow dynamics are examined. Recently, Garcia-Villalba et al., presented analytical research[11] using a large eddy simulation (LES) of unconfined swirling jets (2006). The impact of the swirl on the mean flow and the precessing vortex structures is analyzed. The investigations show that the additional swirl near the axis has a stronger effect than the pilot jet itself, leading to an almost entire removal of coherent structures.

2.2. Flow Instability

Swirl is naturally presented in the exhaust from a turbine or an axial flow pump, and may be deliberately generated, in some cases, to influence jet mixing through design of the jet nozzle[1]. Experiments have revealed that low-speed, swirling jets can, under some conditions, realize higher spreading and entrainment

rates than their non-swirling counterparts[12]. These results have spurred the formulation of several instability studies aimed at elucidating the competition of azimuthal and streamwise vorticity in determining the growth of either axisymmetric or helical disturbances in a circular jet. There are two basic types of inviscid instability which operate concurrently in swirling jets, the shear instability (associated with the inflection point in the streamwise velocity profile, the so-called Kelvin-helmholtz instability), and the centrifugal instability associated with the radial profile of the swirl.

According to Rayleigh's criterion for inviscid instability of rotating flows[3], i.e.,

$$\frac{d\Gamma^2}{dr} < 0 \quad \text{(unstable)} \qquad (2.8)$$

where Γ is the fluid circulation and r is the radial coordinate, Rayleigh regards all free swirling jets as unstable. Rayleigh first suggested the analogy between swirl and density gradient in a gravitational field, the so-called Rayleigh's analogy. Furthermore, Howard and Gupta[13] were the first to derive an inviscid instability criterion for a swirling flow based on Rayleigh's analogy. The non-dimensional

parameter governing the stability of swirling flows was shown to be:

$$J(r) = \frac{\dfrac{1}{r^3}\dfrac{d}{dr}(r^2 W^2)}{(\dfrac{dU}{dr})^2} > 0.25 \quad \text{(stable)} \tag{2.9}$$

for all r in the fluid. Howard-Gupta's criterion is a sufficient condition which maintains for the instability of the axisymmetric flows only. Later, Lalas[14] extended the Richardson number criterion of Howard and Gupta to compressible fluids and non-axisymmetric disturbance modes. By far the most extensive analysis of the stability of a shear layer has been carried out by Michalke[15]. Freymuth's[16] experiments in an acoustically excited shear layer confirmed Michalke's predictions of the growth rates associated with different Strouhal numbers. The Strouhal number is a non-dimensional frequency based on the nozzle exit diameter (d), mass averaged axial velocity (U), and excitation frequency (f) defined as:

$$St = \frac{fd}{U} \tag{2.10}$$

Michalke[17] also analyzed the axisymmetric mixing layer, considering the ratio of the jet diameter (D) to the shear layer momentum thickness (θ) as a

parameter, and found a general agreement with the result of Crow and Champagne's experiments. Bechert and Pfizenmaier,[18] in a subsequent experiment, confirmed Michalke's prediction of phase velocities greater than the jet velocity occurring at low Strouhal numbers and for large D/θ. For the flow stabilization in a channel with a swirled periphery jet, an experimental study was carried out by Volchkov et al., in 2000[19]. They found that the swirling of a peripheral jet significantly weakens its mixing with the main flow. With a rise in the swirling angle, the turbulence intensity at the channel's axis decreases. The suppression effects increase with a rise of the jet injection parameter. Recently, the spatial evolution of small-amplitude unsteady disturbances of an axisymmetric swirling jet has been theoretically examined (Cooper et al., 2002[20]). Numerical results show that the growth of the centrifugal mode is significantly curtailed as a result of rapidly decaying envelope amplitude. The shear instability is significantly more amplified by the addition of swirl.

2.3. Flow Control for Enhanced Mixing

Mixing enhancement in swirling jets by using passive and active means was intensively investigated in the late 1980s[5][21][22]. First, regarding the passive part, the initial swirl distribution as a means of manipulating the growth characteristics of centrifugal instabilities has been shown to dominate the streamwise evolution of swirling jets. Second, on the active control front, turbulent swirling jets were excited via plane acoustic waves[21][22]. At the preferred Strouhal number and larger forcing amplitude, a mixing of a swirling jet (i.e., its rate of spread) was enhanced by using plane acoustic waves. However, linear hydrodynamic stability theory shows that helical disturbances of negative spin exhibit the most effective growth rates. Hence, the augmentation of Taylor-Gortler vortices dominating in the shear layer of a swirling jet is far better achieved by non-axisymmetric excitation of negative helicity. This is in contrast to the non-swirling jets which are dominated by Kelvin-Helmholtz instability waves, and which are more receptive to the plane wave excitation.

Past experimental[23][24] and numerical[25] studies indicate that excitation can increase turbulence intensity and enhance flow mixing in shear flows, resulting in

increased spread rates and a reduction in jet plume temperature. In 2003, Merkle et al. investigated[26] the effect of co- and counter-swirl on the isothermal flow- and mixture-field of an air blast atomizer nozzle. The analysis of turbulence quantities shows a considerable attenuation of the turbulent exchange of momentum perpendicular to the main flow direction for counter-rotating airflows. According to Rayleigh's criterion, this effect is attributed to the weaker reduction of the radial profiles of the time mean tangential velocity within the domain of the near-nozzle outer jet boundary in the case of the counter-swirl configuration. Analogous to the exchange of momentum, the obtained mixture fields feature a reduction of the turbulent mass transfer rate in the radial direction with counter-rotating airflows. The flow structures and turbulence properties of double concentric jets with a large separation between the central jet and swirling annular flows are studied using the smoke-wire flow visualization technique and a two-component laser Doppler velocimetry (Huang et al.[27]). The smoke-streak patterns show that a large spatial separation at the exit between the central and swirling annular jets can expedite the formation of a recirculation zone at low swirl and low Reynolds numbers. Complex flow structures, single bubble, dual rings, vortex breakdown, and vortex shedding, are found in the recirculation zone.

2.4. Experimental Investigations of Swirling Jets

The evolution of a subsonic swirling turbulent jet issuing from a nozzle into ambient fluid depends upon the various methods of swirl generation[4]. This fact was acknowledged by Chigier and Beer[28], Pratte and Keffer[29], and others. The design of swirl generators in practice today, uses the following concepts of swirl generation:

- Adjustable vanes

- Axial and tangential entry swirl generators

- Spinning, fully developed pipe flows emerging from a long rotating tube

- Flow through a rotating perforated plate

Several experimental studies of swirling jets have been performed. One remarkable work that needs to be mentioned here was accomplished by Chigier and Chervinsky[7][30]. They have performed experimental and theoretical studies of turbulent swirling jets issuing from a round nozzle. Swirl was experimentally generated by an axial and tangential entry swirl generator. The mean flow data and

static pressure were taken by means of a five-hole spherical impact tube, and their traverses were made at eight axial stations: x/D=0.2, 1.0, 2.0, 4.1, 6.2, 8.3, 10.0, and 15.0 The swirl numbers tested were S=0.066, 0.134, 0.234, 0.416, 0.600, and 0.640. It was found that in weak-to-moderate swirls (S≤0.416), similarity profiles exist for axial readings (x/D≥2). For strong swirling flows (e.g., S≥0.6), the mean axial velocity distribution shows a central trough, or what is also known as a "double-hump profile", where the similarity was not observed until 10 diameters were reached. For x/D>10, the locations of the maximum mean axial velocity shifted back to the jet centerline, from which point the similarity appeared. Theoretically, Chigier and Chervinsky[29][7] applied boundary layer approximations for assumptions of similarity profiles to integrate the equations of motion for incompressible turbulent flow. The similarity of the mean axial velocity and pressure profiles were described by Gaussian error distributions, and the mean tangential velocity profiles were expressed in terms of third-order polynomials. The empirical constants of the similarity profiles were obtained from curve-fitting of the experimental data. Chigier and Chervinsky's work[7][30] resulted in the analytical-empirical expressions of the mean velocity and static pressure profiles for weak to moderate swirl numbers.

2.4.1. Plane Wave Excitation

The first experiment of the controlled excitation of a cold turbulent swirling jet was done by Rice et al.[8][21]. The experiments were carried out for flow with a swirl number of 0.35 and Mach number of 0.26. The time-mean axial velocity distribution did not have a "top-hat" radial profile at the nozzle exit. The excitation level of plane acoustic waves was held constant at 124dB at various Strouhal numbers ranging from 0.326 to 0.903. The results showed that even if the axial velocity distribution at the nozzle exit did not have a "top-hat" profile, the instability waves were amplified rapidly in the streamwise direction, reaching a maximum in amplitude and then decaying further downstream. Excitation at a Strouhal number of 0.4 exhibited the largest growth. Therefore, the "preferred" Strouhal number was found to be 0.4, based on the nozzle exit diameter, mass averaged axial velocity and excitation frequency. Furthermore, it was observed that the instability waves peaked closer to the nozzle exit, and their maximum amplitudes were only about 50% of their counterparts in non-swirling jets having the same mass flux, Mach number, and Reynolds number. At this forcing level, the mean velocity components of swirling

jets did not experience any change. In addition, Taghavi et al.[22] further investigated the effect of large amplitude plane wave excitation on the turbulent swirling jets. The emphasis of the research was to study the influence of excitation on mean flow characteristics. To accomplish this objective, a new acoustic driver system that was capable of providing a much larger excitation amplitude was used. Also, the experiments were conducted at lower swirl numbers than in the previous study. At a swirl number of 0.12, the radial profiles of axial velocity were nearly of the "top-hat" shape, which was believed to be more susceptible to the excitation. The Mach number for the tests was 0.22, and the maximum forcing amplitude of excitation was at 6.88% to the time-mean axial velocity. The results showed that the "preferred" Strouhal number was about 0.39, and that the time-mean velocity components of swirling jets experienced a change. The axial velocity decayed faster along the jet centerline, reaching about 89% of its unexcited value at x/D=9. Furthermore, the half velocity radius and momentum thickness, at seven nozzle diameters downstream, increased by 13.2 and 5.8%, respectively, indicating more jet spread and enhanced mixing. The comparison of the variation of momentum thickness along the jet axis for unexcited non-swirling jets and swirling jets with a swirl number of 0.12 was

19

made. Hence, the comparison showed that the momentum thickness for the swirling

jet is larger than that of the non-swirling jet. The turbulent-free jet, with a higher

swirl number of 0.18, was also excited at the same amplitude as before, and at

various frequencies. Even though the instability waves exhibited growth along the jet

axis, no effect on the spreading rate and mixing enhancement was observed as a

result of excitation. The experimental data showed that the distribution of turbulence

intensity along the jet axis for an unexcited jet at the swirl number of 0.18 almost

coincides with that of the excited jet with a swirl number of 0.12. It seems that a

swirling jet with higher turbulence intensity is less excitable. Increasing the upstream

turbulence diminishes the excitability of the jet and reduces the effect of excitation

on the spreading rate of the jet.

2.4.2. Helical Wave Excitation

In 1990, Kusek et al. introduced[31] the seeding of helical modes in the initial

region of an axisymmetric jet. They investigated the ability to seed ±m helical modes

with an azimuthal array of twelve miniature speakers. The speakers were mounted at

the face of the jet, in close proximity to the exit lip.

Panda et al. (1993) conducted experiments[12] on the instabilities in swirling and non-swirling jets at Reynolds numbers ranging from 20,000 to 60,000. The excitation system consists of four large acoustic speakers arranged circumferentially around the jet. Their main emphasis was on the instabilities in the near field ($x/D \leq$ 2.5) of free swirling jets with swirl numbers of 0.45 and 0.5. Both axisymmetric (i.e., m=0) and asymmetric (i.e., m=±1) helical disturbances were employed. They found that the shear layer from the nozzle exit of the swirling jet develops Kelvin-Helmholtz instability waves that roll up into large-scale organized motion. This is similar to the behavior of excited non-swirling jets. They found that:

- Kelvin-Helmholtz instability waves of helical (both m=+1 and m=-1) and axisymmetric (m=0) modes are found to exist in the shear layer around the periphery of a swirling jet.
- The growth rate of the helical m=-1 mode is relatively higher than the axisymmetric mode growth rate.
- In general, the total growth of the instability waves is smaller in swirling jets compared to the non-swirling condition.

A numerical approach[32] was done by Hilgers et al., in 2001. The jet is excited with helical and combined helical and axial actuations at the orifice. The optimization procedure searches for the best actuation by automatically varying the parameters and calculating their objective function value. The result shows that a combined axial and helical actuation is much more efficient with respect to jet mixing than a helical actuation alone. Recently, in 2004, experimental study[33] of a free and forced swirling jet was carried out by Gallaire, Rott, and Chomaz. The study concerns the response of a swirling jet to various azimuthal modes and frequencies forced at the nozzle exit. The different unforced dynamical states are first described as a function of the swirl setting, determined from measured velocity fields in the longitudinal plane using particle image velocimetry. A second experimental technique, based on laser induced fluorescence, is described, which is more suited to the description of the low-amplitude response of the jet to the forcing. It is shown that the receptivity of the jet is very poor when the forcing is set to the naturally prevailing azimuthal mode (m=2) and frequency. In contrast, a strong response is observed for both co-rotating and counter-rotating forced azimuthal modes (m=±2, m=±3) for frequencies about one order of magnitude larger than the frequency

prevailing in the absence of forcing. Finally, the actuator is seen to be ineffective in

preventing the appearance of vortex breakdown itself.

3. APPARATUS AND TEST CONDITIONS

Figures 3.1 through 3.3 show the schematic layout and photographs of test facility at the Korea Aerospace Research Institute (KARI) in South Korea. This versatile setup is designed to either supplement KARI's 'Wind Tunnel Laboratory' or as an independent set-up at the 'Propulsion Laboratory'.

3.1. Experimental Test Facility

The "basic" facility consists of pressure vessels, air compressors, stilling chambers, subsonic nozzles, swirl generators, an excitation device, and flow measurement equipment. The mechanical excitation device is located on the inner surface of each subsonic nozzle. The components of the test facility are categorized in three sections (Table 3.1).

Table 3.1 Summary of Test Facility Components

➕ **Flow Supply and Mass Flow Control (Section I)**

Pressure vessels, valves, regulators, thermocouples, pressure differential gage, data acquisition system (DAS), particle generator, air compressors, DC power supply, etc.

➕ **Swirl Generators and Excitation Device (Section II)**

Stilling chambers, flow pipes, plastic tubes, swirlers, hub-cone, subsonic nozzles, etc.

➕ **Measurement Instrumentation (Section III)**

CCD cameras, laser, IMAQ PC, delay generator, DAS, etc.
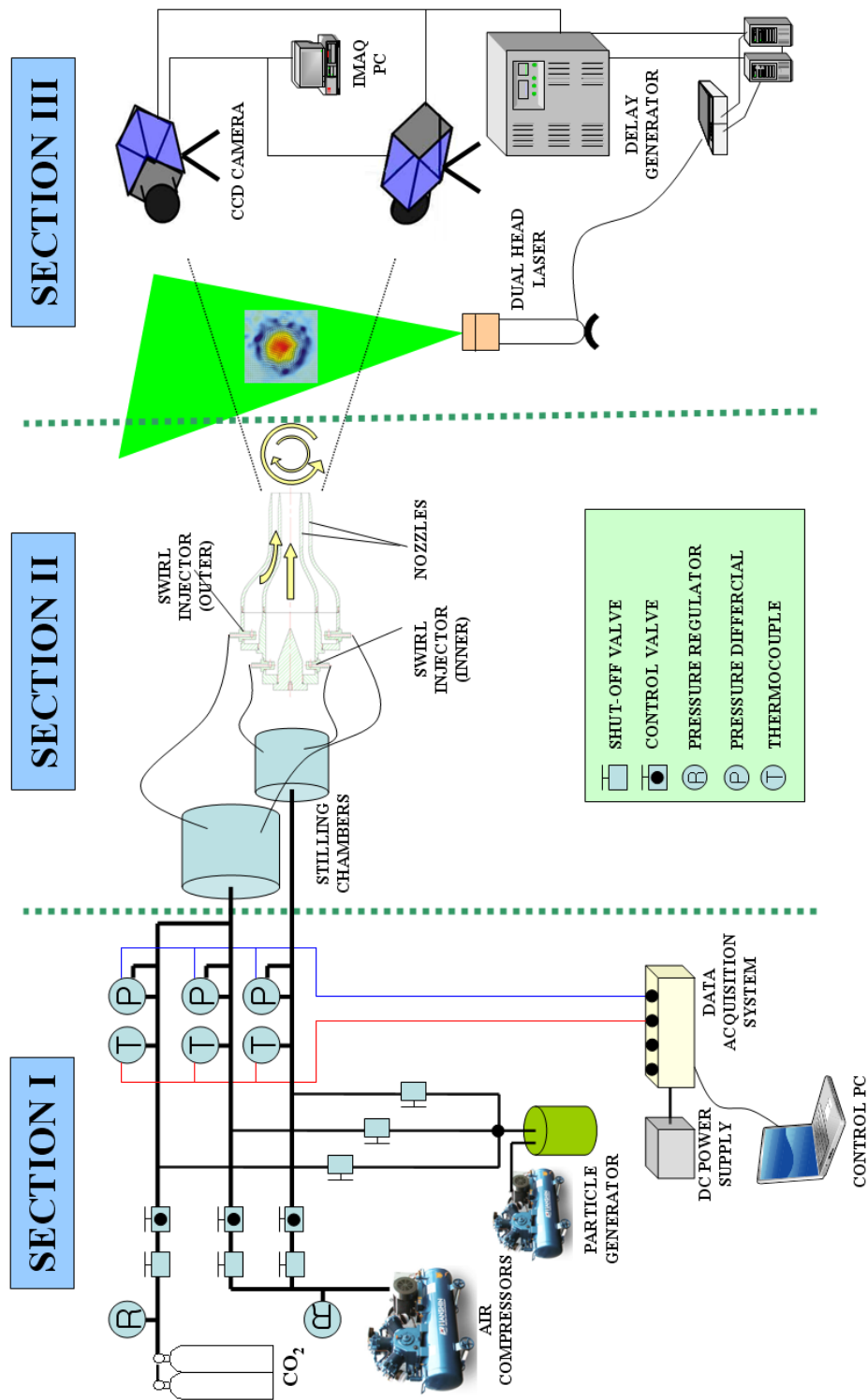
Figure 3.1 General arrangement of test facility

Particle Chamber

Figure 3.2 Test facility with particle chamber
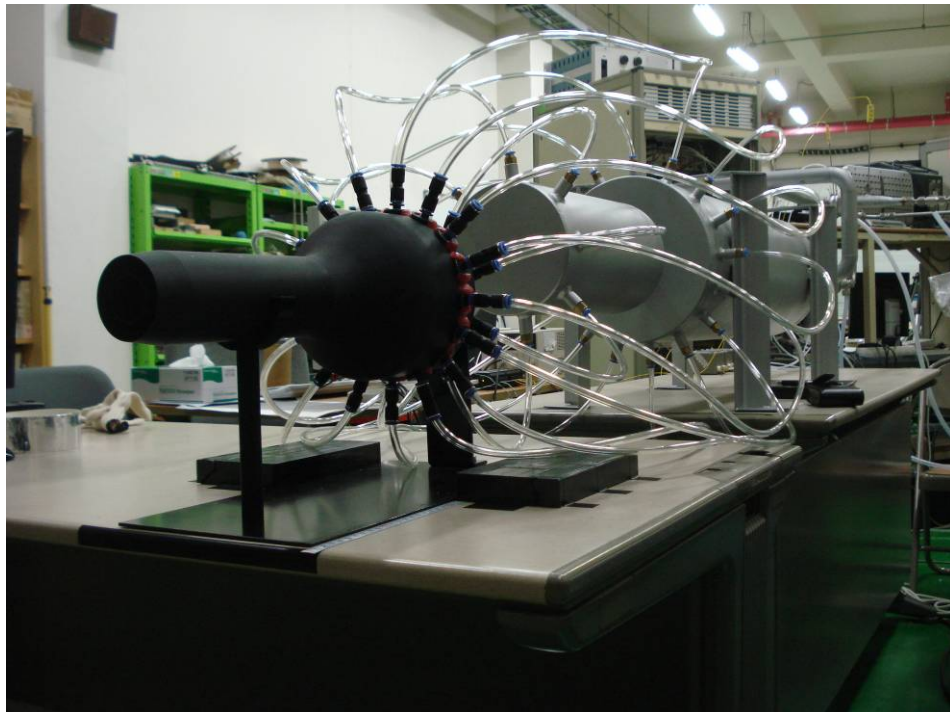
Figure 3.3 Facility of subsonic dual concentric swirl jet

3.2. SECTION I: Flow Supply and Mass Flow Control

This section is composed of pressure vessels, valves, regulators, thermocouples, pressure differential gages, a data acquisition system, a particle generator, air compressors, a DC power supply, and others. Figure 3.4 shows the solid model of major parts for 'SECTION I'.
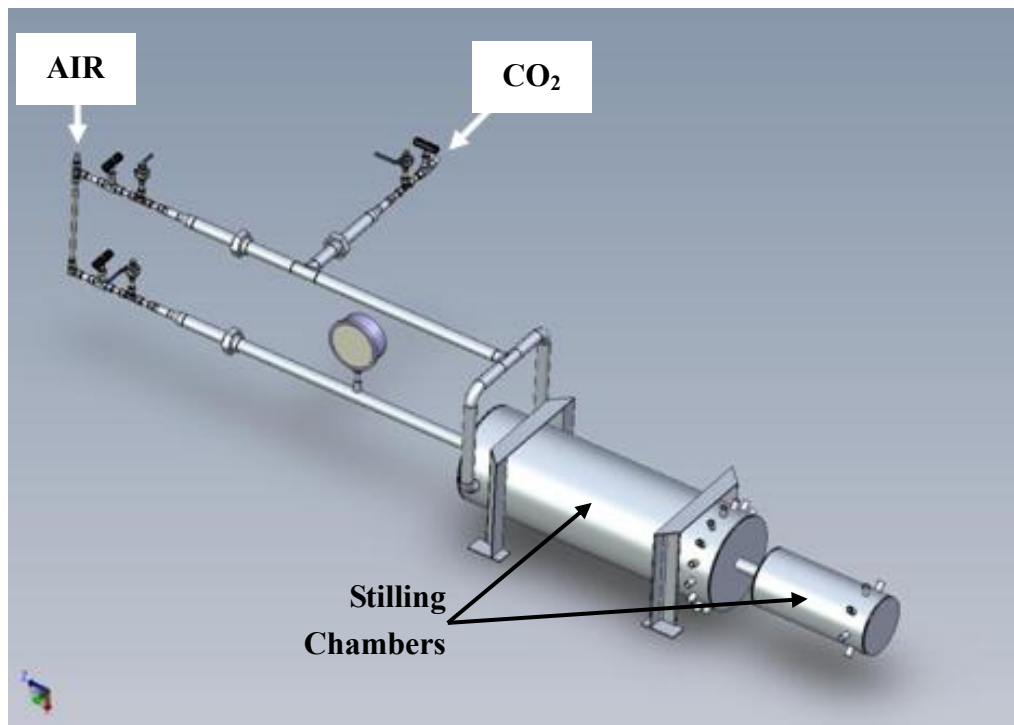
Figure 3.4 Subsonic jet facility

3.2.1. Flow Supply

Two kinds of fluid media, air (ρ=1.16 @ 300K) and CO_2 (ρ=1.77 @ 300K), are selected for the experiments. Especially, to analyze the effects of density difference, CO_2 (ρ=1.77 @ 300K), which is non-toxic and non-inflammable, is selected. To supply the continuous source of air, a piston-type reciprocating compressor (Figure. 3.5) is used. In the case of CO_2, the pressurized (@ 34bar) tanks (Figure 3.6) which contain gases (up to 47 liter per vessel) are used as the source of jet fluid. The specification of the air compressor is summarized in Table 3.2. To avoid the pressure fluctuation from the compressor and the gradual pressure drop from the vessels, high pressure regulators (Figure 3.7) are installed.

Table 3.2 Specification of Air Compressor

Power	7.5 kW
Working Pressure	$7.5 \sim 9.9$ Kgf/cm^2
Piston Displacement	1,272 liter/min

Figure 3.5 Piston-type air compressor

Figure 3.6 Pressure vessels of CO₂

Figure 3.7 High pressure regulator

3.2.2. Mass Flow Control

Figure 3.8 shows the picture of the data acquisition system (DAS) for flow temperature and pressure measurements. This includes orifices, pressure taps, pressure differential gages, a data acquisition board, a DC power supply, thermocouples, and a control computer. To derive the mass flow rate of each pipe, precise information regarding pressure and temperature is required. For this purpose, three different thin plate types of orifices (Figure 3.9) are designed, fabricated, and installed between the pipes (Figures 3.10 and 3.11). The location of the pressure taps

are displayed in Figure 3.10. To measure the static pressure difference between the

upstream and downstream of orifices, tiny flexible tubes (Figure 3.12) are connected

from each pressure tap to a pressure differential gage terminal. Then the signals from

the pressure gages (Figure 3.13 and Table 3.3), which are powered by a 24V DC

power supply (Figure 3.14 and Table 3.4), are transmitted to the control computer

(Figures 3.15 and 5.16) through the data acquisition board (Figure 3.17 and Table

3.5). The orifices and pressure taps are designed and manufactured according to the

design handbook[34] with accuracy. The location of the pressure taps are displayed in

Figure 3.9.

Figure 3.8 Data acquisition system (pressure & temperature)
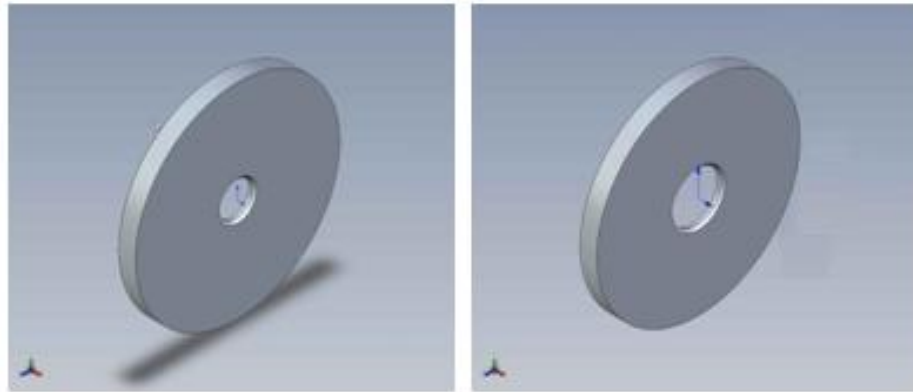
(a) Inner jet flow (air)　　**(b) Outer jet flow (air)**
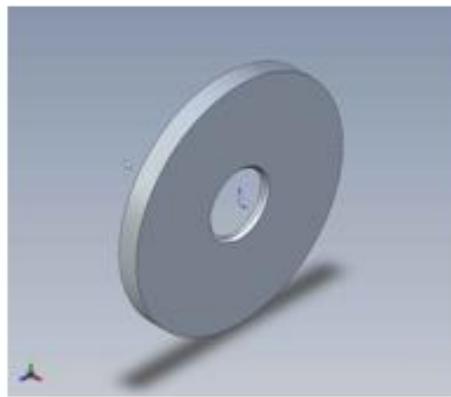
(b) Outer jet flow (CO$_2$)

Figure 3.9 Thin plate type orifices for various flow conditions

(Orifice diameter (a) 7.9 mm (b) 11.8 mm (c) 12.8 mm)
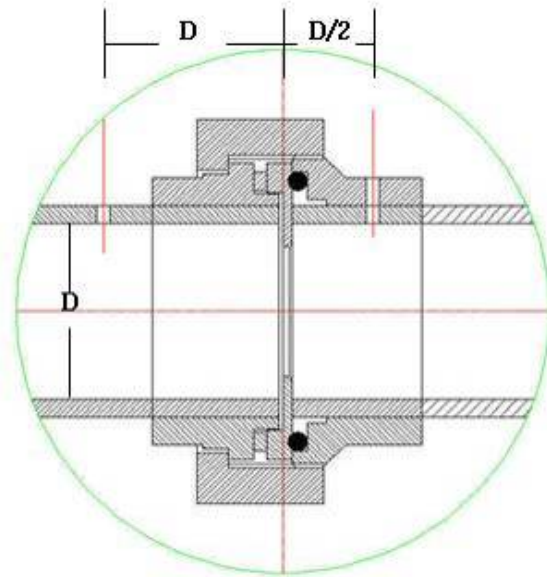
Figure 3.10 Location of orifice and pressure taps for measurement of pressure difference (D = 28.4 mm)
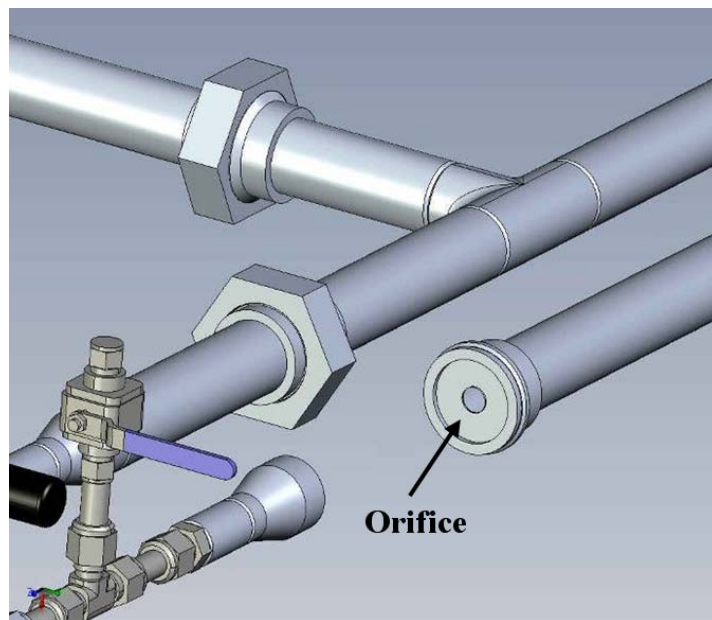
Figure 3.11 Installed orifices between pipes
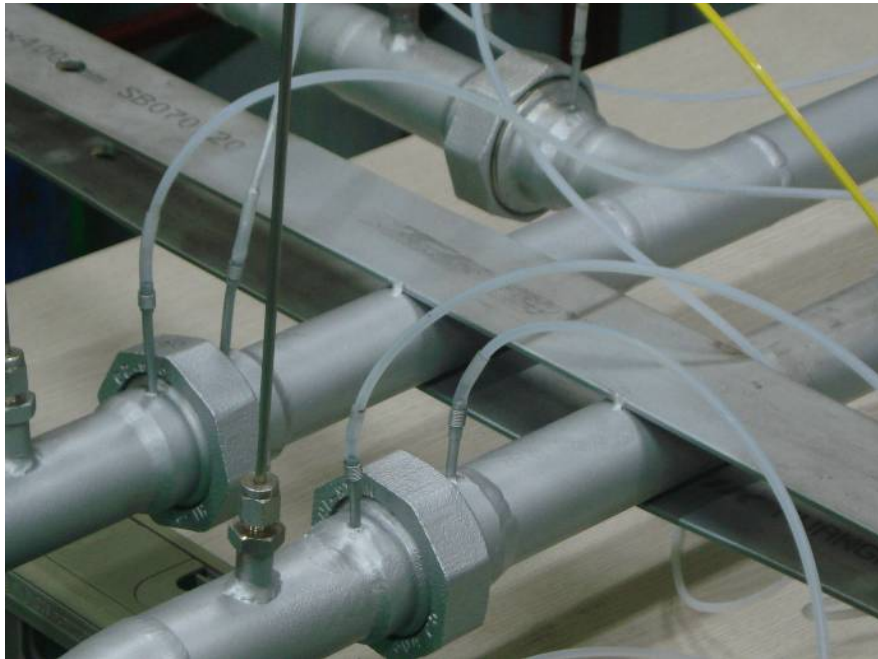
Figure 3.12 Pressure tap tubing with installed orifices

Figure 3.13 Pressure differential gage

Table 3.3 Specification of Pressure Differential Gage

Excitation	12 ~ 36 VDC
Output	4 ~ 20 mA (2 wire)
Repeatability	0.05% FS
Operating Temp	-29 to 85°C
Proof Pressure	10 psi
Burst Pressure	50 psi
Static Pressure	100 psi
Gage Type	capacitance
Response Time	0.25 sec

Figure 3.14 DC power supply

Table 3.4 Specification of DC Power Supply

Company	EZ Digital
Model	GP-4303D
Output Voltage	$0 \sim 30$ V
Output Current	$0 \sim 3$ A
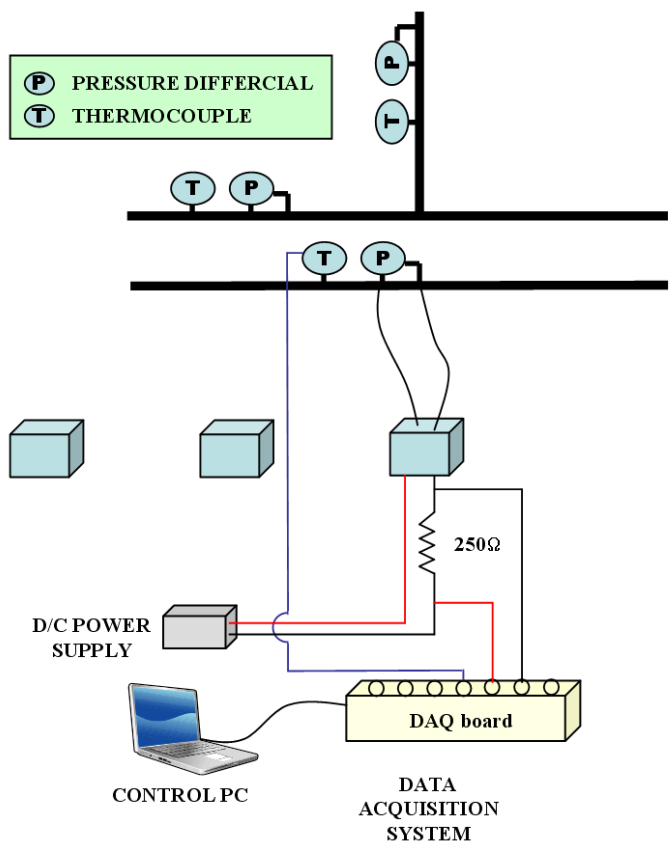
Figure 3.15 Schematic of data acquisition system (pressure & temperature)
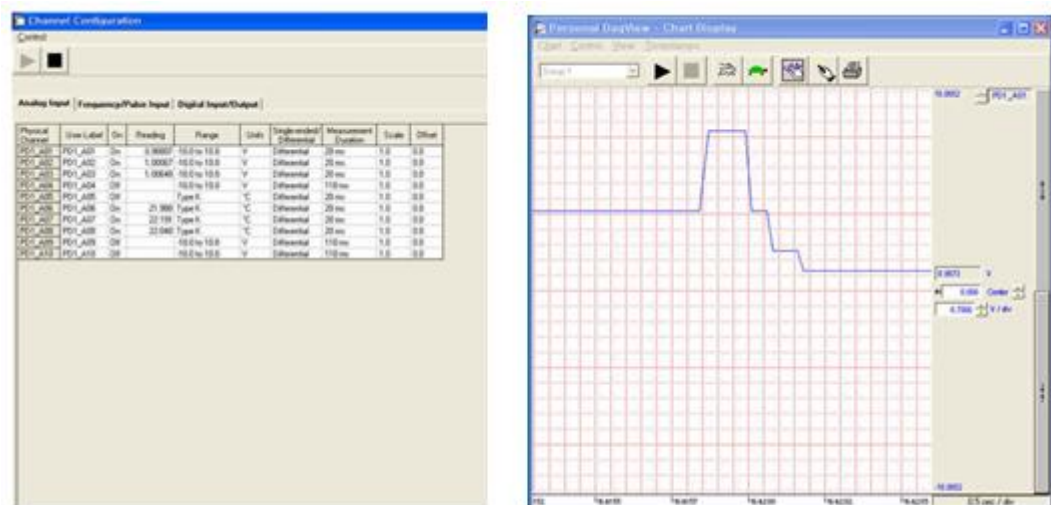
Figure 3.16 View of data acquisition windows (temperature and pressure)

Figure 3.17 Data acquisition board

Table 3.5 Specification of Data Acquisition Board

Company	IOTECH
Model	Personal Daq56
Resolution	up to 22 bit
Sample Rate	up to 80 Hz
Voltage Range	±0.03 ~ 20 V

3.2.3. Temperature

In addition to pressure, temperature measurements are carried out for each of the tube flows (Figure 3.18). Temperatures are acquired using K-type thermocouples (Figure 3.19), and the signals are also transmitted to a control computer through the data acquisition board. The summary of the thermocouple device is tabulated in Table 3.6.
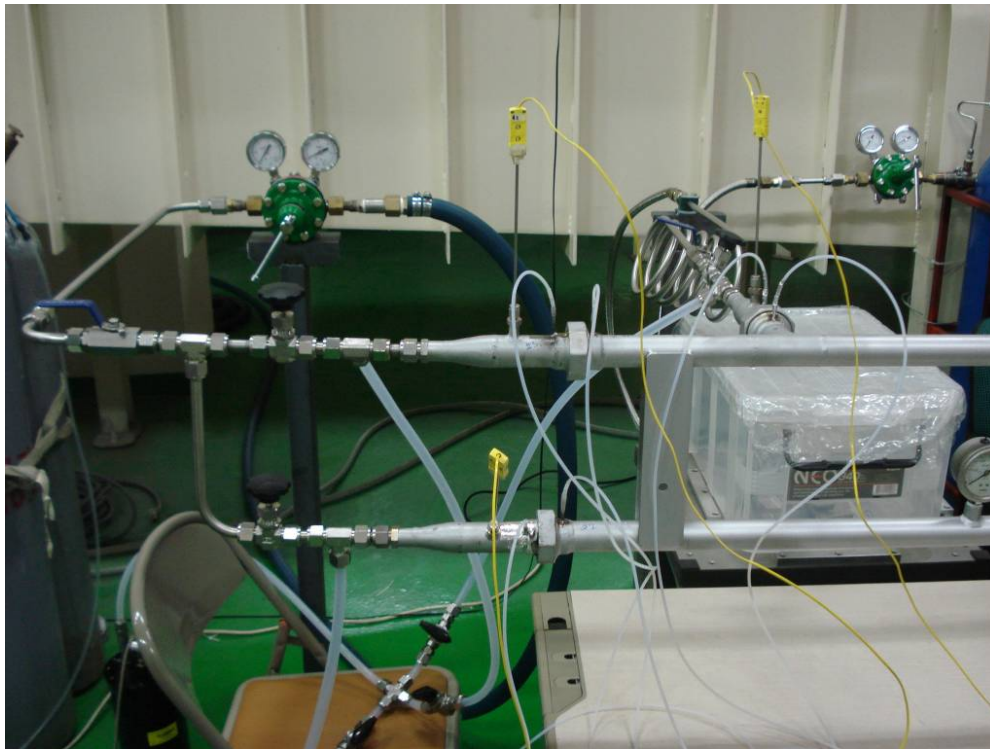
Figure 3.18 Installed thermocouples
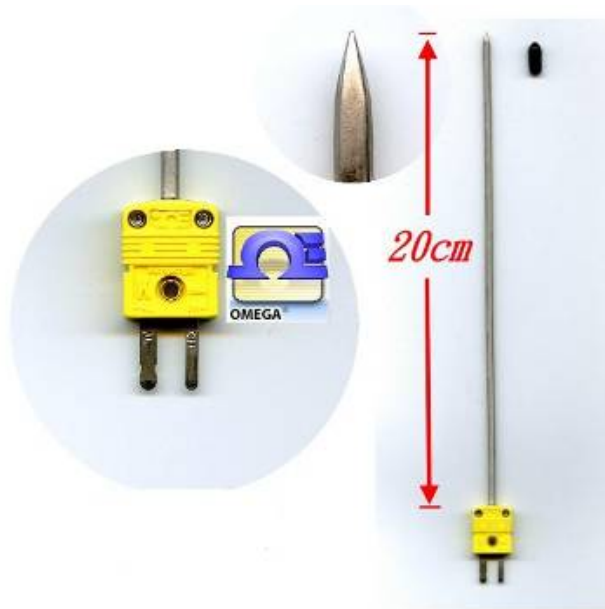
Figure 3.19 Photograph of thermocouples

Table 3.6 Specification of Thermocouple

Company	OMEGA
Type	K-type
Temperature Range	0 ~ 800 °C (using 0.6 mm diameter wire)

3.2.4. Particle Seeding

For a particle image velocimetry (PIV) application (i.e., illumination) the particle generator (Figure 3.20 left) is utilized. It supplies tracing particles to the measurement fields with enough flux and concentration. In a wind-tunnel environment, for instance, oil smoke produces relatively uniform seeding. The minimum detectable particle diameter is a function of the recording optics and the laser input energy. Generally, the particles which have approximately a one micrometer size are required for stereoscopic PIV applications (air). In this research, di-ethyl-hexyl-sebacat (DEHS) fluid (Figure 3.20 right) is selected, and the details of its particle generator are illustrated in Table 3.7.

The step response of U_p typically follows an exponential law if the density of the particle is much greater than the fluid density:

$$U_p(t) = U\left[1 - \exp(\frac{t}{\tau_s})\right] \qquad (3.1)$$

with the relaxation time τ_s given by:

$$\tau_s = d_p{}^2 \frac{\rho_p}{18\mu} \qquad (3.2)$$

where U_p is the particle velocity, and d_p is the diameter of the particles.

The result of equation (3.1) is illustrated in Figure 3.21[35] where the time response of particles with different diameters is shown for a strong deceleration in air flow.

Figure 3.20 Particle generator (left) and DEHS fluid for particle seeding (right)

Table 3.7 Specification of Particle Generator

Operating principle	Laskin atomizer nozzles (up to 45 nozzles). fully adjustable through control of individual seeding nozzles (cascading)
Typical particle size	1 µm
Tested seeding materials	DEHS (Di-Ethyl-Hexyl-Sebacat) vegetable oils $C_{26} H_{50}O_4$
Operating pressure	up to 3 bar overpressure, safety valve set at 5 bar
Supply pressure	10 bar max, uses regulator
Applications	laser Doppler velocimetry (LDV) particle image velocimetry (PIV) planar (global) Doppler velocimetry (PDV) laser light sheet visualization
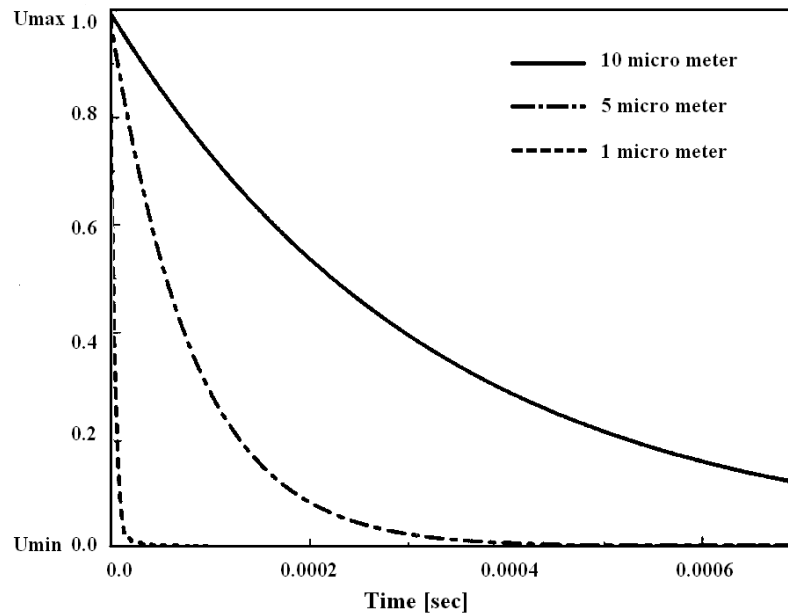
Figure 3.21 Time response of DEHS particles with different diameters in a decelerating air flow

3.3. SECTION II: Swirl Generators and Excitation Device

The components of SECTION II are as follows: stilling chambers, flow pipes, swirlers, a hub-cone, subsonic nozzles, and others.

3.3.1. Stilling Chambers and Connecting Tubes

Two stilling chambers, inner and outer, are located at the upstream part of the swirlers. The stilling chambers play a role in producing a uniform and equally pressurized flow, and these are made of large cylinders with enough axial length (i.e., more than ten times the upstream pipe diameter). Each stilling chamber has one-touch fitting orifices (eight fittings for the inner, and sixteen for the outer), and each orifice is connected to the swirl injectors by transparent flexible plastic tubes (Figure 3.22).

Figure 3.22 Photograph of SECTION II

3.3.2. Swirl Generators

To produce coaxial dual swirl flows, a unique device that is capable of generating co- and counter-swirl is designed, fabricated, and assembled. Solid models of inner- and outer-swirl generators are shown in Figure 3.23. Each swirl generator is composed of swirl injectors (eight for the inner and sixteen for the outer), a supporter, a hub-cone, and a reducer. Each injector (Figure 3.24) is connected to the fittings, which are located at the stilling chambers by the plastic tubes. Also, each reducer is fitted to inner and outer nozzles.

The swirl injectors can be controlled at angles with respect to the nozzle axial direction. The unique device can produce various swirl numbers (i.e., intensities) by adjusting the angles in the range between -45° and +45°. Figures 3.25 to 3.26 show a photograph of a manufactured swirl injector and the assembled swirl generators.
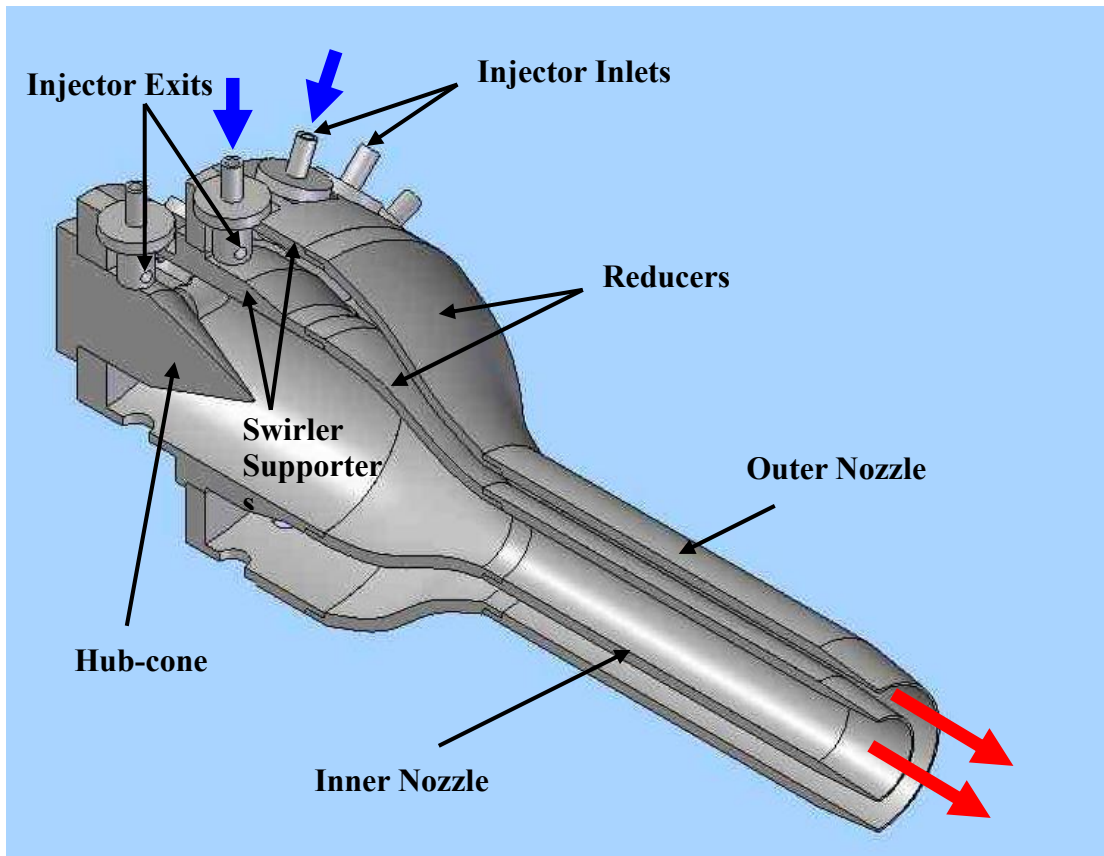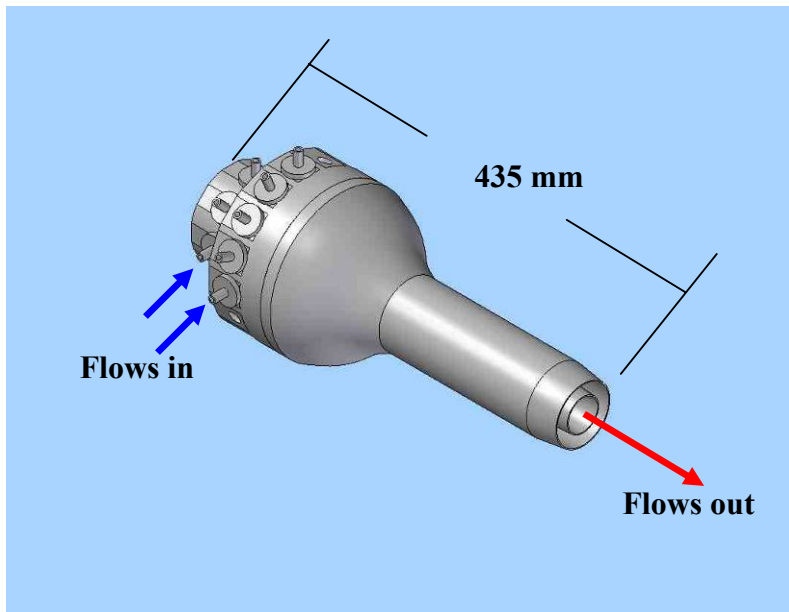
Figure 3.23 Combined swirl generators and nozzles
full view (upper), half cut-view (lower)
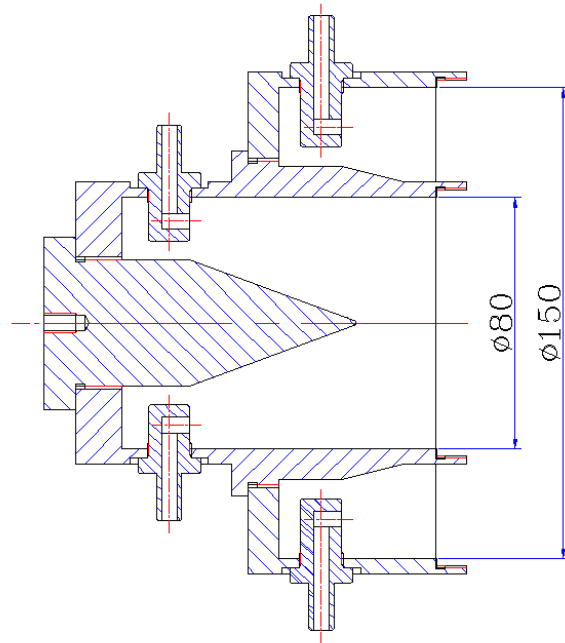
Figure 3.24 Two-dimensional assembly drawing of swirl generator (mm)
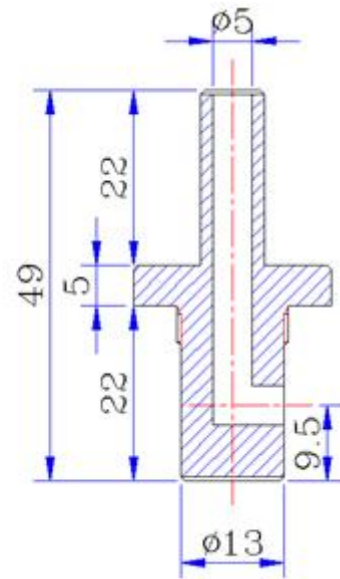
Figure 3.25 Swirl injector and one-touch fitting (left)
Drawing of swirl injector (mm, right)

Figure 3.26 Installed swirl injectors (inner and outer)
rear view (upper), front view (lower)

3.3.3. Excitation Devices

To incorporate a novel, robust mechanical excitation that is capable of generating exciting waves, mechanically and passively, a unique facility was designed and built. It facilitates future hardware design for practical applications. Figure 3.27 presents the layout of excitation disturbances. The excitation device is the most important part in this investigation. A tube (i.e., nozzle) with straight lobes is used as an excitation device, instead of using the conventional acoustic drivers. This unique device induces an azimuthal displacement/velocity perturbation normal to the shear layer. The perturbation amplitude induced by the internally contoured shape (with the prescribed lobe numbers) will remain invariant during testing. The up- and down-stream part of the contoured lobe(s) on the excitation device are flush with the inner contour of the circular nozzle exit to prevent vortex shedding and flow separation from the sharp corners, as shown in Figure 3.28. For all excitation tests, disturbances are imposed on the flow from four different lobe configurations on the inside surface of each nozzle. The lobe consists of straight '1~5mm' height thin plates (Figure 3.29) running the length of the nozzle. This height represents less than

10% of the inside diameter of the tube. It is also selected as "small" to prevent flow

from the vortex shedding and flow separation. A thin adhesive sheet of plastic is

wrapped around the inner surface of the tube and lobes. One-, two-, three-, and four-

lobed (i.e., m=1, 2, 3, and 4) nozzles are used for the excitation of swirling jets. In

addition, Figure 3.27 shows the definition of 'co-swirl' and 'counter-swirl.'
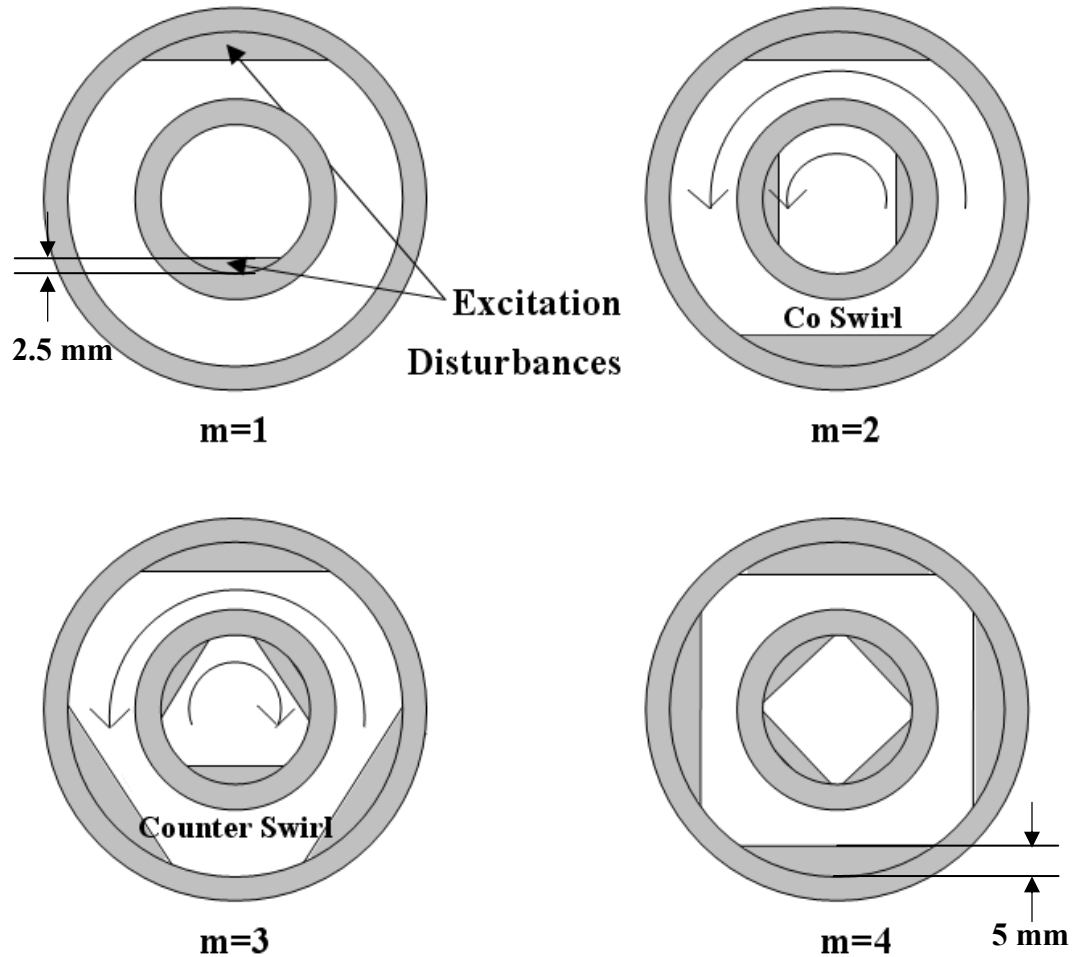
Figure 3.27 Layout of excitation disturbances for experimental set-up
(NOT IN SCALE)
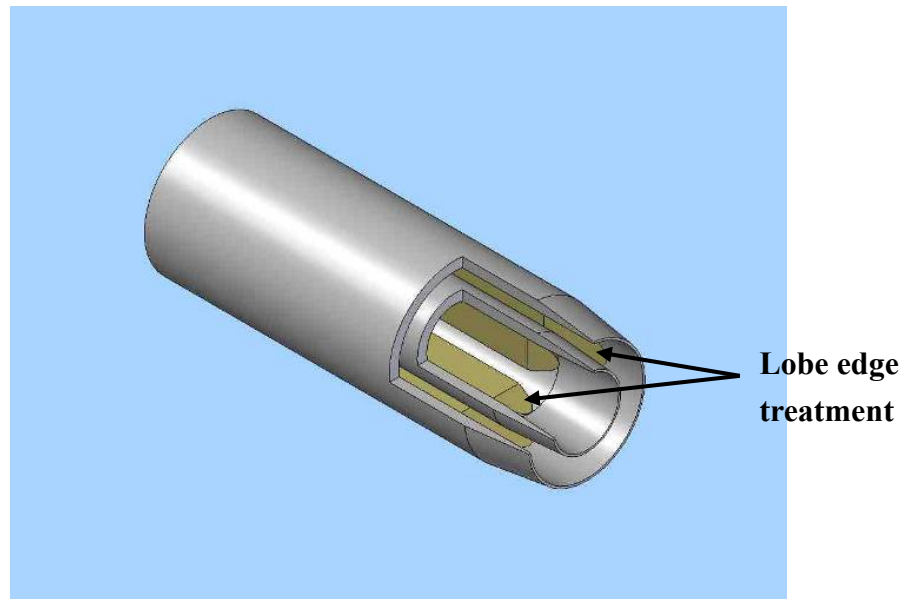
Figure 3.28 Detailed view of excitation disturbances and their edge treatment

Figure 3.29 Photograph of excitation devices for inner jet (upper) and outer jet (lower)

3.3.4. Subsonic Nozzles

The inner subsonic nozzle is surrounded by the outer nozzle concentrically (Figure 3.30). The inner nozzle is made of aluminum with an inside diameter of 30mm, but the exit is edged sharply. The outer nozzle is also made with an inside diameter of 60mm. The drawings with the major dimensions and photographs of nozzles are shown in Figures 3.31 to 3.36. In addition, a hub-cone (Figures 3.37 and 3.38) is placed at the rear side of the inner-swirl jet assembly to avoid the abrupt change of cross-sectional flow area.
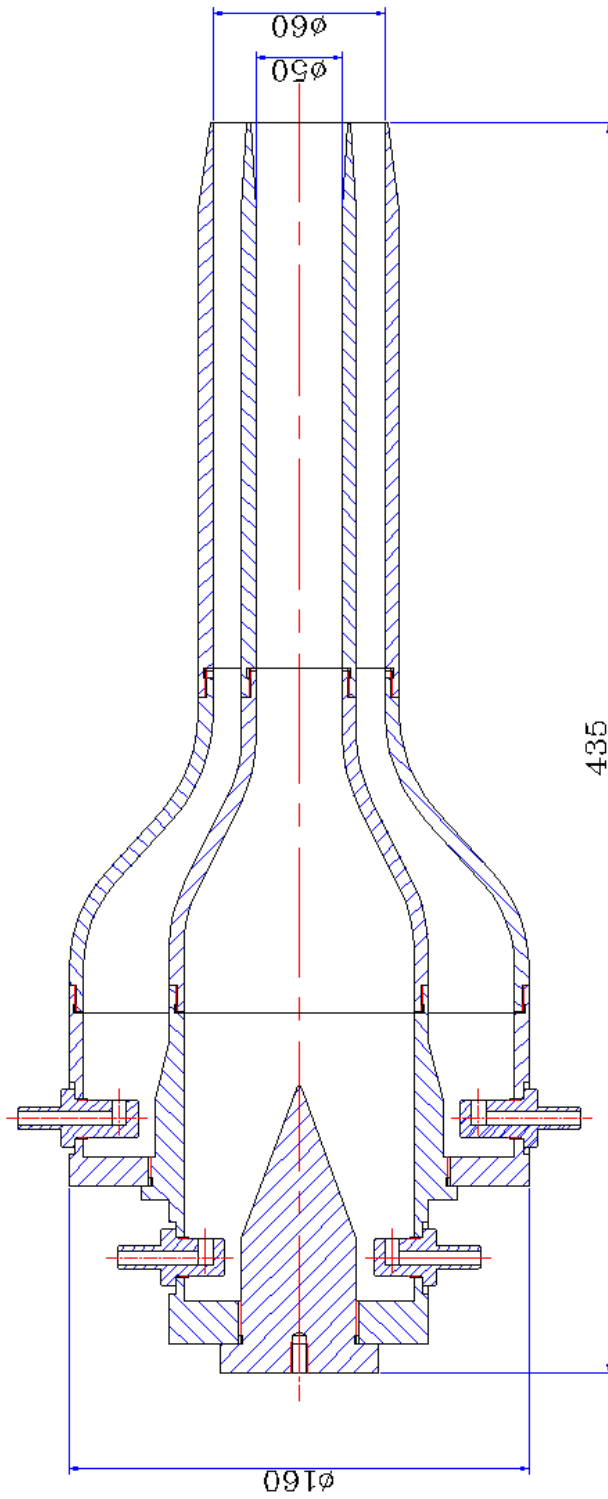
Figure 3.30 Subsonic nozzle and swirl generator assembly (mm)
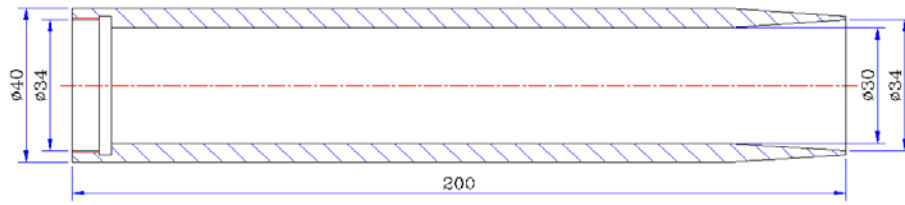
Figure 3.31 Two-dimensional drawing of inner nozzle (mm)
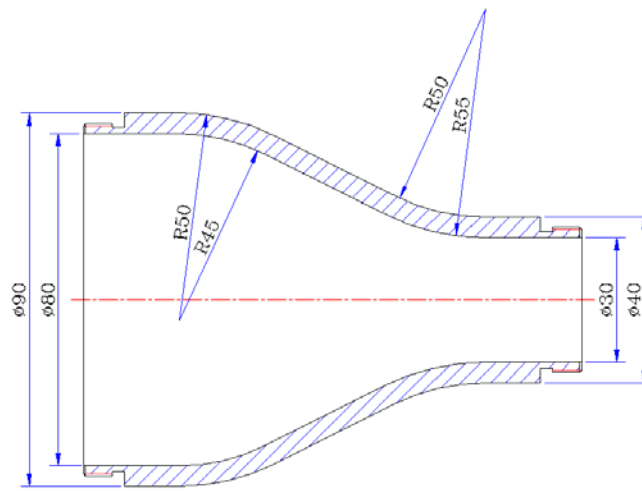
Figure 3.32 Two-dimensional drawing of inner reducer (mm)

Figure 3.33 Fabricated subsonic nozzle and reducer (inner)
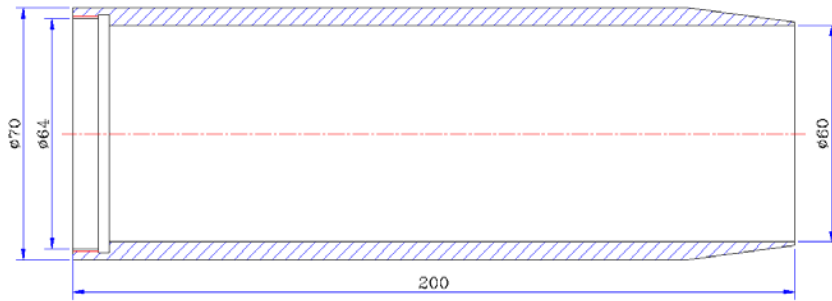
Figure 3.34 Two-dimensional drawing of outer nozzle (mm)
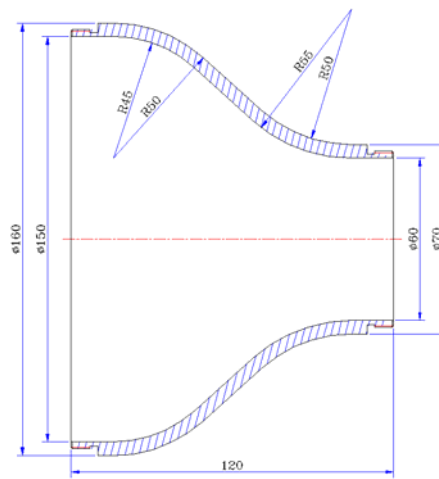
Figure 3.35 Two-dimensional drawing of outer reducer (mm)

Figure 3.36 Fabricated subsonic nozzle and reducer (outer)
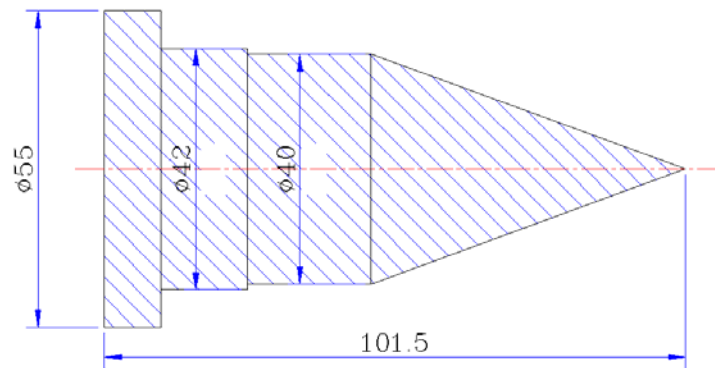
Figure 3.37 Two-dimensional drawing of hub-cone (mm)

Figure 3.38 Photograph of hub-cone

3.4. SECTION III: Measurement Instrumentation

One of the most challenging and time-consuming problems in the experimental aerodynamic society is the measurement of the overall flow field properties, such as the velocity, vorticity, and pressure fields.

3.4.1. Turbulence Flow Measurements

Local measurements of the flow (or pressure) field (i.e. at individual points) are done routinely in many experiments using a pitot-tube, hot-wire anemometer (HWA) or laser Doppler velocimetry (LDV). However, many of the flow fields of current and future interest, such as coherent structures in shear layer flows, wake flows, or vortices, have highly unsteady and out-of-plane properties. HWA or LDV data of such flows are difficult to interpret for both time-dependant and planar complex information of the entire flow field. These methods are commonly limited to simultaneous measurements at only a few spatial locations. Interpretation of these flow fields would be easier if a quantitative flow visualization technique was used in

conjunction with the flow field measurements. For this purpose, since the introduction of laser speckle velocimetry (LSV) in 1977, recent developments in flow measurement include the stereoscopic particle image velocimetry techniques.

3.4.1.1. Principles of PIV

PIV measurement is a whole-flow-field technique providing instantaneous velocity vector in a cross-section of a flow. In PIV the velocity vectors are derived from sub-sections of the target area of the particle-seeded flow by measuring the movement of particles between two light pulses:

$$\overline{V} = \frac{\Delta \overline{X}}{\Delta t} \qquad (3.3)$$

The flow is illuminated in the target area with a light sheet. The camera lens images the target area onto CCD array of a digital camera. The CCD is able to capture each light pulse in a separate image frames. Once a sequence of two light pulses is recorded, the images are divided into small subsections called interrogation areas (IA). The interrogation areas from each image frame I_1 and I_2, are cross-

correlated with each other, pixel by pixel. The correlation produces a signal peak, identifying the common particle displacement, ΔX. An accurate measure of the displacement and thus also the velocity is achieved with sub-pixel interpolation. A velocity vector map over the whole target area is obtained by repeating the cross-correlation for each interrogation area over the two image frames captured by the CCD camera (Figure 3.39[36]).
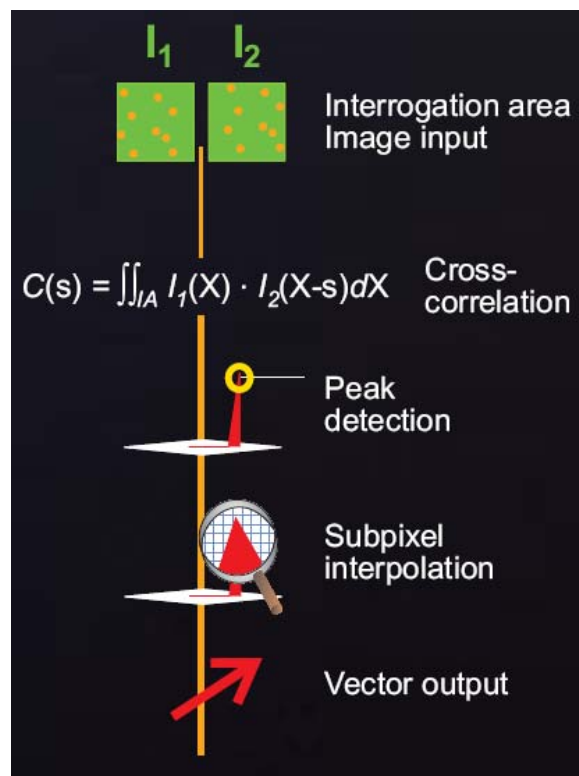
Figure 3.39 Typical procedure for vector extraction

Recording both light pulses in the same image frame to track the movements of the particles gives a clear visual sense of the flow structure. In air flows, the seeding particles are typically oil drops in the range 1µm to 5µm. For water applications, the seeding is typically polystyrene, polyamide or hollow glass spheres in the range 5µm to 100µm. Any particle that follows the flow satisfactorily and scatters enough light to be captured by the CCD camera can be used. The number of particles in the flow is of some importance in obtaining a good signal peak in the cross-correlation. As a rule of thumb, 10 to 25 particle images should be seen in each interrogation area.

Other properties, such as mean vorticity, turbulence intensity, and other higher order flow statistics, can also be calculated from the time-dependent velocity vector field.

3.4.1.2. Stereoscopic PIV

Two-dimensional stereoscopic PIV is a method for extracting the third, out-of-plane, velocity component from two cameras, and is based on the principle of

parallax. In PIV, by placing two cameras so they observe the light-sheet plane from two different angles, the parallax effect means that you obtain slightly different two-velocity component vector maps from each camera. The differences between them arise from the third, out-of-plane velocity component, and the geometrical configuration of the two cameras. After image calibration, this third velocity component can be evaluated. In addition, the two in-plane velocity components can be recalculated, correcting for parallax errors. The stereoscopic PIV technique has many advantages over conventional flow measurement devices, including:

- Measurement in an unsteady flow field: three component, simultaneous, multi-points (vs. point-wise hot-wire, LDV)

- Coherent structures in a turbulent boundary layer

- Non-intrusive to flow field (vs. intrusive pitot-tube, hotwire)

- Direct expansion of conventional qualitative visualization technique

- Reproducibility from original image data

- Increased measurement efficiency proportional to the capability of advanced hardware

- Relatively easy to build and integrate system for various flow-field regimes

- Sole experimental compatibility (or verification tool) for modern Computational Fluid Dynamics (CFD)

The performance of a PIV system highly depends on having a high-speed host computer as the hardware, and a reliable and accurate extraction algorithm as the software.

3.4.1.3. PIV Measurement Flow

The summarized flow chart for a typical PIV measurement process is shown

in Figures 3.40 and 3.41[36].
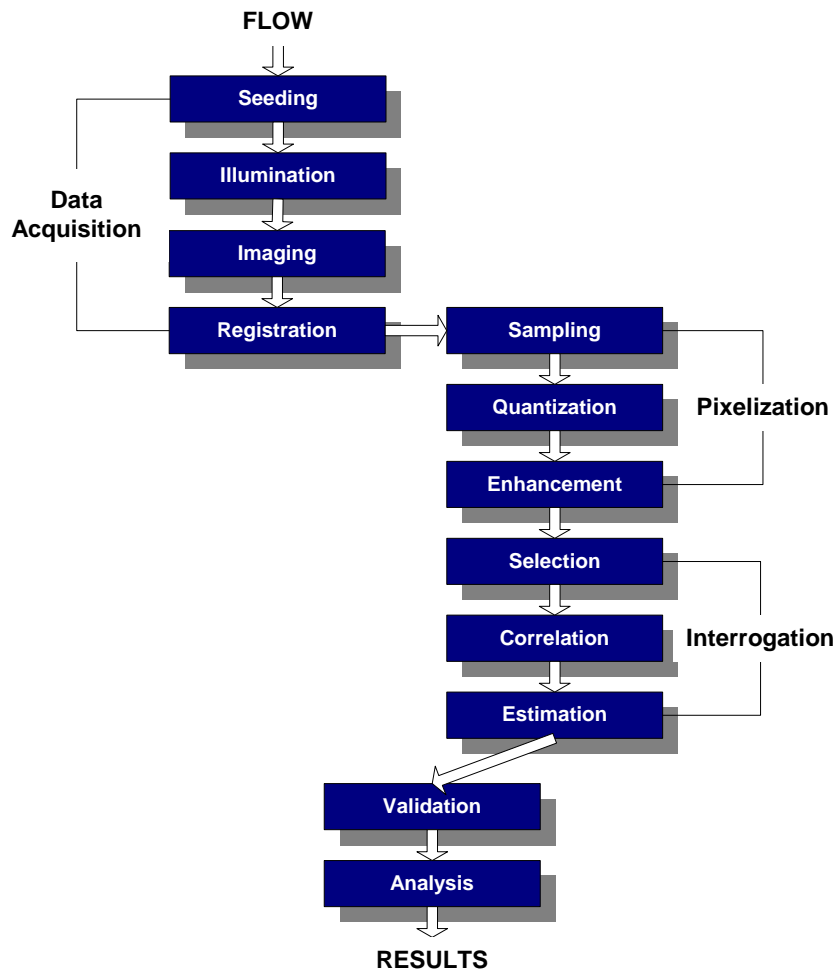
Figure 3.40 Major image processing steps
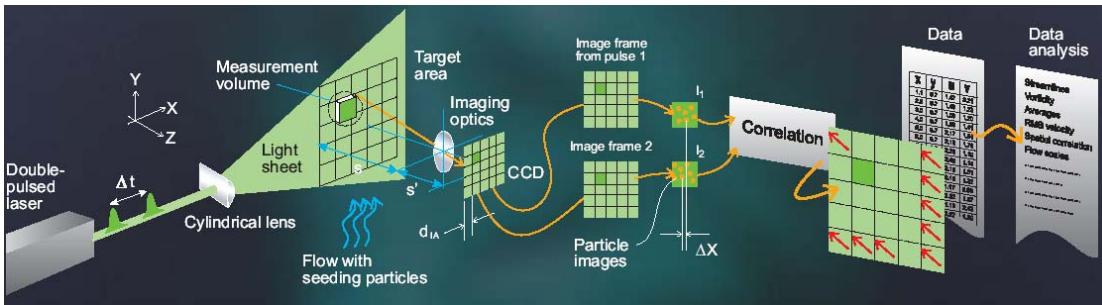
Figure 3.41 PIV measurement flow

Left and right camera images are recorded simultaneously. Conventional PIV processing produces two-dimensional vector maps representing the flow field as seen from left and right. The vector maps are re-sampled in points corresponding to the interrogation grid. Combining the left/right results, three-dimensional velocity vectors are estimated.
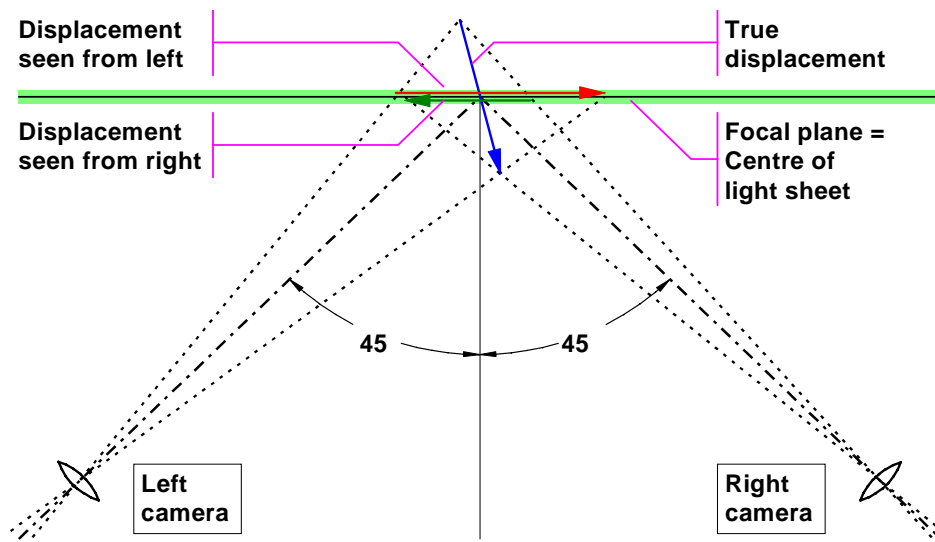
Figure 3.42 Fundamentals of stereo vision

The three-dimensional PIV is based on the same fundamental principle as human eye-sight: Stereo vision. Our two eyes see slightly different images of the world surrounding us, and comparing these images, the brain is able to make a three-dimensional interpretation. With only one eye you will be perfectly able to recognise motion up, down or sideways, but you may have difficulties judging distances and motion towards or away from yourself (Figure 3.42[36]).
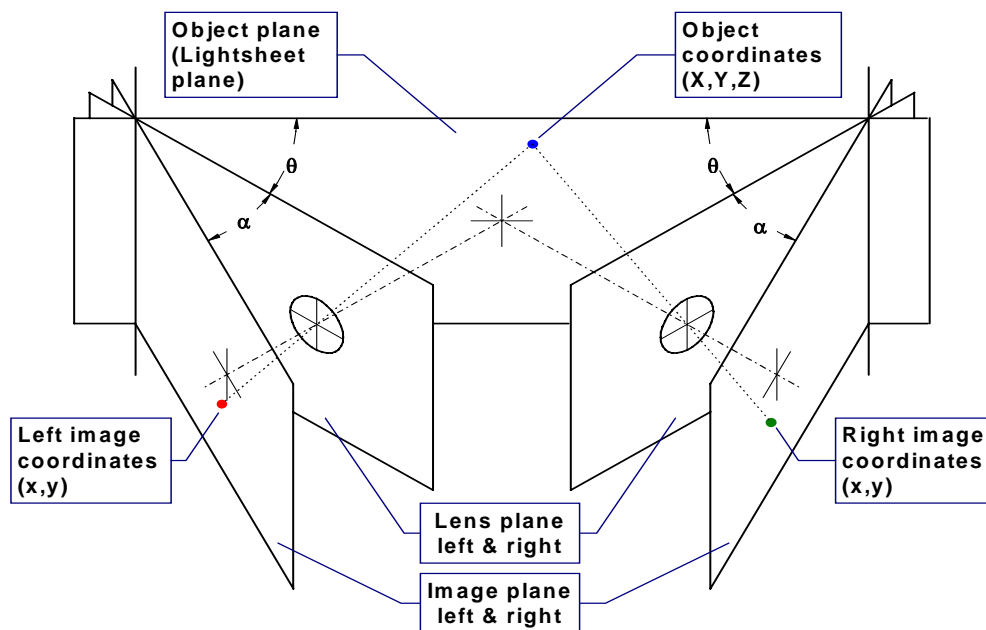
Figure 3.43 Stereo recording geometry and Scheimpflug conditions

When viewing the light sheet at an angle, the camera backplane (i.e. the CCD-chip) must be tilted in order to properly focus the camera's entire field of view.

It can be shown that the image, lens and object plane must cross each other along a common line in space for the camera images to be properly focused in the entire field of view. This is referred to as the Scheimpflug condition, and is used in most three-dimensional PIV systems (Figure 3.43[36]). Focusing an off-axis camera requires tilting of the CCD-chip by using a Scheimpflug adapter (Figure 3.44).

Figure 3.44 Scheimpflug adaptor

Performing the three-dimensional evaluation requires a numerical model describing how objects in three-dimensional space are mapped onto the two-dimensional image recorded by each of the cameras. The pinhole camera model is

based on geometrical optics, and leads to the so-called direct linear transformation.
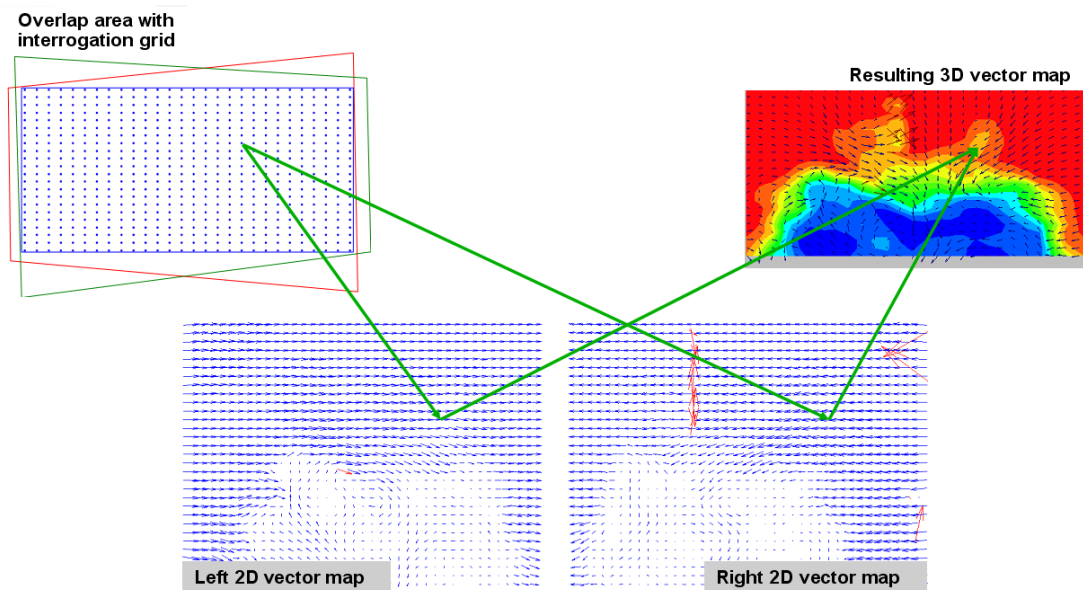
Figure 3.45 Spatial reconstruction

A large number of matching two-dimensional vector map pairs can quickly be recorded, yielding a corresponding number of three-dimensional vector maps after a bit of post-processing. A large number of vector maps are required to calculate reliable statistics, such as three-dimensional mean velocities, RMS values, and cross-correlation coefficients (Figure 3.45[36]).

3.4.2. PIV System at KARI

KARI's PIV system (Figures 3.46 to 3.49), which is located at the 'Wind Tunnel Laboratory,' is utilized for this investigation. This PIV enables the user to analyze the planar flow field using the stereoscopic technique. Flow properties, such as vorticity and strain rates, are calculated within the interrogation grid (Figure 3.45). Other properties, such as mean, turbulence, and other higher order flow statistics, can also be calculated from the time-dependent vector field. Tables 3.8 and 3.9 illustrate the stereoscopic PIV and the LASER system at KARI.
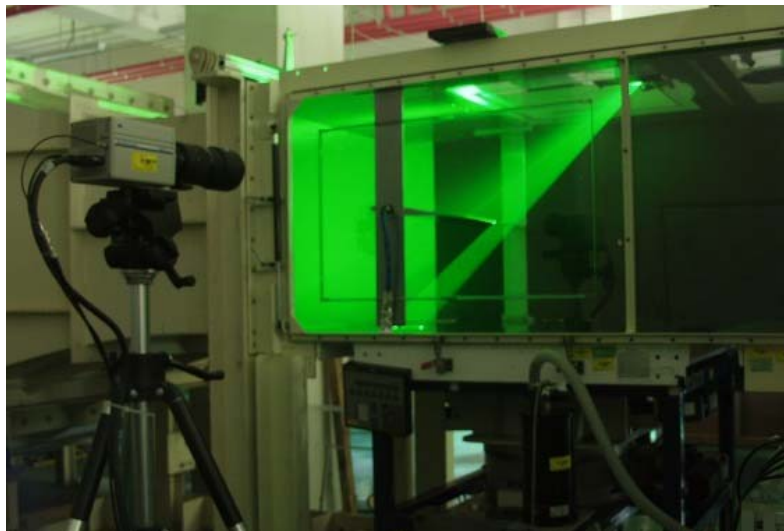
Figure 3.46 PIV system for wind tunnel application

Figure 3.47 Stereoscopic PIV system arrangement

Table 3.8 Summary of PIV System at KARI

Type	two-frame PIV
Laser	200mmJ Nd:YAG pulse laser
Synchronization	8 Ch. delay generator
Camera	2k × 2k CCD camera
Particle	1 μm Laskin nozzle (DEHS)
Optics	4 mirrors + cylindrical lens + convex lens
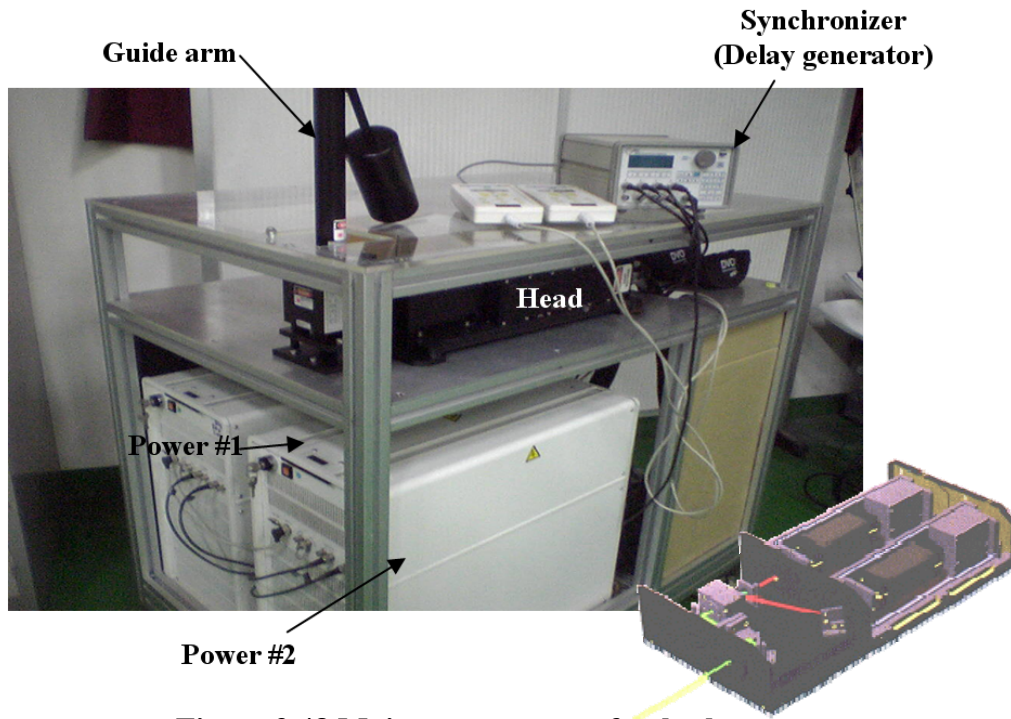
Figure 3.48 Major component of pulse laser

Table 3.9 Specification of Pulsed LASER at KARI

Energy	200 mJ
Wave Length	532nm harmonic generator (from 1,064 nm)
Repetition Rate	15Hz
Beam Diameter	3 ~ 5mm
Beam Divergence Angle	0.3 ~ 0.5mrad
Cooling	air cooling (power supply) water cooling (laser head)
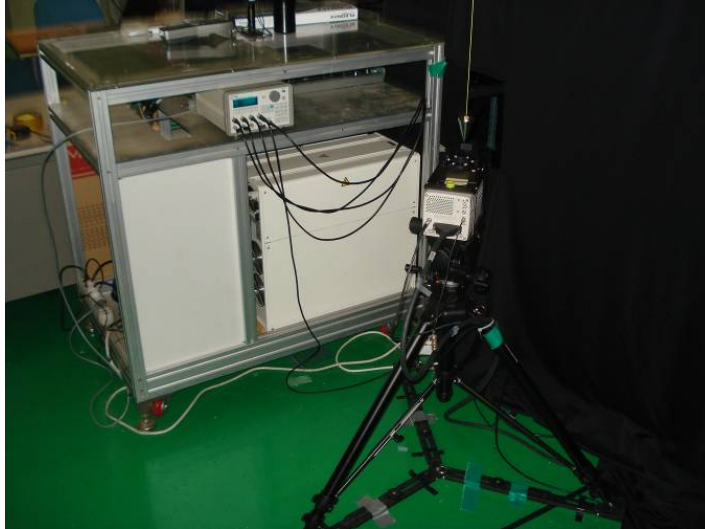
Figure 3.49 Photograph of CCD camera (upper) and optics (lower)

3.4.2.1. Flow Field Data Acquisition

The data acquired from the PIV system are processed by means of the following computer analysis software:

PIVview for MS-Windows

Copyright © 2001, PivTec GmbH

3.5. Calibration

The calibration of instruments is important, for it affords the opportunity to check the instrument against a known standard and subsequently to reduce errors in accuracy. The calibration is carried out for pressure differential gages (for mass flow rate), thermocouples (for temperature), and the PIV system (for velocity vector straightness and its magnitude).

3.5.1. Mass Flow Rate and Temperature

Even though the orifices and pressure taps are designed and manufactured according to the design handbook[34] with accuracy, the high quality mass flow controller (MFC, Figure 3.50, Table 3.10) is adopted for mass flow rate calibration. The calibration is categorized in three areas: inner air jet, outer air jet, and outer CO_2 jet. The MFC is installed, and operated between the pipes. The calibration results are tabulated in Figures 3.51 to 3.53, and these show square root curves well.

$$\dot{m} = \frac{A_2}{\sqrt{1-(\frac{A_2}{A_1})^2}} \sqrt{2\rho(p_1 - p_2)} \tag{3.4}$$

A_1: up-stream area, A_2: down-stream area

P_1: up-stream static pressure, P_2: down-stream static pressure

The thermocouples that are used in this experiment are also calibrated with ice water (i.e., zero degrees Celsius). Overall both the designed pressure differential gage and thermocouple have an accuracy of 97% or higher.

Figure 3.50 Mass flow controller (MFC)

Table 3.10 Specification of Mass Flow Controller

Excitation	±15VDC
Output	35 ~ 180mADC
Output Signal into 2k ohm	0 ~ 5V
Operating Temp	5 to 65°C
Pressure Sensitivity	±0.03% per psi (up to 200 psig)
Operating pressure ratings	1500 psig maximum
Materials of Construction	Wetted Parts - 316 Stainless Steel with Viton®
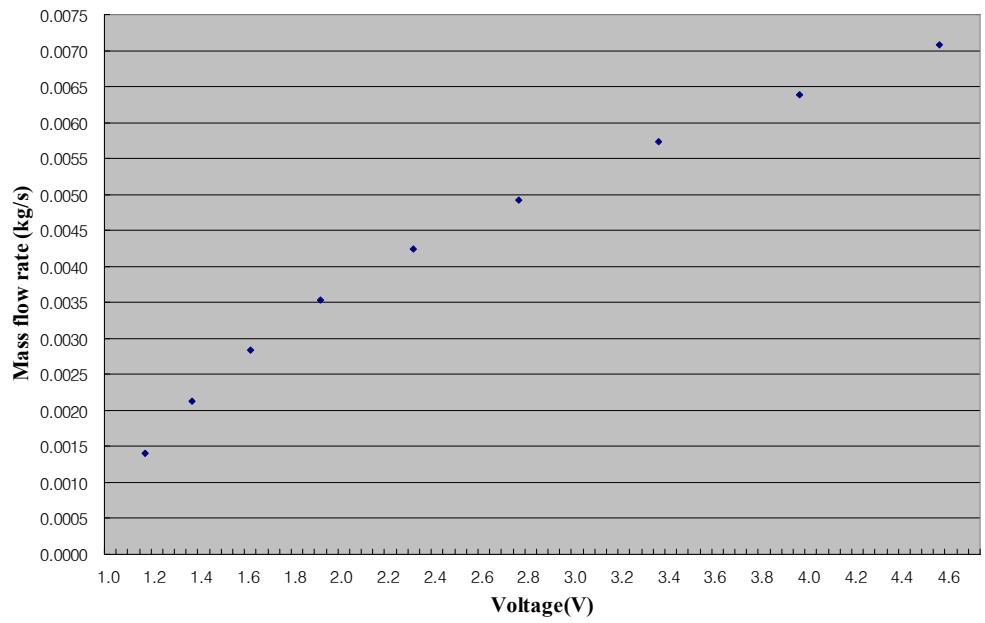
Figure 3.51 MFC data for calibration (air, inner jet flow)
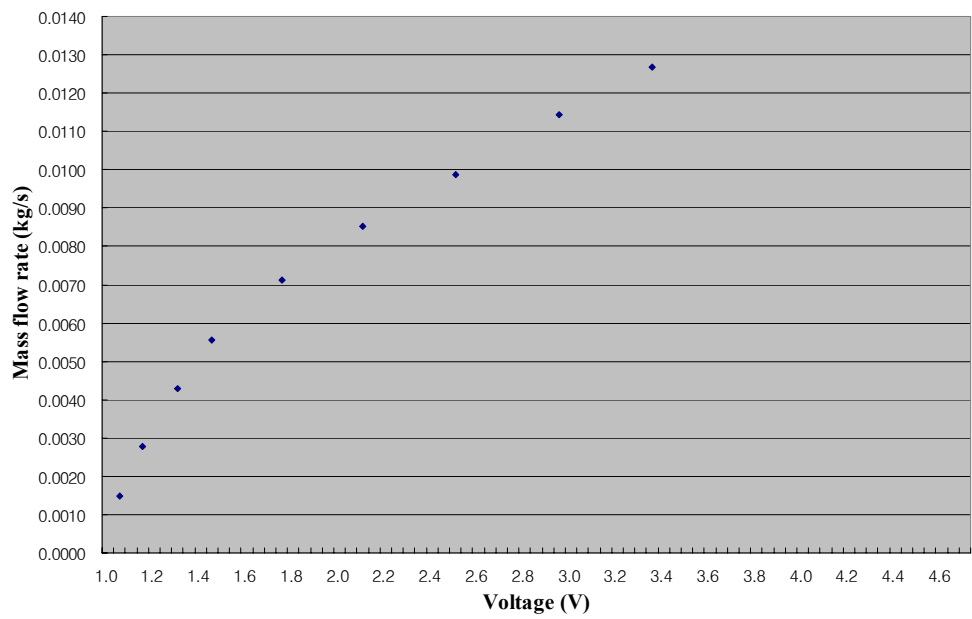
Figure 3.52 MFC data for calibration (air, outer jet flow)
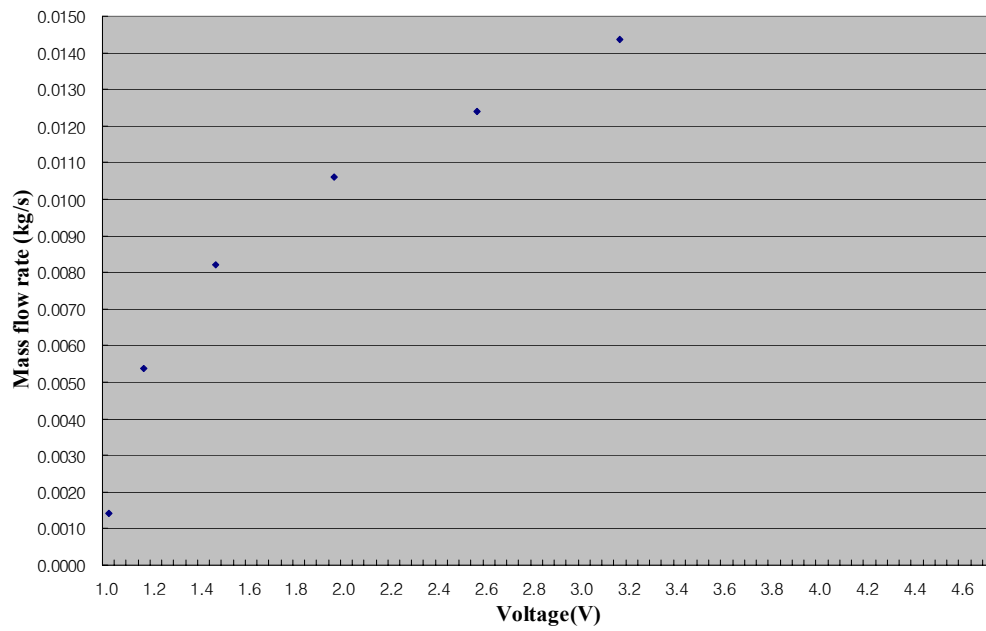
Figure 3.53 MFC data for calibration (CO$_2$, outer jet flow)

3.5.2. PIV System

KARI's PIV system is calibrated in two ways. One is for velocity magnitude, and the other is for velocity direction. The velocity magnitude is compared with the pitot tube measurement results using a plain circular jet. The deviation of results between the two devices falls at less than 4% at the nozzle exit velocity of 10m/s.
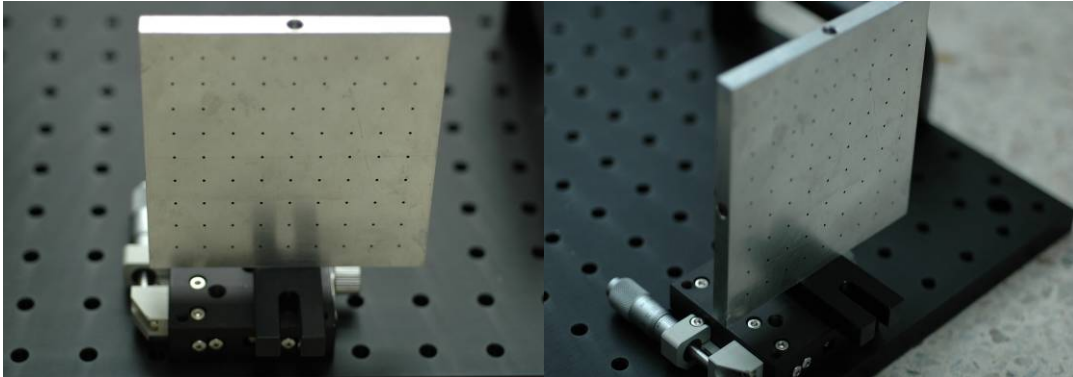
Figure 3.54 Calibration target for PIV system

For vector directional calibration, the images of a calibration target are required (Figure 3.54). The plane target must be parallel with the light sheet, and the target is traversed along its own normal surface to acquire calibration images covering the full thickness of the light sheet. Calibration markers on the target

identify the y- and z-axes of the coordinate system, and the traversely moving target identifies the x-axis. Since the calibration target and traverse movement identifies the coordinate system, care should be taken in aligning the target and the traverse area within the experiment. The overall calibration results shows 98% accuracy.

3.5.3. Camera Set-up

Before getting into taking pictures with particles, the image plane should be converted to the physical plane, and overlapped via the following procedures.

- Images of a calibration target are recorded (Figure 3.55[36]).

- The target contains calibration markers in known positions.

- Comparing known marker positions with corresponding marker positions on each camera image, model parameters are adjusted to give the best possible fit.

- Transform image plane into physical plane (Figure 3.56[35]).

- Three-dimensional evaluation is possible only within the area covered by both cameras.

- Due to perspective distortion, each camera covers a trapezoidal region of the light sheet.

- Overlap the fields of views (Figure 3.57[36]).

- Careful alignment is required to maximize the overlap area.

- Interrogation grid is chosen to match the spatial resolution.
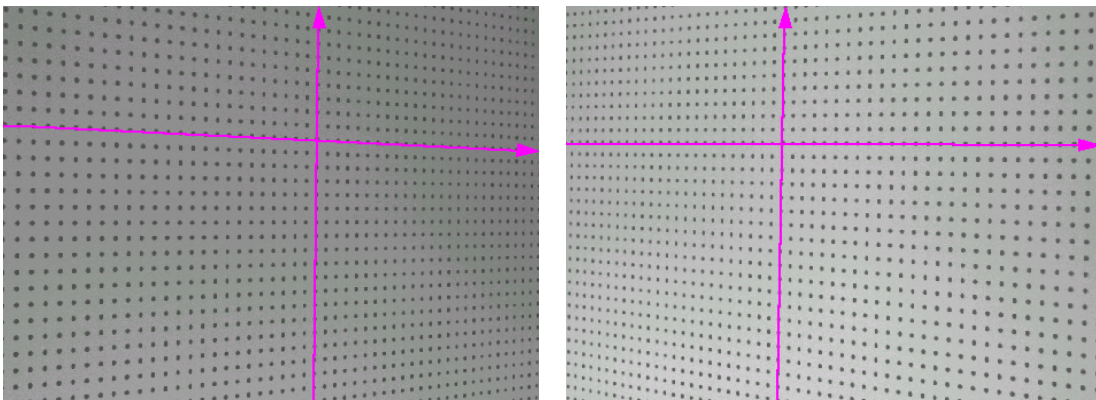
Figure 3.55 Target image recording

First, the images of a calibration target are recorded. The calibration target contains calibration markers (for example dots), the true x, y, z-position of which are known. Then, comparing the known marker positions with the positions of their respective images on each camera image, model parameters can be estimated.
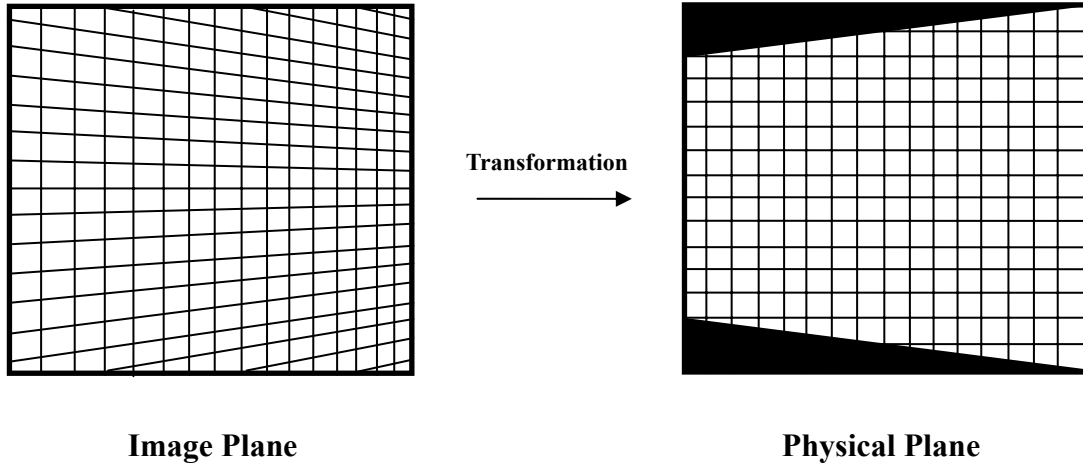
Image Plane   **Physical Plane**

Figure 3.56 Image dwarping
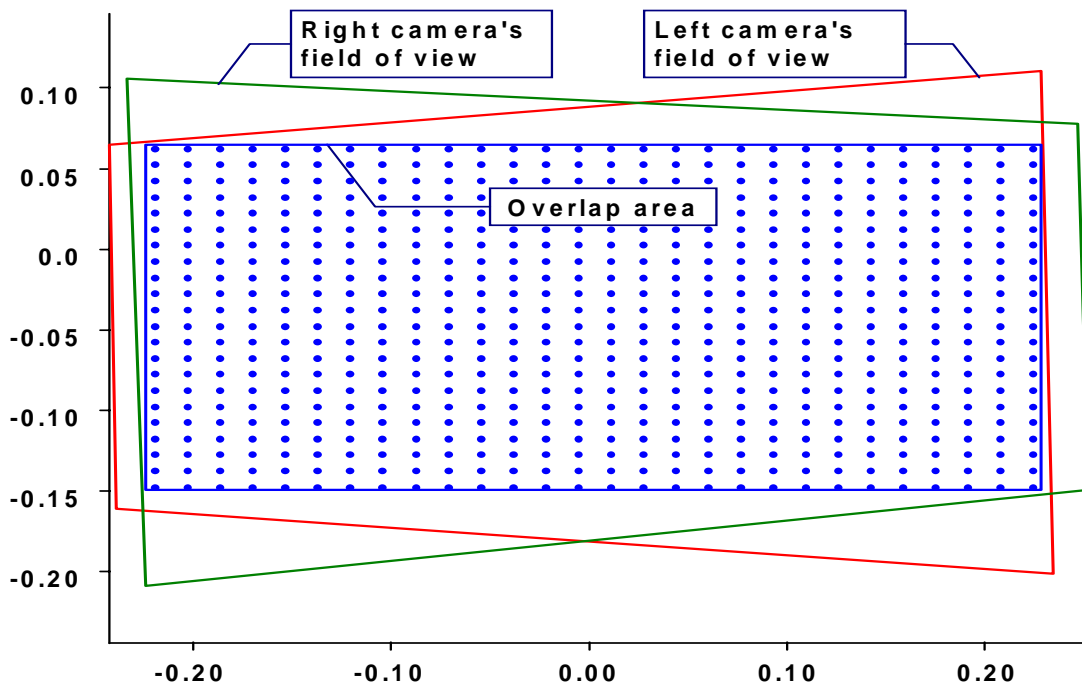
Figure 3.57 Overlapping fields of view

Obviously, three-dimensional reconstruction is possible only where information is available from both cameras. Due to perspective distortion, each camera covers a trapezoidal region of the light sheet, and even with careful alignment of the two cameras, their respective fields of view will only partly overlap each other. Within the region of overlap, interrogation points are chosen in a rectangular grid. In principle, three-dimensional calculations can be performed in an infinitely dense grid, but the two-dimensional results from each camera have limited spatial resolution, and using a very dense grid for three-dimensional evaluation will not improve the fundamental spatial resolution of the technique.

3.6. Test Procedures

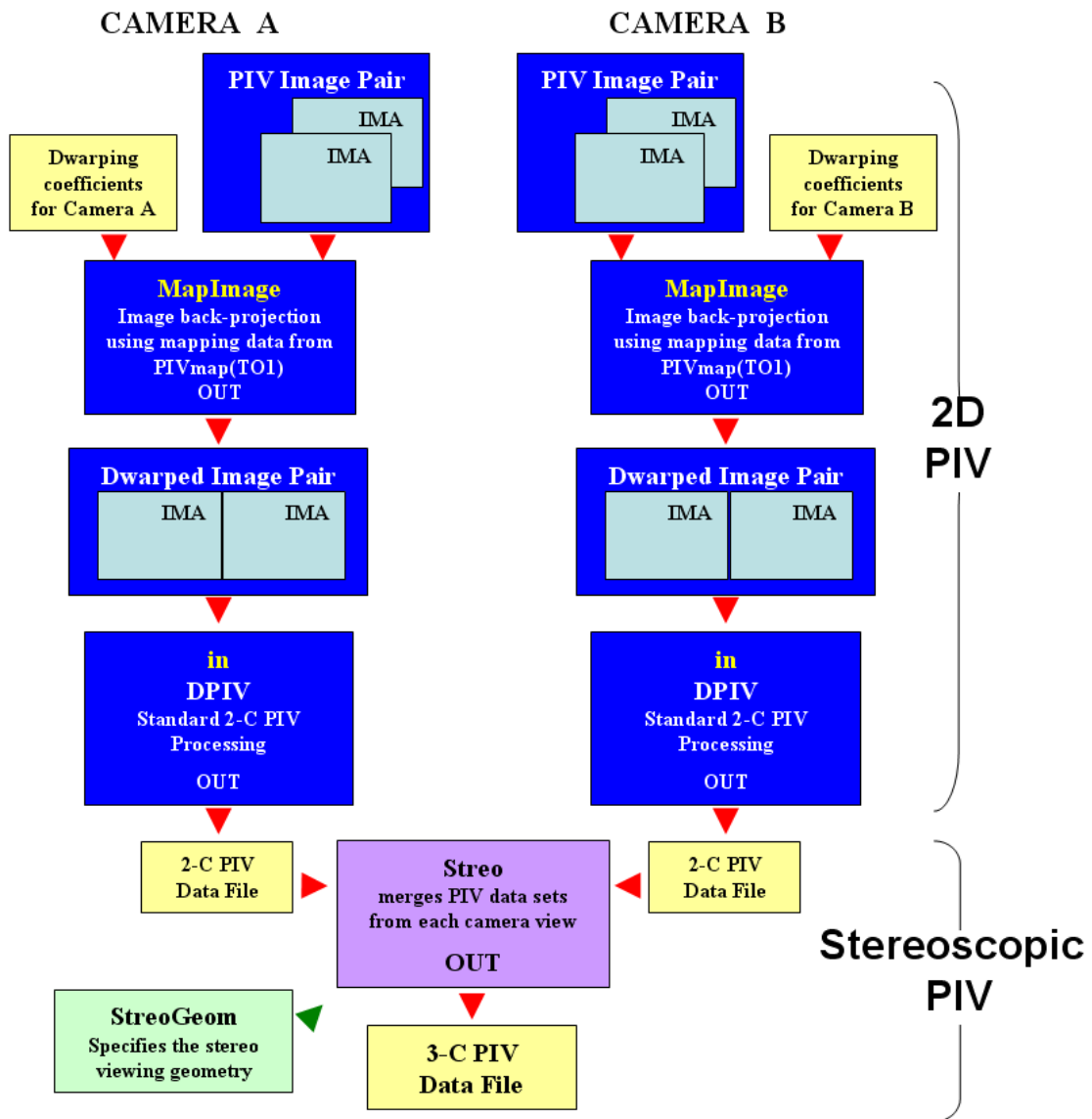This section explains the overall test procedures of PIV image acquisition

(Figure 3.58).

Figure 3.58 General process of PIV image acquisition

3.6.1. Test Set-up

The general arrangement of the PIV set-up is shown in Figure 3.59. The focal plane and laser plane are located in an identical location. At the same time, two CCD cameras' planes should be parallel to the focal plane. In order to place cameras at the exact location, and to set the center of the cameras accurately, the pendulums are utilized (Figure 3.60). The measurement conditions are tabulated in Table 3.11.

Table 3.11 Summary of Measurement Conditions

CCD Camera Resolution (Total No. of Pixels)	2,048 × 2,048 (approx. 4 million)
No. of Interrogation Area	8,100 (90 × 90)
Resolution per Interrogation Area	20 × 20
Measurement Area (cm^2)	207.36 (14.4 × 14.4)
No. of Image Pairs	120
Laser Pulse Delay (µs)	20
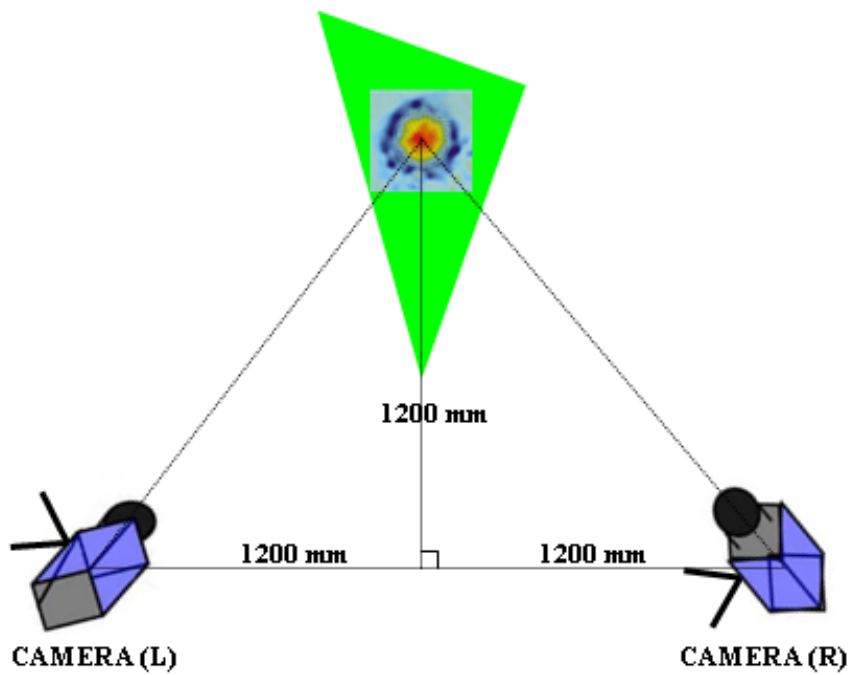
Figure 3.59 Layout of focal plane and CCD cameras
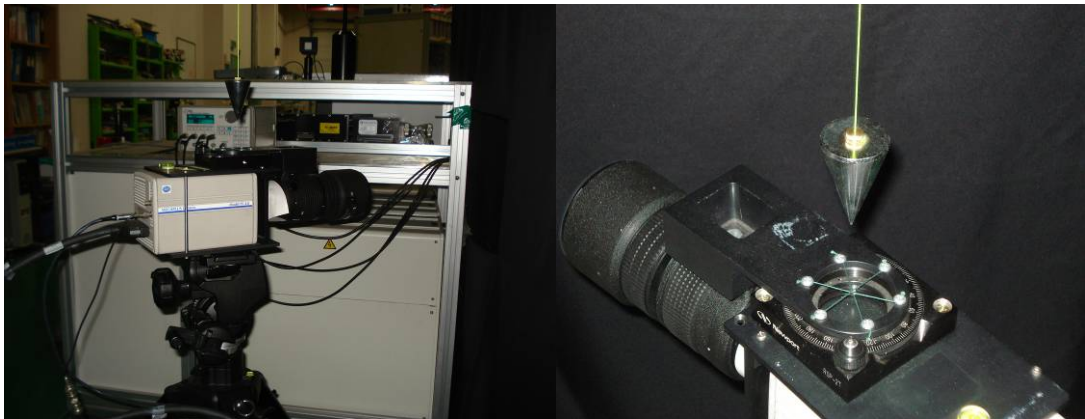
Figure 3.60 CCD camera (left) and camera center-fitting with pendulum (right)

3.6.2. Test Conditions

This section summarizes the experimental conditions (Table 3.12).

Table 3.12 Summary of Test Conditions

Flow Type		subsonic dual co-axial swirl jets
Control (Excitation) Type		azimuthal perturbation, passive
Swirl No.	inner	0.7
	outer	1.2
Reynolds No.	inner	6.87×10^3
	*outer	4.64×10^3 (air), 8.78×10^3 (CO_2),
Swirl Direction		co & counter-swirl direction (in & out relatively)
Lobed Disturbance		straight plate type
Flow Medium	inner	air (at 300K)
	outer	air or CO_2 (at 300K)
Measurement	device	particle image velocimetry
	type	three component vector, stereoscopic
	method	simultaneous multi-points in plane

* Hydraulic diameter is used for outer nozzle 'Re'.

3.6.3. Measurement Cases

This section is presented for the experimental cases (Table 3.13). The sign which is used in 'S' denotes the rotational direction by the "Law of Clockwise Screw".

Table 3.13 Summary of Test Cases

| | S | | mode | Re | | fluid | measurement |
	in	out	(m)	in	out		plane @
CASE #01	0.0	0.0	0	6.87×10^3	4.64×10^3	air	x/D=1.00
CASE #02	+0.7	+1.2	0	6.87×10^3	4.64×10^3	air	x/D=1.00
CASE #03	-0.7	+1.2	0	6.87×10^3	4.64×10^3	air	x/D=1.00
CASE #04	-0.7	+1.2	0	6.87×10^3	8.78×10^3	air, CO_2	x/D=1.00
CASE #05	+0.7	+1.2	0	6.87×10^3	6.96×10^3	air	x/D=1.00
CASE #06	-0.7	+1.2	0	6.87×10^3	6.96×10^3	air	x/D=1.00
CASE #07	+0.7	+1.2	0	10.30×10^3	4.64×10^3	air	x/D=1.00
CASE #08	-0.7	+1.2	0	10.30×10^3	4.64×10^3	air	x/D=1.00
CASE #09	+0.7	+1.2	1	6.87×10^3	4.64×10^3	air	x/D=1.00
CASE #10	-0.7	+1.2	1	6.87×10^3	4.64×10^3	air	x/D=1.00
CASE #11	+0.7	+1.2	2	6.87×10^3	4.64×10^3	air	x/D=1.00
CASE #12	-0.7	+1.2	2	6.87×10^3	4.64×10^3	air	x/D=1.00
CASE #13	+0.7	+1.2	3	6.87×10^3	4.64×10^3	air	x/D=1.00
CASE #14_1	-0.7	+1.2	3	6.87×10^3	4.64×10^3	air	x/D=0.25
CASE #14_2	-0.7	+1.2	3	6.87×10^3	4.64×10^3	air	x/D=0.50
CASE #14_3	-0.7	+1.2	3	6.87×10^3	4.64×10^3	air	x/D=0.75
CASE #14_4	-0.7	+1.2	3	6.87×10^3	4.64×10^3	air	x/D=1.00
CASE #14_5	-0.7	+1.2	3	6.87×10^3	4.64×10^3	air	x/D=1.25
CASE #14_6	-0.7	+1.2	3	6.87×10^3	4.64×10^3	air	x/D=1.50
CASE #15	+0.7	+1.2	4	6.87×10^3	4.64×10^3	air	x/D=1.00
CASE #16_1	-0.7	+1.2	4	6.87×10^3	4.64×10^3	air	x/D=0.25
CASE #16_2	-0.7	+1.2	4	6.87×10^3	4.64×10^3	air	x/D=0.50
CASE #16_3	-0.7	+1.2	4	6.87×10^3	4.64×10^3	air	x/D=0.75
CASE #16_4	-0.7	+1.2	4	6.87×10^3	4.64×10^3	air	x/D=1.00
CASE #16_5	-0.7	+1.2	4	6.87×10^3	4.64×10^3	air	x/D=1.25
CASE #16_6	-0.7	+1.2	4	6.87×10^3	4.64×10^3	air	x/D=1.50

4. NUMERICAL ANALYSIS

To explore the further study on swirl analysis, a numerical approach is carried out. The simulations have mainly been performed in the area that the experiment practically cannot cover (i.e., helical excitation, high flow speed & temperature, and spatial analysis at far fields). Especially, due to the difficulty and excessive cost of fabricating the test model for convex spiral lobes, a computational analysis can be a solution as a substitution for experiments. Furthermore, regardless of the practical limitations of compressor capacity, acoustic jet noise, and so on, a numerical analysis enables us to investigate the relatively high speed subsonic flow (i.e., ten times the experimental case) or thermal jets.

In this study, a commercial code, 'FLUENT' which is based on Navier-Stokes equation is utilized for this analysis. 'FLUENT' can analyze the viscous rotating flow, and its preprocessor, 'GAMBIT' has a "Journaling Function" for auto-grid generation. This function is useful to mesh the similar types of models repeatedly[37]. The numerical tools which are used in this investigation are illustrated in Table 4.1. "Realizable k-ε" is selected as a turbulence model, which is a variant of

the "Standard k-ε" model. Its "realizability" stems from changes that allow certain

mathematical constraints to be obeyed, which ultimately improves the performance

of this model. Among the two equation Reynolds Average Navier-Stokes (RANS)

turbulence models, "Realizable k-ε" is known as the most suitable for rotating flow

like swirls, vortices, and so on.

As a reference, the comparison of some RANS turbulence models and their

usage is tabulated in Table 4.2[38].

Table 4.1 Summary of Numerical Software

> **＋ Pre-processor**
>
> GAMBIT 2.0.4 Copyright 1988-2008, Fluent, Inc.
>
> **＋ Solver & Post-processor**
>
> FLUENT Release 6.3.26, Graphics Version 11.26-1, Copyright(c) 2006 Fluent, Inc.
>
> **＋ Graphic viewer**
>
> Hummingbird Exceed V7.0 X server for Win32 Version: 7.0.0.0

Table 4.2 RANS Turbulence Model Behavior and Usage

MODEL		Behavior and Usage
Spalart Allmaras (One Eq.)		Economical for large meshes. Performs poorly for 3D flows, free shear flows, flows with strong separation. Suitable for mildly complex (quasi-2D) external/internal flows and BL flows under pressure gradient (e.g., airfoils, wings, airplane fuselages, missiles, ship hulls).
k-ε (Two Eq.)	**Standard**	Robust. Widely used despite the known limitations of the model. Performs poorly for complex flows involving severe $\triangledown$p, separation, and strong stream line curvature. Suitable for initial iterations of alternative designs, and parametric studies.
	RNG	Suitable for complex shear flows involving rapid strain, moderate swirl, vortices, and locally transitional flows (e.g., BL separation, massive separation and vortex-shedding behind bluff bodies, stall on wide-angle diffusers, room ventilation).
	Realizable	Offers largely the same benefits and has similar applications as RNG. Possibly more accurate and easier to converge than RNG.
k-ω (Two Eq.)	**Standard**	Superior performance for wall-bounded BL free shear, and low Re flows. Suitable for complex boundary layer flows under adverse pressure gradient and separation (external aerodynamics and turbo-machinery). Can be used for transitional flows (though tends to predict early transition). Separation is typically predicted to be excessive and early.
	SST	Similar benefits as SKO. Dependency on wall distance makes this less suitable for free shear flows.
RSM (Seven Eq.)		Physically the most sound RANS model. Avoids isotropic eddy viscosity assumption. Large amount of CPU time and memory required. Tougher to converge due to close coupling of equations. Suitable for complex 3D flows with strong streamline curvature, strong swirl/rotation (e.g., curved duct, rotating flow passages, swirl combustors with very large inlet swirl, cyclones).

4.1. Numerical Set-up

Similar to the experimental approach, the lobe configurations that are capable of generating excitation waves are numerically modeled. As can be seen from the experimental results, the size of lobes is large to reduce the flow passage itself, and even quench the jet expansion area. To complement the above argument and to enhance the possibility of mixing effects, basically, the lobe configuration is modified from the flat type to convex one, and the height of the lobe is reduced to half of the experiments'. Figure 4.1 presents the newly designed layout of excitation disturbances for numerical simulation.

The helical lobes have the relative angles, 30° for the inner and 45° for the outer angles, with respect to the horizontal plane. An identical number of zero (no lobe; baseline configuration), one, two, three, and four lobes are used for both inner and outer nozzles. The total four helical-instability modes are set-up; i.e., h=-1, -2, -3, and -4 (ref. Figure 4.1), and the negative sign denotes the counter-spiral shape to the swirl direction.

1.25 mm

h=-1

Co Swirl

h=-2

2.5 mm

Excitation
Disturbances

Counter

h=-3

h=-4
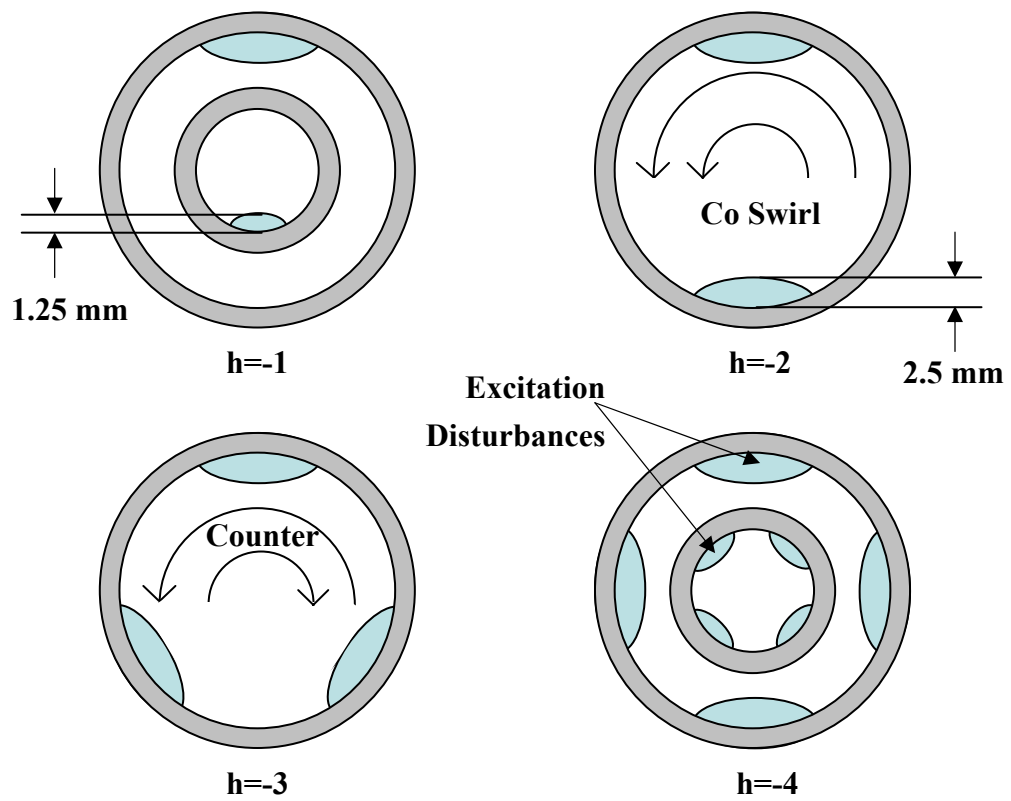
Figure 4.1 Layout of excitation disturbances for numerical set-up

(NOT IN SCALE)

4.1.1. Computational Domain and Grid

The various views of the domain for the CFD calculation are shown in Figure 4.2. The domain is mainly divided into four parts; swirl generators, subsonic nozzles, excitation devices, and the free jet expansion region. The inner- and outer-swirlers and nozzle assembly with two kinds of lobes (i.e., straight and helical) are presented in Figures 4.3 and 4.4. Different from the experimental application, in this numerical analysis, the lobe runs helically along the length of the nozzle at the inner surface of each nozzle, and the mesh model of the helical lobes is depicted in the Figure 4.4.

Furthermore, Figure 4.5 shows the detailed view of swirl generators with the swirl injectors. The angle of each injector is adjustable, and this can produce co- and counter-clockwise swirling flows with various swirl strengths. Helical instability waves are induced by the convex contoured lobes that are placed on the inside surface of each nozzle. Approximately 2.8 million cells are distributed throughout the computational domain using a hybrid mesh (i.e., mostly structured and partially unstructured in this analysis).
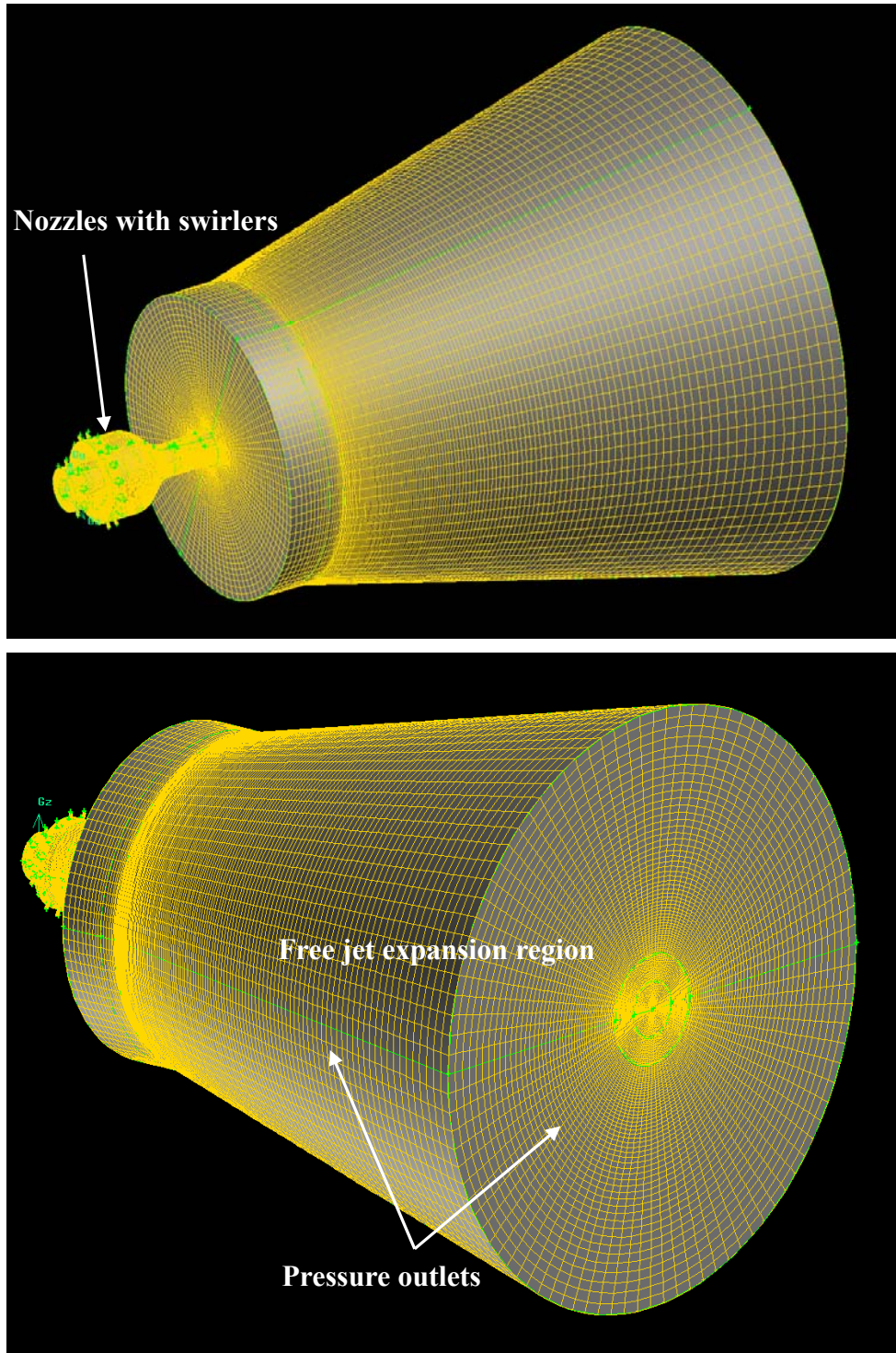
Figure 4.2 Various views of computational domain and grid front view (upper), rear view (lower)
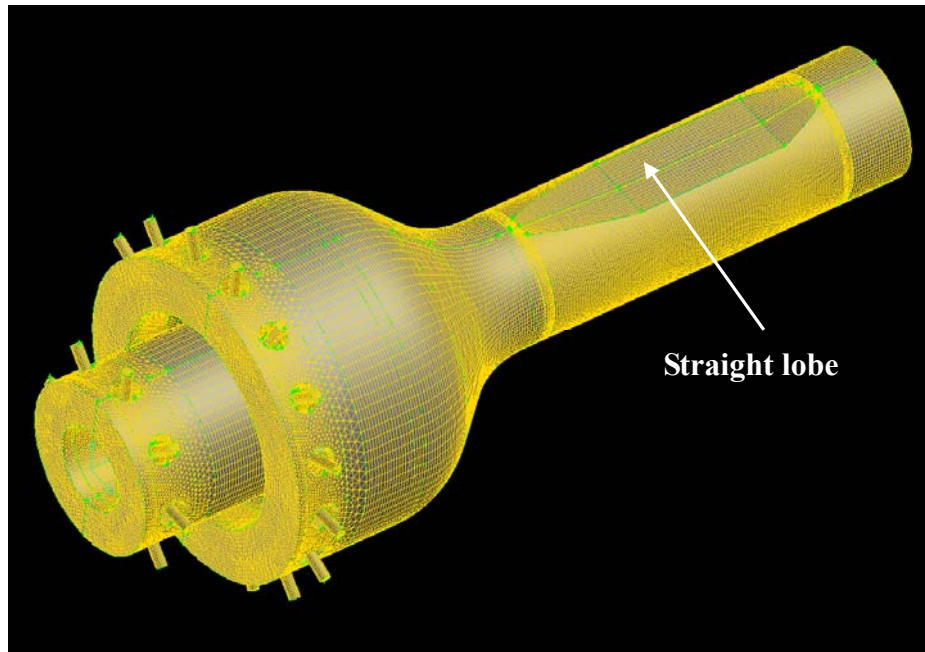
Figure 4.3 Grid for swirler and nozzle assembly with straight lobes (example)
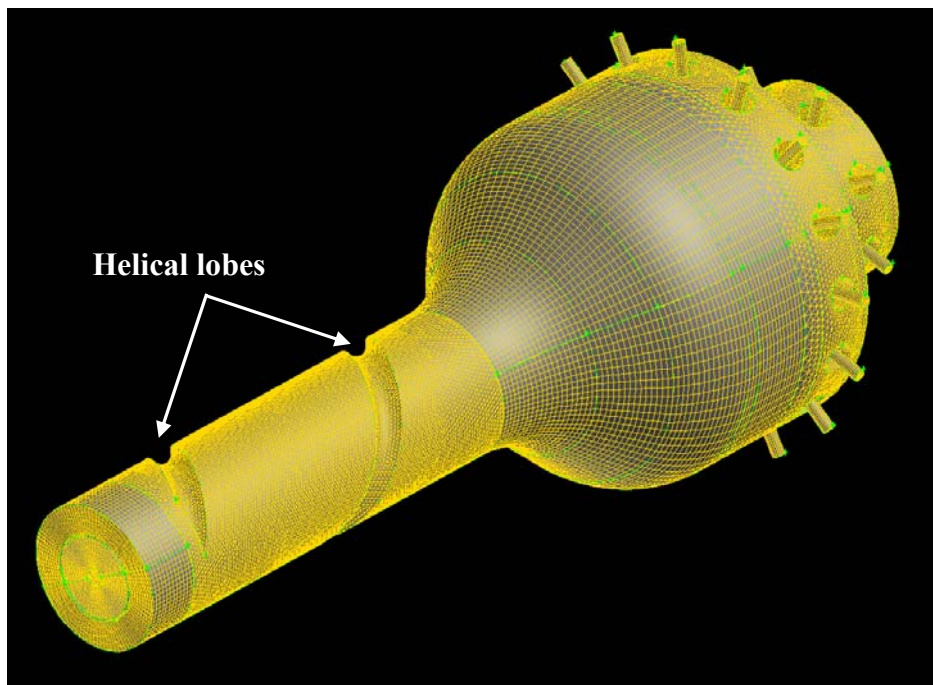
Figure 4.4 Grid for swirler and nozzle assembly with helical lobes
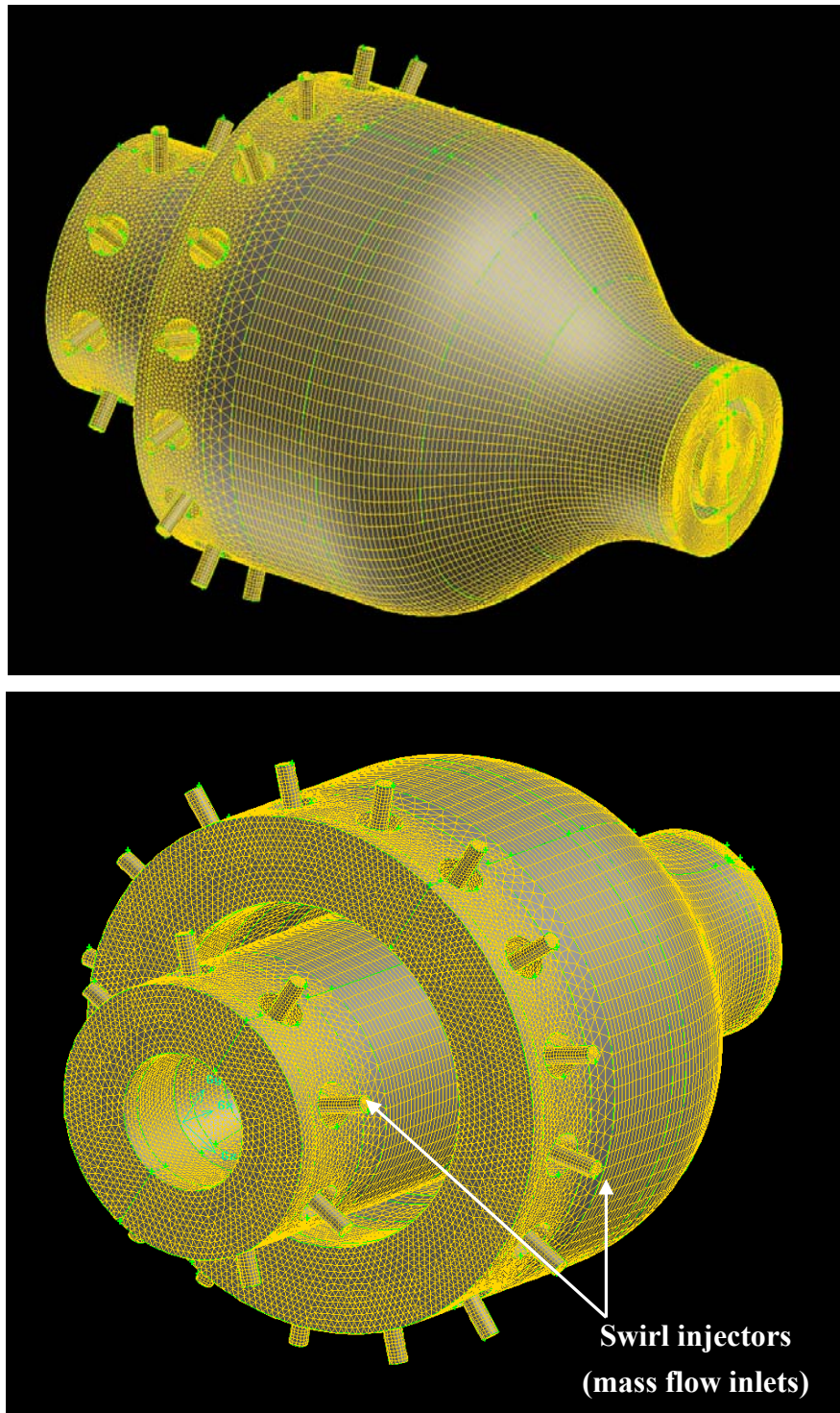
**Figure 4.5 Detailed views of swirl generators
front view (upper), rear view (lower)**

4.1.2. Code Set-up

Even though the commercial code (i.e., 'FLUENT') which is used in this analysis is known as reliable software, the appropriateness of set-up conditions (e.g., turbulence model and boundary conditions) and its simulation results need to be confirmed with experimental results. For this purpose, the PIV result of 'CASE #02' (i.e., co-swirl, unexcited) is selected as a benchmark problem, and the radial profile of the axial velocity (u) along the z-axis is compared (Figure 4.6). Among the RANS two-equation turbulence models, "Standard k-ω", "SST k-ω", and "Realizable k-ε" are tested. All the numerical cases show quite symmetric patterns compared to the experimental data.

The overall numerical results show the slight under-estimation in the vortex core. The deviation could arise from the simplifying of the complicated prototype to a computational model. The swirl intensity setting (i.e., swirl injector angle, etc.) can also be considered as one of the possible errors. Generally, the numerical simulation traces the curve of the experimental data well, but the maximum deviation is found when the "Standard k-ω" is applied. Obviously the numerical approach with the

"Realizable k-ε" model simulates the unique swirl characteristics, vortex cores and double hump profile (i.e., peaks), most accurately.

Consequently, the concurrence with the experimental data proves the selected code (FLUENT) and the turbulence model (realizable k-ε) are acceptable, despite a few flaws.
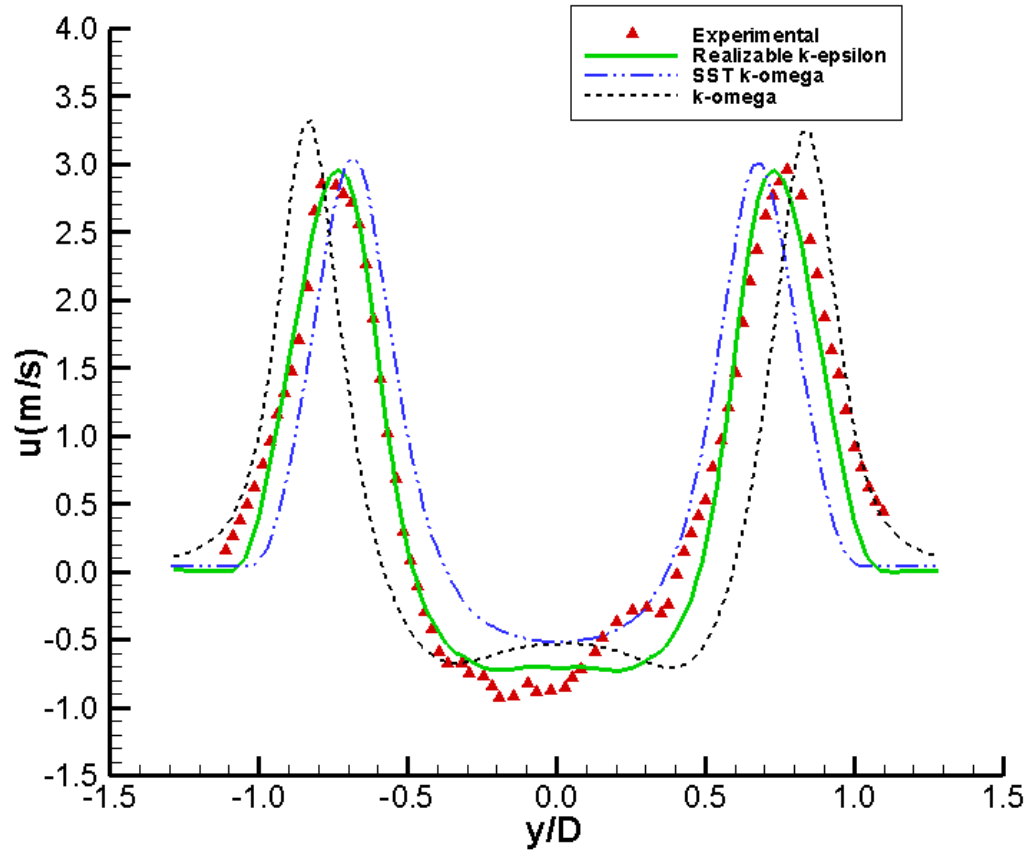
Figure 4.6 Comparison of CFD results with experimental data (CASE #02)
Axial velocity distribution at x/D=1, z/D=0

4.2. Numerical Solving

Normally 6,000 to 8,000 numerical iterations are performed until all the residuals become flat, using a twelve CPU clustered machine. All the six scaled residuals (i.e., continuity, x-, y-, z-velocity, k, and ε) are converged in less than '10e-5' for every case (Figure 4.7).
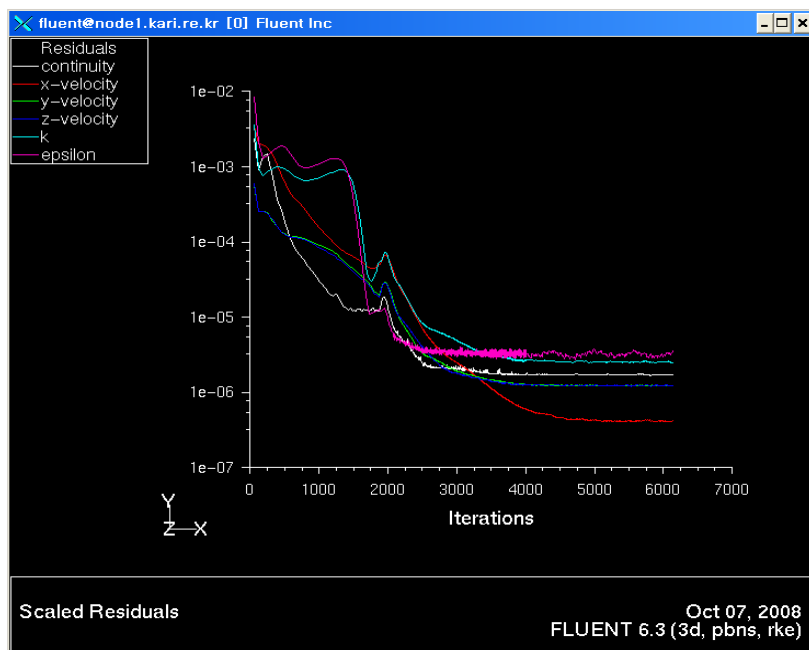
Figure 4.7 Convergence of scaled residuals (MODEL #09)

4.2.1. Analysis Conditions

The conditions used for this study are summarized as:

- Viscous model: realizable k-epsilon

- Near-wall treatment : standard wall function

- Discretization (momentum, turbulence kinetic energy, turbulence dissipation rate): first order upwind (for early iterations) and second order upwind (for the rest of the iterations)

4.2.2. Numerical Simulation Cases

A total of nine cases are investigated, and each model is presented in Table 4.3. All the signs which are used in 'S' and 'helicity' denote the rotational directions by the "Law of Clockwise Screw".

Table 4.3 Summary of Numerical Models

	S		helicity	Re		fluid
	in	out	(h)	in	out	
MODEL #01	+0.0	+0.0	0	6.87×10^4	4.64×10^4	Cold Air
MODEL #02	+0.0	+0.0	0	4.13×10^4	2.79×10^4	Hot Air (T_o=400K)
MODEL #03	+0.7	+1.2	0	6.87×10^4	4.64×10^4	Cold Air
MODEL #04	-0.7	+1.2	0	6.87×10^4	4.64×10^4	Cold Air
MODEL #05	+0.7	+1.2	-1	6.87×10^4	4.64×10^4	Cold Air
MODEL #06	+0.7	+1.2	-2	6.87×10^4	4.64×10^4	Cold Air
MODEL #07	+0.7	+1.2	-2	4.13×10^4	2.79×10^4	Hot Air (T_o=400K)
MODEL #08	+0.7	+1.2	-3	6.87×10^4	4.64×10^4	Cold Air
MODEL #09	+0.7	+1.2	-4	6.87×10^4	4.64×10^4	Cold Air

5. PRESENTATION AND DISCUSSION OF RESULTS
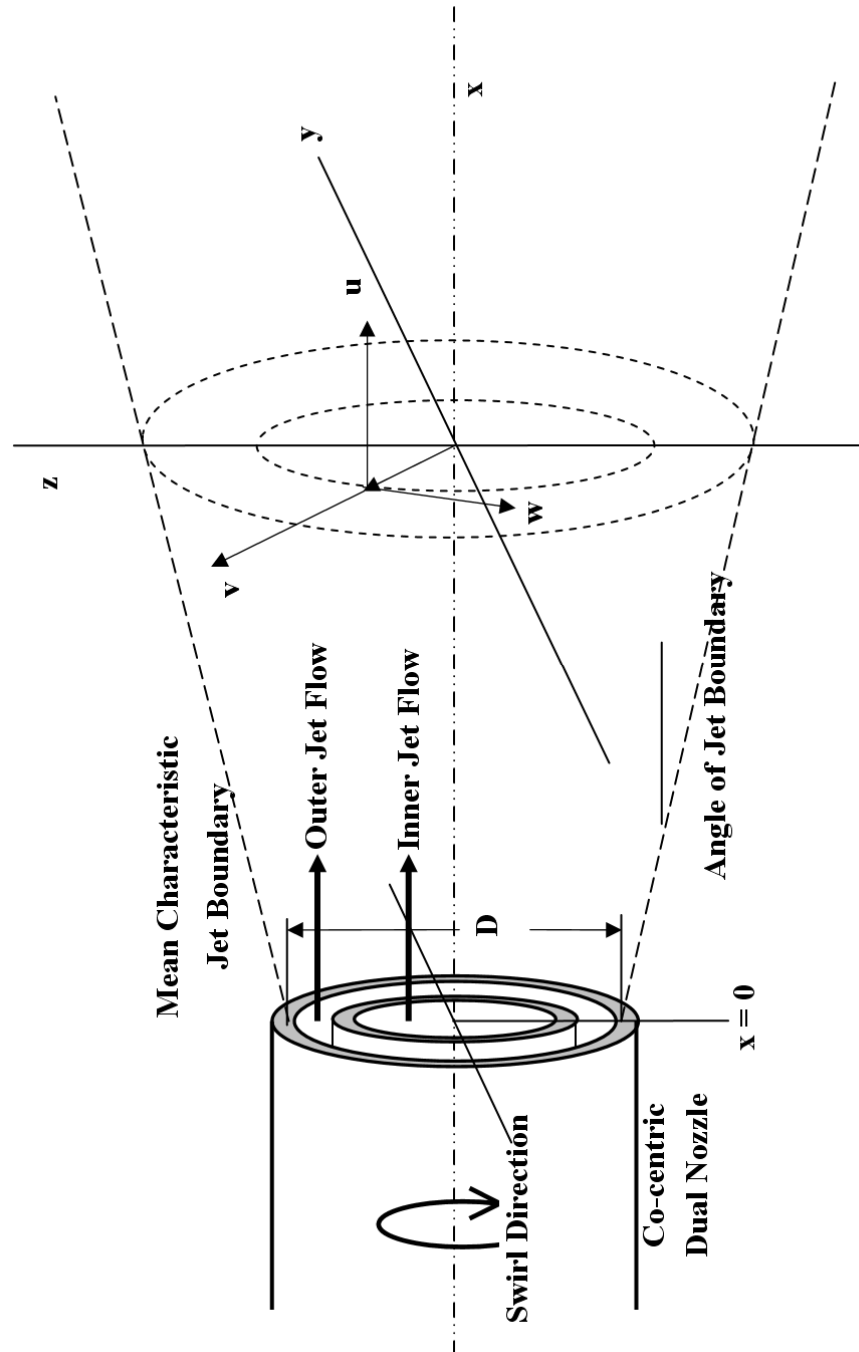
Figure 5.1 Definition sketch for a concentric dual swirl jet

5.1. Experimental Results

The effects of excitation on the growth of the natural instability waves and the resulting phenomena are investigated by the mean and fluctuating (i.e., turbulent) velocity measurements using a particle image velocimetry. A definition sketch is shown in Figure 5.1. A stereoscopic PIV is used to measure the time mean velocity in three components: the fluctuating turbulent quantities, and even vorticities. Comparisons of the profiles between jets at various excitation conditions provide a coherent structure variation and the remarkable indication of shear jet control.

Plotting is executed in three ways: a three-dimensional out-of-plane plot, a two-dimensional contour plot, and an X-Y plot. The contour plot shows the same velocity, turbulence intensity, and vorticity, distribution by using an identical color code in an equivalent level. In addition, the three-dimensional plot enables us to observe those distributions instantly by a cubic effect. Not only the axial properties, but also the radial and tangential velocity distributions are illustrated to reveal the characteristic behavior of swirl flows.

5.1.1. Verification of Shear Control

The test results of the jets at various conditions are plotted in Figures 5.3

through 5.80. Because enough data (i.e., total 8,100 points, 90×90 matrix) are

measured simultaneously, a numerical interpolation (e.g., the cubic spline method) is

not applied to smooth the contour plots. Each case is presented in three ways, based

on the display methods and the flow property of interest:

- The first part exhibits the overall shape of the mean axial velocity

  distribution in 3-D plots. The velocity field of the swirling jet is displayed by

  the height of the u (axial velocity) axis in this part. In addition, to help in

  analyzing the detailed velocity profile of potential cores and peaks, both

  translucency and cross-sectional half cut views are supplemented.

- The second part presents the same velocity distribution using a 2-D contour

  plot method. All figures are plotted in the same range of z- and y-

  coordinates, and these axes are normalized by the outer nozzle exit diameter

  (D, inner diameter). Velocity distributions are presented by colored contours

with the interval of 0.25m/s. Also, radial (v) and tangential velocity (w) distribution along a positive y-axis are presented in the so-called X-Y plots.

● The last part of each figure displays the derived properties of velocity (i.e., turbulence intensity and vorticity). The axial turbulence intensity distribution plots are shown with an interval of 10% (a total of twenty steps). The contour of vorticity is shown in the same manner with an interval of $20s^{-1}$ (a total of twenty-two steps).

The presented figures are also categorized according to the following investigation purposes:

● First, Figures 5.3 through 5.6 show the concentric dual round jet, and this is used as the baseline for the excited swirl cases.

● Figures 5.7 through 5.14 illustrate the effects of the existence of swirl.

● The results from kinematic viscosity gradient are presented in Figures 5.15 to 5.18.

● Velocity gradient effects are provided from Figures 5.19 to 5.34.

- Last, the shear excitation effects from lobed disturbance are displayed in Figures 5.35 to 5.66.

5.1.1.1. Graphic Generator

The data acquired by the PIV are plotted by means of the following computer graphics software:

Tecplot version: 9.0-0-9 (Mar. 26 2001) for MS-Windows

Copyright(c) 1988-2001 Amtec. Engineering, Inc.

5.1.1.2. Uncertainty Analysis and Repeatability Check

For this analysis, the inner and outer radii of the nozzles are known to be accurate within ±0.047mm (i.e., the tolerance).

The presented percentage errors in the following sections are acquired by the iteration of measurements under the same conditions. For instance, mass flow rate is

measured by the mass flow controller (MFC) ten times under the exactly same flow conditions. After the calculation of mean value of the acquired data, the absolute value of maximum deviation is divided by the mean value and multiplied by 100 to be expressed as a percentage. Even though the PIV data acquisition itself is using the time-averaged method, the same iteration concept is applied to the PIV system using a calibration target (ref. Figure 3.54). Here are some estimated errors in this analysis.

First, even though the supplying tank pressure is maintained by a high quality regulator, there is an unavoidable ±2.15% error in pressure measuring.

Second, ±2.45% of error is from the PIV system. These measurements are performed ten times at the point of 'x/D=1' with the calibration target.

Last, the maximum possible error in the measurement can occur when the author set the relative distances (or angles) between the cameras and various planes, horizontal (i.e., altitude) settings of measurement equipment, swirl generator angle setting, and others. It has been estimated that the setting errors are accumulated as ±3.52%.

Therefore, the total percentage error in the measurements is ±4.79% (square root of the squared possible errors).

In addition, to check the repeatability of test results, a selected case (CASE #03) is measured twice. The second measurement is carried out two weeks after the first performance with fully re-assembled conditions for the nozzle, swirl generators, and PIV system. Figure 5.2 shows good agreement, with approximately less than ±4% deviation, when the mean values between the two results are compared, and it also falls into the estimated error range.
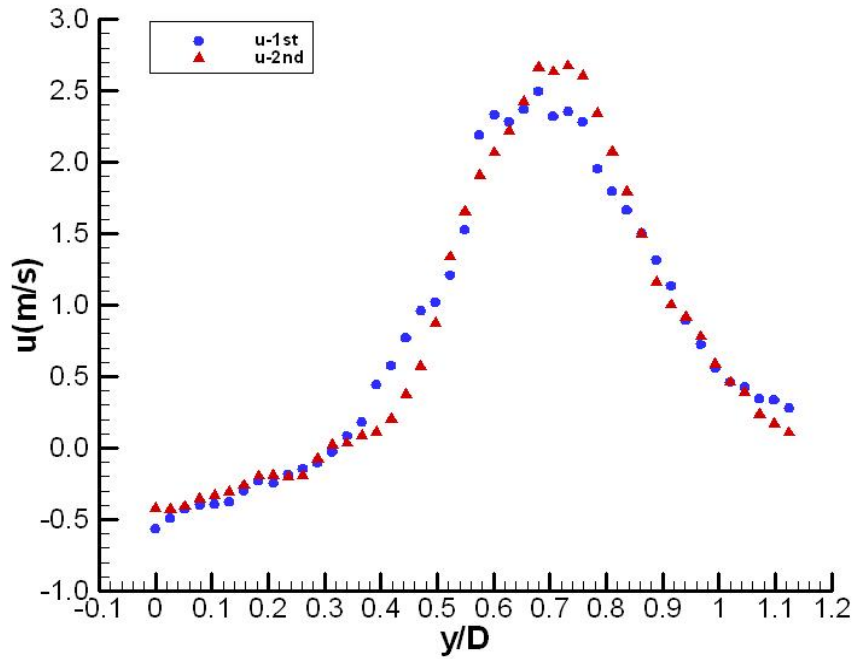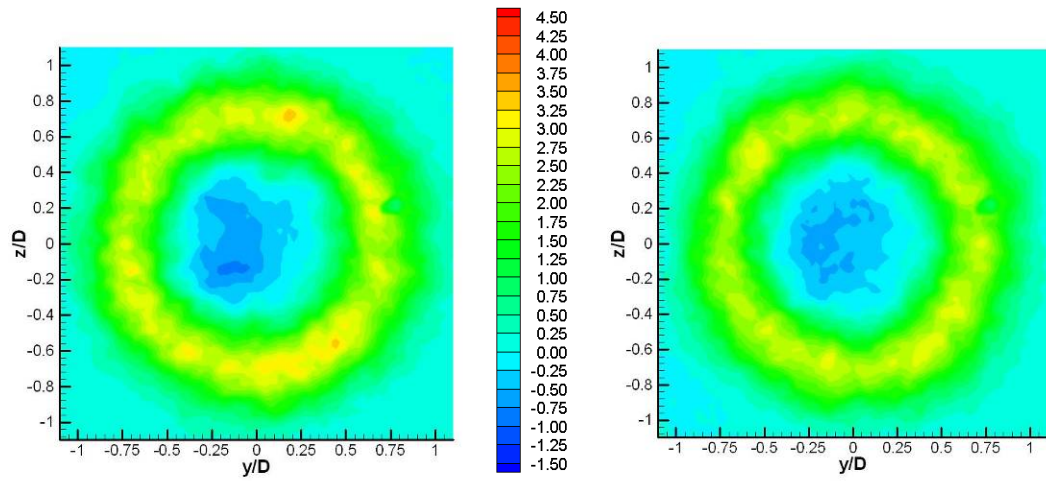
Figure 5.2 Repeatability of PIV measurement results (CASE #03)
axial velocity (u, m/s) distribution: contour of first measurement (upper left),
second measurement (upper right), comparison at z/D=0 (lower)

5.1.1.3. Velocity Fluctuation and Vorticity Analysis

The concept of turbulence intensity led by Osborne Reynolds in 1895 resulted in writing the continuity and momentum equations in terms of mean and time-averaged turbulent variables[34].

The time mean 'u' of a turbulent function u(x, y, z, t) is defined by:

$$\bar{u} = \frac{1}{T}\int_0^T u\,dt \qquad\qquad (5.1)$$

where T is an averaging period.

The mean square of a fluctuation is a measure of the intensity of the turbulence.

$$\overline{u'}^2 = \frac{1}{T}\int_0^T u'^2\,dt \qquad\qquad (5.2)$$

where $u' = u - \bar{u}$

The results of turbulence intensity ($\frac{\sqrt{\overline{u'^2}}}{\overline{u}} \times 100$, %) measurements for the

axisymmetric swirling jets at x/D=1 are plotted partially in Figures 5.3 through 5.80.

All the numbers used are non-dimensional, and the z- and y-axis are also normalized

by D.

The derivation of differential quantity (e.g., vorticity) is also performed, and

it relies on calculating differences between neighboring vectors. It can therefore be

very noisy, especially if the seeding density is low and the data points are closely

spaced. As can be seen in Figure 5.6, overall, enough seeding density makes the

pictures clear.

The vorticity (s⁻¹) is defined as:

$$\omega = \frac{\partial v}{\partial x} - \frac{\partial u}{\partial y} \tag{5.3}$$

$$\zeta = 2\omega = \text{curl } V \tag{5.4}$$

5.1.2. Configuration of Baseline

CASE #01, no swirl and unexcited, is selected as a baseline, and this will be a major counterpart of the comparison to the other experimental cases. The subsonic jet facility produces dual concentric flow without swirl. As a working fluid, air is chosen. The environmental temperature and pressure are maintained in the range of 294~296K and 1.0 atm, respectively, throughout all the experiments. Each jet has the Reynolds number of 6.87×10^3 (inner) and 4.64×10^3 (outer). The measurement plane (i.e., focal plane) is located '60mm' from the nozzle exit, and it is the same as the inside diameter (ID) of the outer nozzle (i.e., x/D=1). The purpose of this experimental study mainly concerns the near region (i.e., x/D<2) from the nozzle exit, not the far field, due to the consideration of the application for combustion chambers. The characteristics of wave propagation into the far field (i.e., x/D>5 for the exhaust jet applications) will be discussed in the numerical analysis section.

CASE #01: Unexcited without Swirl

Figures 5.3 and 5.4 show that the averaged axial velocity at the vortex core is 3.3m/s, and the peak value is around 4.2m/s. The normalized distance from the origin to the detected peak (i.e., normalized radius, r/D) is 0.3, and to the jet boundary is 0.7. A subsonic swirl-free jet experiences, theoretically, no static pressure gradient in the radial or axial direction. The radial velocity (v) along the positive y-traverse stays at zero, except in the range of 'y/D=0.25~0.60'. The existence of the shear layer between the inner and outer jet creates the outward (i.e., positive) radial velocity component. On the other hand, it is natural that a relatively small variation (i.e., disturbance) is found in the tangential velocity distribution.

Throughout the whole field, the turbulence intensity shows the value of 10 to 20% (Figure 5.5). Getting close to the shear layer between the outer jet and free stream, its value reaches approximately up to 120%. Even though there are a few spots of over 180% seen at the edge of the jet boundary, they can be negligible. As shown in Figure 5.6, the general behavior of vorticity stays calm within $\pm20s^{-1}$. Some angular motions with the vorticity level of '100~120' are created at each shear layer region.
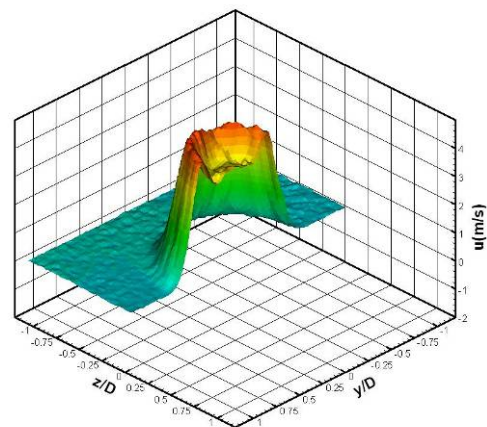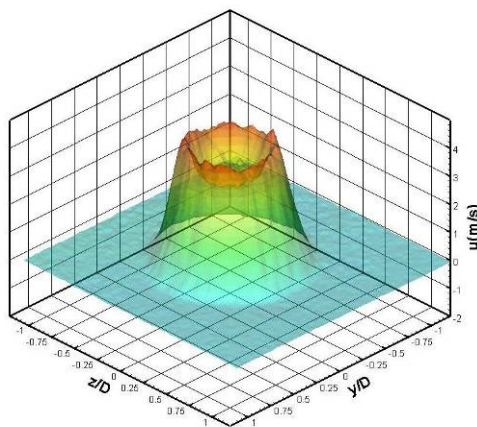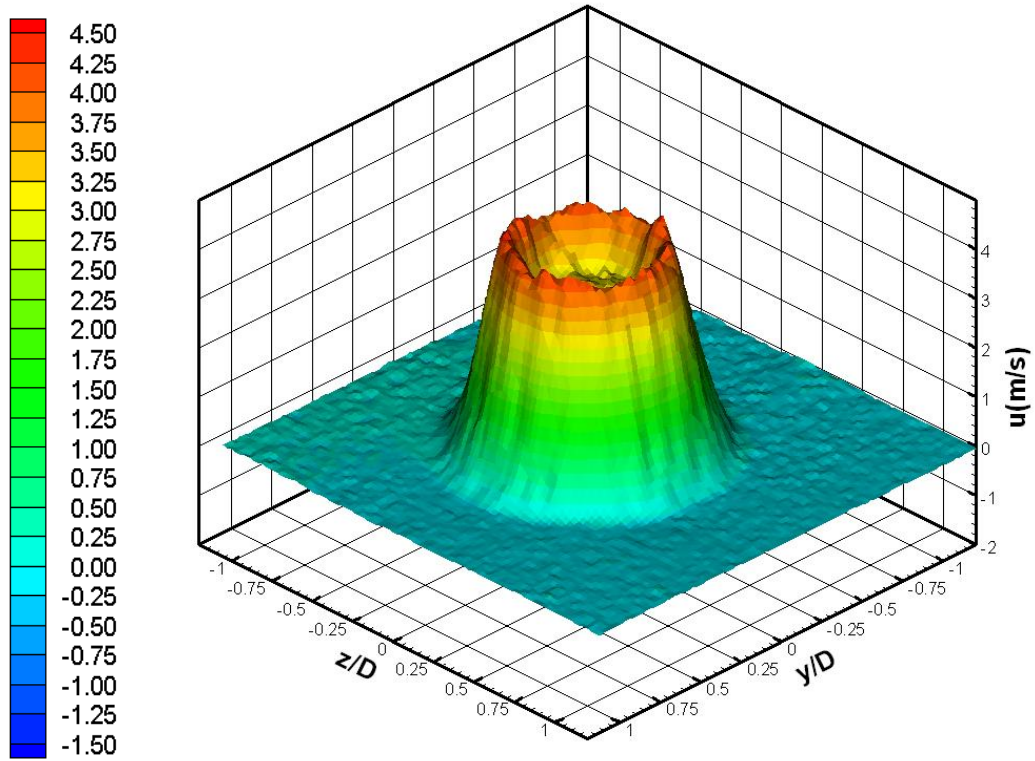
Figure 5.3 CASE #01: Axial velocity (u) distribution
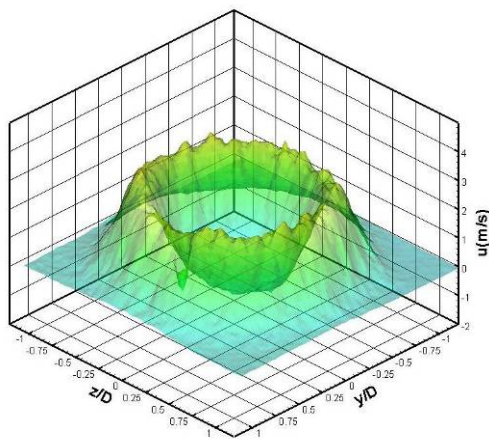**3D full (upper), translucency (lower left), cross-sectional (lower right) views**
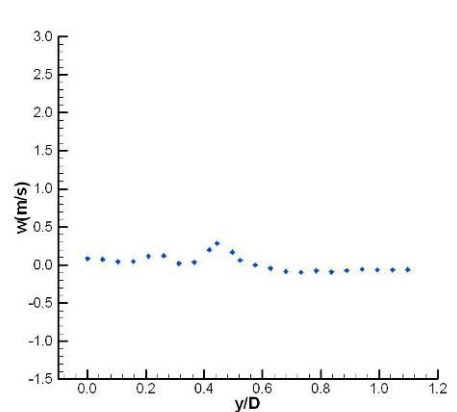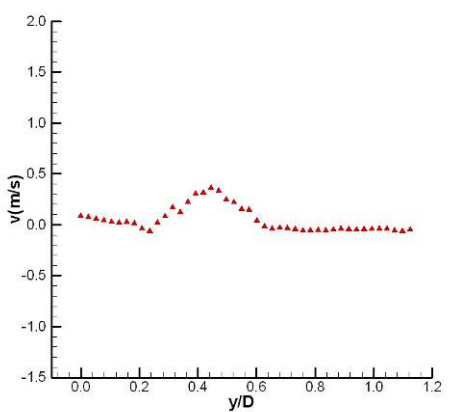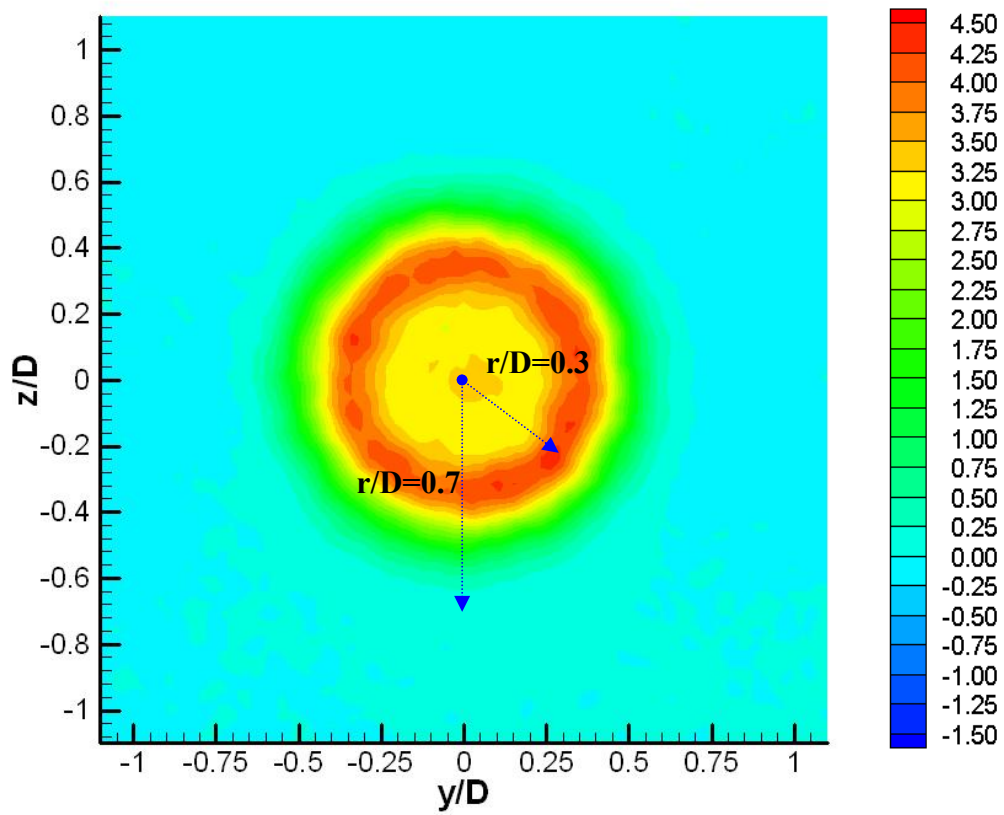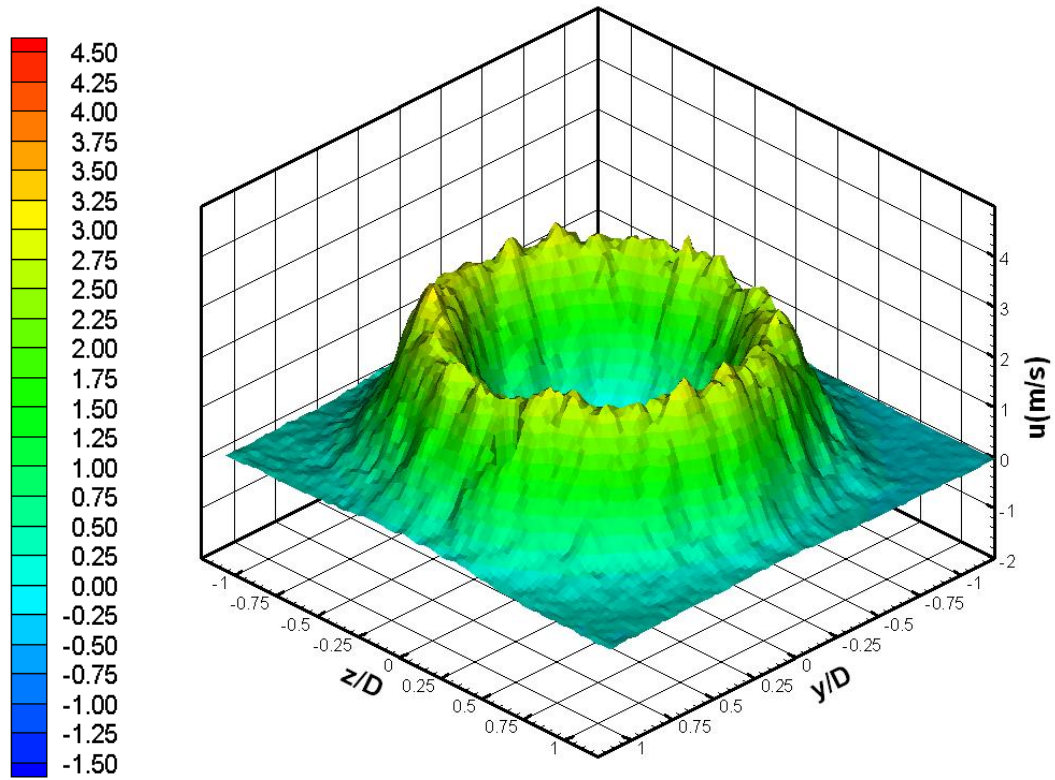
Figure 5.4 CASE #01: Contour of axial velocity (u, m/s) (upper),
radial velocity (v) along positive y-axis (lower left),
tangential velocity (w) along positive y-axis (lower right)
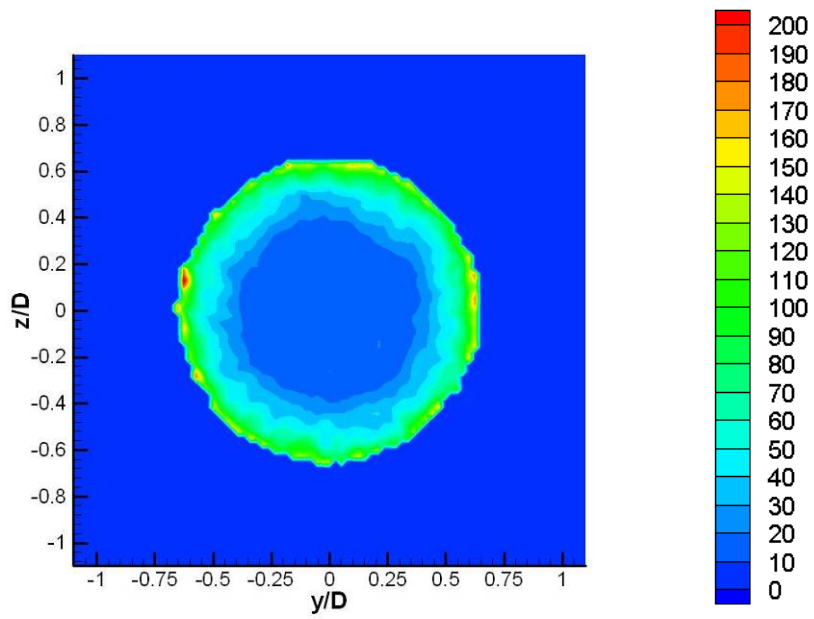
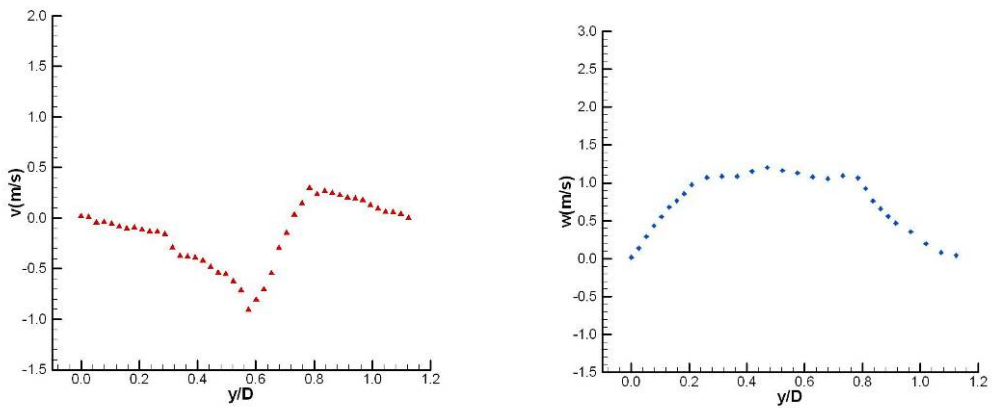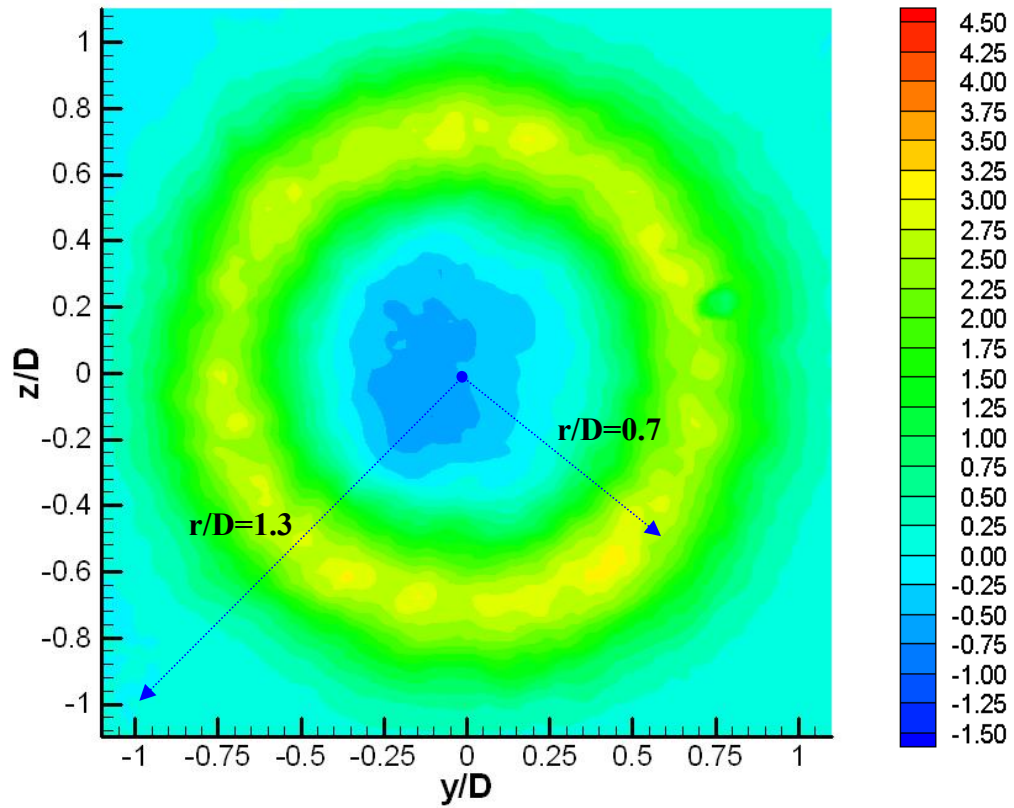**Figure 5.5 CASE #01: Contour of axial turbulence intensity (%)**
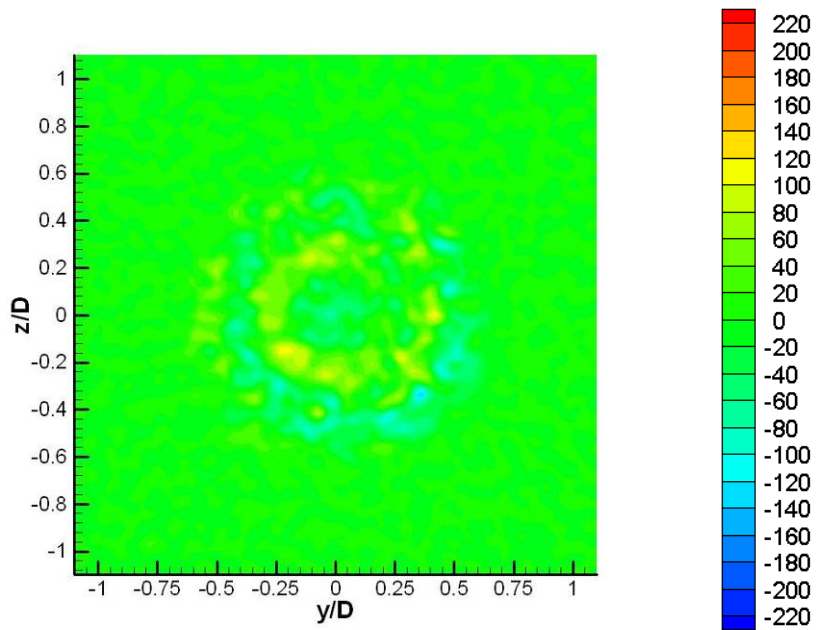
**Figure 5.6 CASE #01: Contour of vorticity (s^{-1})**

5.1.3. Existence of Swirl

The following section presents the test result of swirl effects on concentric round jets (CASES #02 and #03, Figures 5.7 to 5.14).

CASE #02: Unexcited with Co-swirl

Three-dimensional plots enable us to observe the swirl influence instantly by a cubic effect (Figure 5.7). Noticeable changes are found in the radii of the peak and the jet boundary compared to the baseline (Figure 5.8). The radius of the peak (=r/D) is extended from 0.3 to 0.8 (167% up) in the outward direction, and the jet boundary's is doubled at the same time (r/D=0.7 to 1.4). Furthermore, the peak of the axial velocity is reduced to 3.2m/s, and the depth of the core is deepened to -1.2m/s. This is 136% down compared to the core velocity of the baseline, and a 24% reduction occurs for the peak one.

Regarding radial distribution comparison, the radial velocity (v) changed to negative values throughout the entire region. This is an interesting swirl jet

phenomenon caused by a central toroidal recirculation zone (CTRZ). A typical jet flow with a high degree of swirl (i.e., strong swirl, S>0.6) experiences the significant lateral and longitudinal pressure gradients (a much wider and slower jet than its non-swirling counterpart) and a toroidal recirculation. As expected, due to a swirl effect, the tangential velocity components are intensified, and the location of maximum value (=1.3m/s) is found around 'y/D=0.6' (Figure 5.8).

In case of the velocity fluctuation (Figure 5.9), both shear layer regions show the agitated effects by the rotating flow, especially at the shear layer between the jets (i.e., inner and outer), where they have the intensity value of 180 or above. Also, the regionally intensified turbulences appear at the outer edge of the jet boundary. Compared to CASE #01, the vorticity is intensified, especially at the vortex core, and the peak value lies between 160 and 180 (Figure 5.10). Generally, the direction of angular motion (i.e., vorticity) is positive (Law of Clockwise Screw), and the negative values can be found near the edge of the jet boundary caused by the shear interaction with the environmental air.

CASE #03: Unexcited with Counter-swirl

To analyze the counter-swirl effects, negative rotating flow is generated at the inner jet. Curiously, the overall trend of the counter-swirl cases is similar to the co-swirl counterparts. In both radii of peaks and jet boundary, expanding (in radial) effects are relieved approximately 10% compared to CASE #02. The depth of the vortex core is reduced to -0.8m/s, and the maximum velocity at the peak also shrinks to 2.8m/s at the same time (Figure 5.12).

In the y-axis traverse comparison, the counter-swirl of the inner jet strongly influences the tangential velocity distribution. The inward flow in radial direction (i.e., centripetal) is intensified strongly, and it reaches down to -1.0m/s at between the jets flows.

In the case of the velocity fluctuation, both shear layer regions show no remarkable difference between CASES #02 and #03.
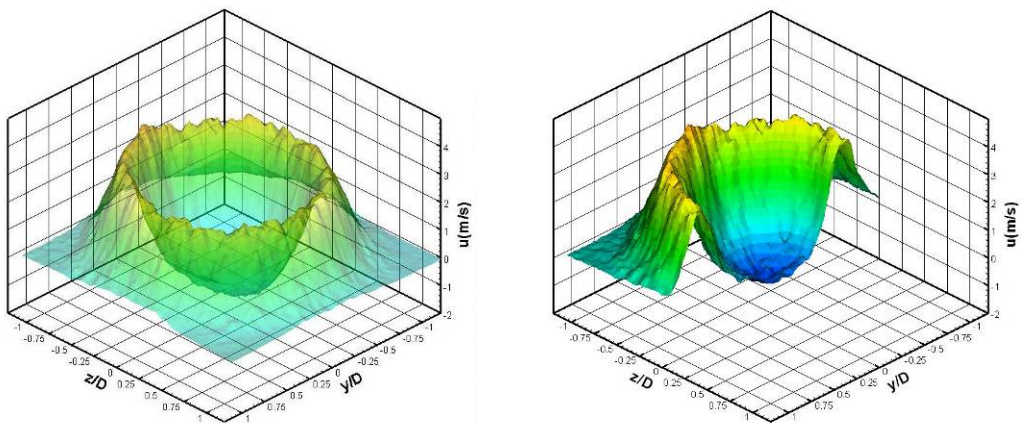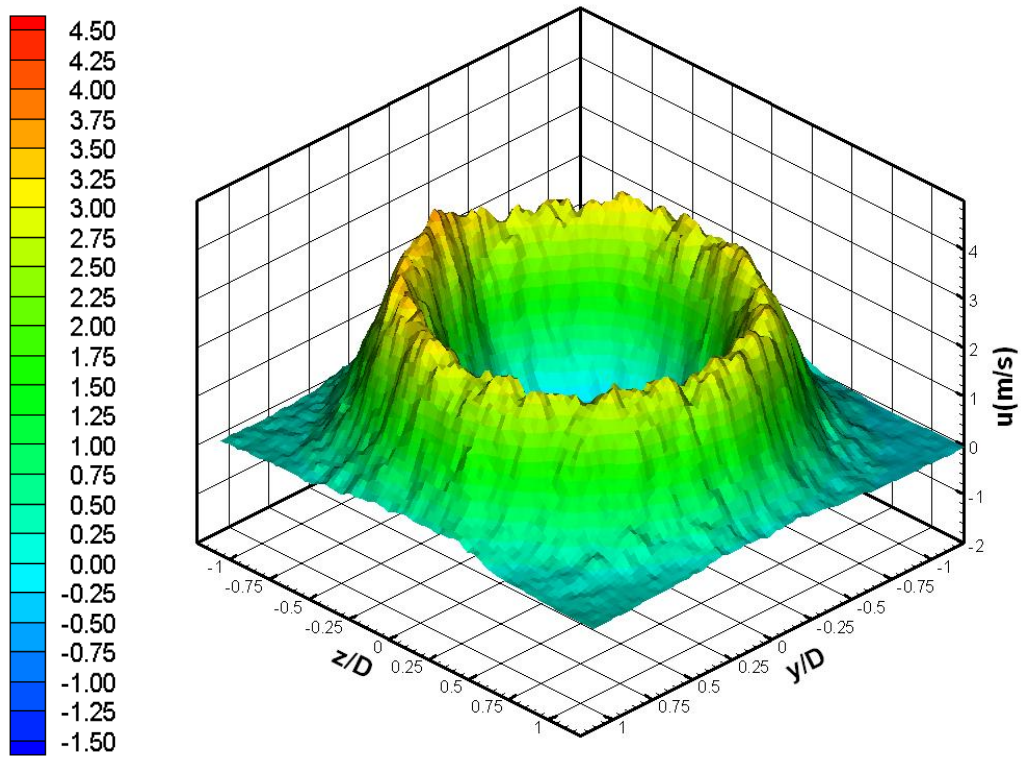
Figure 5.7 CASE #02: Axial velocity (u) distribution
3D full (upper), translucency (lower left), cross-sectional (lower right) views

123
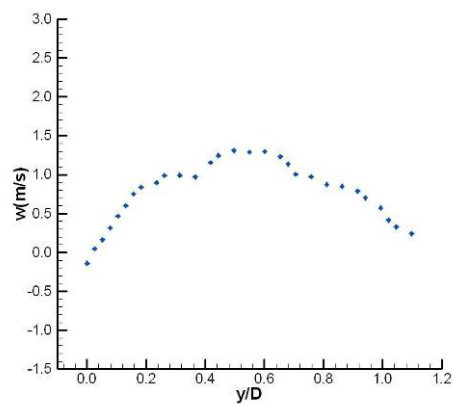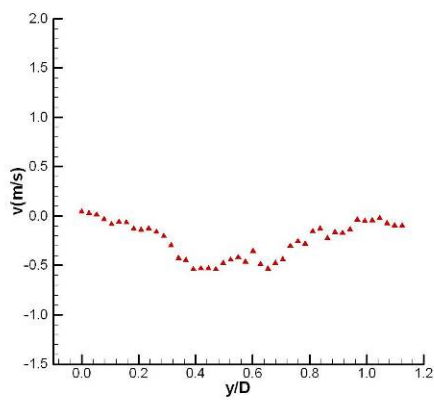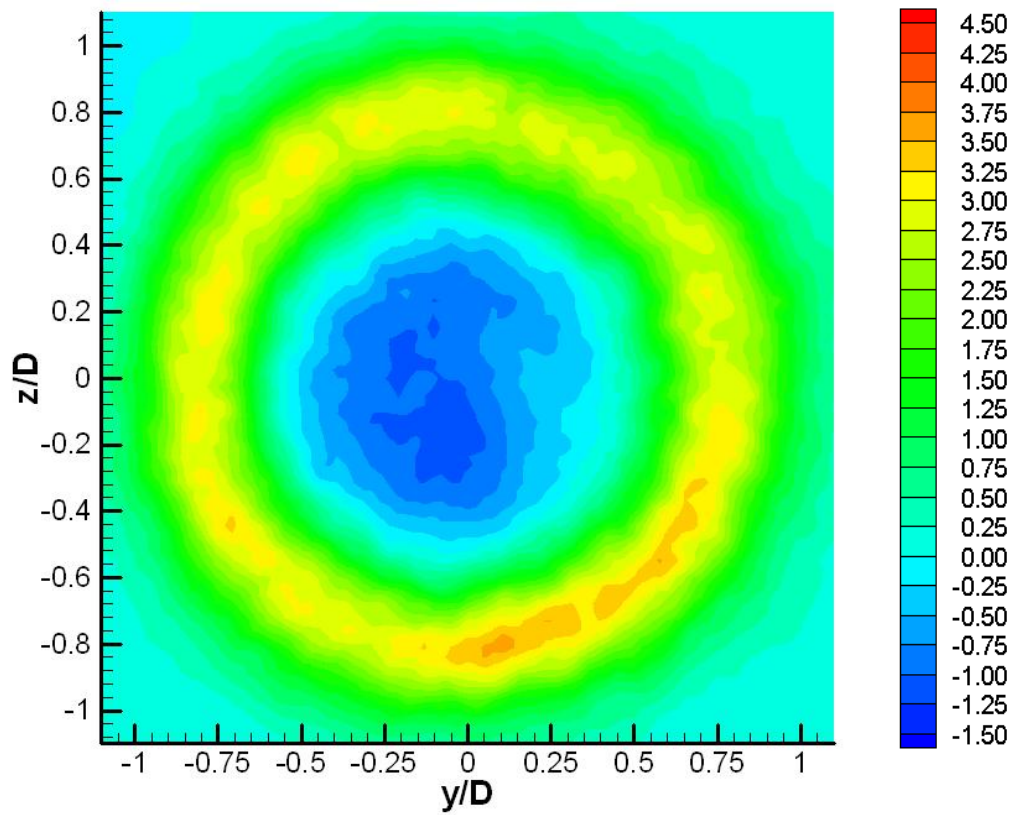
Figure 5.8 CASE #02: Contour of axial velocity (u, m/s) (upper),
radial velocity (v) along positive y-axis (lower left),
tangential velocity (w) along positive y-axis (lower right)
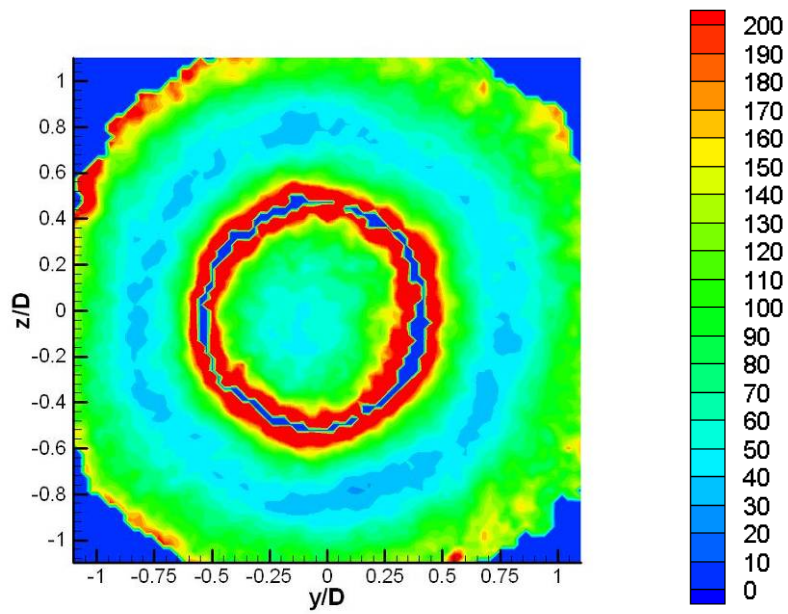
Figure 5.9 CASE #02: Contour of turbulence intensity (%)
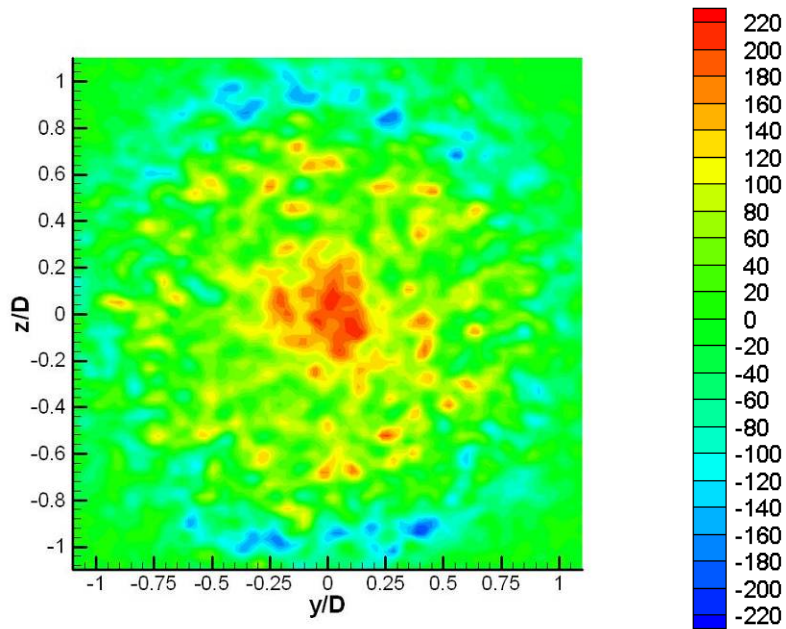
Figure 5.10 CASE #02: Contour of vorticity (s^{-1})
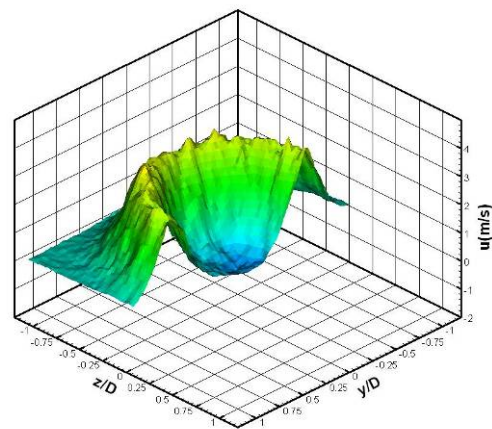
Figure 5.11 CASE #03: Axial velocity (u) distribution
3D full (upper), translucency (lower left), cross-sectional (lower right) views

**Figure 5.12 CASE #03: Contour of axial velocity (u, m/s) (upper),
radial velocity (v) along positive y-axis (lower left),
tangential velocity (w) along positive y-axis (lower right)**
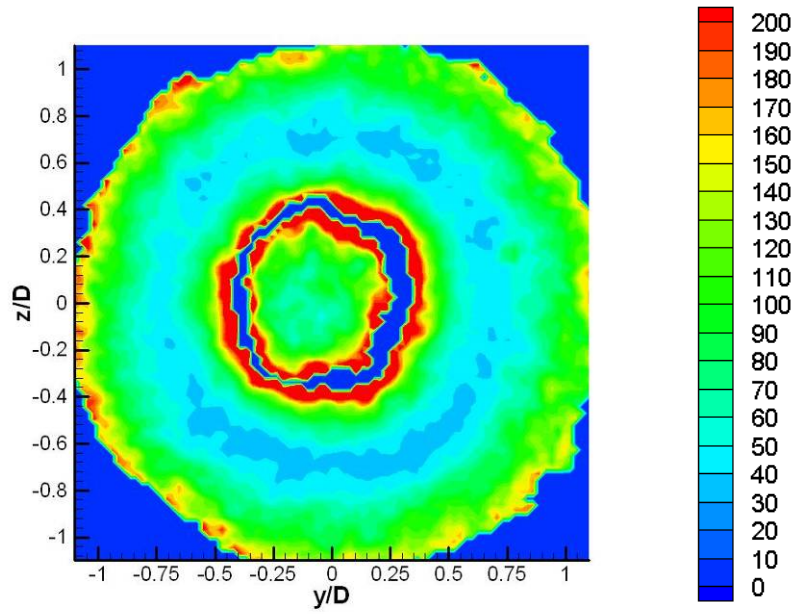
Figure 5.13 CASE #03: Contour of turbulence intensity (%)
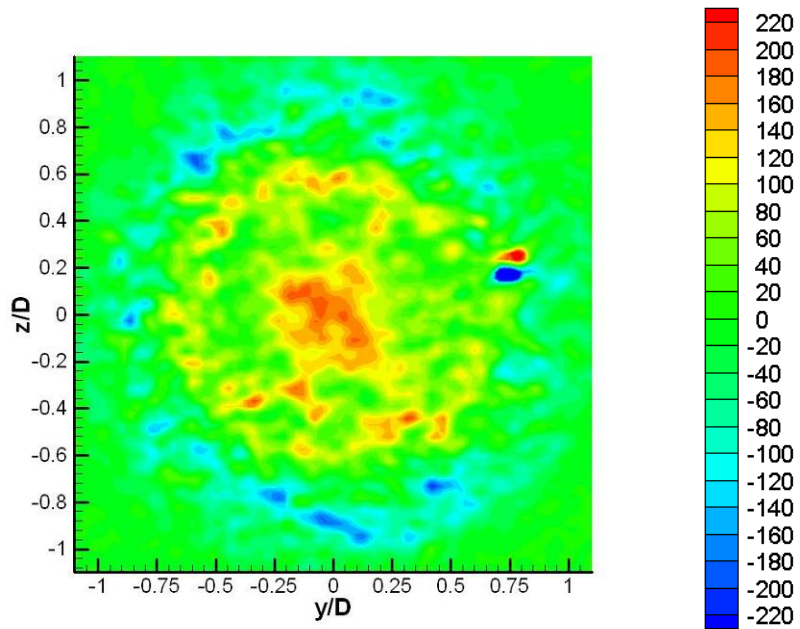
Figure 5.14 CASE #03: Contour of vorticity (s⁻¹)

5.1.4. Kinematic Viscosity Gradient

To investigate the effects of kinematic viscosity ($\nu = \mu / \rho$) variation between the jets (CASE #04, Figures 5.15 to 5.18), the following section is presented. For this purpose, CO_2 (ρ=1.77, μ=149x10^{-7} @ 300K) gas is adopted for the outer jet instead of air (ρ=1.16, μ=184.6x10^{-7} @ 300K). Even though the nozzle exit velocity is set to the same level as its counterpart's (CASE #03), the Reynolds number is changed to 8.78×10^3 due to relatively low kinematic viscosity of CO_2. From the three- and two-dimensional contour plots (Figure 5.15 and 5.16), the maximum axial velocity and the depth of the vortex core are increased at the same time. On the other hand, both the location of peaks and the jet boundary is quite similar to their counterparts (CASE #03). Due to the increased density effect, the profile of the radial velocity is pushed down to the negative region, and the tangential distribution is changed from a flat top shape to a convex one.

The kinematic viscosity gradient, especially density, between the jets creates the centripetal force, and it results in the negative values in the radial velocity profiles. The decreased outer kinematic viscosity effects show a similar pattern to the

129

raised outer velocity one (CASE #06).

Consequently, this can be explained in that the augmented Re, either by kinematic viscosity or velocity, stimulates the flow in a similar pattern. But the result shows that the variation of velocity is more effective in the control of double hump profile and vortex core.
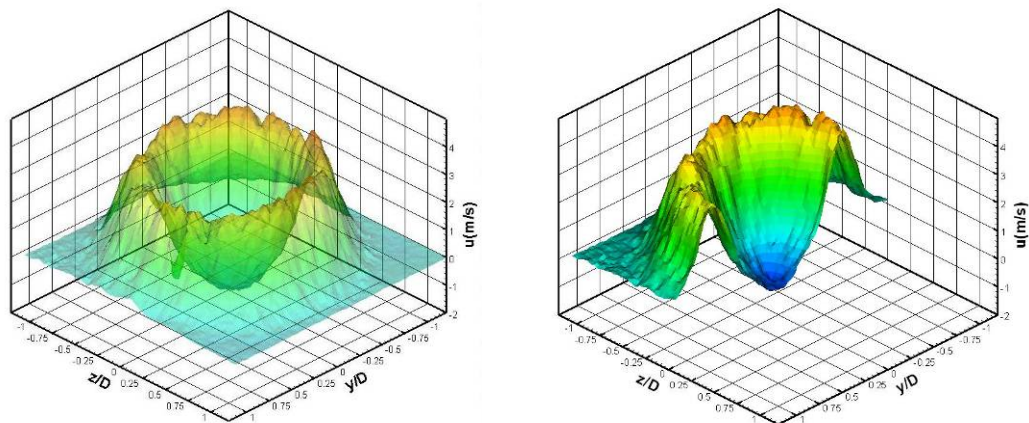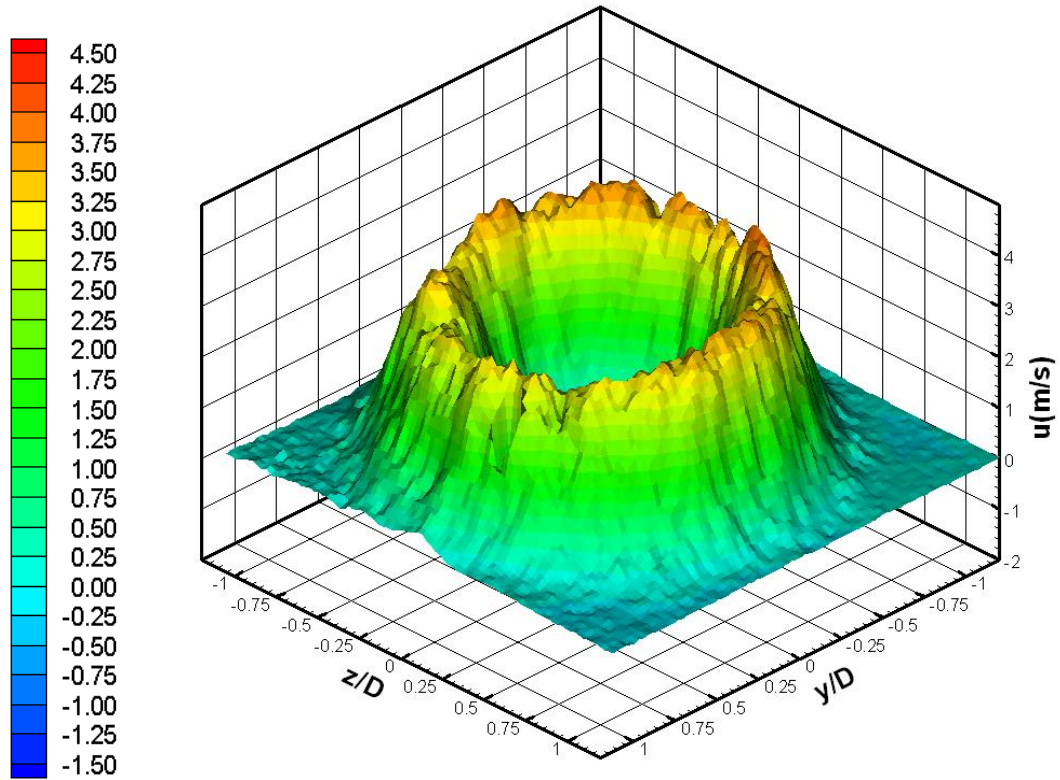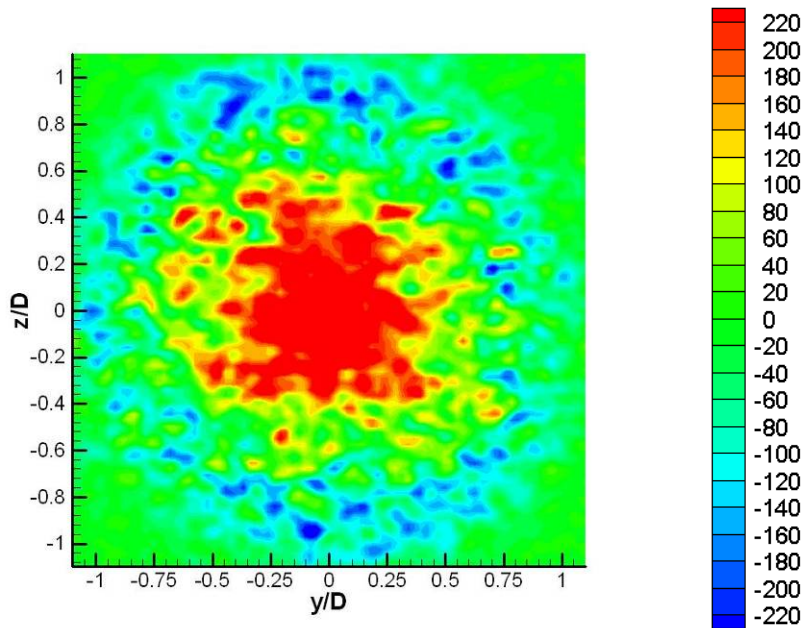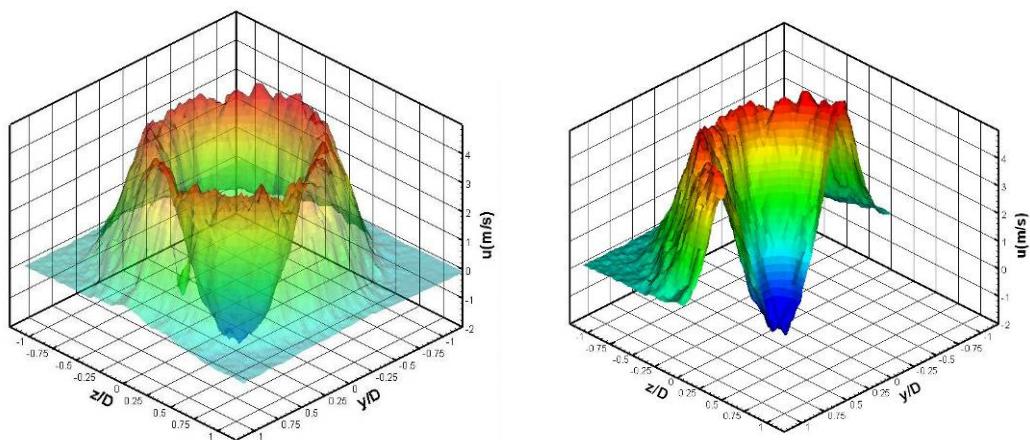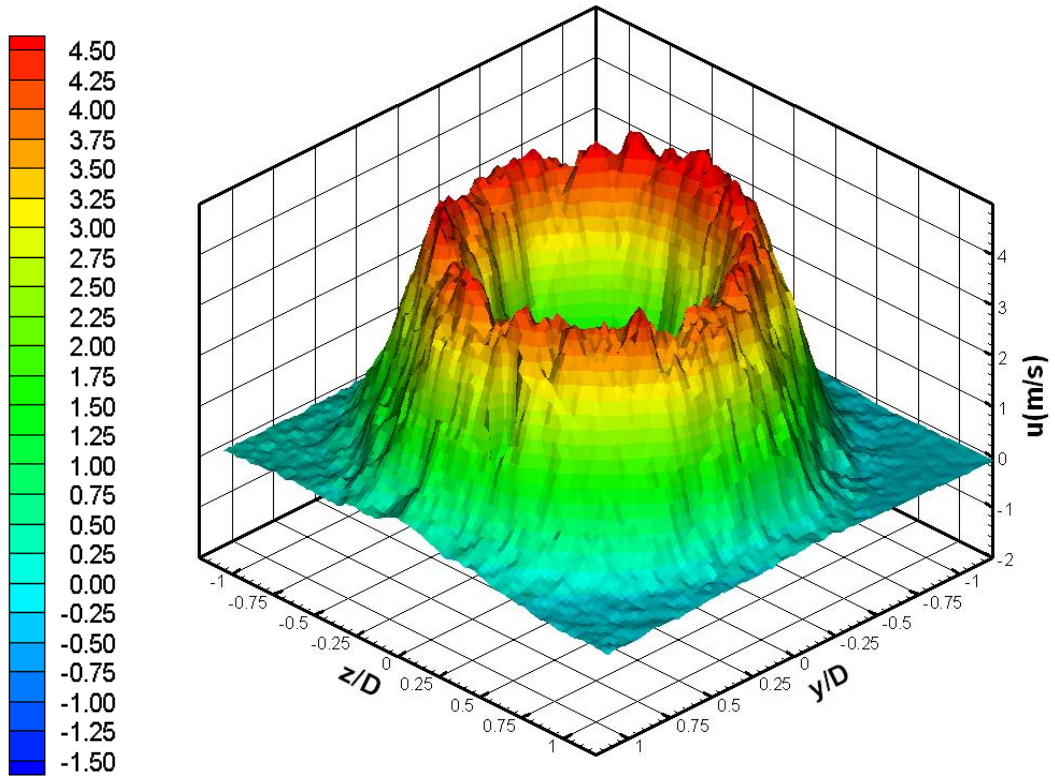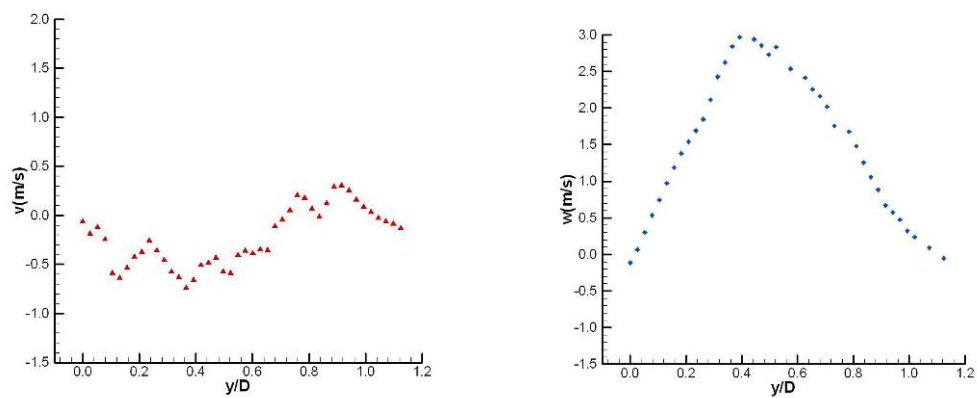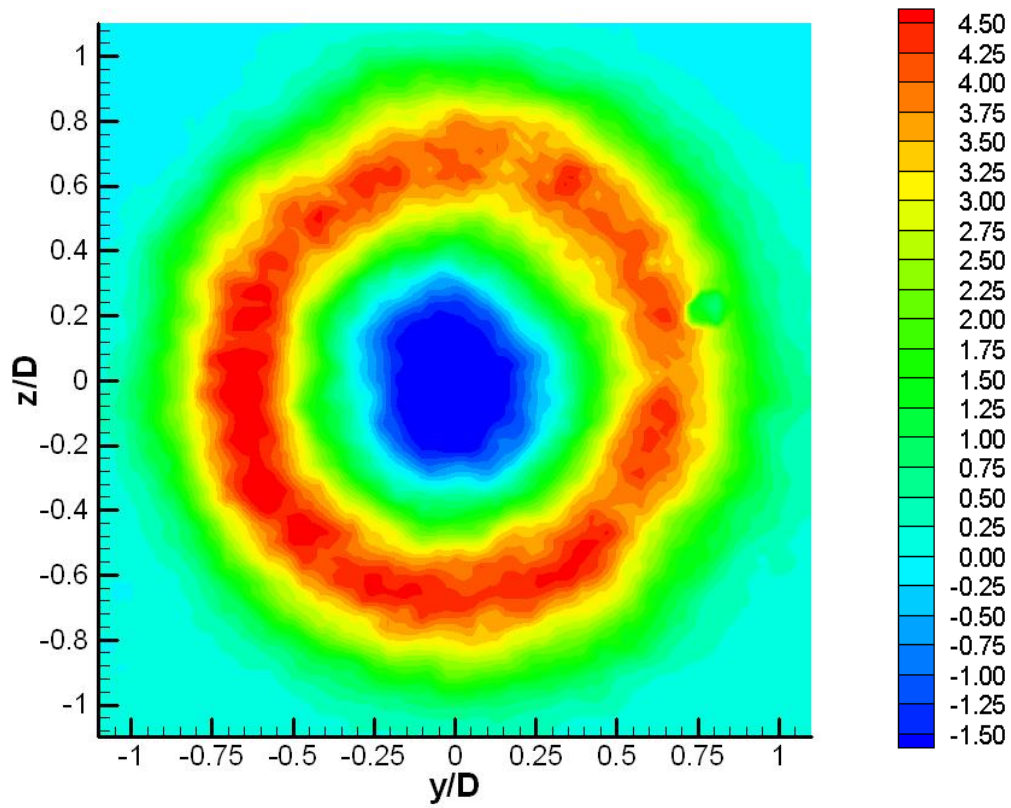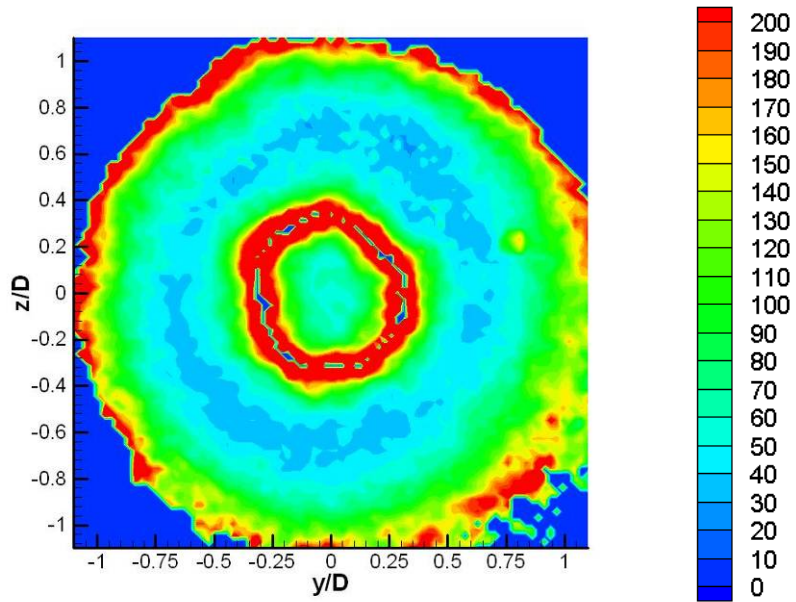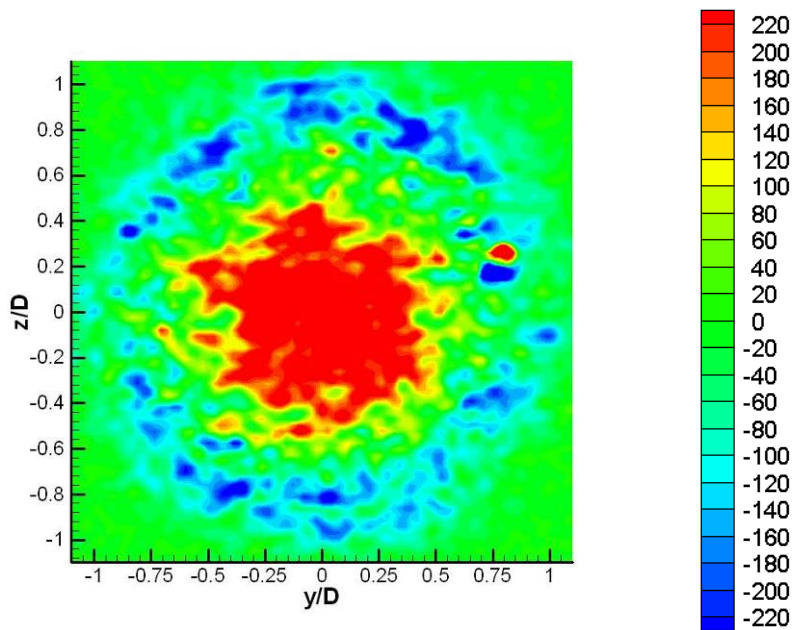
Figure 5.15 CASE #04: Axial velocity (u) distribution
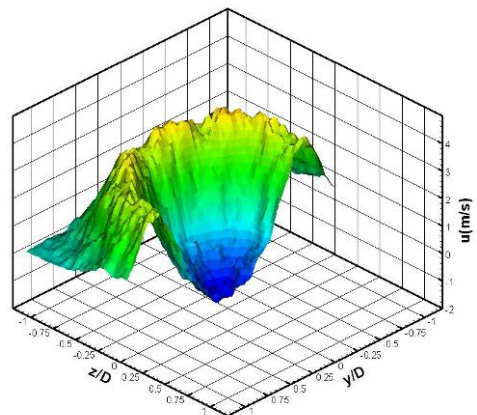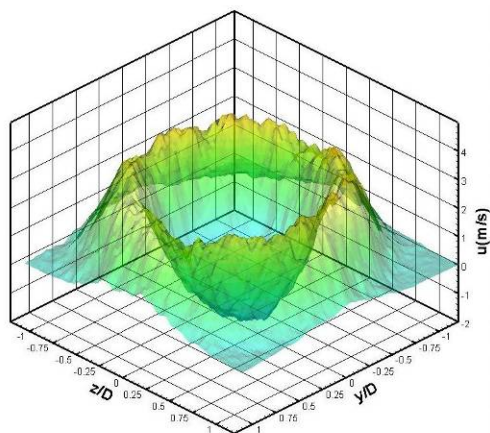**3D full (upper), translucency (lower left), cross-sectional (lower right) views**
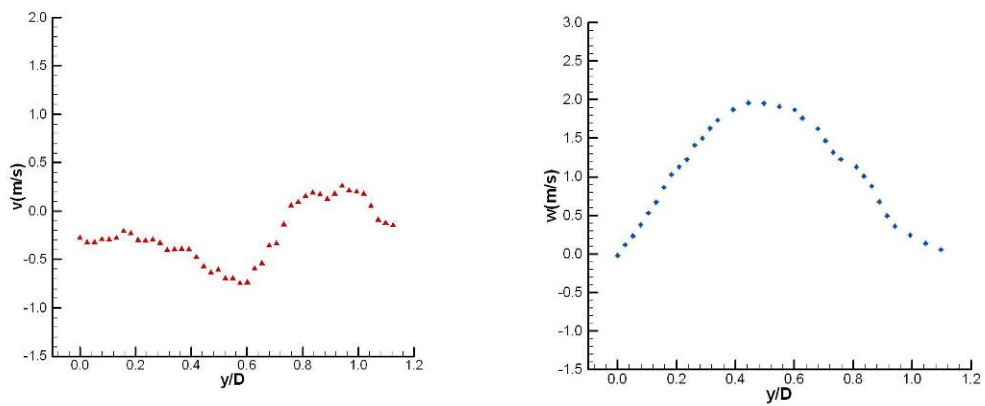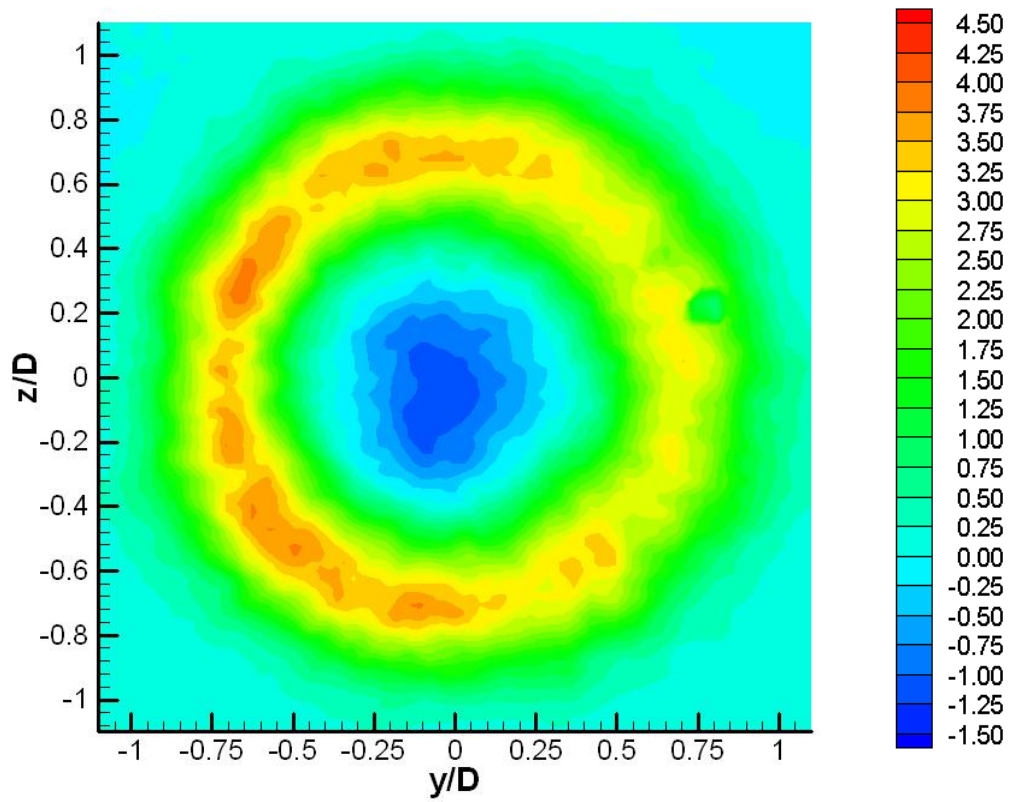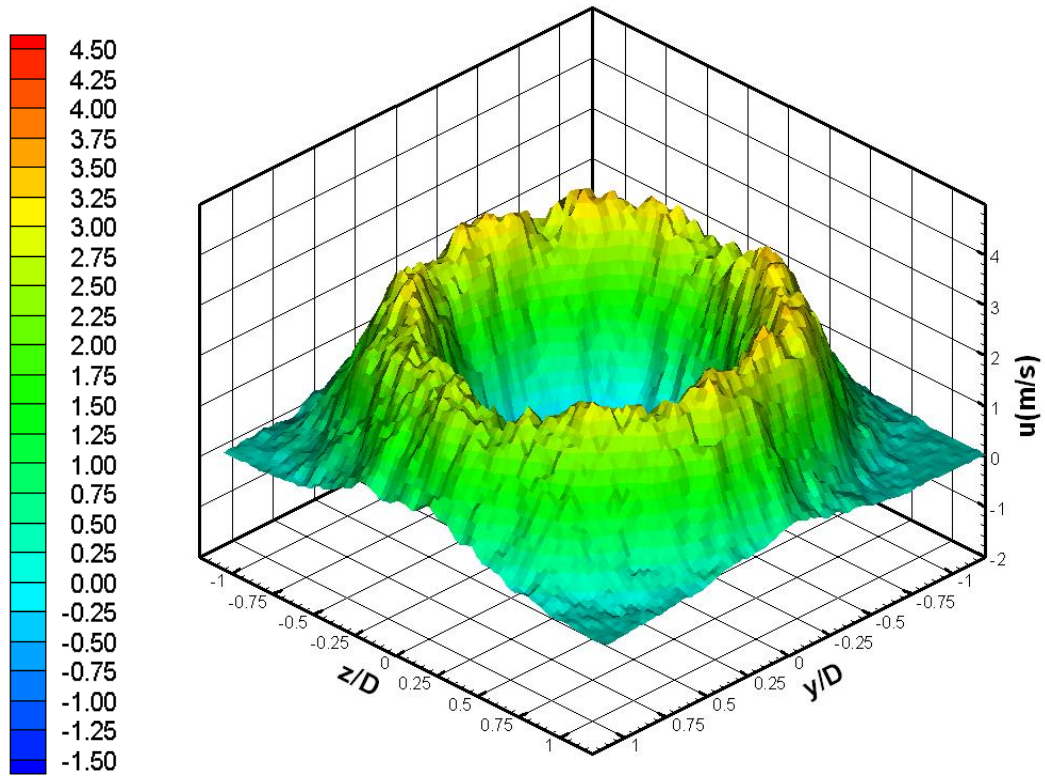
**Figure 5.16 CASE #04: Contour of axial velocity (u, m/s) (upper),
radial velocity (v) along positive y-axis (lower left),
tangential velocity (w) along positive y-axis (lower right)**
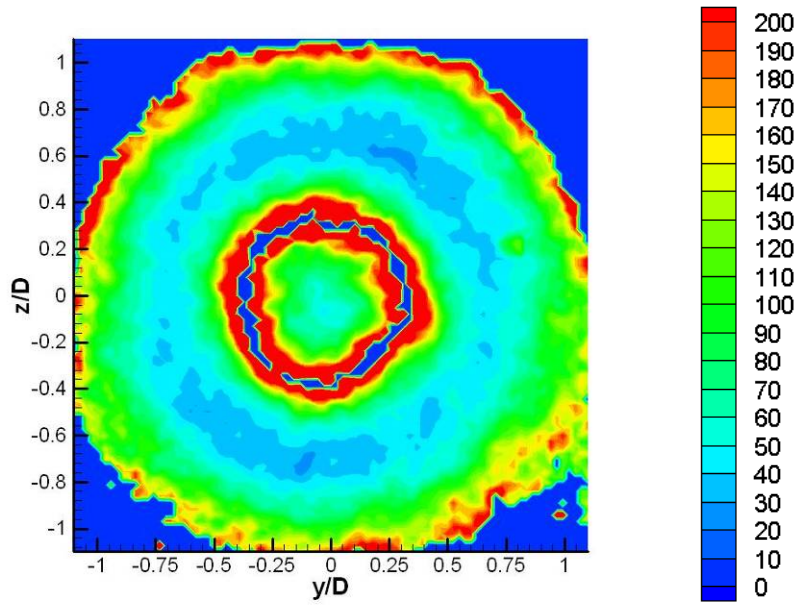
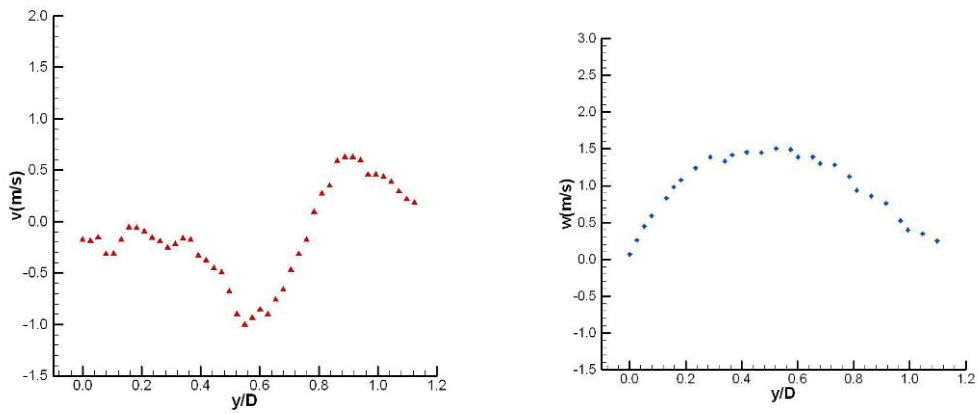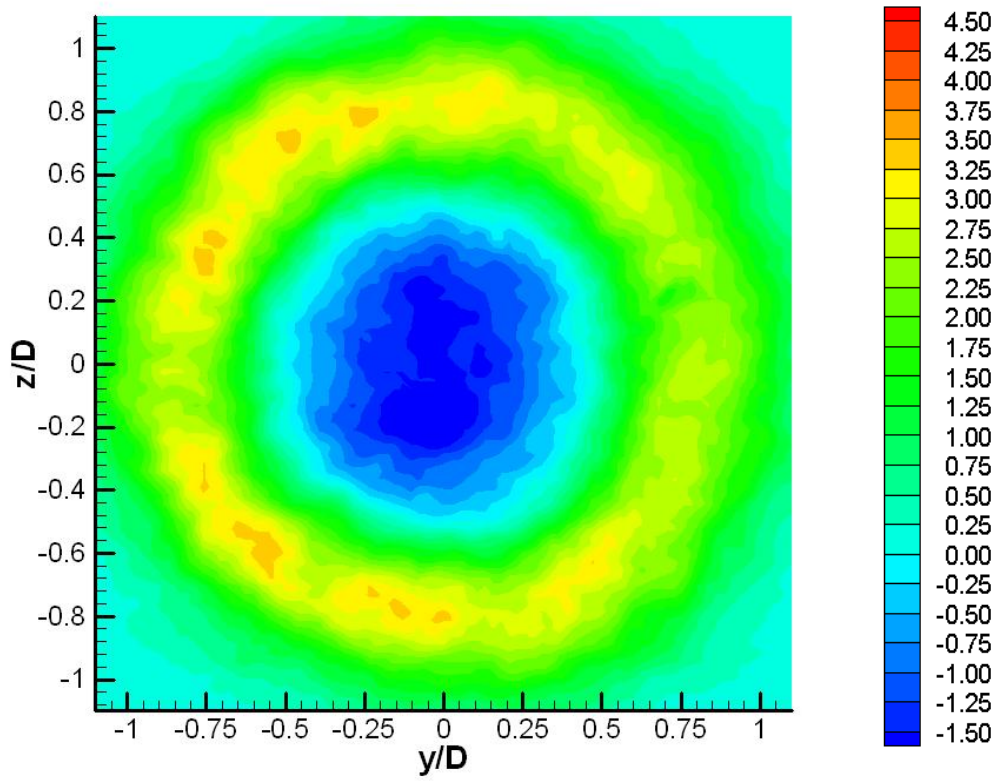**Figure 5.17 CASE #04: Contour of turbulence intensity (%)**
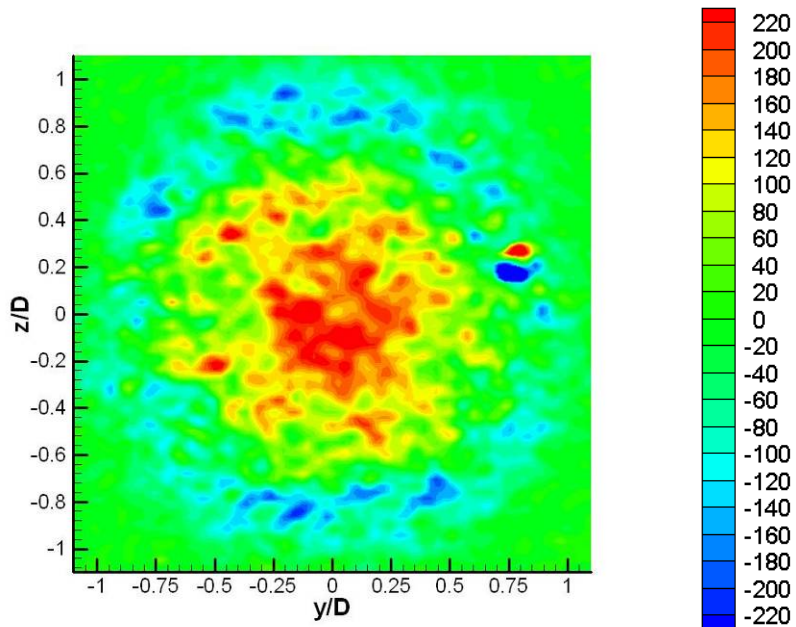
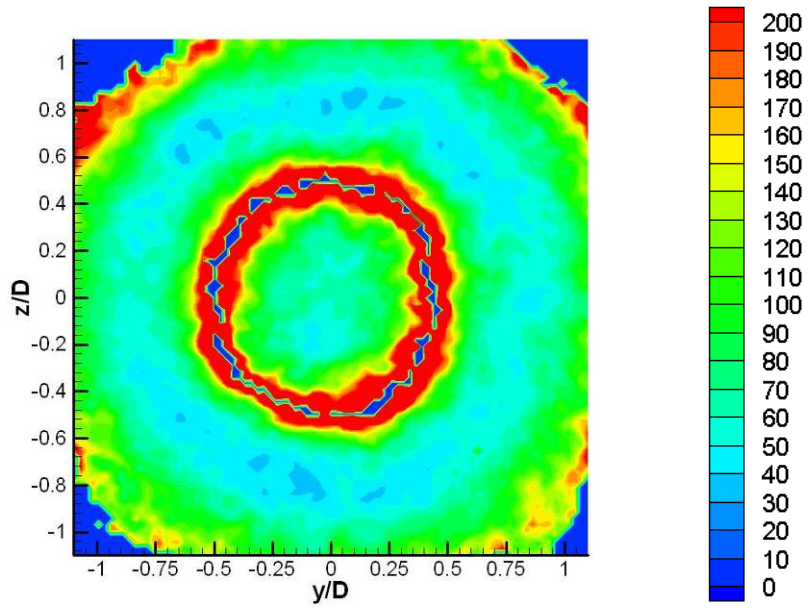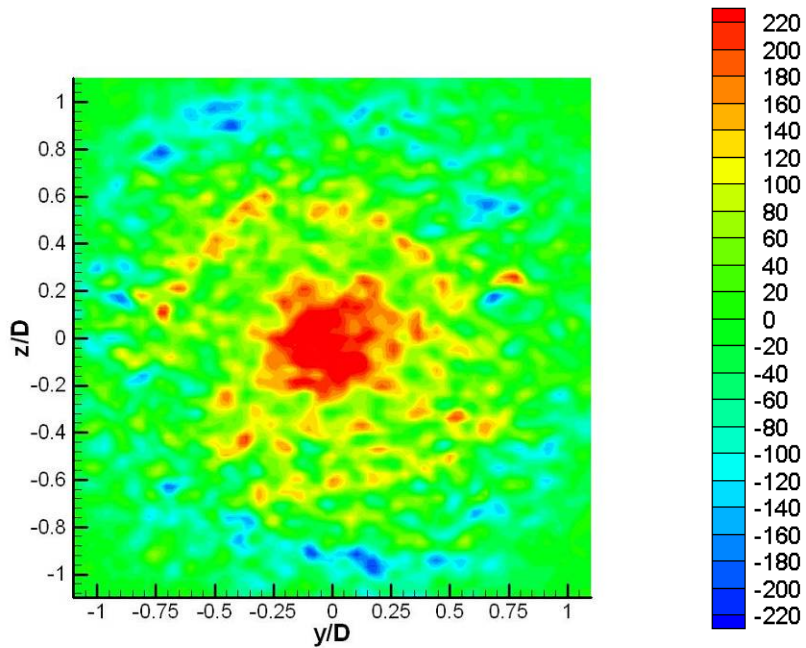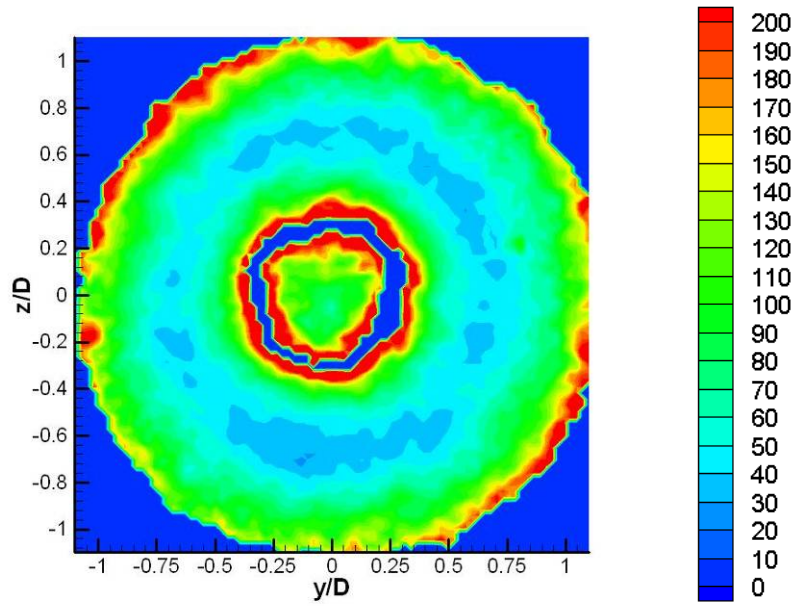

Figure 5.18 CASE #04: Contour of vorticity (s^{-1})

5.1.5. Velocity Gradient

The following section presents the results of velocity gradient effects on swirl jets (CASES #05, #06, #07, and #08, Figures 5.19 to 5.34). For this purpose, 50% of the each exit velocity is increased compared to CASES #02 and #03. As a result, the Reynolds number (Re) of the outer nozzle is increased from 4.64×10^3 to 6.96×10^3 (CASES #05 and #06), and the Re of the inner nozzle is raised from 6.87×10^3 to 10.30×10^3, too (CASES #07 and #08).

The main concern of this section lies in investigating the influence on turbulence and vorticity, rather than on velocity. Intuitively, no remarkable contribution of the augmented inner jet velocity is found in CASES #07 and #08 (Figures 5.29, 5.30, 5.33, and 5.34) in comparison with CASES #02 and #03. Obviously, the increased inner velocity slightly affects vorticity and turbulence intensity around the vortex core, or the shear layer between jets. It can be explained by the rotational and centrifugal forces of the inner jet being relatively weak compared to the outer-swirl strength. Therefore, the increased inner-swirl velocity effects dissipate, and the outer dominates the whole flow field. The supporting

investigation will be presented in section 5.2.2 Configuration of Plain Round Jet and Baseline.

On the other hand, the interesting results are shown in Figures 5.21, 5.22, 5.25, and 5.26 (CASES #05 and #06). The augmented outer velocity affects the entire region of measurement. The intensified velocity of the outer-swirl not only fortifies the peak velocities, but also deepens the depth of the vortex core simultaneously. Figures 5.19 and 5.23 show instantly the strengthened reverse zone, and this highly unstable condition creates the intensified vorticity at the core regardless of the inner-swirl direction (Figures 5.22 and 5.26). Furthermore, the turbulence intensity around the periphery of the outer jet is fortified in CASES #05 and #06 (Figures 5.21 and 5.25). The radial velocity plots (Figures 5.20 and 5.24) depict a negative and irregular distribution, and the tangential component plots show a large velocity gradient in a radial direction. These also support the indication of an intensified reverse flow region.
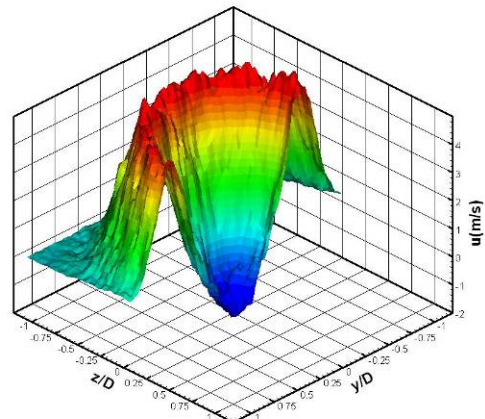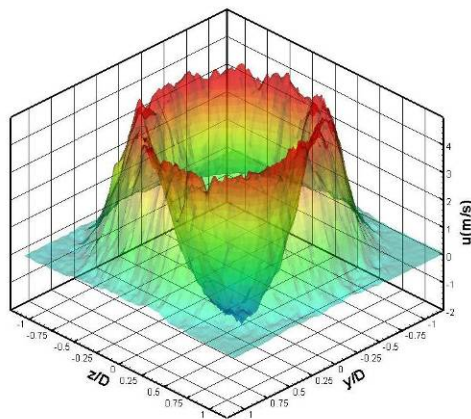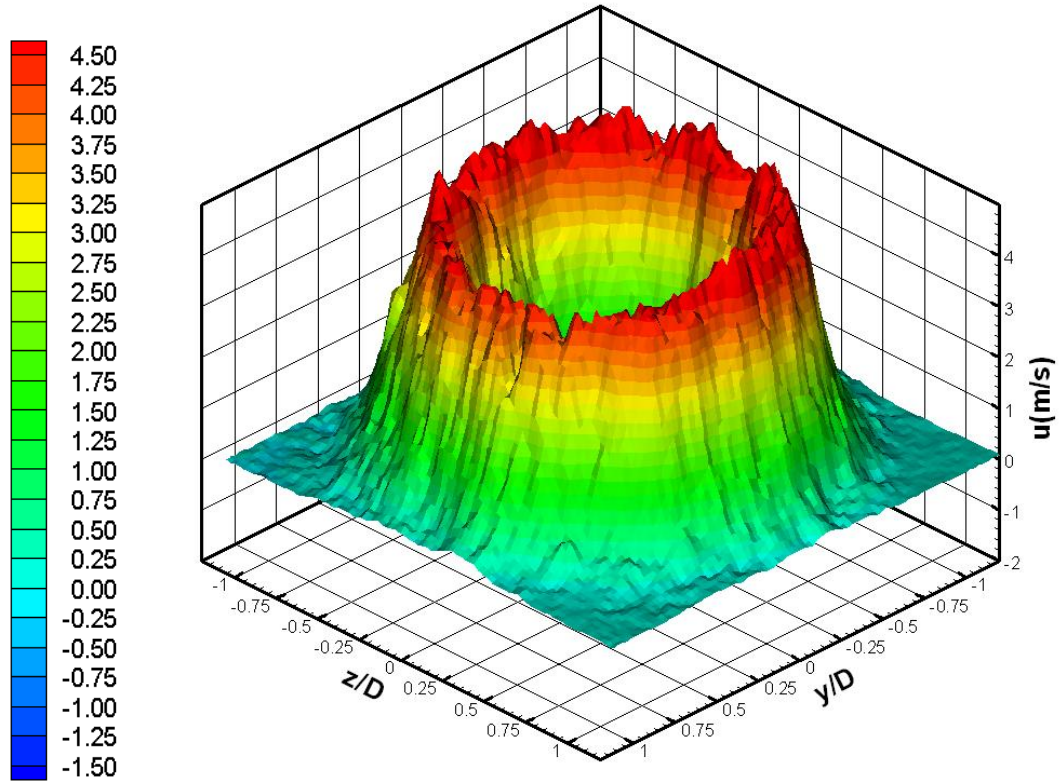
Figure 5.19 CASE #05: Axial velocity (u) distribution
3D full (upper), translucency (lower left), cross-sectional (lower right) views
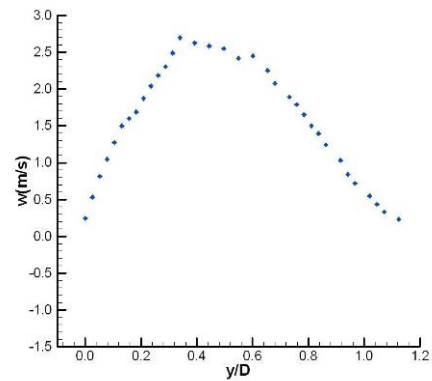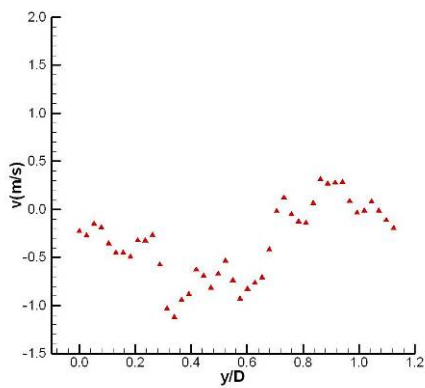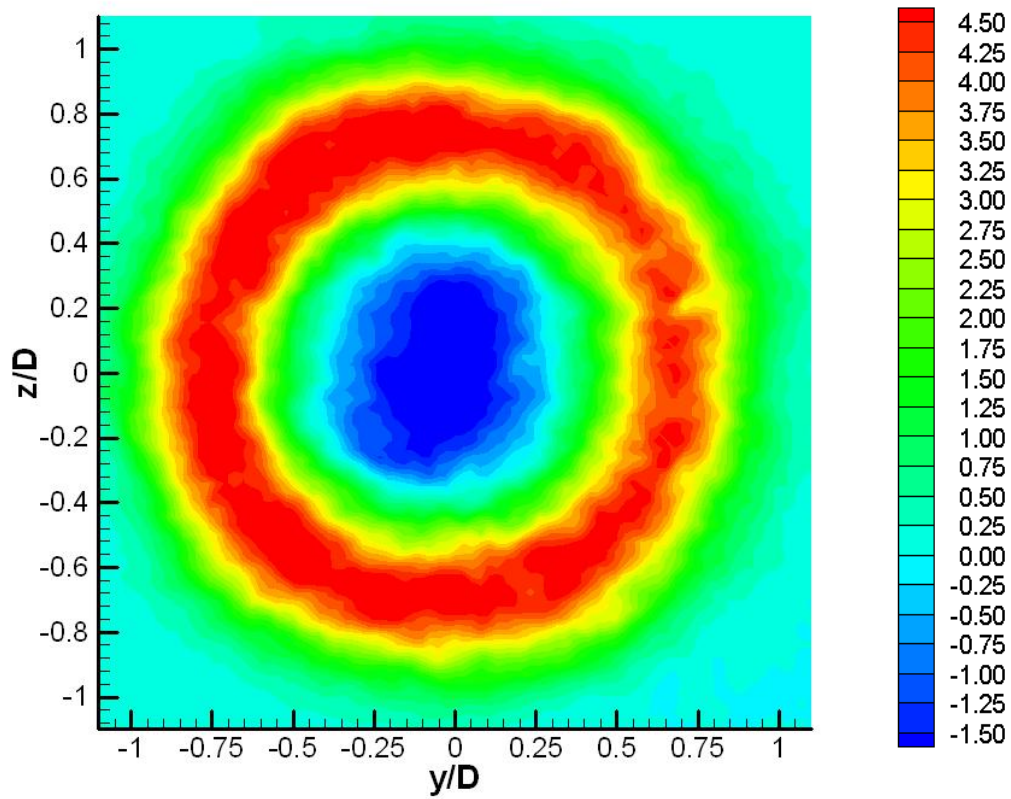
Figure 5.20 CASE #05: Contour of axial velocity (u, m/s) (upper),
radial velocity (v) along positive y-axis (lower left),
tangential velocity (w) along positive y-axis (lower right)
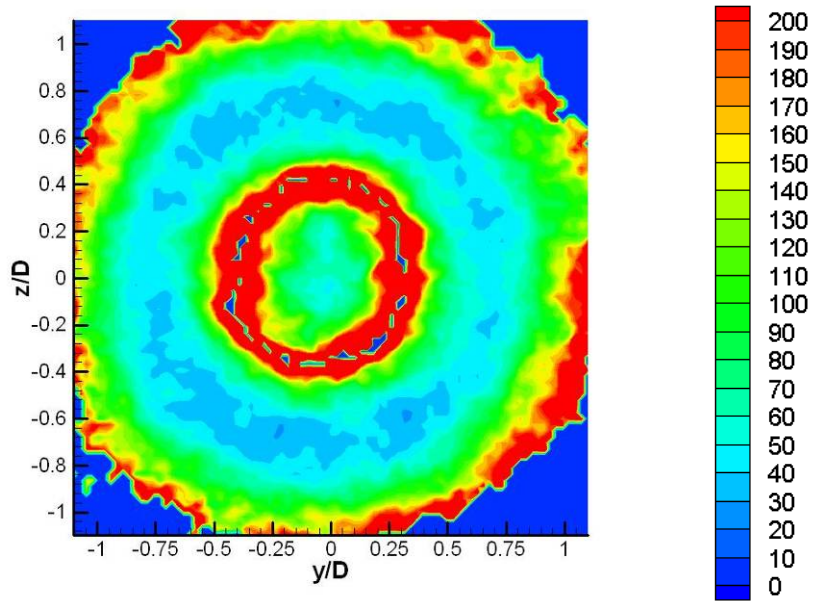
Figure 5.21 CASE #05: Contour of turbulence intensity (%)

Figure 5.22 CASE #05: Contour of vorticity (s^{-1})

Figure 5.23 CASE #06: Axial velocity (u) distribution
3D full (upper), translucency (lower left), cross-sectional (lower right) views

**Figure 5.24 CASE #06: Contour of axial velocity (u, m/s) (upper),
radial velocity (v) along positive y-axis (lower left),
tangential velocity (w) along positive y-axis (lower right)**

Figure 5.25 CASE #06: Contour of turbulence intensity (%)

Figure 5.26 CASE #06: Contour of vorticity (s⁻¹)

Figure 5.27 CASE #07: Axial velocity (u) distribution
3D full (upper), translucency (lower left), cross-sectional (lower right) views

**Figure 5.28 CASE #07: Contour of axial velocity (u, m/s) (upper),
radial velocity (v) along positive y-axis (lower left),
tangential velocity (w) along positive y-axis (lower right)**

Figure 5.29 CASE #07: Contour of turbulence intensity (%)

Figure 5.30 CASE #07: Contour of vorticity (s^{-1})
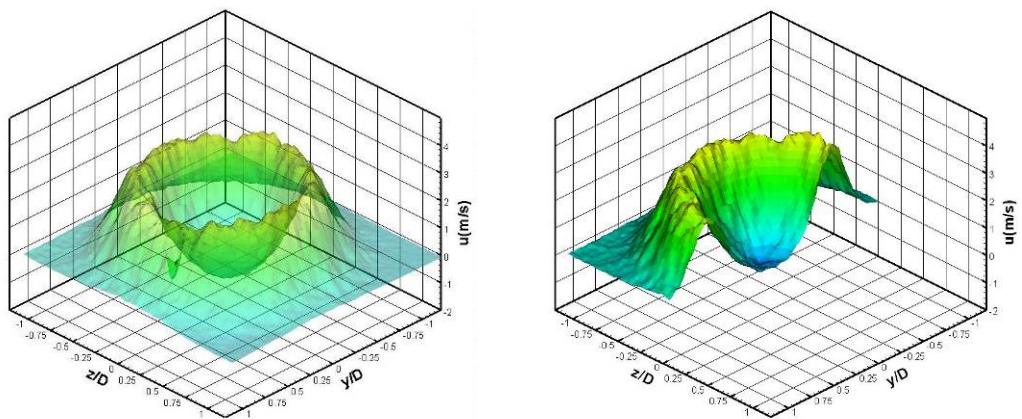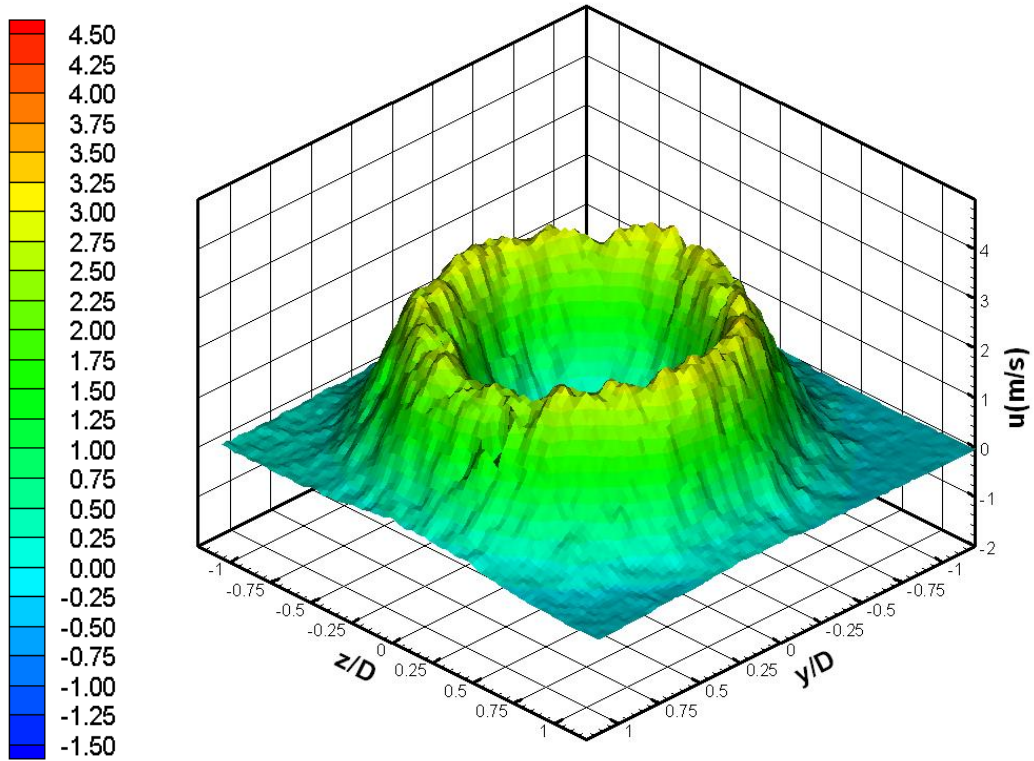
Figure 5.31 CASE #08: Axial velocity (u) distribution
3D full (upper), translucency (lower left), cross-sectional (lower right) views

145
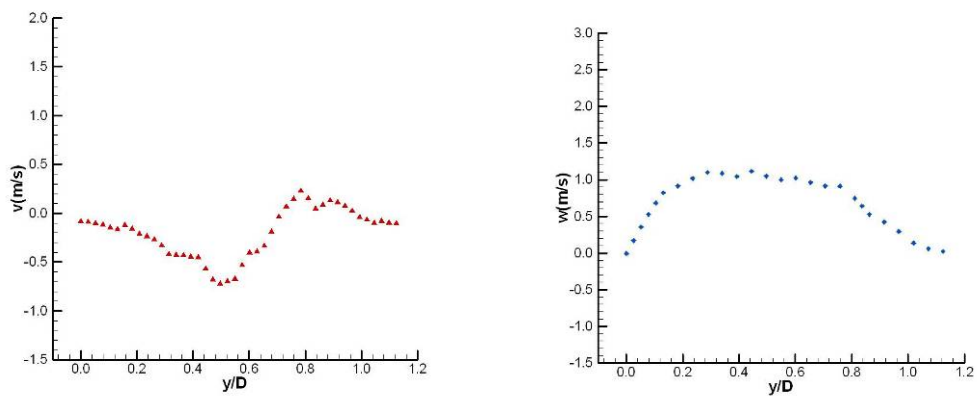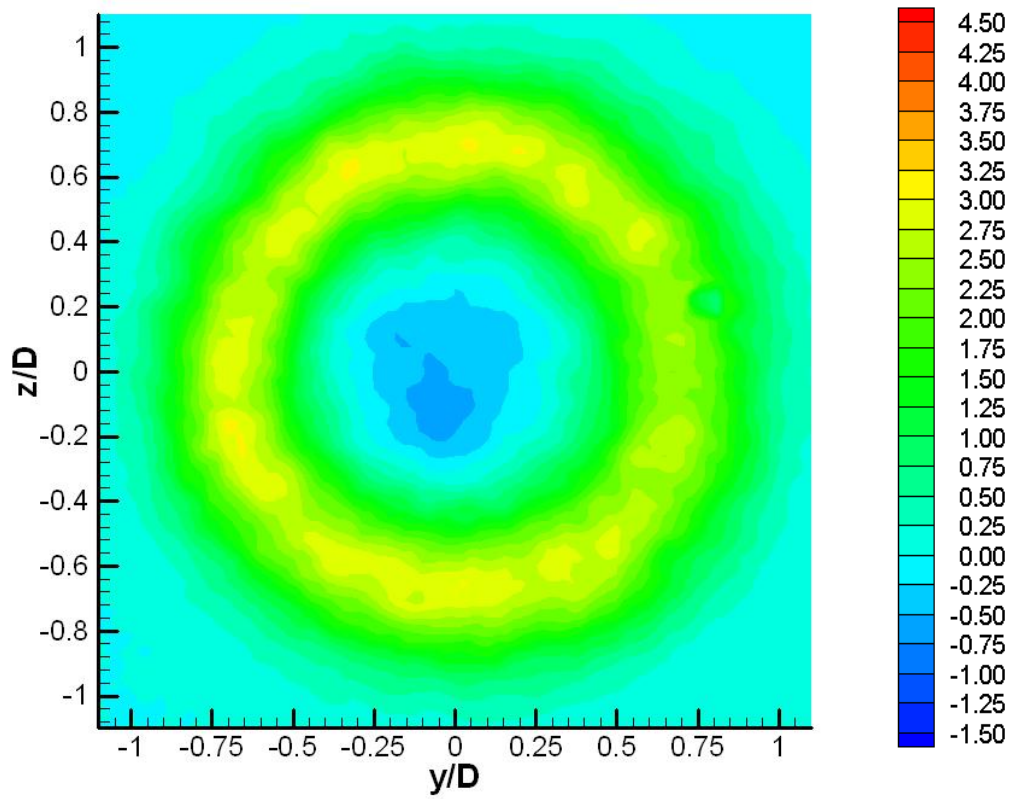
**Figure 5.32 CASE #08: Contour of axial velocity (u, m/s) (upper),
radial velocity (v) along positive y-axis (lower left),
tangential velocity (w) along positive y-axis (lower right)**

Figure 5.33 CASE #08: Contour of turbulence intensity (%)
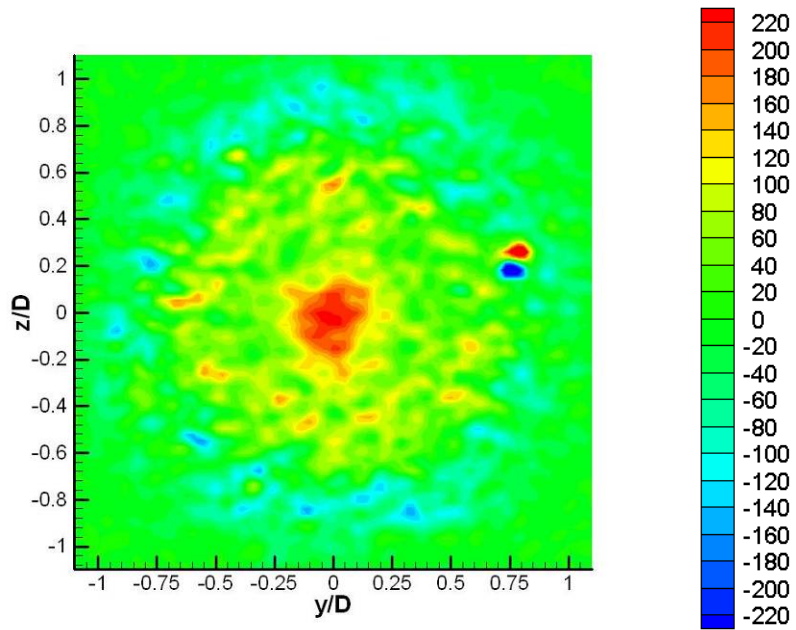
Figure 5.34 CASE #08: Contour of vorticity (s^{-1})

5.1.6. Shear Excitation Effects

The following section presents the results of shear excitation effects on swirl jets (CASES #09, #10, #11, #12, #13, #14, #15, and #16, Figures 5.35 to 5.66).

In Figures 5.67 through 5.72, the plots are assembled for the easy comparison of the axial-, radial-, and tangential-velocity variation. The main purpose of applying lobes is to create a shear perturbation wave and to control coherent structure for flow excitation. Furthermore, as seen from Figure 3.27, the installed lobes also change the inside shape of the nozzle itself. For instance, two lobes make it rectangular, three lobes make it triangular, and four lobes make it square.

Influence on Axial Velocity

As shown in Figure 5.67 (co-swirl) and Figure 5.70 (counter-swirl), three major changes are noticed from the contour plots.

First, the jet periphery shape of the axial velocity is transformed, and corresponds to the number of lobes.

Second, the maximum distance of the shear layer at the mean characteristic

jet boundary from core generally decreases in comparison with the unexcited one.

Last, the depth of the vortex core is also reduced in all cases.

The radius of the jet boundary for CASE #02 (m=0) is 'r/D=1.4', but it is

reduced to 'r/D=1.1' (approx. 22% down) in both CASE #13 and #15 (m=3 and 4).

At the same time, the negative velocity around the vortex core, which is shown in

CASE #02 (Figure 5.67(a)), is raised up to the neutral range (i.e., -0.25~0.25) in all

cases (Figure 5.67(b) through Figure 5.67(e)). Figure 5.36 displays an eccentric

velocity profile caused by an asymmetric lobe layout inside the nozzles.

In the case of counter-swirl (Figure 5.70), the overall response of excitation

is similar to their co-swirl counterparts (ref. Figure 5.67) in axial velocity profile.

Influence on Radial and Tangential Velocity

From Figures 5.68 and 5.71, regardless of co- and counter-swirl, generally

the centripetal velocity components vanish when one lobe is applied. Furthermore,

the radial velocity is maximized (i.e., intensified) in both m=1 cases (Figure 5.68(b)

and Figure 5.71(b)) compared to any other perturbation mode. On the other hand, for

m=2 counter-swirl (Figure 5.71(c)), an interesting profile appears. The inward

velocity is dramatically fortified (-0.1m/s @ y/D=0.25 for Figure 5.71(a), -1.9m/s @

y/D=0.25 for Figure 5.71(c)), and this implies the CTRZ is dominating the vortex

core region.

Even the lobed shear perturbation affects the radial velocity component

noticeably, yet it does not play a relatively major role in tangential behavior

compared to the no-lobed counterparts (Figures 5.69 and 5.72). This reveals that the

straight lobed perturbation wave effectively affects the swirl flow in radial not in

tangential.

Influence on Turbulence Intensity and Vorticity

From the comparison between the unexcited (Figures 5.9 and 5.13) and

excited cases (Figures 5.37, 5.41, 5.45, 5.49, 5.53, 5.57, 5.61, and 5.65), two major

characteristics are found in turbulence intensity analysis. First, the size of area for

the fluctuation field is relatively reduced compared to the no-lobed condition.

Second, the turbulence intensity around the shear layer between the inner and outer jets is significantly relieved throughout all the perturbed cases.

The intensified fluctuation (i.e., high value of turbulence intensity) is generally known as it is favorable to turbulent mixing. In the perturbed cases (m=1~4), even though the result figures show that the velocity fluctuation is quenched, it may not be regarded that the lobed excitation is ineffective. The supporting investigation will be presented in section 5.1.7 on Wave Propagation Analysis.

In vorticity analysis, the overall angular motion is augmented. The unexcited swirl cases (i.e., CASES #02 and #03, Figures 5.10 and 5.14) show that the rotational behavior is relatively evenly distributed regardless of swirl direction. In the case of excited co-swirl cases (Figures 5.38, 5.46, 5.54, and 5.62), the strong vorticities are concentrated in the vortex core. The fortified vortical behavior is shown around the shear layer between the inner and outer jets for excited counter-swirl cases (Figures 5.42, 5.50, 5.58, and 5.66).
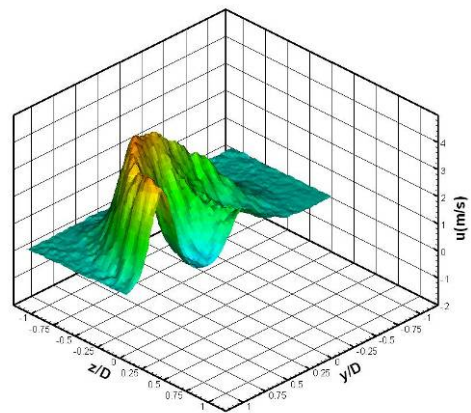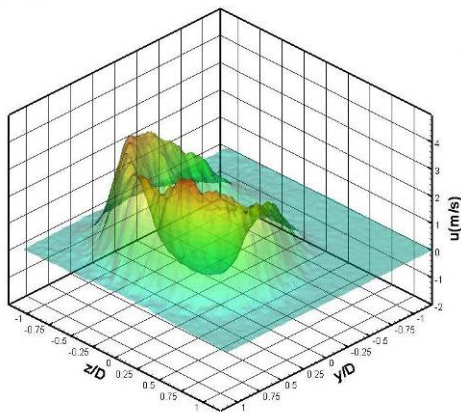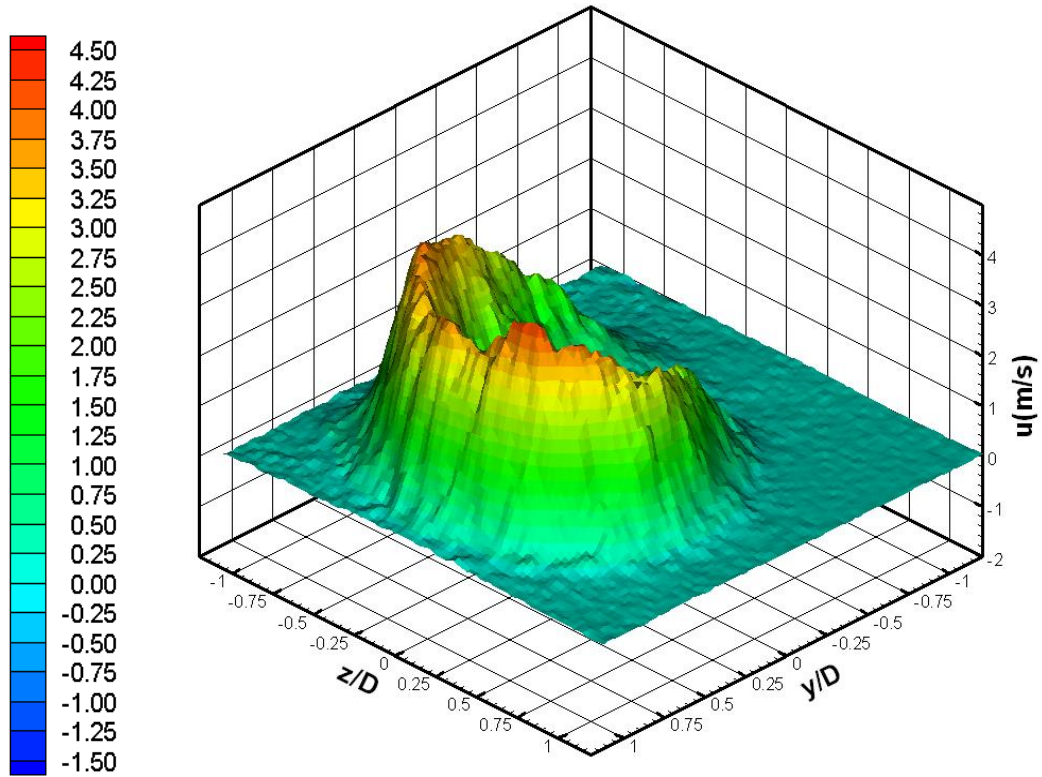
Figure 5.35 CASE #09 (m=1): Axial velocity (u) distribution
3D full (upper), translucency (lower left), cross-sectional (lower right) views
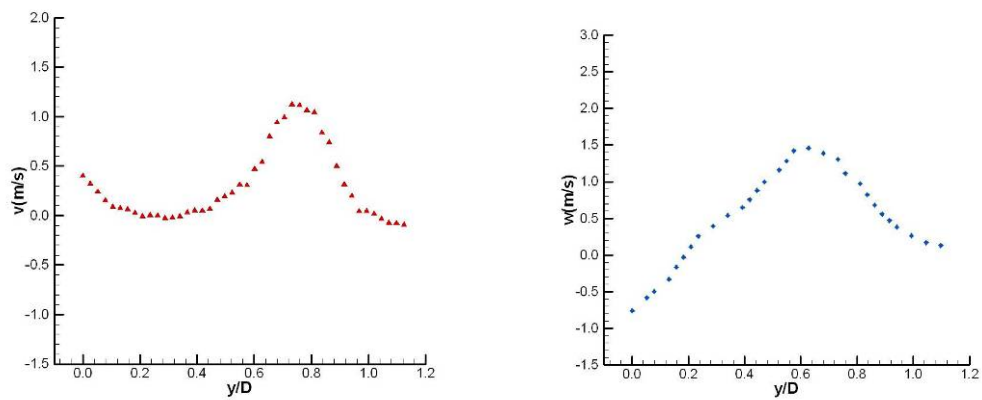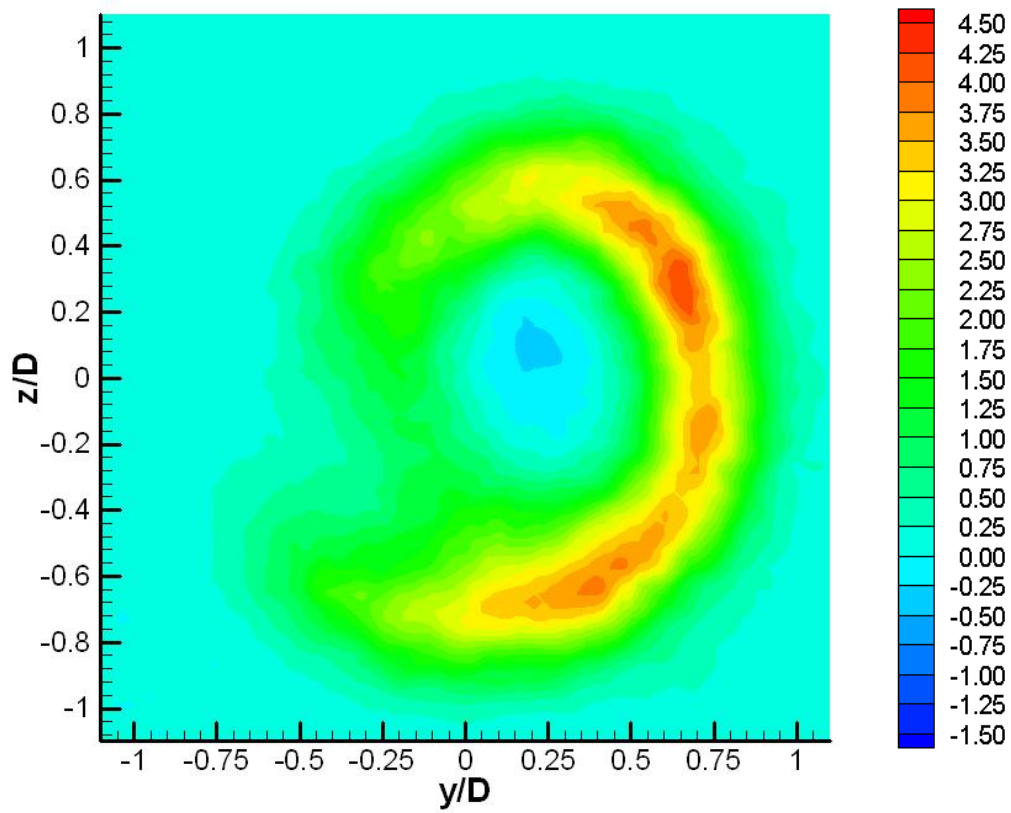
Figure 5.36 CASE #09 (m=1): Contour of axial velocity (u, m/s) (upper),
radial velocity (v) along positive y-axis (lower left),
tangential velocity (w) along positive y-axis (lower right)
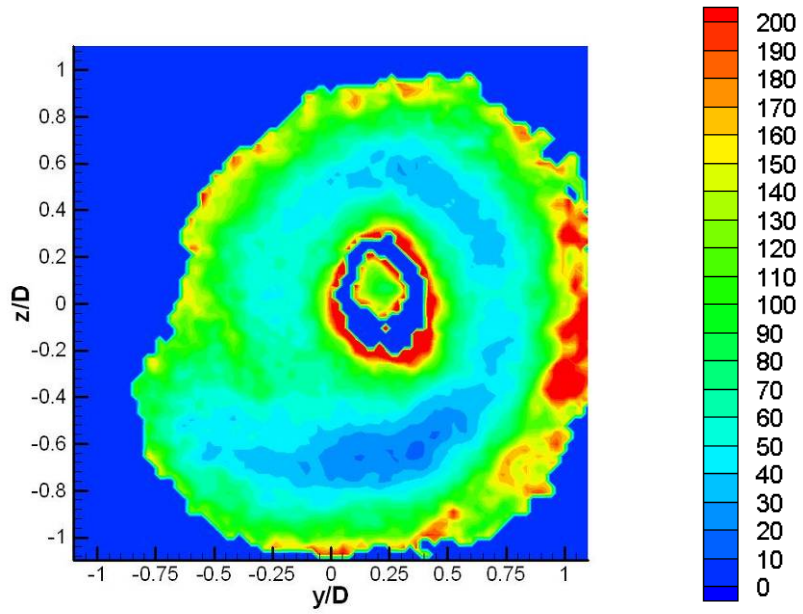
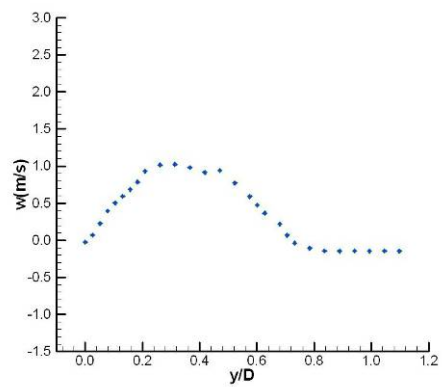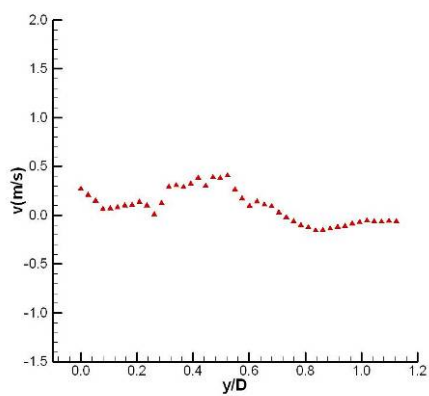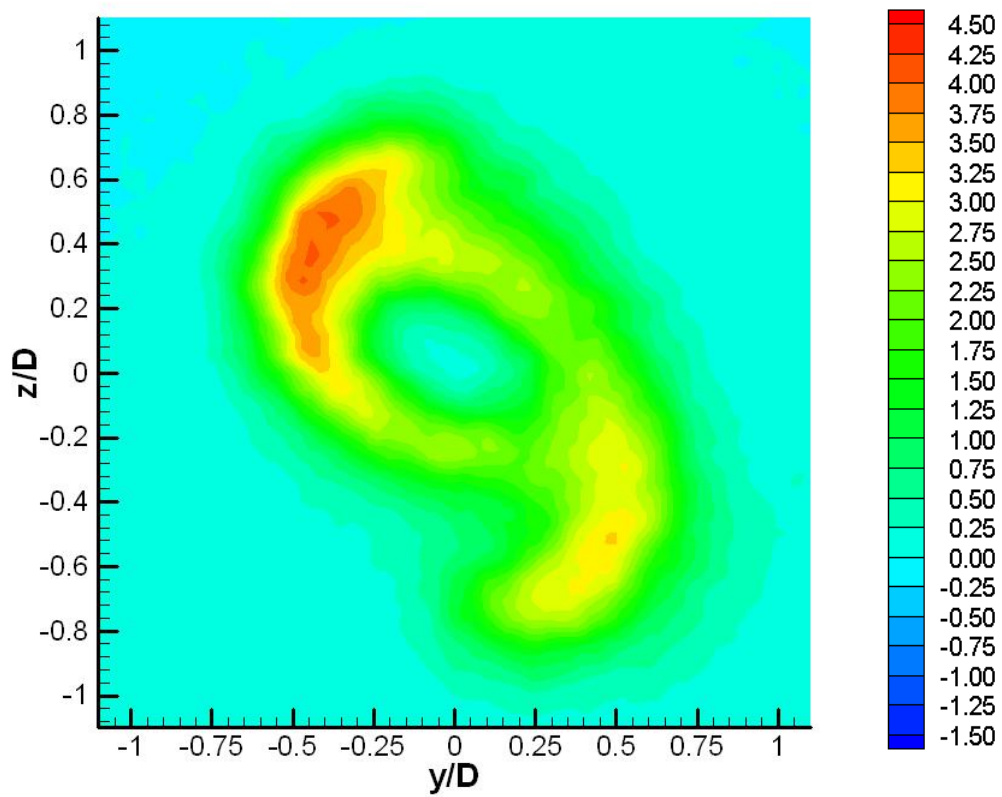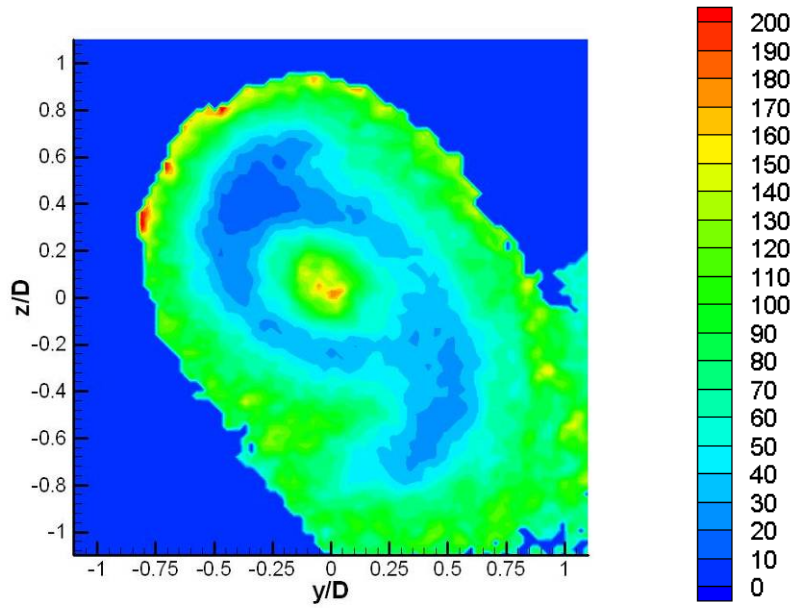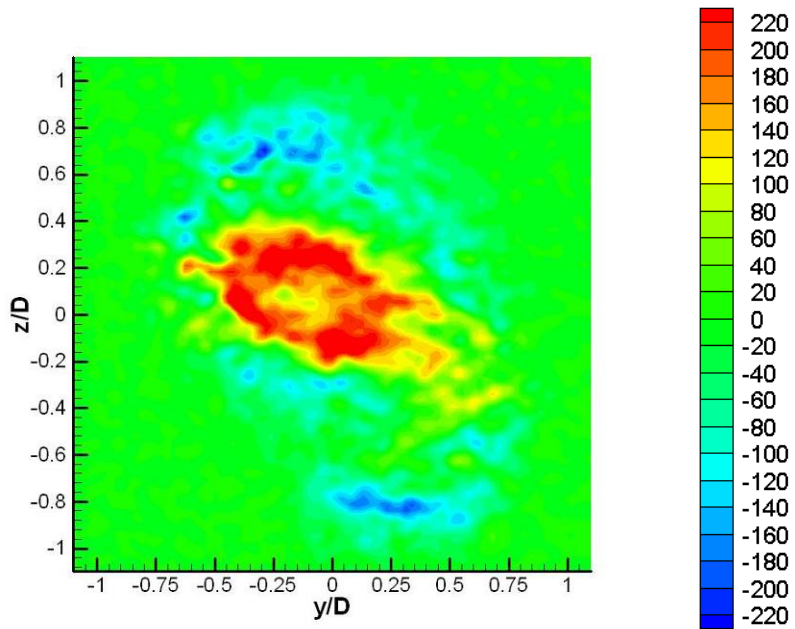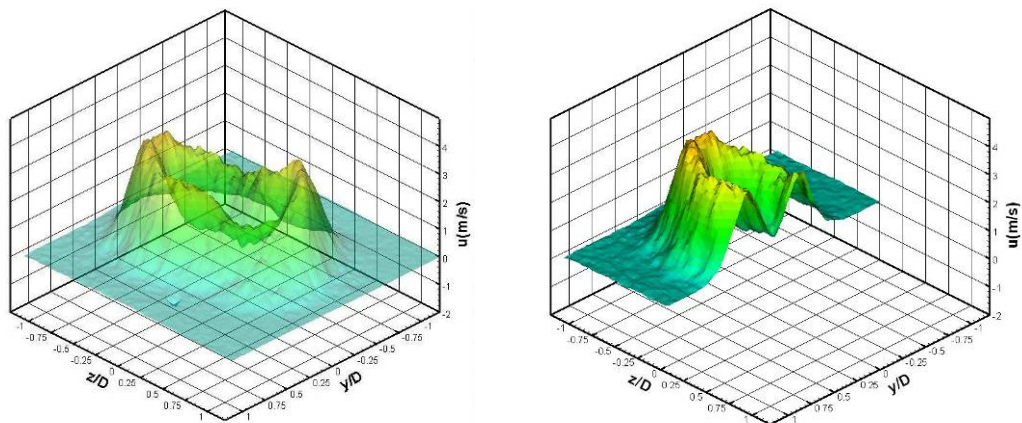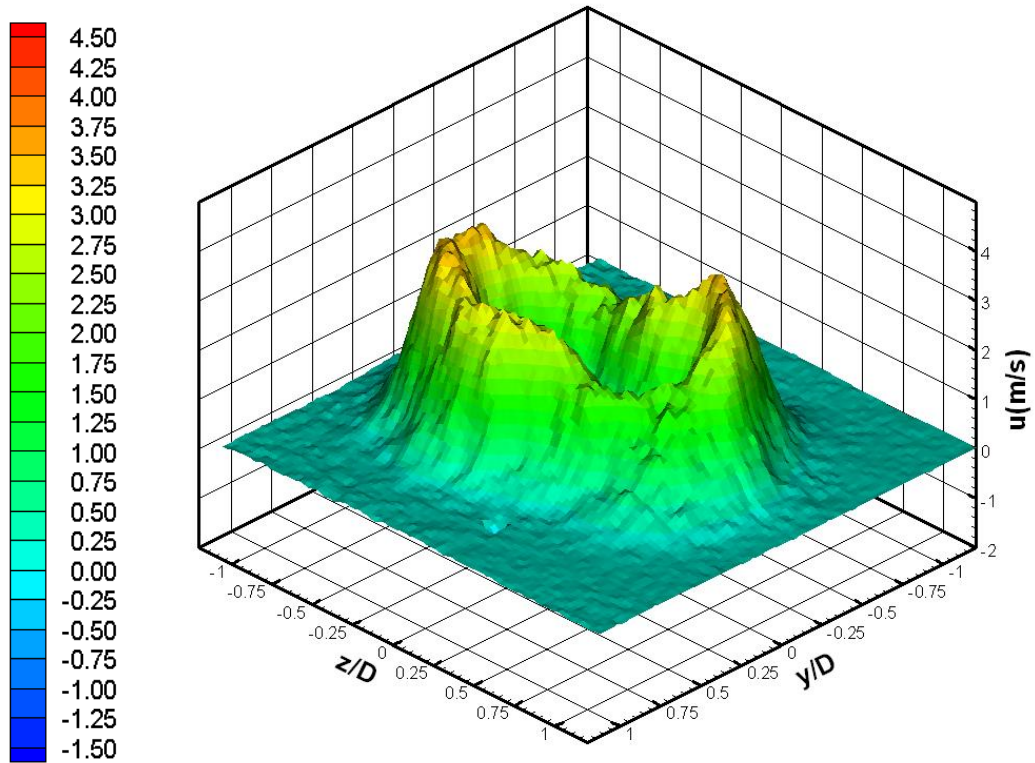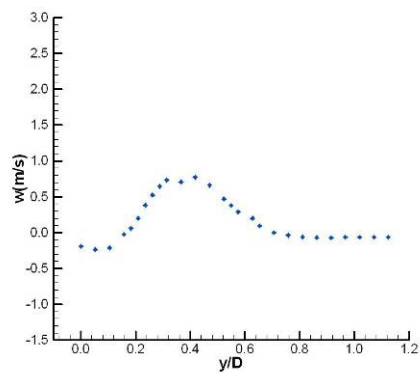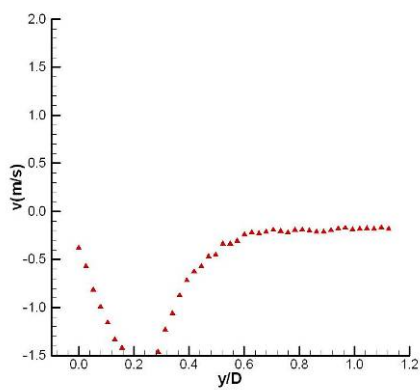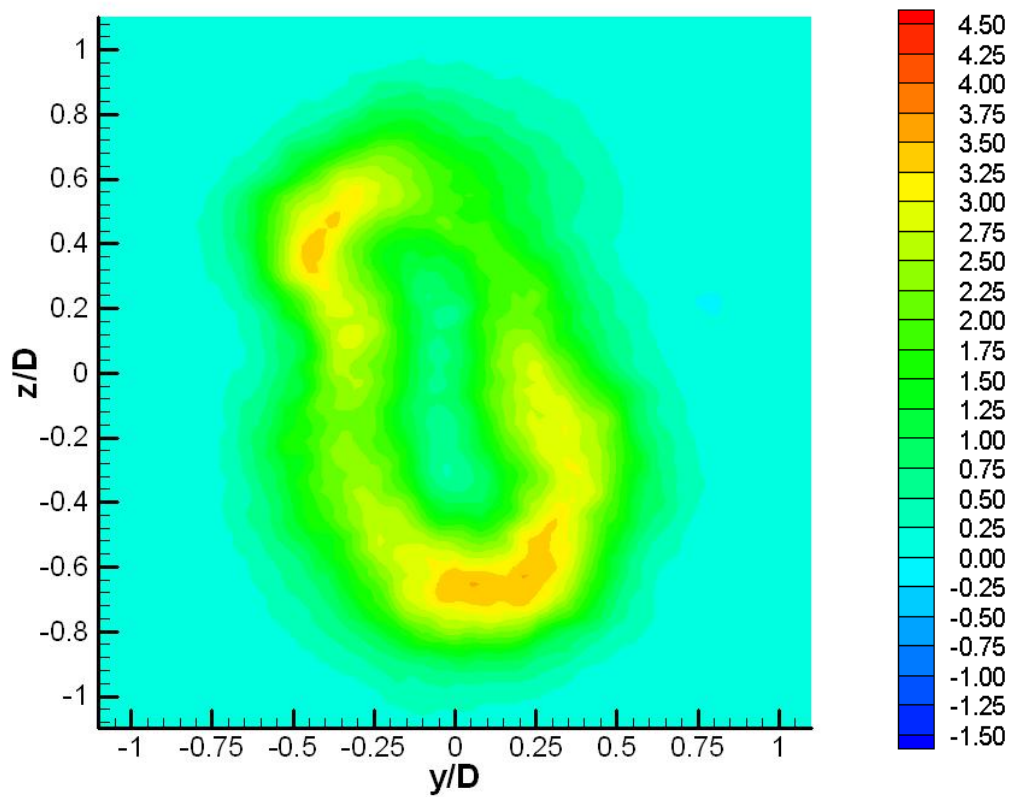**Figure 5.37 CASE #09 (m=1): Contour of turbulence intensity (%)**
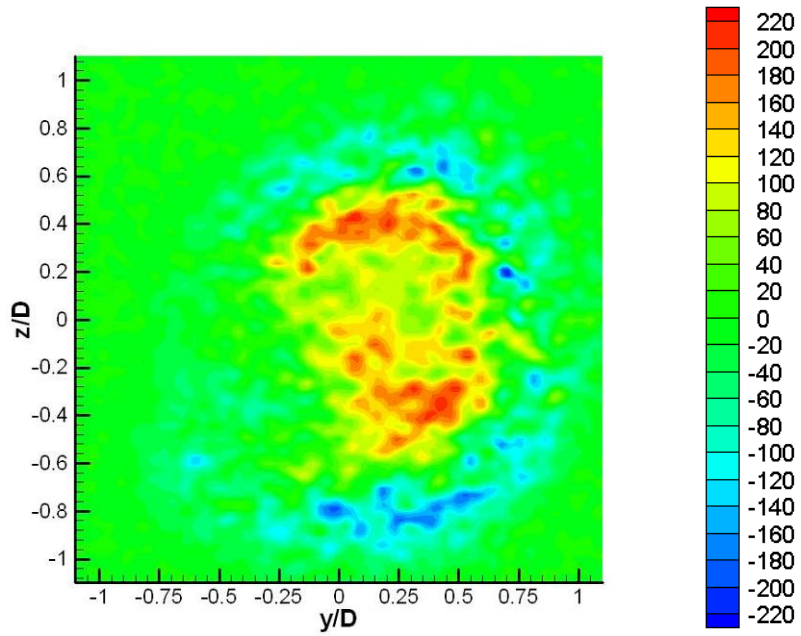
Figure 5.38 CASE #09 (m=1): Contour of vorticity (s⁻¹)
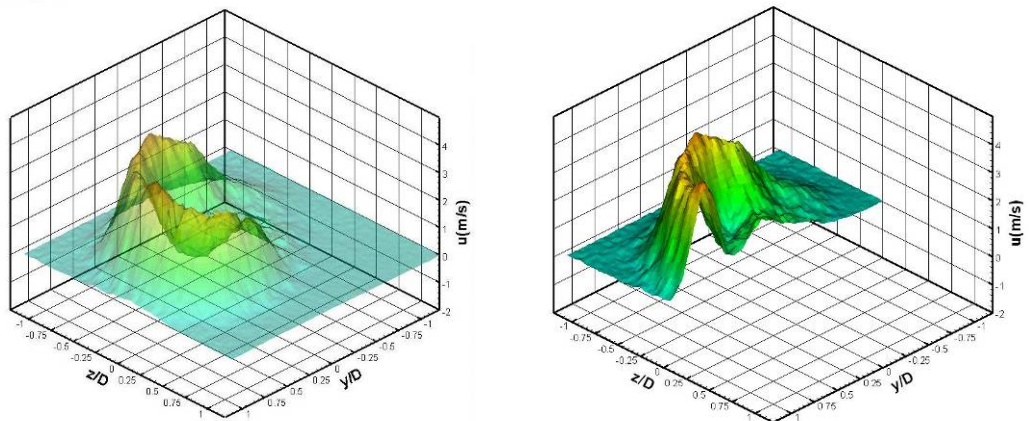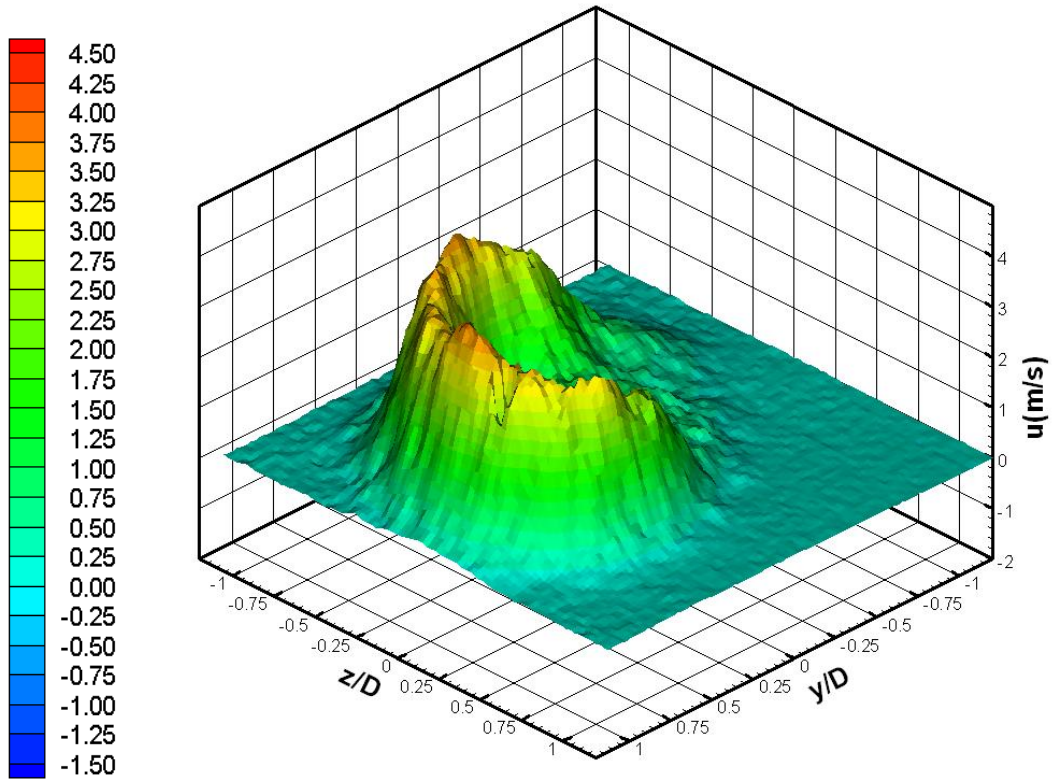
Figure 5.39 CASE #10 (m=1): Axial velocity (u) distribution
3D full (upper), translucency (lower left), cross-sectional (lower right) views
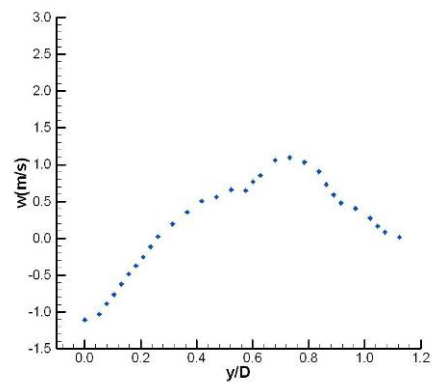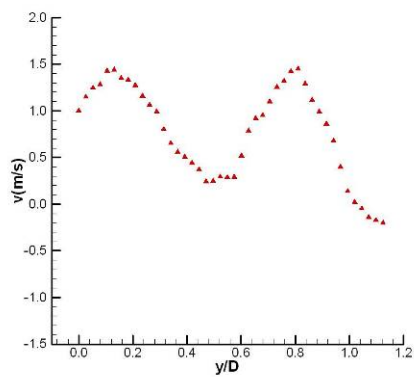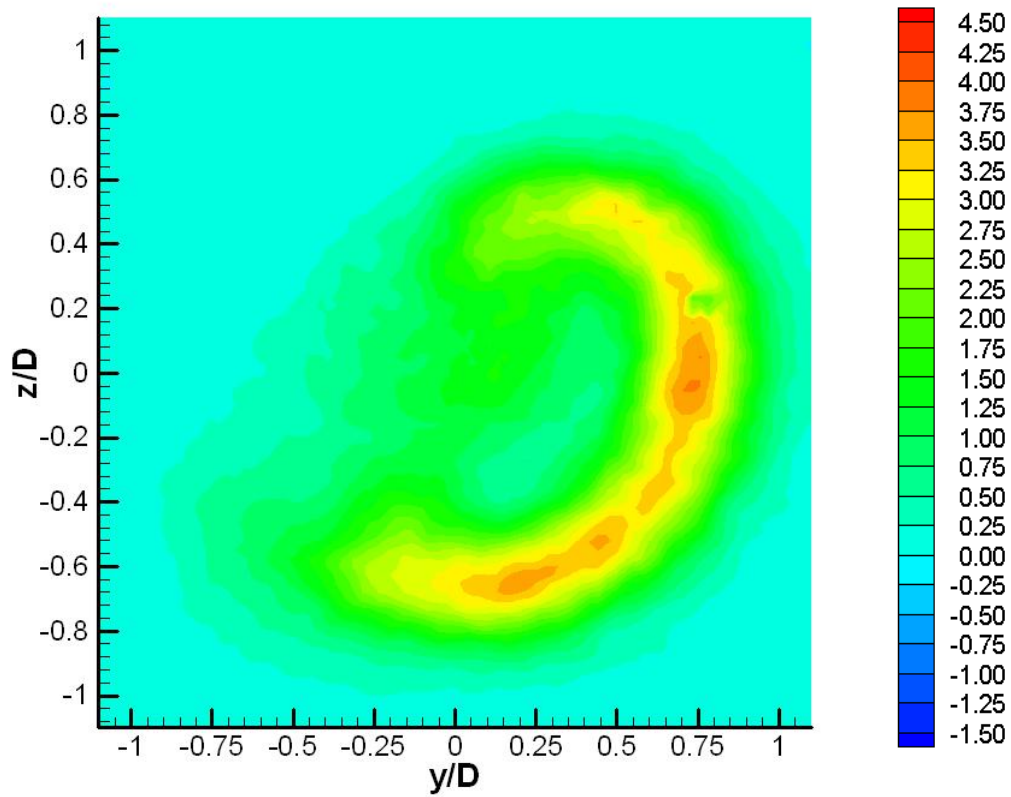
Figure 5.40 CASE #10 (m=1): Contour of axial velocity (u, m/s) (upper), radial velocity (v) along positive y-axis (lower left), tangential velocity (w) along positive y-axis (lower right)
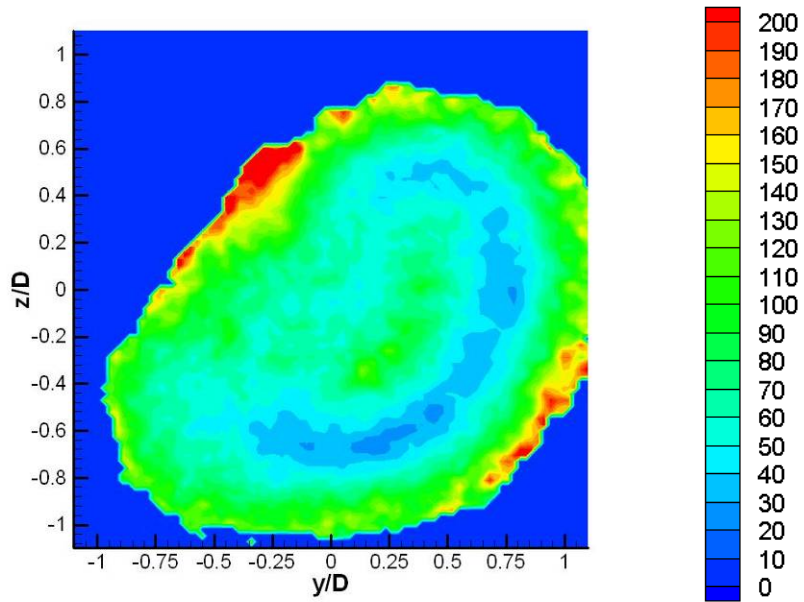
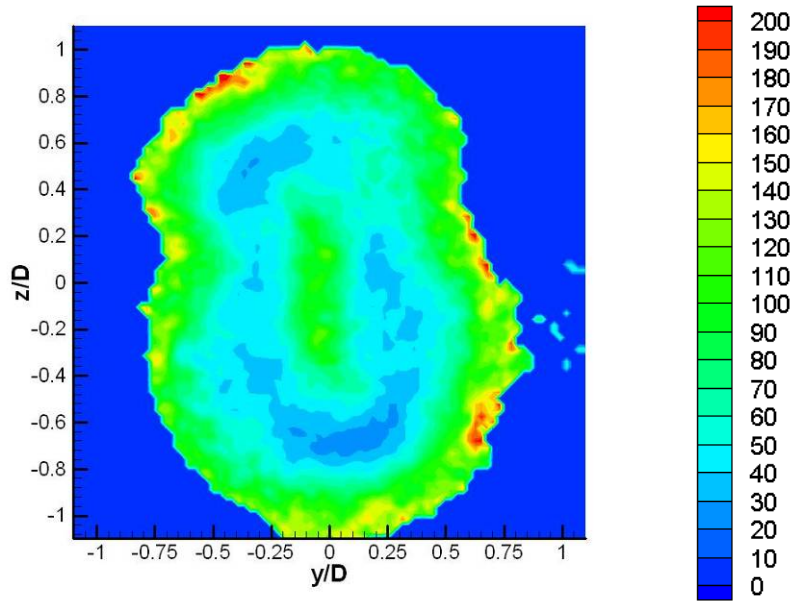**Figure 5.41 CASE #10 (m=1): Contour of turbulence intensity (%)**
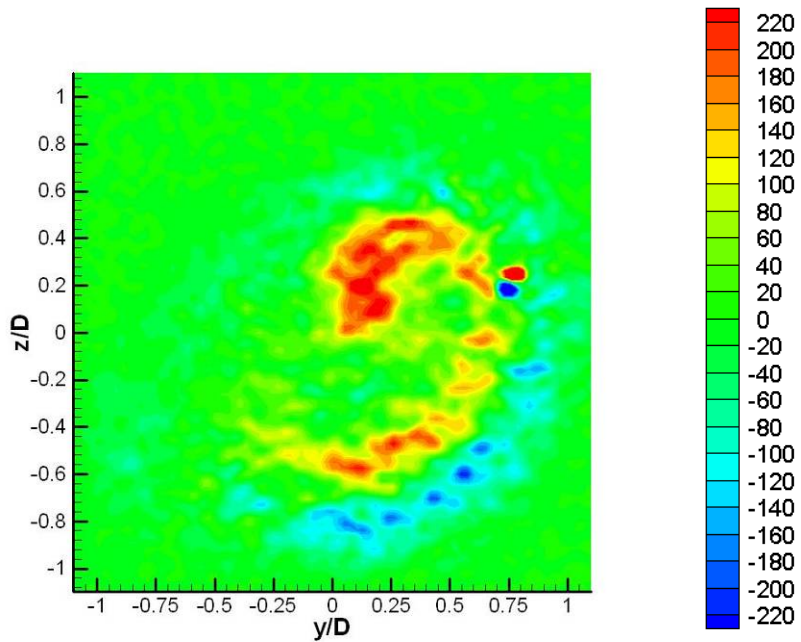
Figure 5.42 CASE #10 (m=1): Contour of vorticity (s⁻¹)
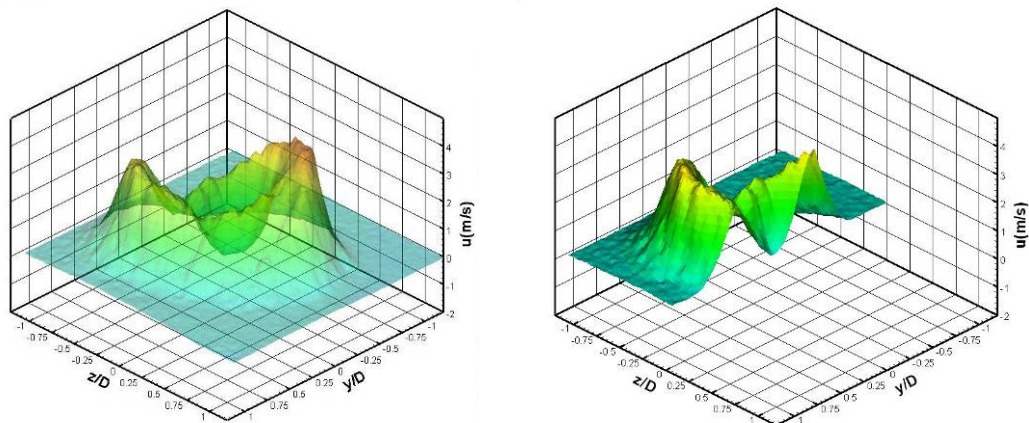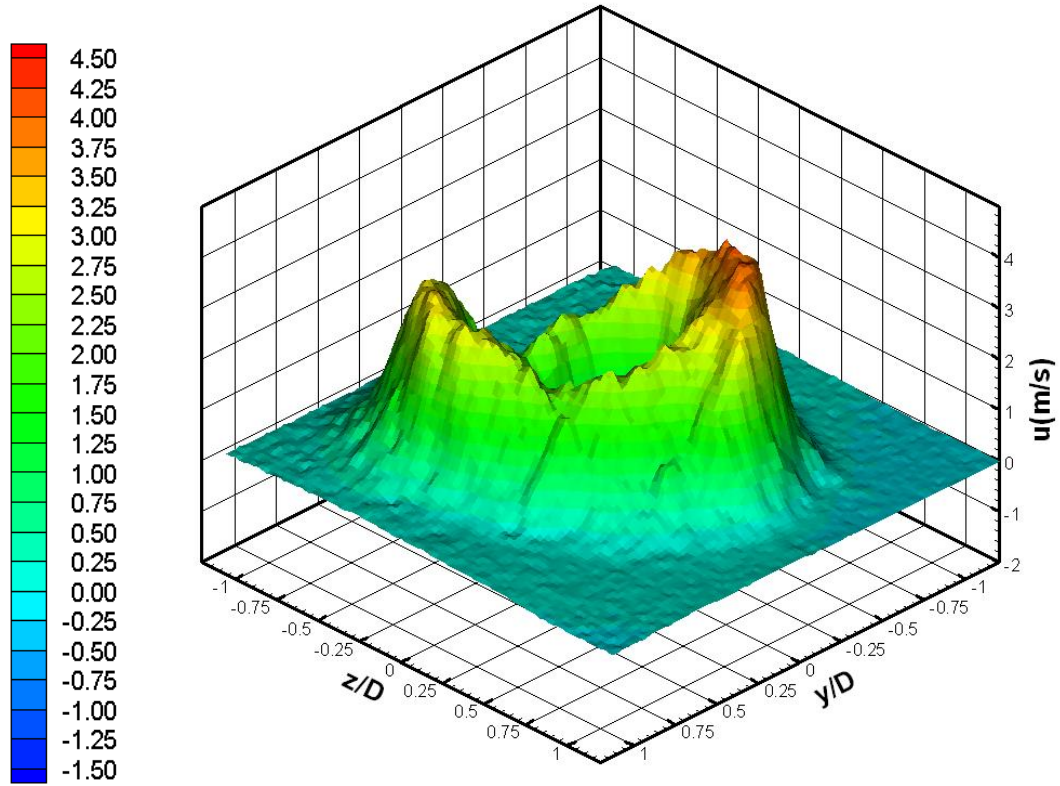
Figure 5.43 CASE #11 (m=2): Axial velocity (u) distribution
3D full (upper), translucency (lower left), cross-sectional (lower right) views

**Figure 5.44 CASE #11 (m=2): Contour of axial velocity (u, m/s) (upper),
radial velocity (v) along positive y-axis (lower left),
tangential velocity (w) along positive y-axis (lower right)**

Figure 5.45 CASE #11 (m=2): Contour of turbulence intensity (%)

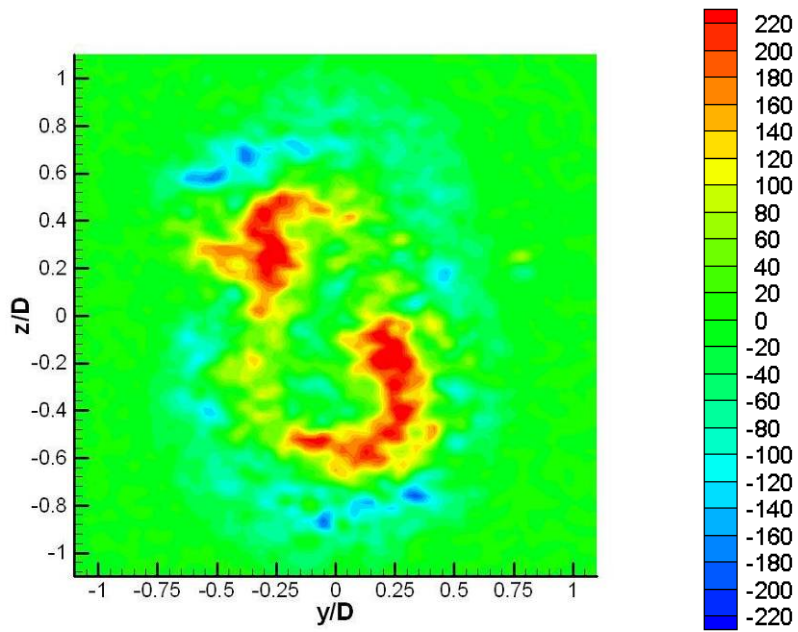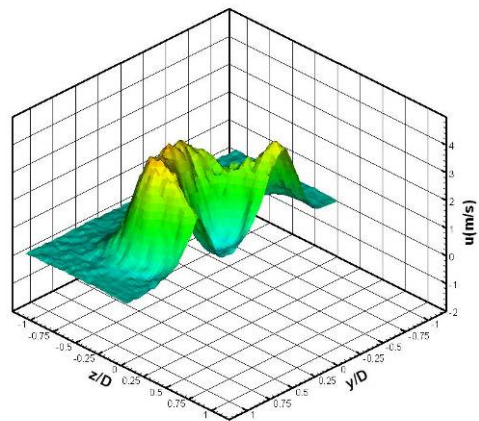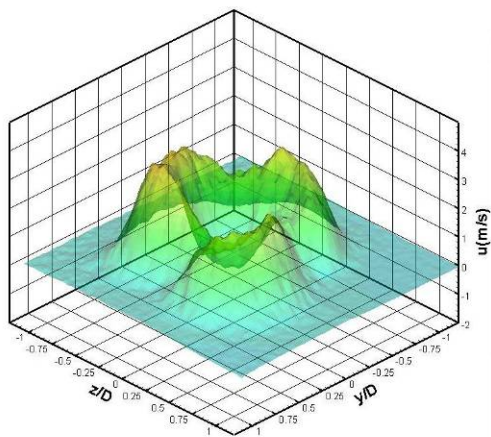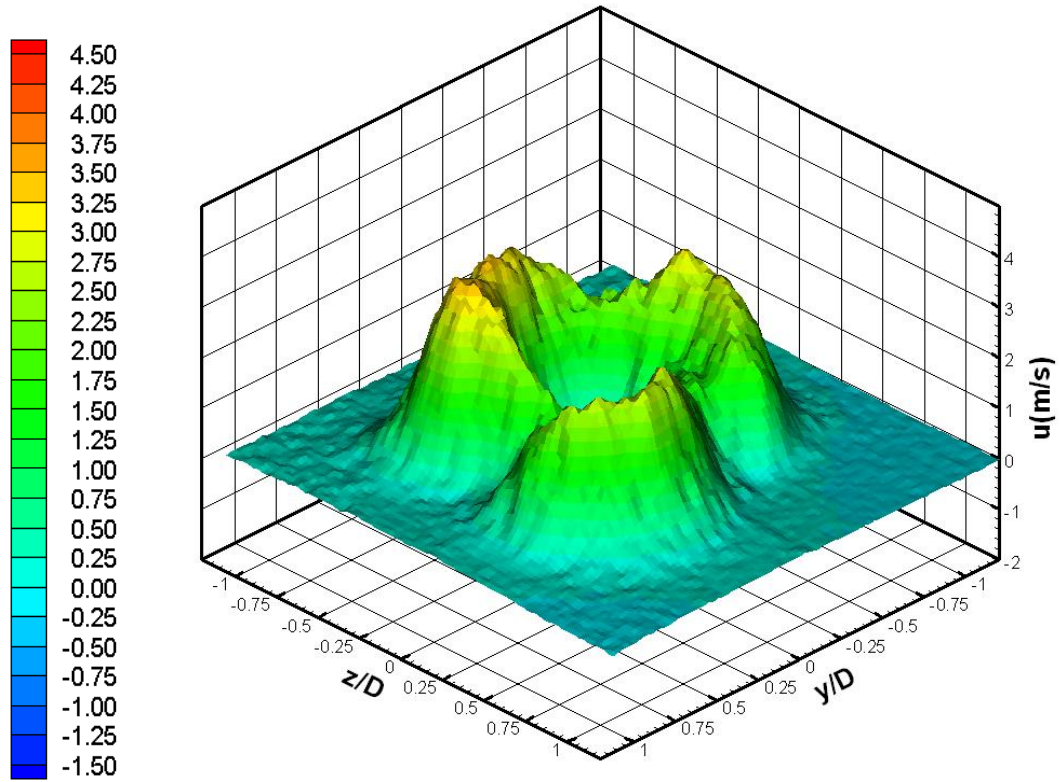
Figure 5.46 CASE #11 (m=2): Contour of vorticity (s^{-1})

Figure 5.47 CASE #12 (m=2): Axial velocity (u) distribution
3D full (upper), translucency (lower left), cross-sectional (lower right) views

**Figure 5.48 CASE #12 (m=2): Contour of axial velocity (u, m/s) (upper),
radial velocity (v) along positive y-axis (lower left),
tangential velocity (w) along positive y-axis (lower right)**

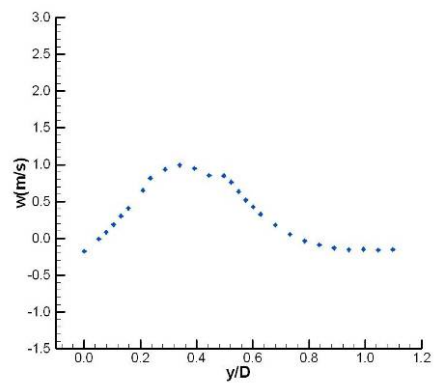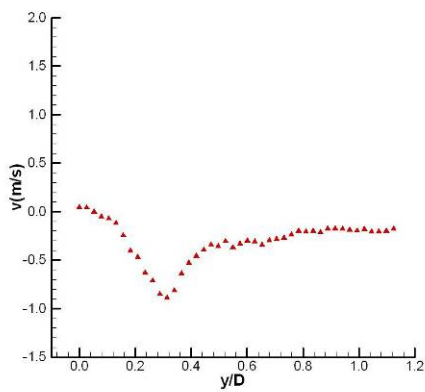**Figure 5.49 CASE #12 (m=2): Contour of turbulence intensity (%)**

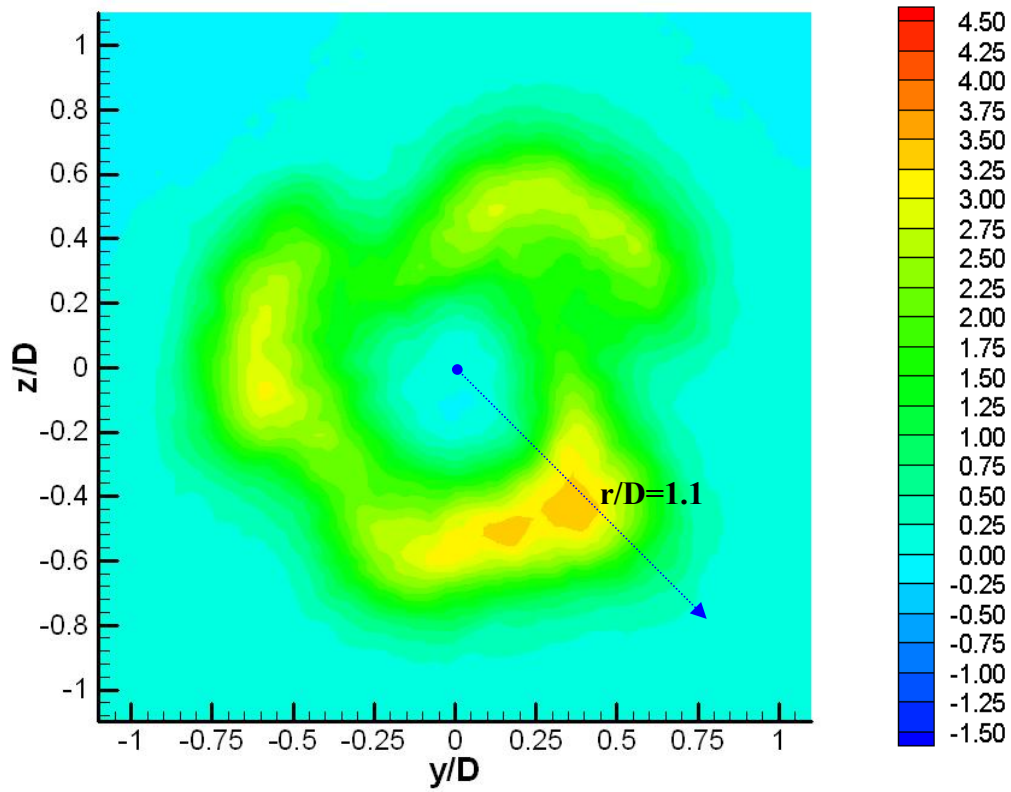**Figure 5.50 CASE #12 (m=2): Contour of vorticity (s^{-1})**

Figure 5.51 CASE #13 (m=3): Axial velocity (u) distribution
3D full (upper), translucency (lower left), cross-sectional (lower right) views

Figure 5.52 CASE #13 (m=3): Contour of axial velocity (u, m/s) (upper),
radial velocity (v) along positive y-axis (lower left),
tangential velocity (w) along positive y-axis (lower right)

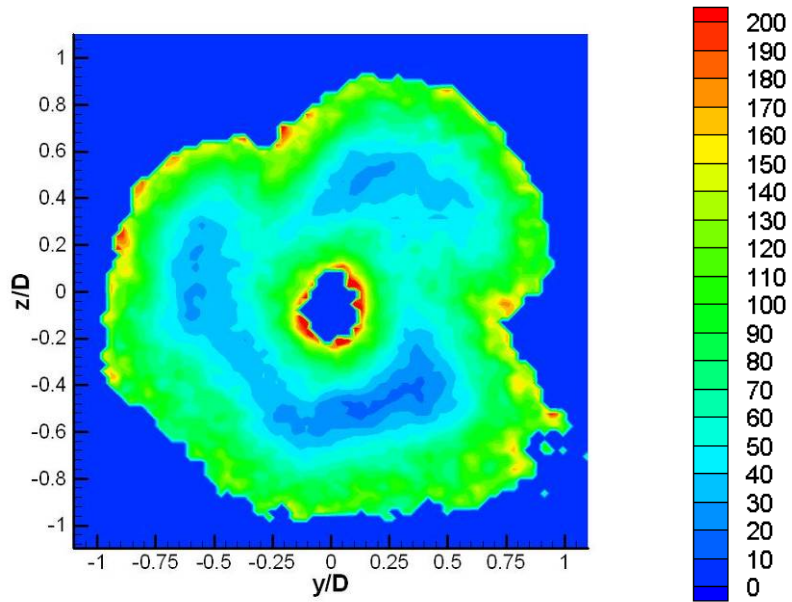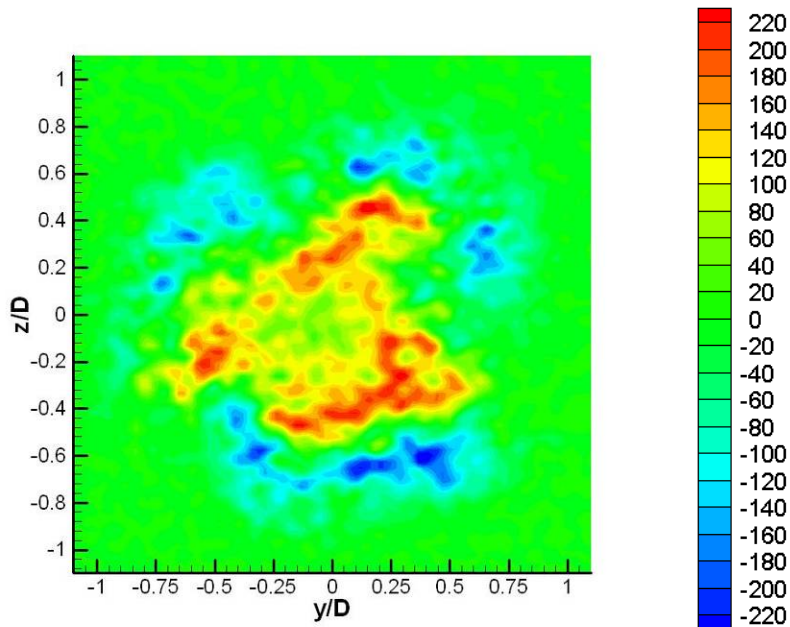**Figure 5.53 CASE #13 (m=3): Contour of turbulence intensity (%)**

Figure 5.54 CASE #13 (m=3): Contour of vorticity (s^{-1})

Figure 5.55 CASE #14 (m=3): Axial velocity (u) distribution
3D full (upper), translucency (lower left), cross-sectional (lower right) views

**Figure 5.56 CASE #14 (m=3): Contour of axial velocity (u, m/s) (upper),
radial velocity (v) along positive y-axis (lower left),
tangential velocity (w) along positive y-axis (lower right)**

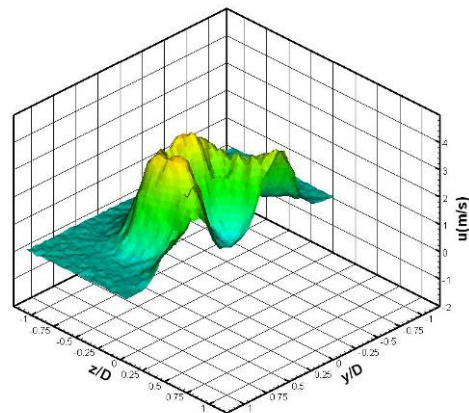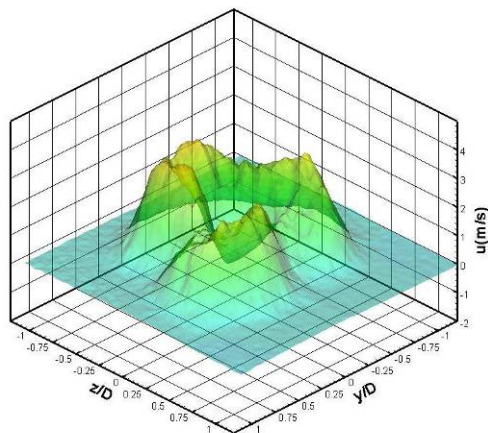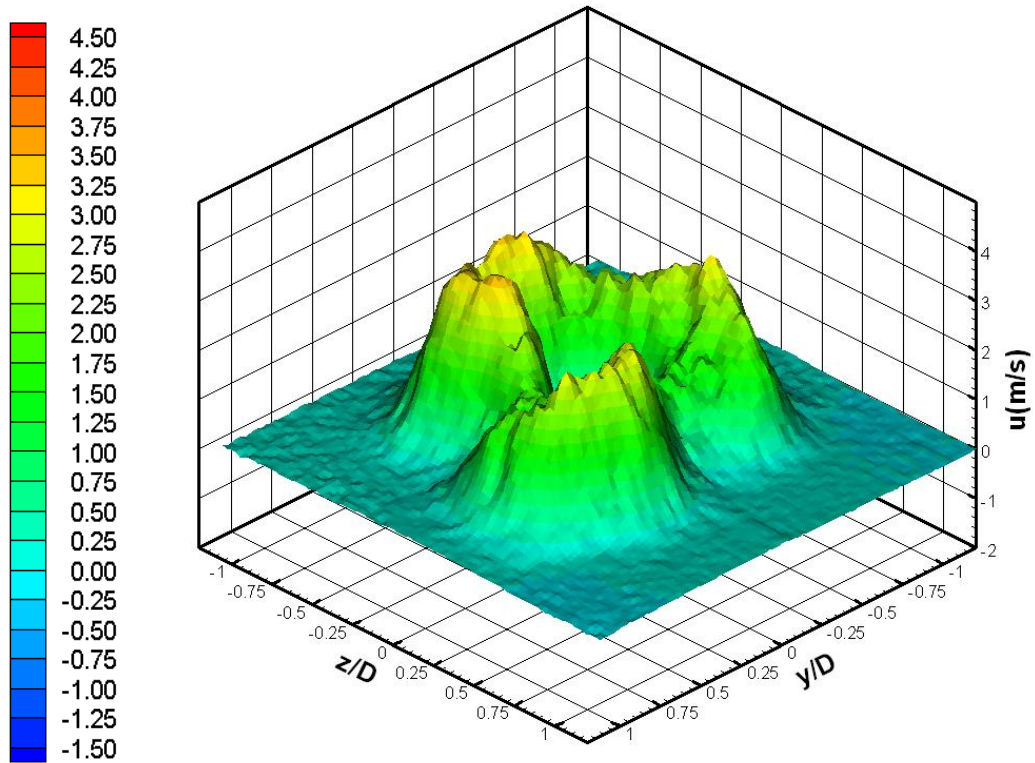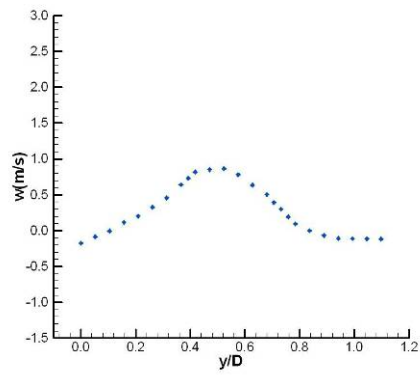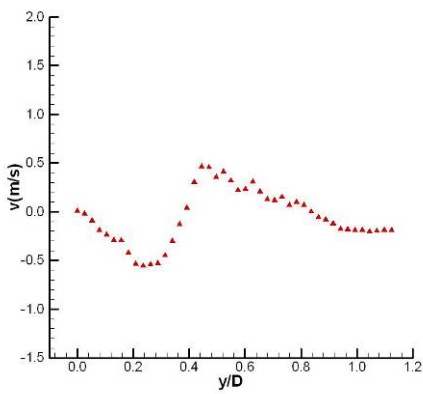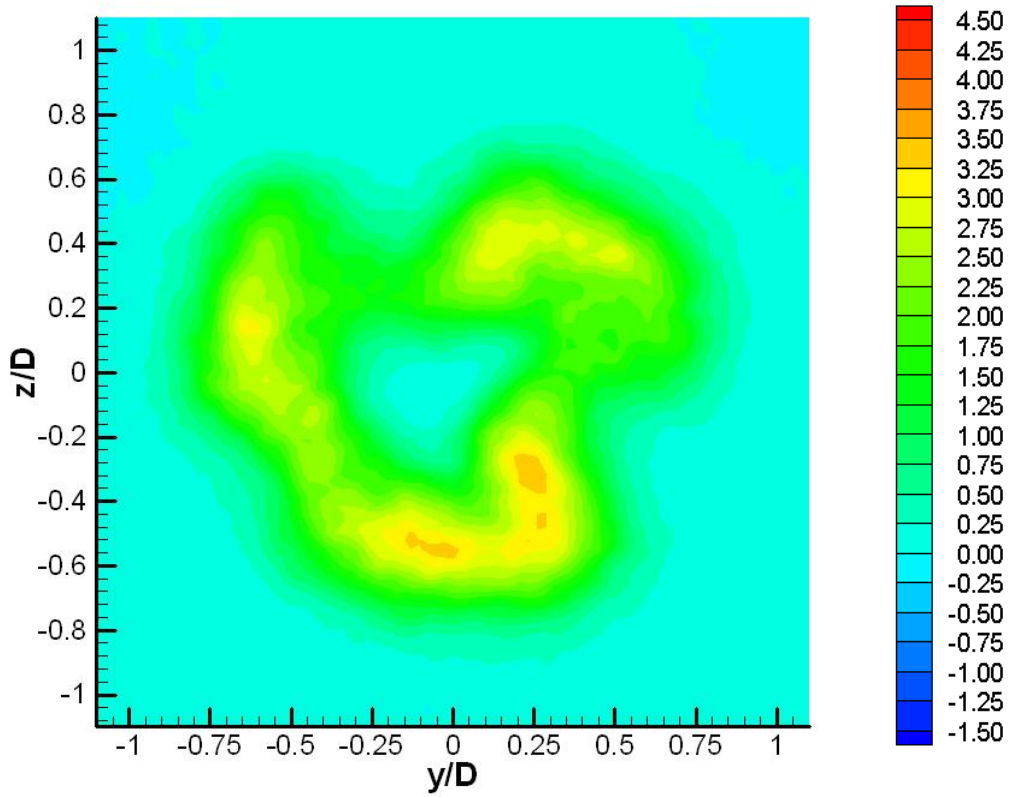**Figure 5.57 CASE #14 (m=3): Contour of turbulence intensity (%)**

Figure 5.58 CASE #14 (m=3): Contour of vorticity (s^{-1})

Figure 5.59 CASE #15 (m=4): Axial velocity (u) distribution
3D full (upper), translucency (lower left), cross-sectional (lower right) views

170
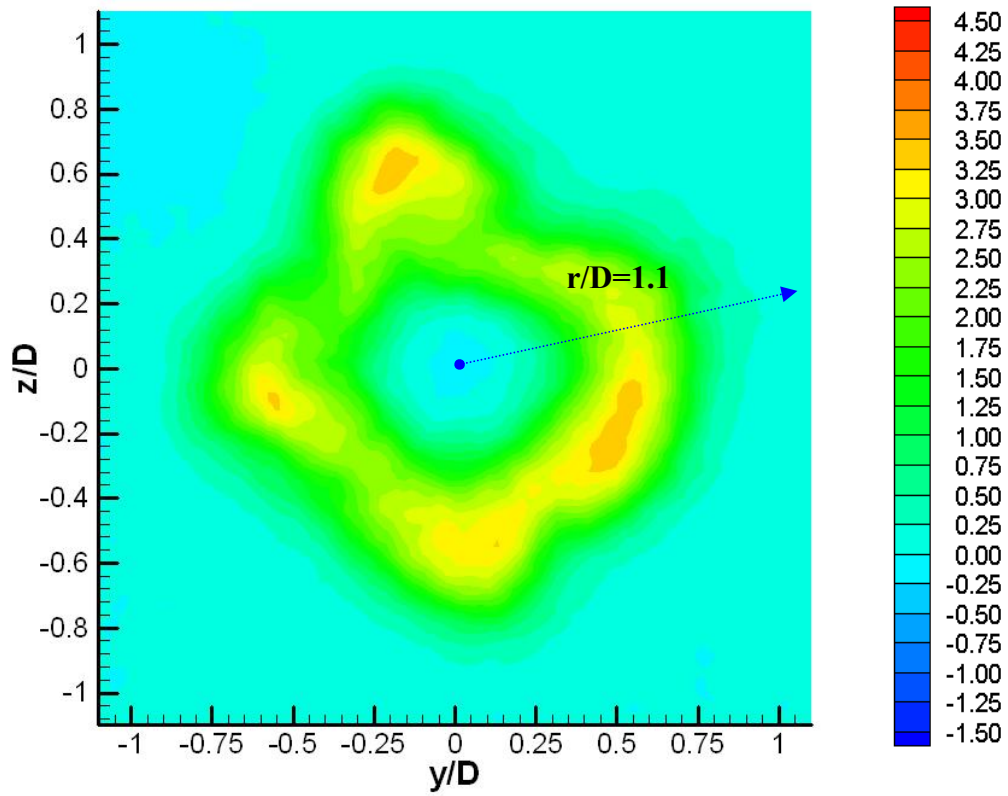
**Figure 5.60 CASE #15 (m=4): Contour of axial velocity (u, m/s) (upper),
radial velocity (v) along positive y-axis (lower left),
tangential velocity (w) along positive y-axis (lower right)**
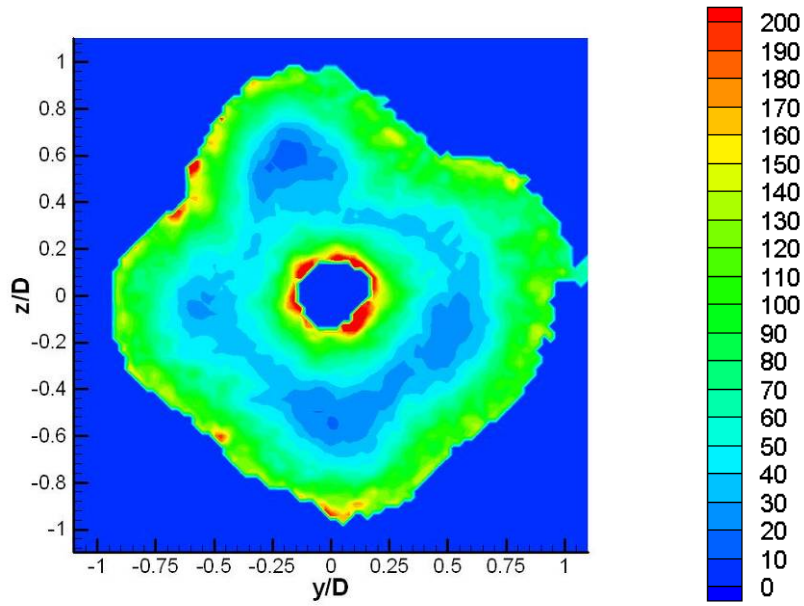
Figure 5.61 CASE #15 (m=4): Contour of turbulence intensity (%)
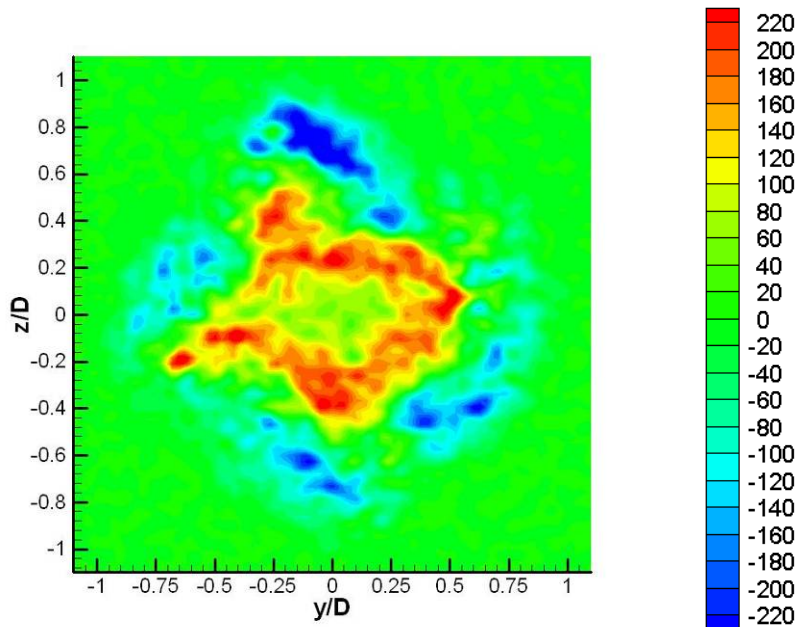
Figure 5.62 CASE #15 (m=4): Contour of vorticity (s⁻¹)
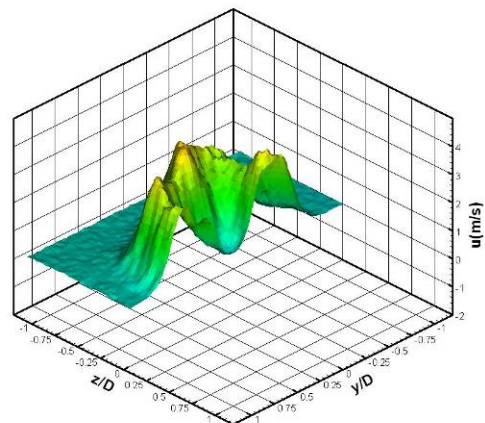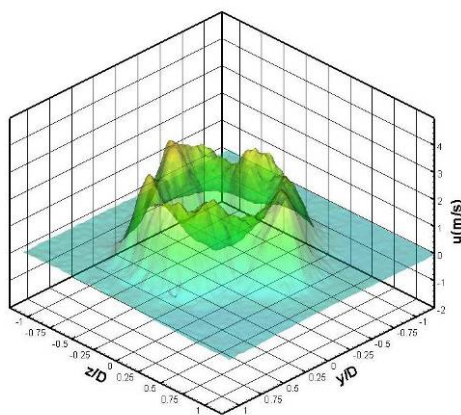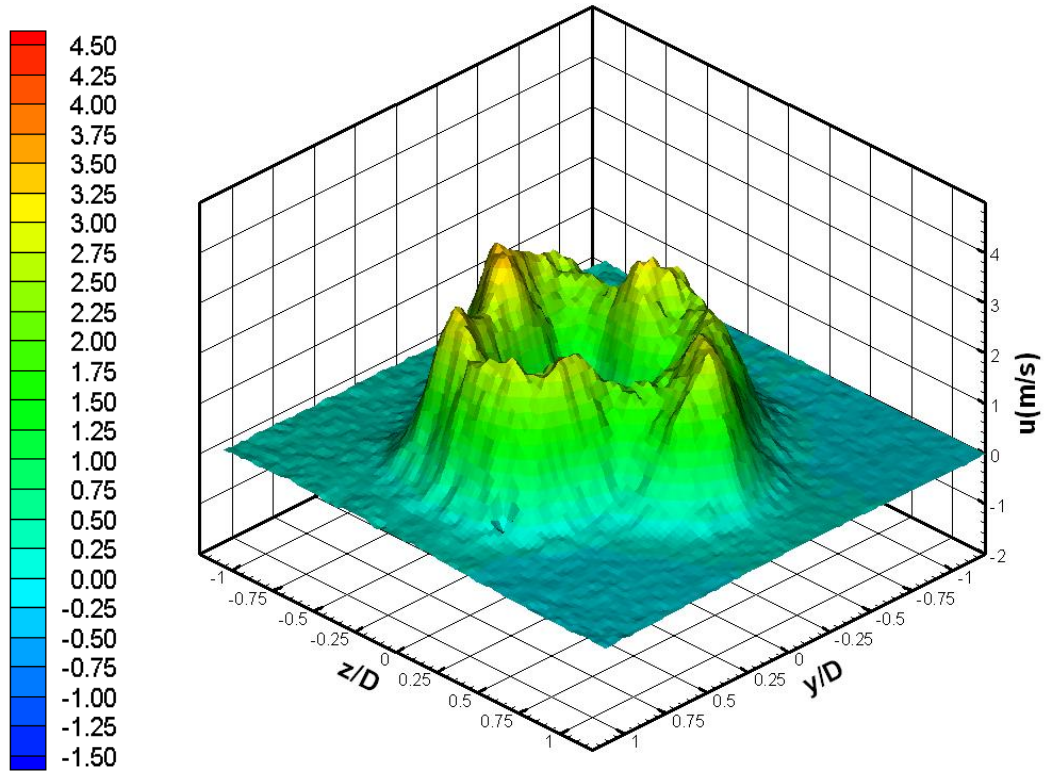
Figure 5.63 CASE #16 (m=4): Axial velocity (u) distribution
3D full (upper), translucency (lower left), cross-sectional (lower right) views

173
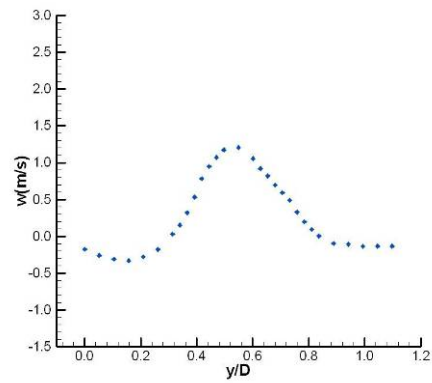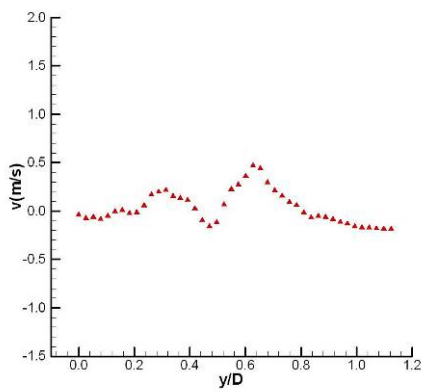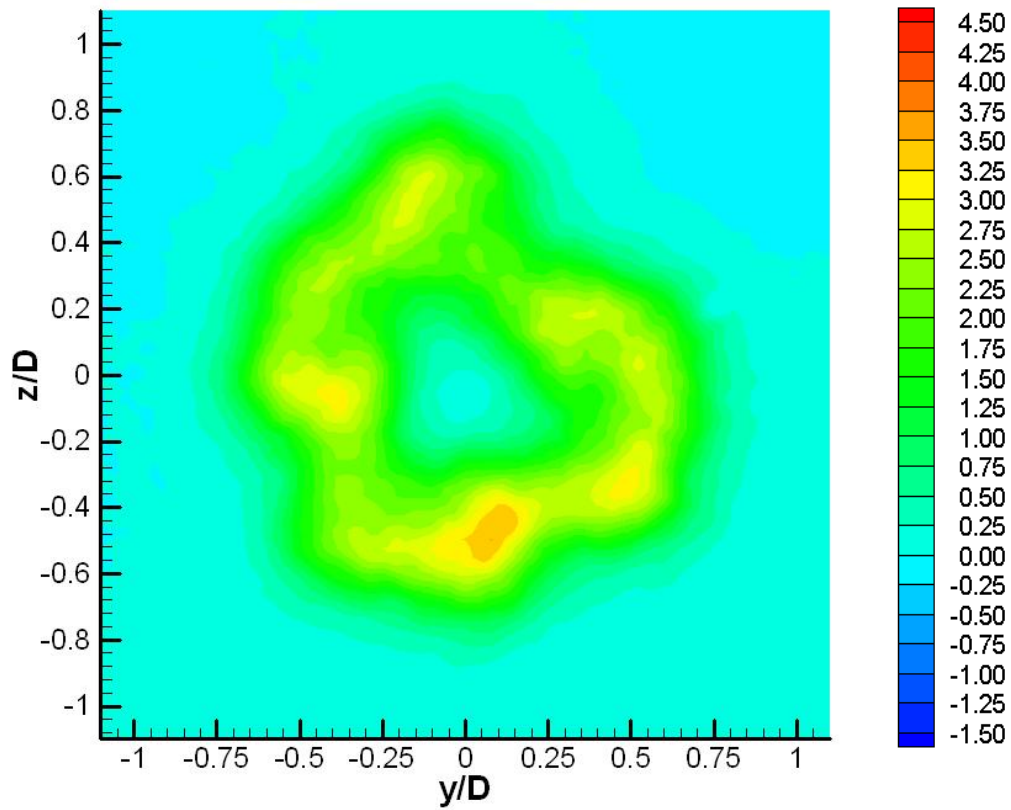
**Figure 5.64 CASE #16 (m=4): Contour of axial velocity (u, m/s) (upper),
radial velocity (v) along positive y-axis (lower left),
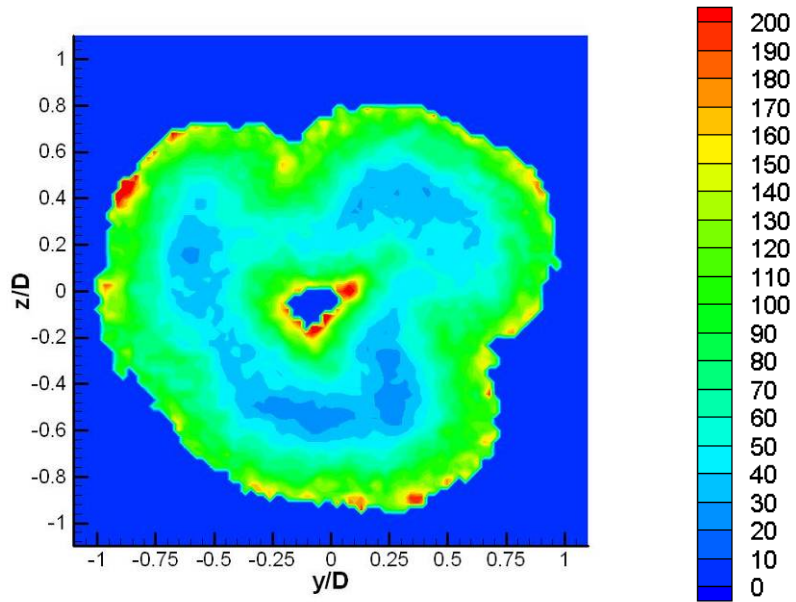tangential velocity (w) along positive y-axis (lower right)**

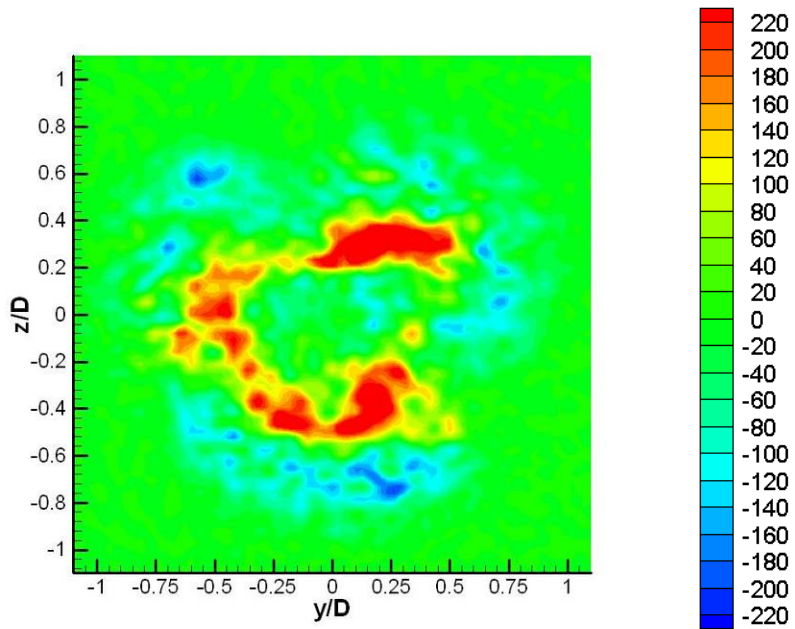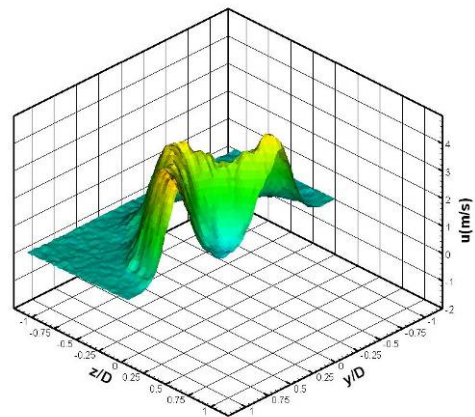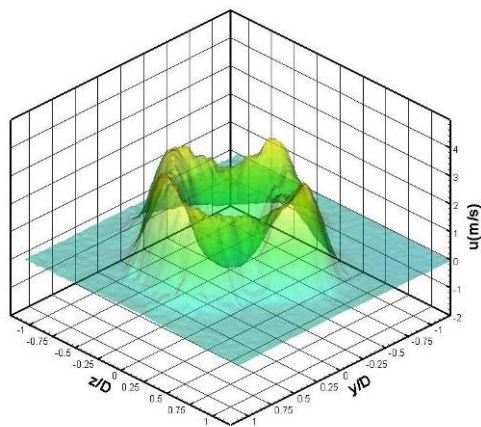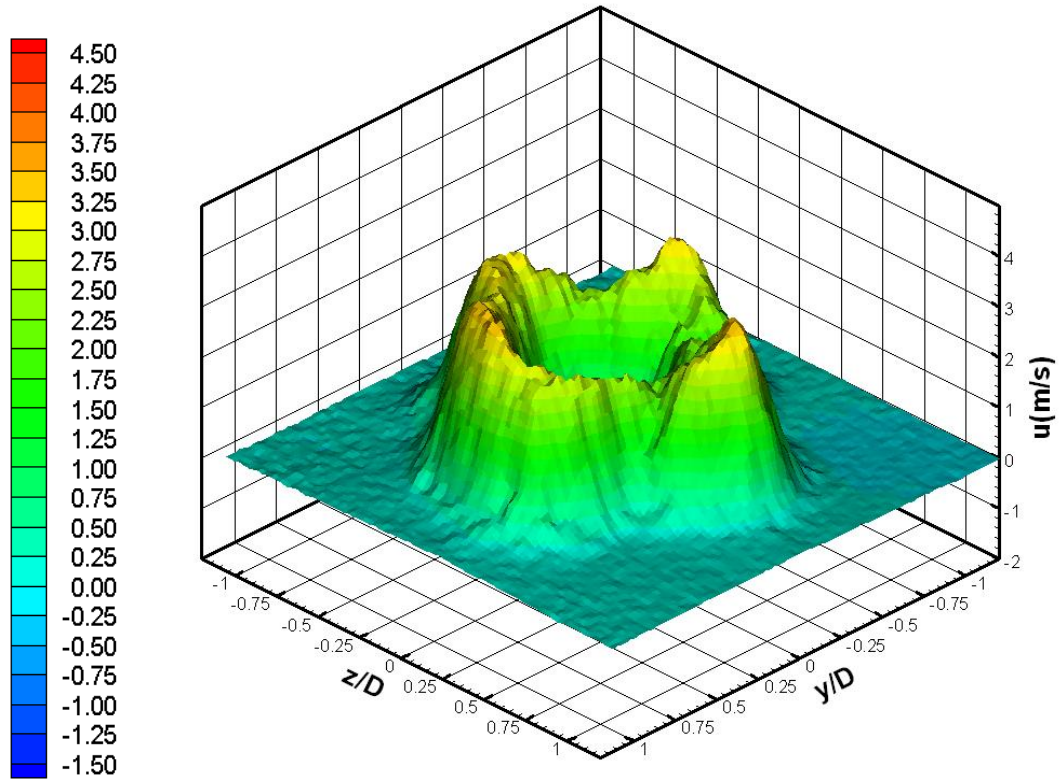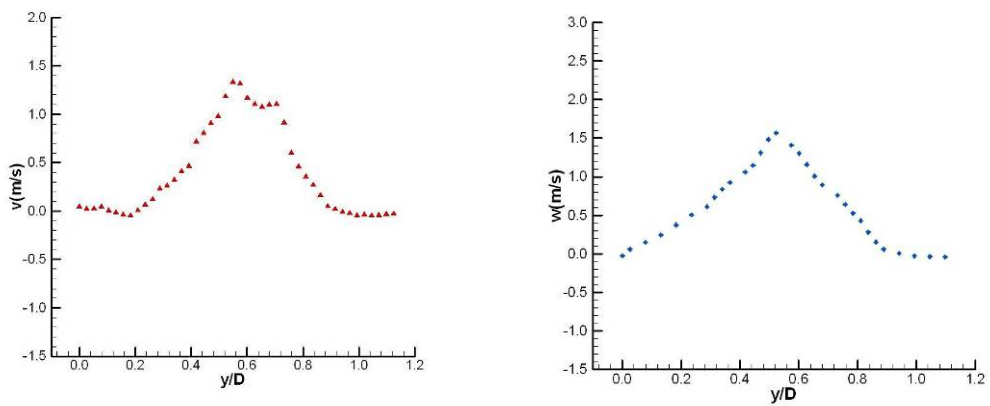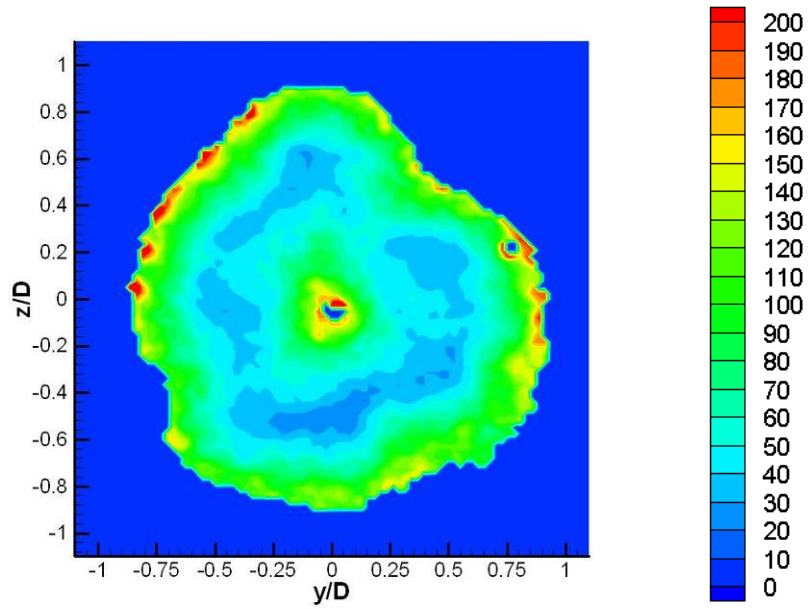**Figure 5.65 CASE #16 (m=4): Contour of turbulence intensity (%)**
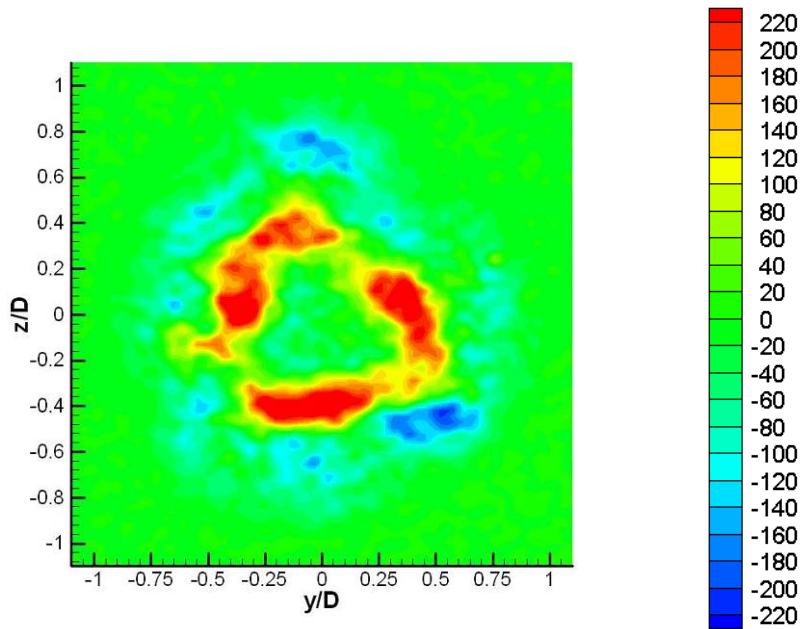
Figure 5.66 CASE #16 (m=4): Contour of vorticity (s^{-1})
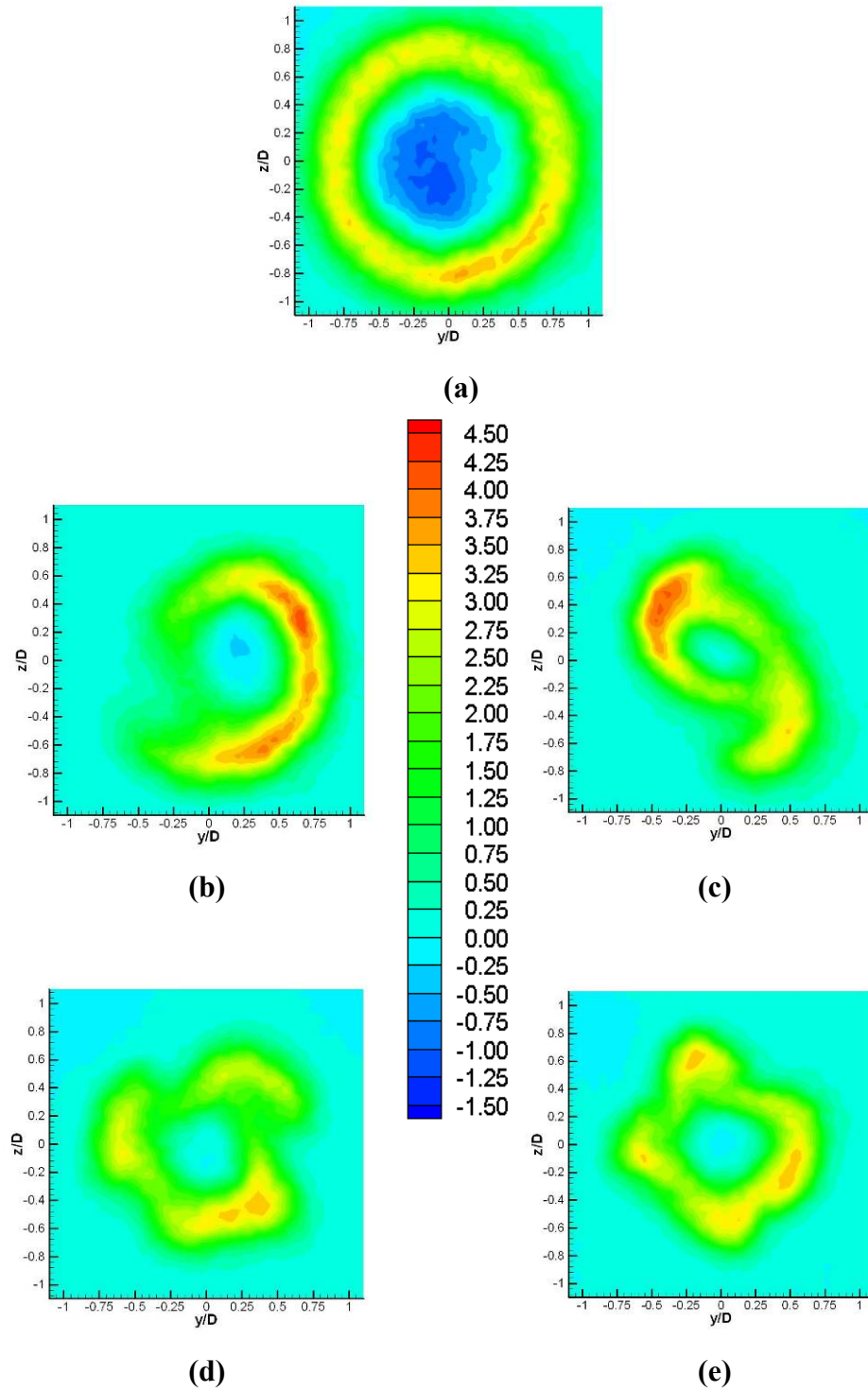
Figure 5.67 Comparison of axial velocity (u, m/s) contours at x/D=1, co-swirl cases (a) m=0 (b) m=1 (c) m=2 (d) m=3 (e) m=4
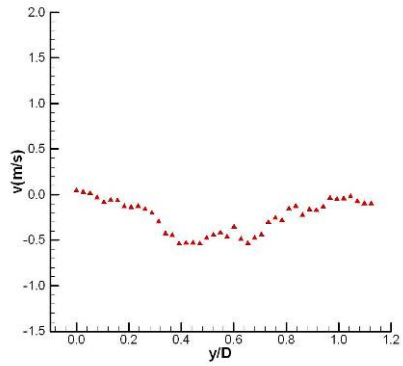
(a)
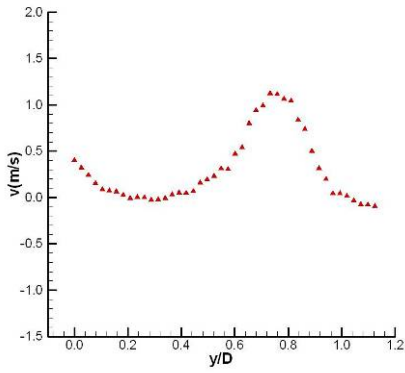
(b)
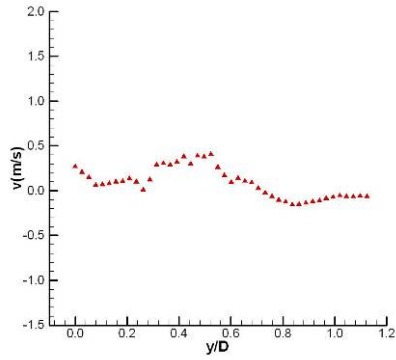
(c)
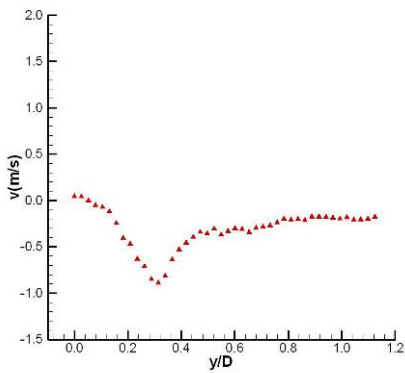
(d)
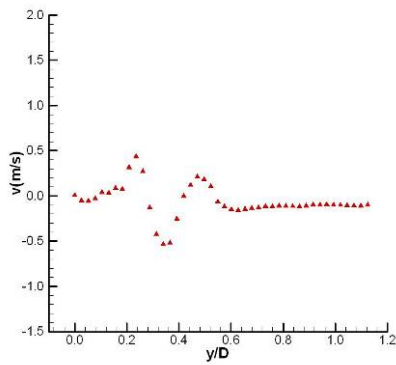
(e)

Figure 5.68 Comparison of radial velocity (v) distribution at z/D=0, x/D=1, co-swirl cases, (a) m=0 (b) m=1 (c) m=2 (d) m=3 (e) m=4
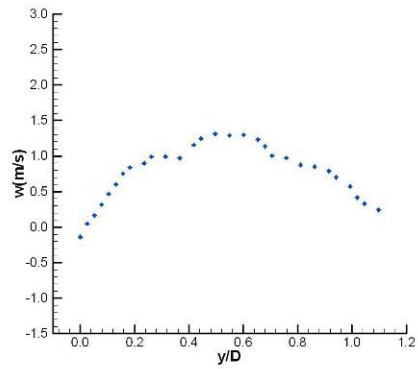
(a)
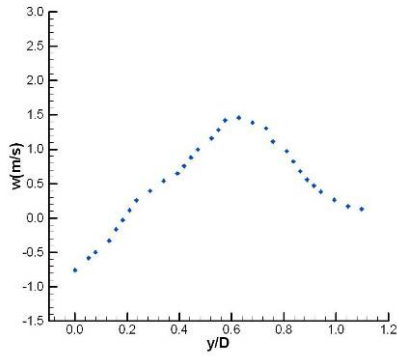
(b)
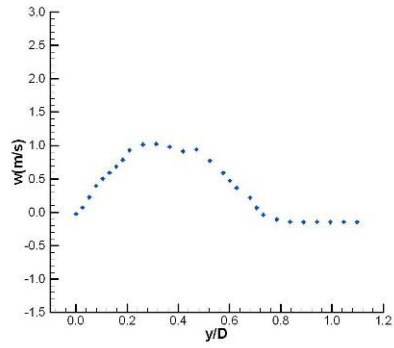
(c)
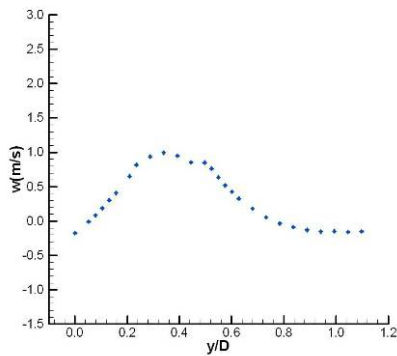
(d)
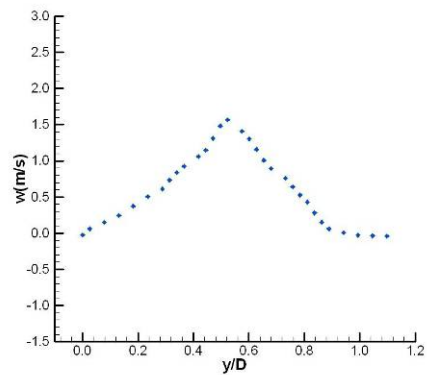
(e)

Figure 5.69 Comparison of tangential velocity (w) distribution at z/D=0, x/D=1, co-swirl cases, (a) m=0 (b) m=1 (c) m=2 (d) m=3 (e) m=4

178
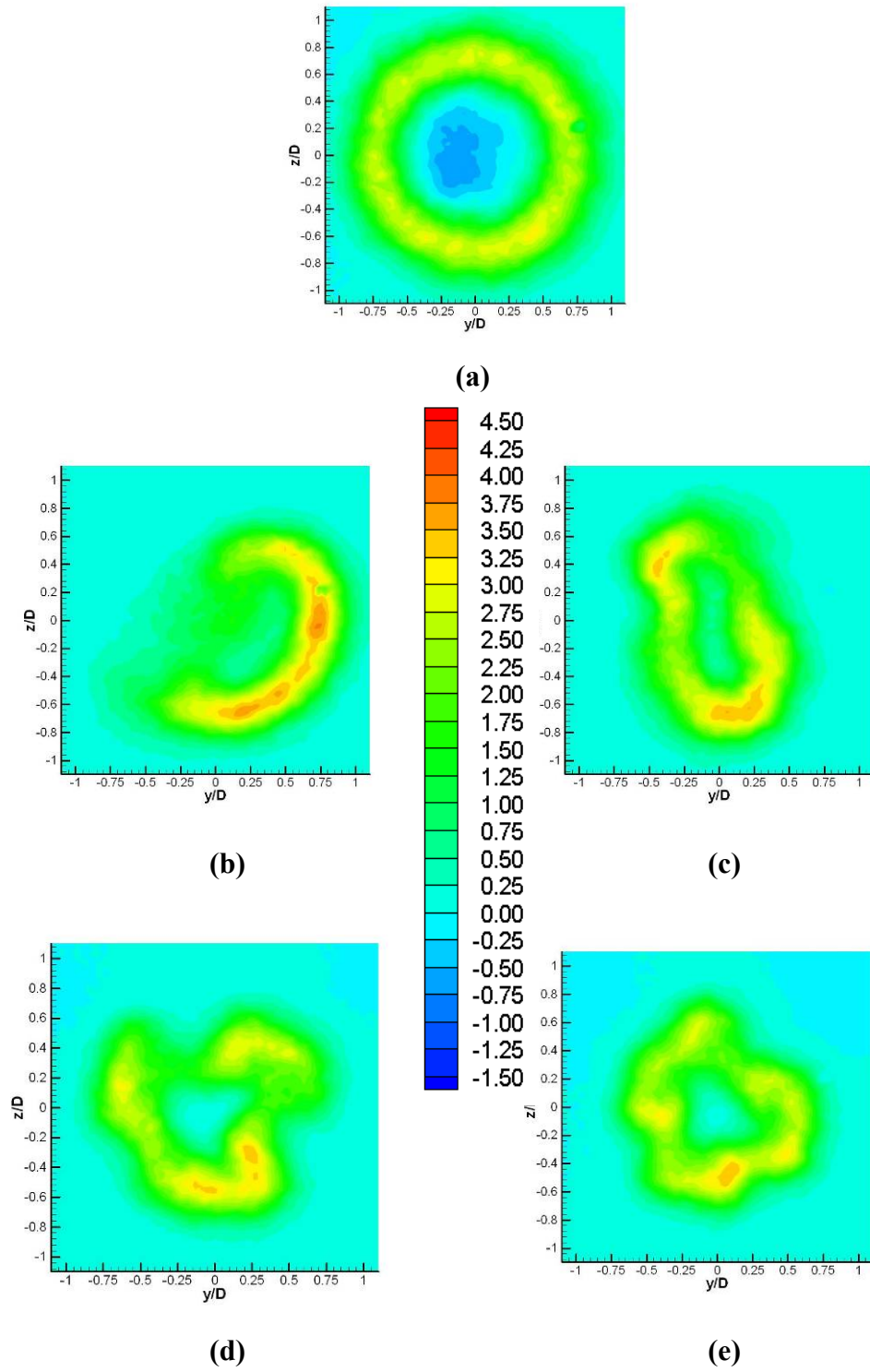
Figure 5.70 Comparison of axial velocity (u, m/s) contours at x/D=1, counter-swirl cases (a) m=0 (b) m=1 (c) m=2 (d) m=3 (e) m=4
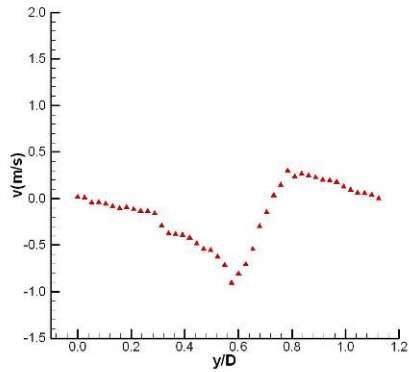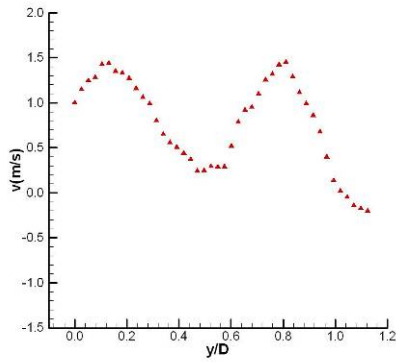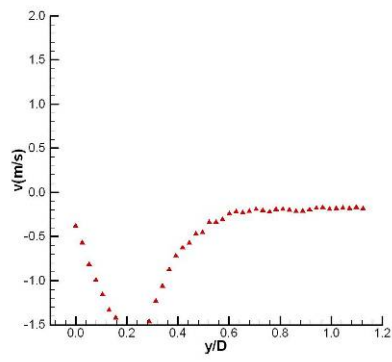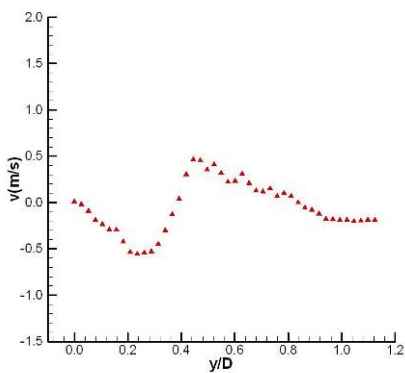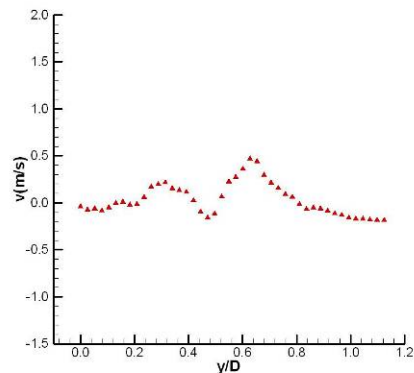
Figure 5.71 Comparison of radial velocity (v) distribution at z/D=0, x/D=1, counter-swirl cases, (a) m=0 (b) m=1 (c) m=2 (d) m=3 (e) m=4
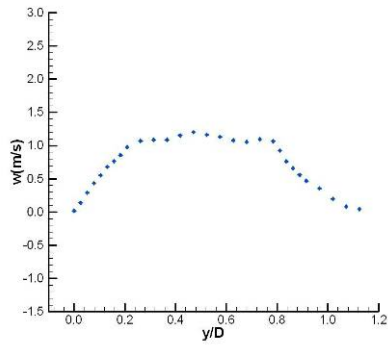
(a)
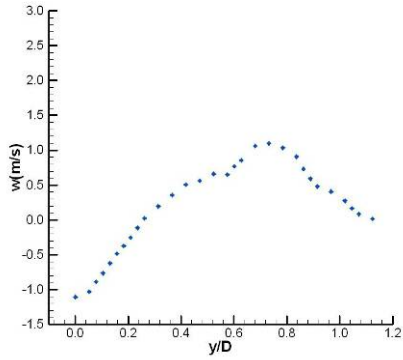
(b)
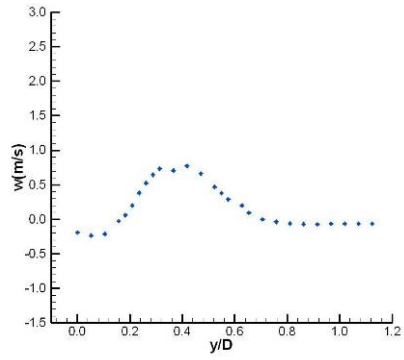
(c)
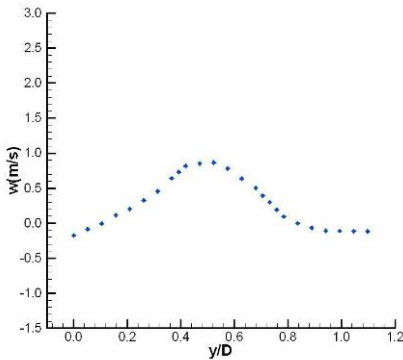
(d)
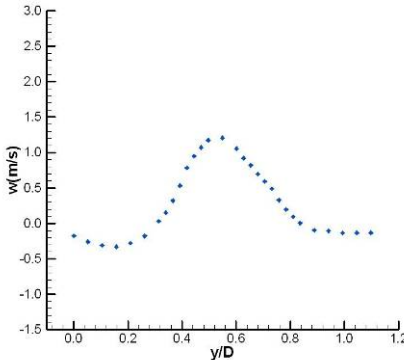
(e)

Figure 5.72 Comparison of tangential velocity (w) distribution at z/D=0, x/D=1, counter-swirl cases, (a) m=0 (b) m=1 (c) m=2 (d) m=3 (e) m=4

5.1.7. Wave Propagation Analysis for Selected Cases

To investigate the swirl jet behavior and its excitation effects into still air, the measurements are carried out at various axial distances from the nozzle exit for the selected cases, CASES #14 and #16. The total measured number of stations are six, and these are x/D=0.25, 0.50, 0.75, 1.00, 1.25, and 1.50. For convenient comparison, the results of axial velocity and turbulence intensity are assembled in one page. Also, the radial profiles of radial and tangential velocity components are plotted together in a single X-Y line plot.

Axial Velocity

Figures 5.73 and 5.74 show the excited swirl jets propagate into ambient air in both directions, axial and radial. In the excited case with three lobes (CASE #14_6), the maximum normalized radial distance from the center to the contour-line of velocity at '0.00 m/s' reaches up to approximately 'r/D=1.56'. Even within the short distance (i.e., x/D≤1.5, relatively near to the nozzle exit) the distance of the jet

boundary is increased by approximately 210% compared to the nozzle exit radius.

The four-lobed case shows the characteristic jet boundary located around 'r/D=1.25'

(CASE #16_6). This can be caused by the reduced nozzle exit area compared to the

'm=3' case.

Radial and Tangential Velocity

Compared to the plain circular jets, the radial and tangential velocity

components are relatively important in swirl analysis. As displayed in Figures 5.75

to 5.76, the three-lobed perturbation case (CASE #14) has a stabilized radial

distribution at the axial range of 'x/D=1.25~1.50'. In the case of 'm=4' (CASE #16),

at 'x/D=1.25', and even 'x/D=1.50' still shows the agitated radial motion around

'y/D=0.6~1.0'. Apparently, it appears that the 'm=3' case has stabilized more

quickly than 'm=4'. In fact, it cannot be compared directly, because the y-traverse

measurements experience the different phase angles for each case. This phenomenon

happens to the tangential behavior in a similar way. The plots of the tangential

velocity component (Figure 5.77 and 5.78) depict a more regular pattern compared

with the radial counterparts (Figure 5.75 and 5.76). In CASE #14 the tangential velocity mostly stays calm below 0.5m/s at the station x/D=1.25 and 1.50, but the tangential component of CASE #16 shows 0.8m/s at 'y/D=0.65, x/D=1.5'.

Turbulence Intensity

Turbulence intensity can also be regarded as a reference to determine the turbulence mixing. Then, turbulent mixing becomes a major factor only when the strong pressure gradients are weakened through rapid initial jet spread. As shown in Figures 5.79 and 5.80, the intensified fluctuation (over 180%) dominates both shear layers (i.e., the mean characteristic boundary and between two jets) at the near exit (x/D=0.25). As we progress in the axial direction, regardless of the number of lobes, this high intensity decays fast, and almost vanishes, except for a few spots when it approaches 'x/D=1.00'. In comparison to unexcited swirl cases, the excited cases show fortified mixing at the near exit and a relatively short period of stabilization time in both 'm=3 and 4' cases.
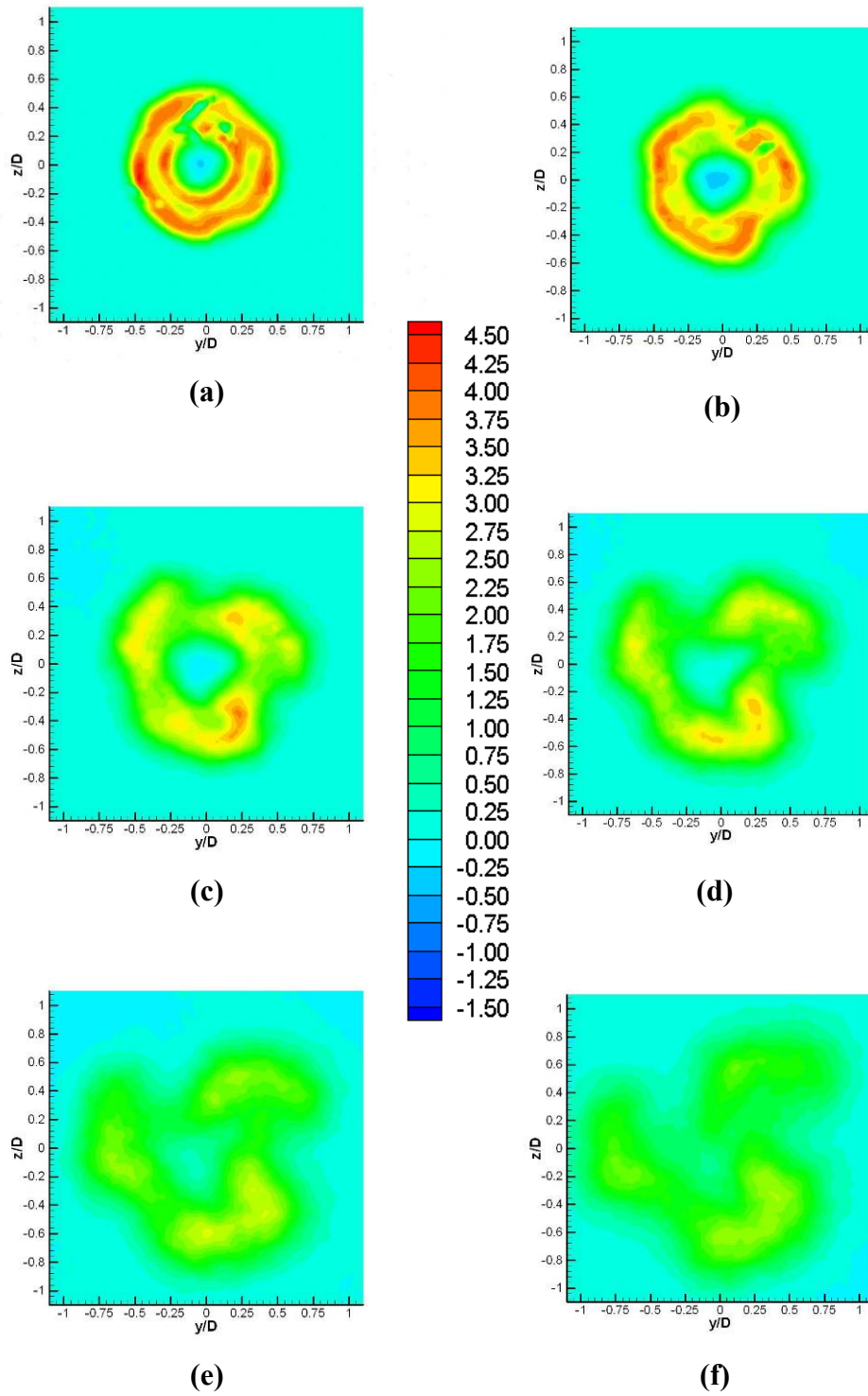
Figure 5.73 CASE #14: Contour of axial velocity at various stations (u, m/s)
(a) x/D=0.25 (b) x/D=0.50 (c) x/D=0.75 (d) x/D=1.00 (e) x/D=1.25 (f) x/D=1.50

185
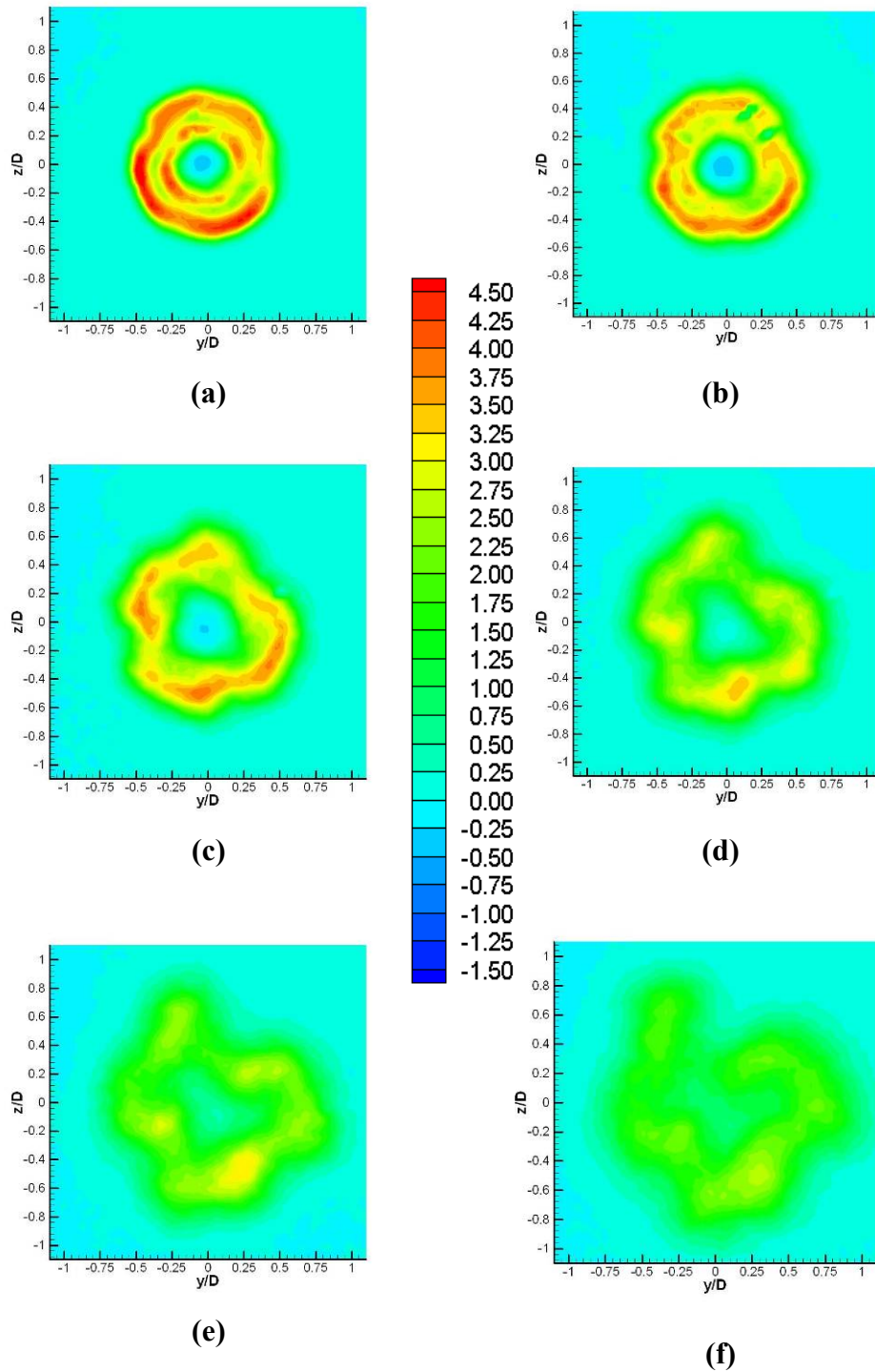
Figure 5.74 CASE #16: Contour of axial velocity at various stations (u, m/s) (a) x/D=0.25 (b) x/D=0.50 (c) x/D=0.75 (d) x/D=1.00 (e) x/D=1.25 (f) x/D=1.50
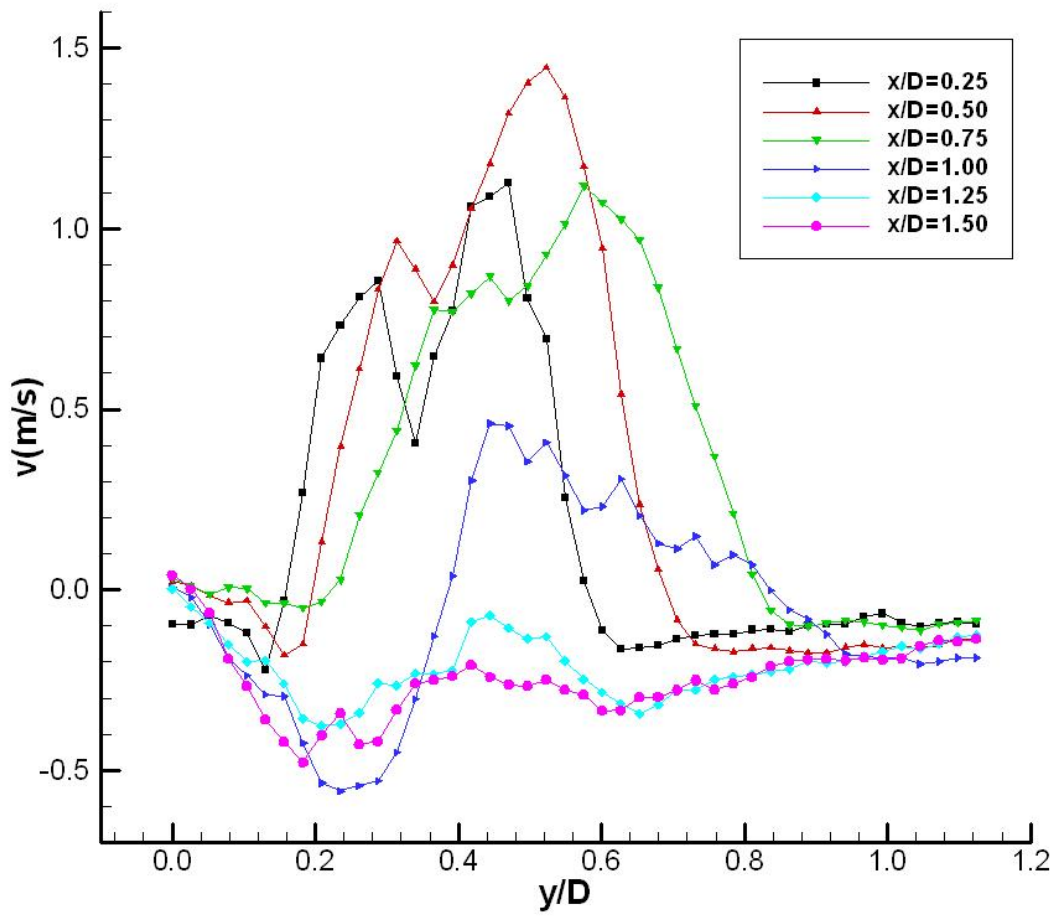
Figure 5.75 CASE #14: Radial velocity (v) profile at various stations, z/D=0
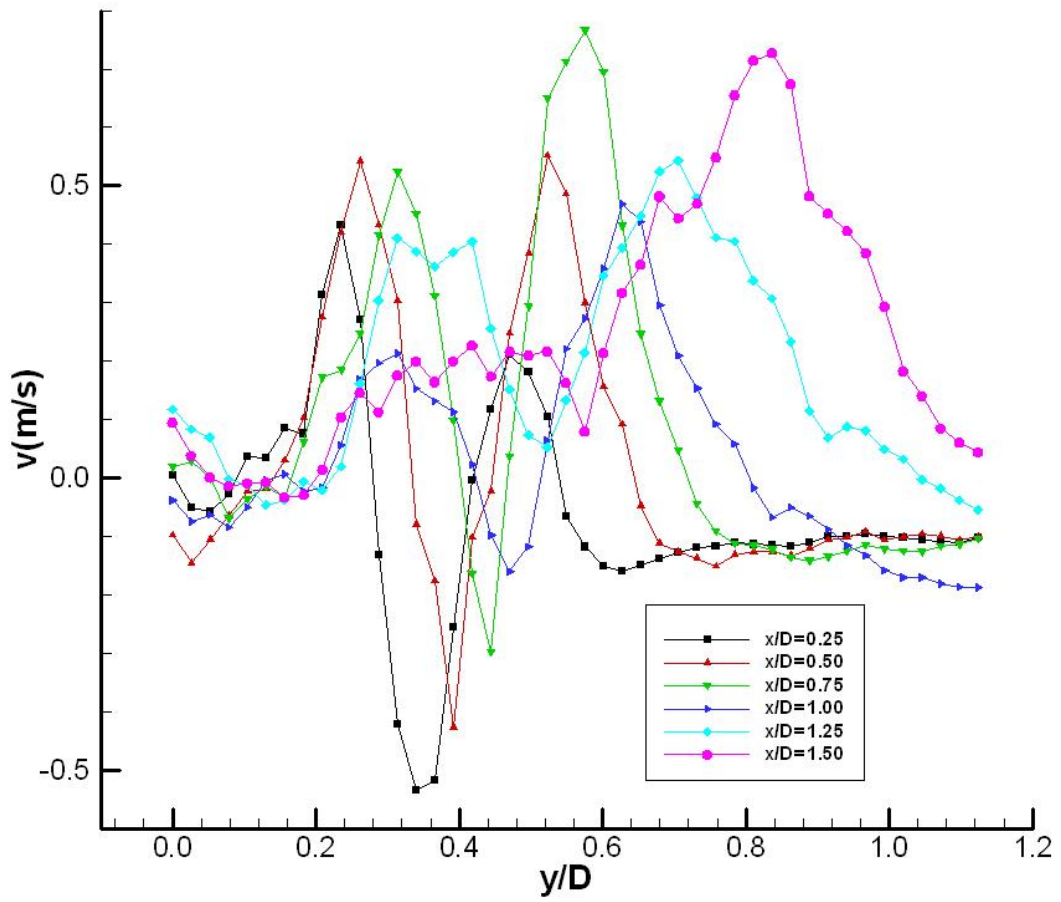
Figure 5.76 CASE #16: Radial velocity (v) profile at various stations, z/D=0
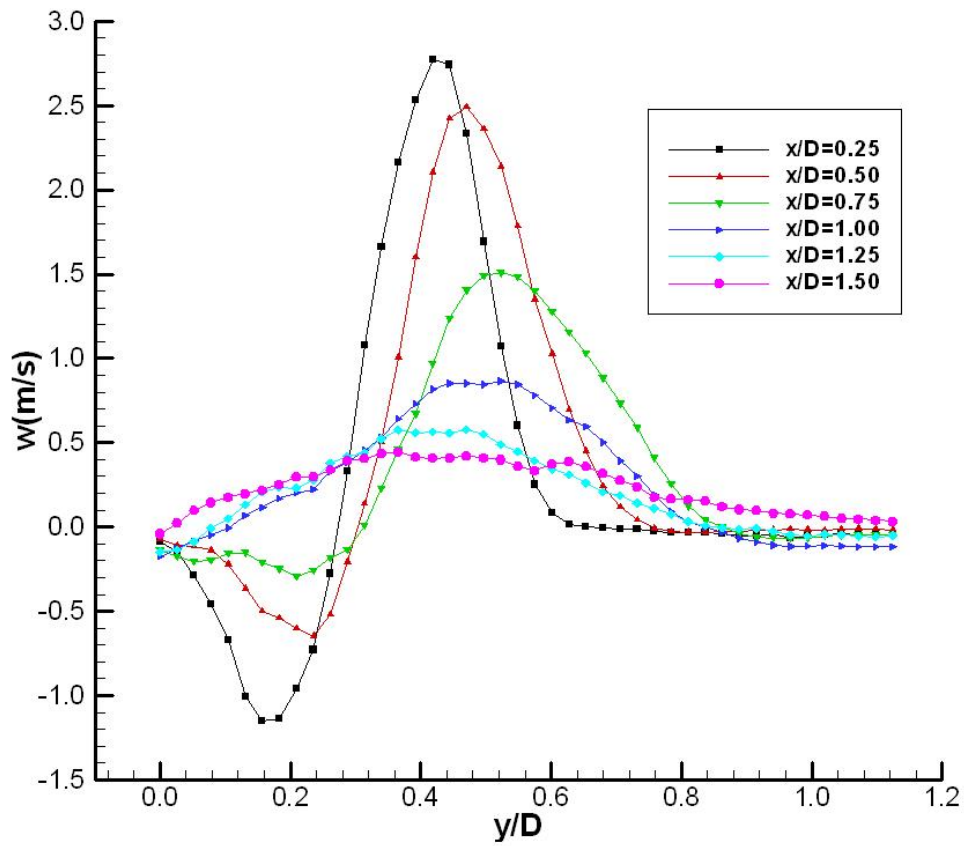
Figure 5.77 CASE #14: Tangential velocity (w) profile at various stations, z/D=0
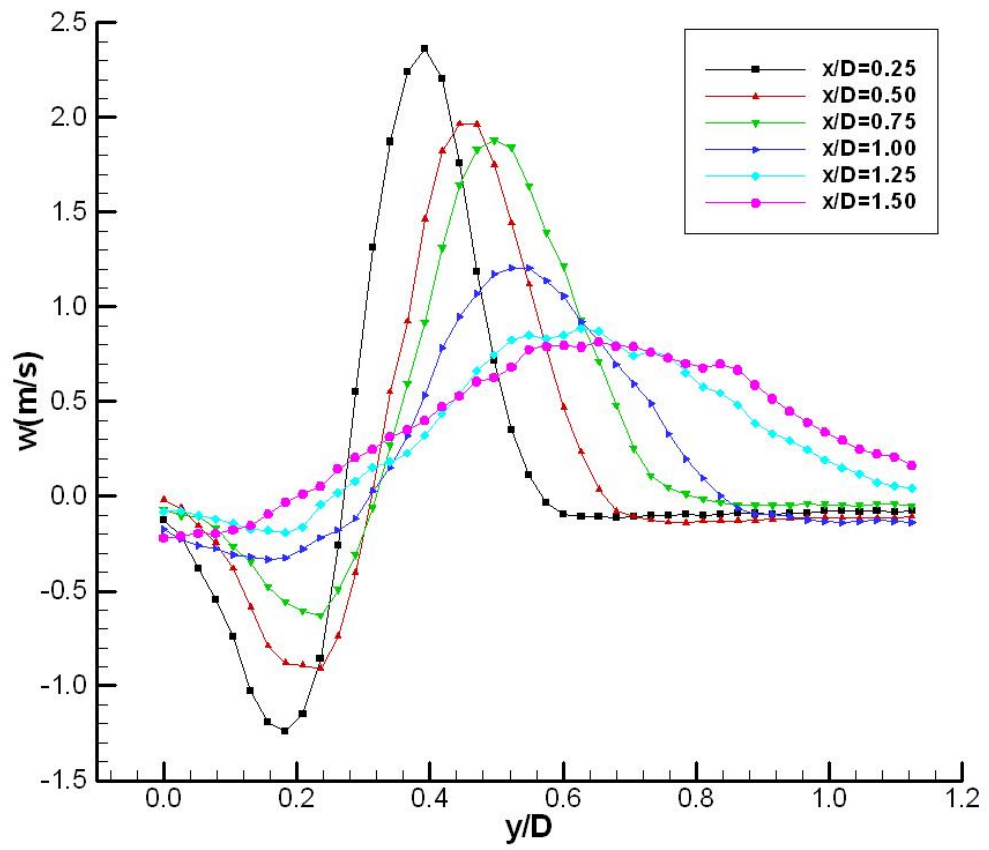
Figure 5.78 CASE #16: Tangential velocity (w) profile at various stations, z/D=0
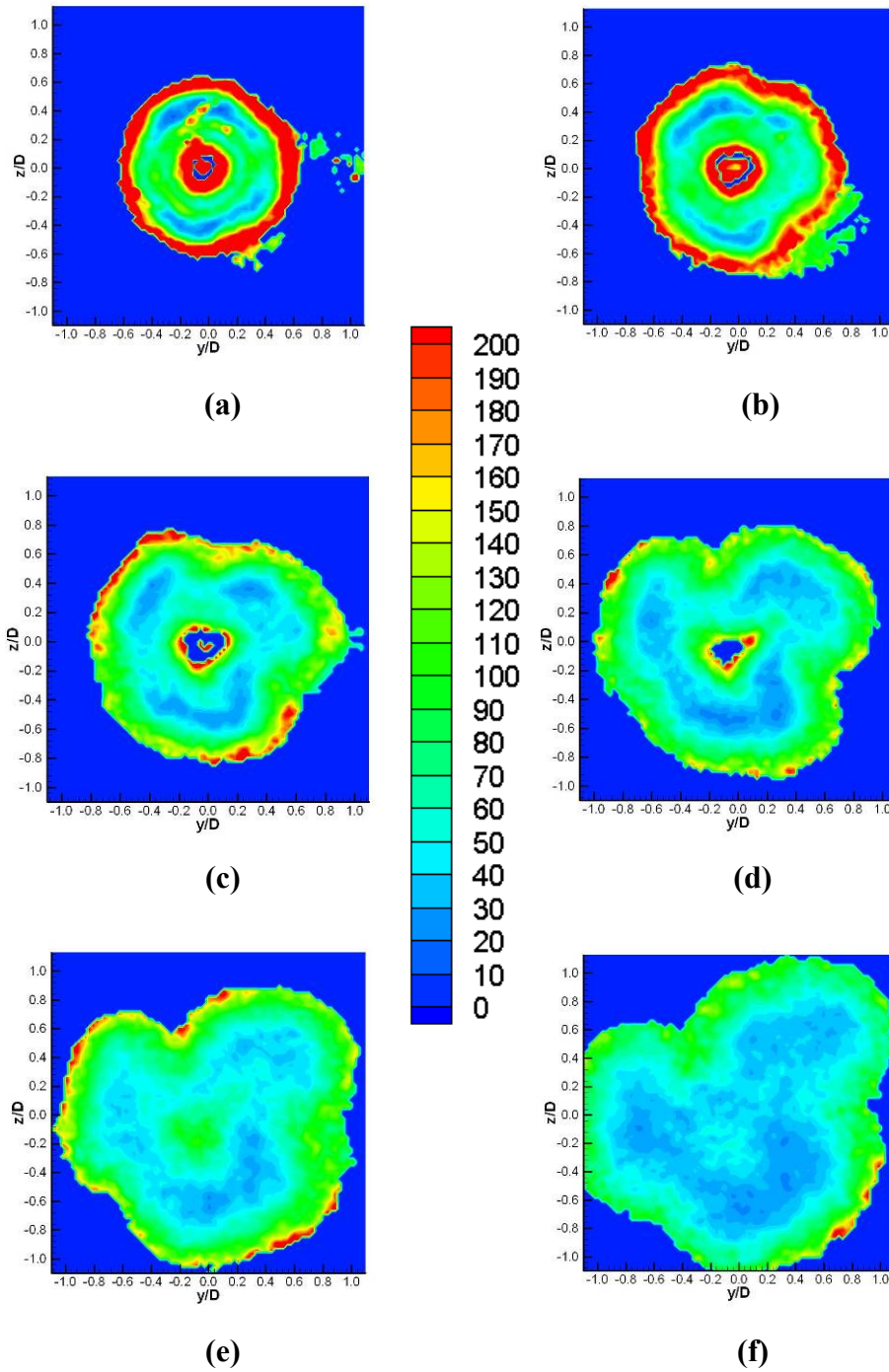
Figure 5.79 CASE #16: Contour of turbulent intensity (%) at various stations
(a) x/D=0.25 (b) x/D=0.50 (c) x/D=0.75 (d) x/D=1.00 (e) x/D=1.25 (f) x/D=1.50
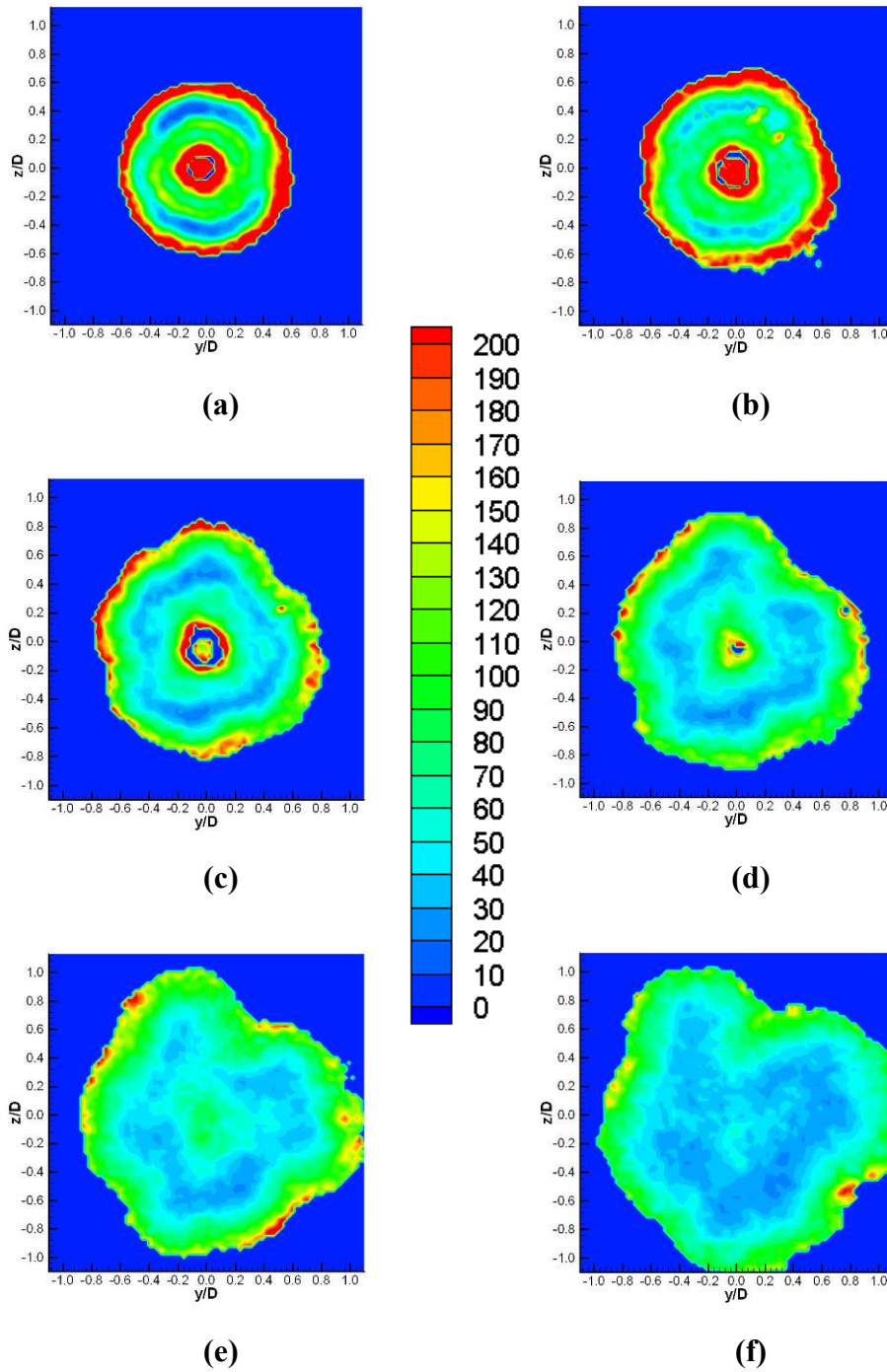
Figure 5.80 CASE #16: Contour of turbulent intensity (%) at various stations (a) x/D=0.25 (b) x/D=0.50 (c) x/D=0.75 (d) x/D=1.00 (e) x/D=1.25 (f) x/D=1.50

5.1.8. Statistics of Results

Table 5.1 is presented for the statistical results of various axial velocity data

in comparison with the baseline (i.e., unexcited plain round jet, CASE #01).

Table 5.1 Statistics of Experimental Cases

| | Axial velocity (m/s) at | | | | Radius (r/D) of | | | |
	vortex core		peak		peak		jet boundary	
CASE #01	+3.3	0%	4.2	0%	0.30	0%	0.70	0%
CASE #02	-1.2	-136%	3.2	-24%	0.80	167%	1.40	100%
CASE #03	-0.8	-124%	2.8	-33%	0.70	133%	1.30	86%
CASE #04	-1.2	-136%	3.6	-14%	0.70	133%	1.35	93%
CASE #05	-2.2	-167%	5.0	19%	0.80	167%	1.35	93%
CASE #06	-2.2	-167%	4.8	14%	0.70	133%	1.35	93%
CASE #07	-1.8	-155%	3.2	-24%	0.75	150%	1.45	107%
CASE #08	+0.6	-82%	2.8	-33%	0.70	133%	1.30	86%
CASE #09	-0.2	-106%	3.6	-14%	0.70	133%	1.25	79%
CASE #10	+0.6	-82%	3.8	-10%	0.70	133%	1.25	79%
CASE #11	+0.2	-94%	4.0	-5%	0.55	83%	1.30	86%
CASE #12	+0.4	-88%	3.5	-17%	0.70	133%	1.25	79%
CASE #13	+0.0	-100%	3.4	-19%	0.40	33%	1.10	57%
CASE #14_4	-0.1	-103%	3.4	-19%	0.25	-17%	1.10	57%
CASE #15	-0.2	-106%	3.4	-19%	0.60	100%	1.10	57%
CASE #16_4	-0.2	-106%	3.4	-19%	0.50	67%	0.90	29%

5.2. Numerical Results

In the numerical approach, the analysis deals with the swirl flow characteristics of the high speed region compared to experimental cases, and helical excitation on initial jets for the effects in ambient air (i.e., far fields). The mass flow rate is raised ten times by velocity augmentation, and the spiral lobes are applied for a helical perturbation, instead of the straight ones which are used for experimental cases. The analysis plane, same as the measurement plane in experiments, is also varied from 'x/D=1' and its vicinity to the various planes up to 'x/D=8'. In addition, the propagation of injected flow particles in spatial behavior is traced up to 'x/D=20'.

5.2.1. Verification of Shear Control

The simulation results from the various jet models are plotted in Figures 5.82 through 5.128. All the plots are generated using a post-processing tool built in the 'FLUENT' solver. Each case is presented in four types, based on the display methods and the flow property of interest:

- The first part exhibits the overall shape of mean axial velocity distribution in two-dimensional (i.e., horizontal and/or vertical) planes. All the figures are plotted in the same range of x- and y-coordinates, and these axes are normalized by the outer nozzle exit diameter (D, inside diameter) for Figures 5.82, 5.83, and 5.86 through 5.97.

- To get the detailed information about the wave propagation into the far fields, the axial velocity distributions are presented at several stations from the nozzle exit to ambient air, x/D=0, 2, 4, 6, and 8 (ref. Figure 5.81). For comparison, the same contour level is applied to all figures regardless of the stations (Figures 5.98 to 5.109).

- To analyze the three dimensional flow behavior, the trace of particles (i.e., path-line) departing from each swirl injector, inner and outer, is presented (Figures 5.111 to 5.122). Also, the behavior of jet entrainment is analyzed, and presented in Figures 5.123 and 5.124.

- The last part of the figures displays the static temperature distribution to reveal the excitation effects on hot gas (Figure 5.125 and 5.127).

Release line for flow entrainment analysis (Fig 5.123 & 5.124)
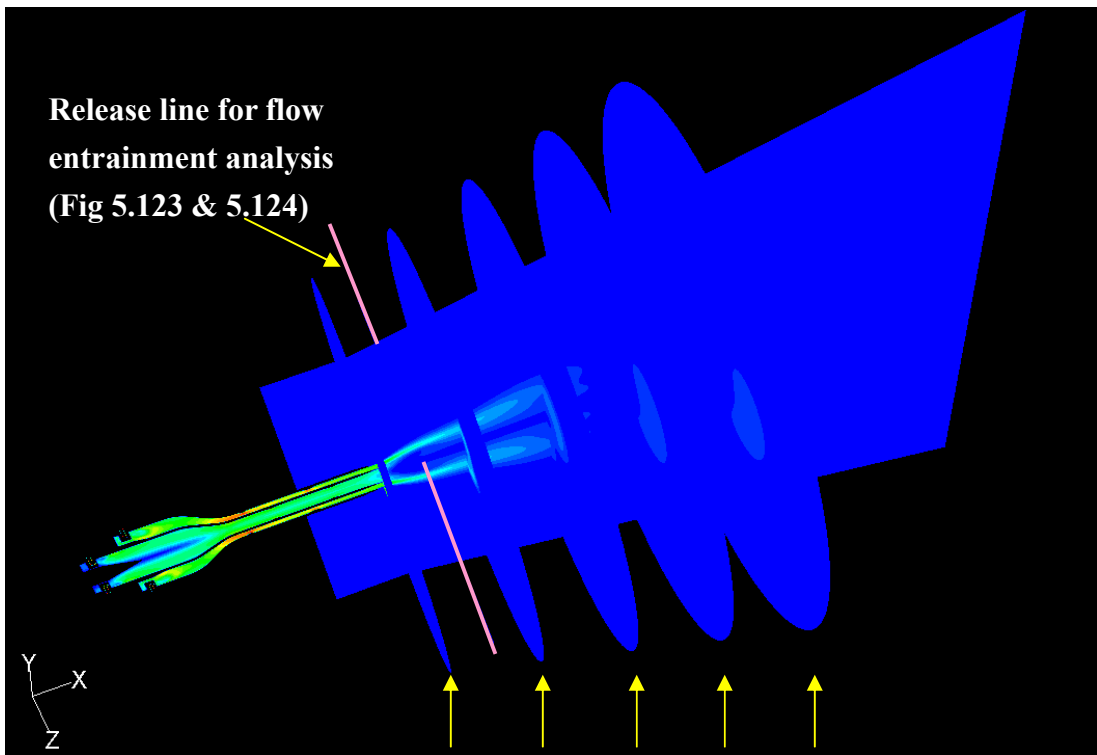
x/D=0 x/D=2 x/D=4 x/D=6 x/D=8

Figure 5.81 Definition sketch of various view planes for numerical presentation

5.2.2. Configuration of Plain Round Jet and Baseline

In this analysis, the baseline is selected as MODEL #03 which has swirl and no excitation. It depicts fairly different shape from concentric circular jet (Figure 5.82 and 5.83) and two noticeable phenomena are as follows.

First, the mean characteristic boundary has a wide angle. For example, the radial distance from the point of $(x/D, y/D, z/D) = (1, 0, 0)$ to '2.0m/s' contour line is 'r/D=0.55' for plain round jet (Figure 5.82). On the other hand, the distance for the baseline is 'r/D=0.94', and it is increased value by 71% compared to the circular jet (Figure 5.83). Even more the augmented axial velocity is found at 'x/D=5.0' (i.e., from r/D=1.11 to r/D=2.25, 103% up).

Second, the reverse flow motion is found at the near exit region (x/D<5). Also the Figure 5.82 shows the u-velocity of round jet at $(x/D, y/D, z/D) = (1, 0, 0)$ is '23.0m/s', but the value of '-7.0m/s' is detected at the same point in the swirled case (Figure 5.83). As explained in the experimental study with high degree of swirl, this is an interesting swirl jet phenomenon due to significant lateral and longitudinal pressure gradients and a toroidal recirculation. This also supports that the code

simulates the important swirl characteristics well. Even gross features of the flow are not known quantitatively with certainty; for example, the factors affecting the existence, size, and shape of the corner recirculation zone, CRZ, and the central toroidal recirculation zone are:

- Swirl strength

- Central hub, or not

- Expansion to main chamber

- Swirl vane angle constant with radius, or not

Figures 5.84 and 5.85 display the detailed view of recirculation with enough swirl strength to produce CTRZ. When the confined swirl flow is released to free ambient region, the rotating flow suddenly expands in a radial direction. At the same time, a relatively low static pressure region is formed, and it induces the reverse flow motion. Regardless of the helical excitation effects, the CTRZ exists throughout the entire set of simulation cases (Figure 5.86 and Figures 5.88 to 5.91 in this investigation).

In addition, an intriguing effect is presented in Figure 5.87 (MODEL #04). It possesses the counter-swirl flow regime (i.e., counter-clockwise spin for the inner flow and clockwise for the outer) and no disturbances. Even the inner jet is set to turn in a counter-clockwise direction; its rotating direction is abruptly changed to the reverse, to be the same as the rotating direction of the outer jet, as it leaves the nozzle. It makes for a highly intensified reverse flow, and the velocity falls to -16m/s at 'x/D=1.2, y/D=0.0' (Figure 5.86). This phenomenon can be explained, as the relatively high degree of outer-swirl strength induces the entrainment from the inner flow, and it contributes to creating the severe reversed angular force by shear interaction (i.e., momentum exchange) between the inner and outer jets. This can be regarded as a mixing enhancement effect, but this effect is limited to the exit and its vicinity region only. Eventually, beyond 'x/D=2.0', the governing motion is pretty similar to co-swirl cases (MODEL #03).

This phenomenon explains that the shear force of the outer-swirl, which has a relatively large rotating radius, dominates throughout the entire downstream region. The result provides the reason that the overall counter-swirl phenomena are similar to the co-swirl ones, which are shown in several experimental cases. Furthermore, it

presents the reason that the effects of increased inner-swirl velocity vanishes easily

compared to the outer velocity augmented case (ref. section 5.1.5).
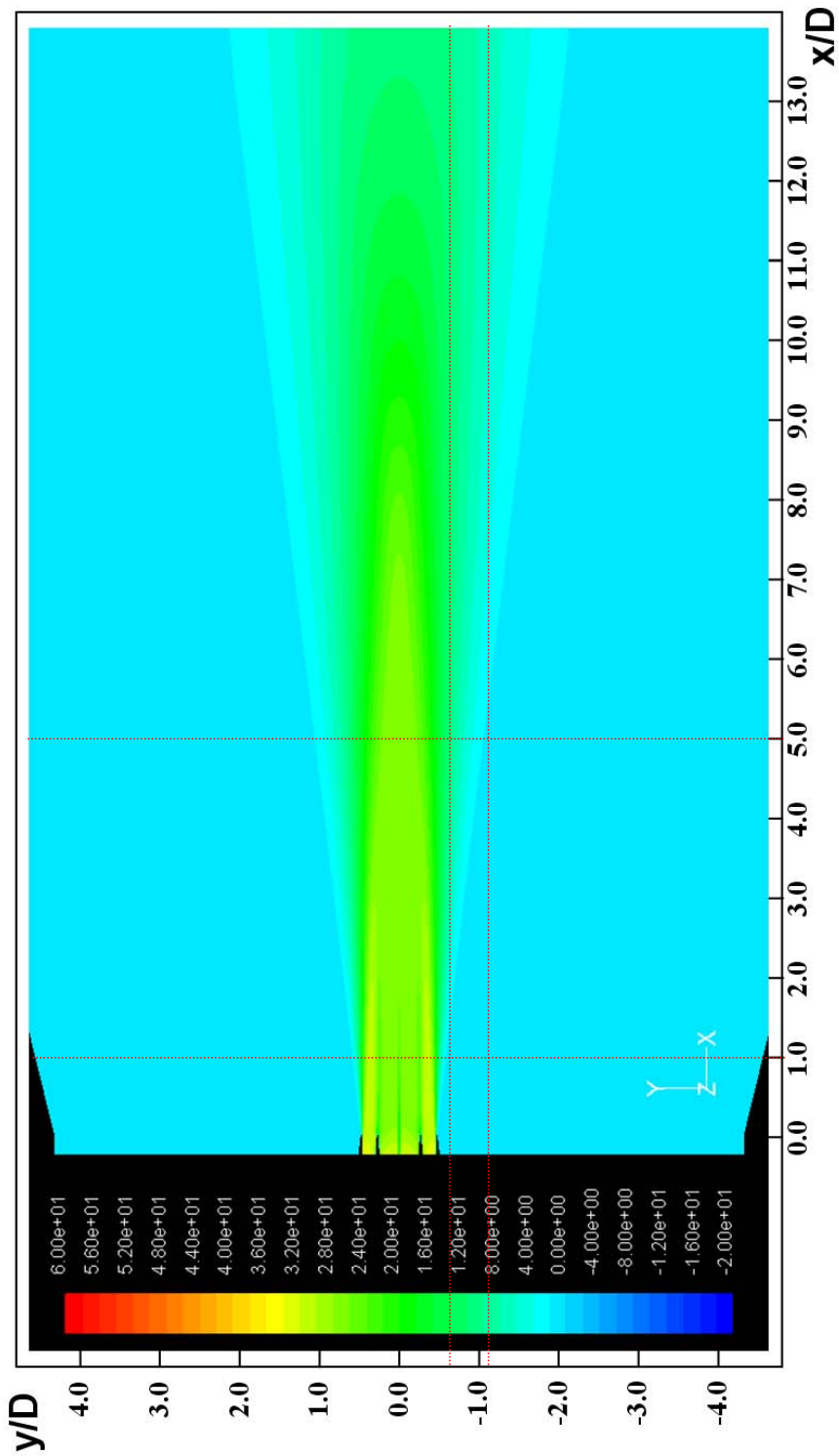
Figure 5.82 MODEL #01: Contour of axial velocity (u, m/s @ z-normal plane)
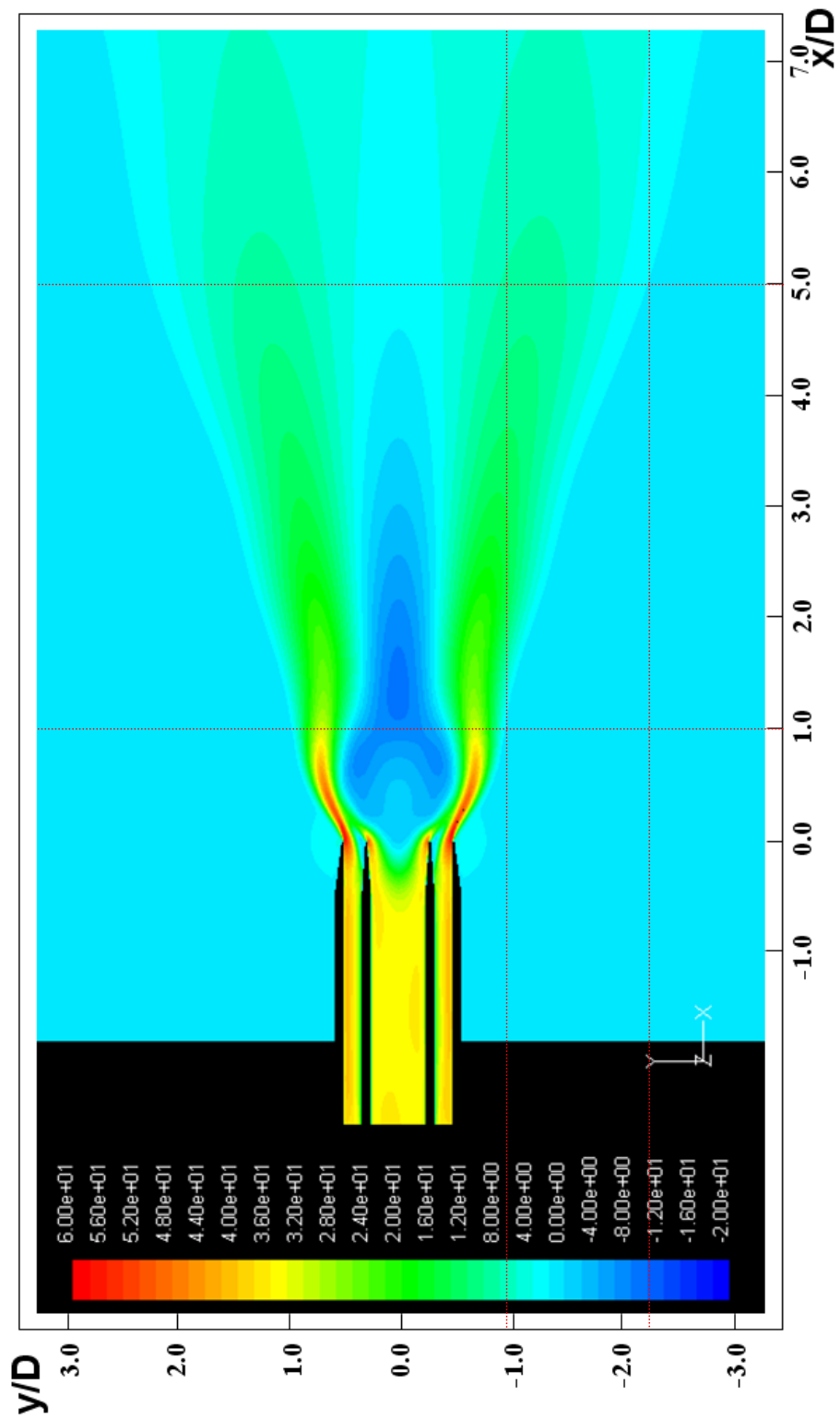
Figure 5.83 MODEL #03: Contour of axial velocity (u, m/s @ z-normal plane)
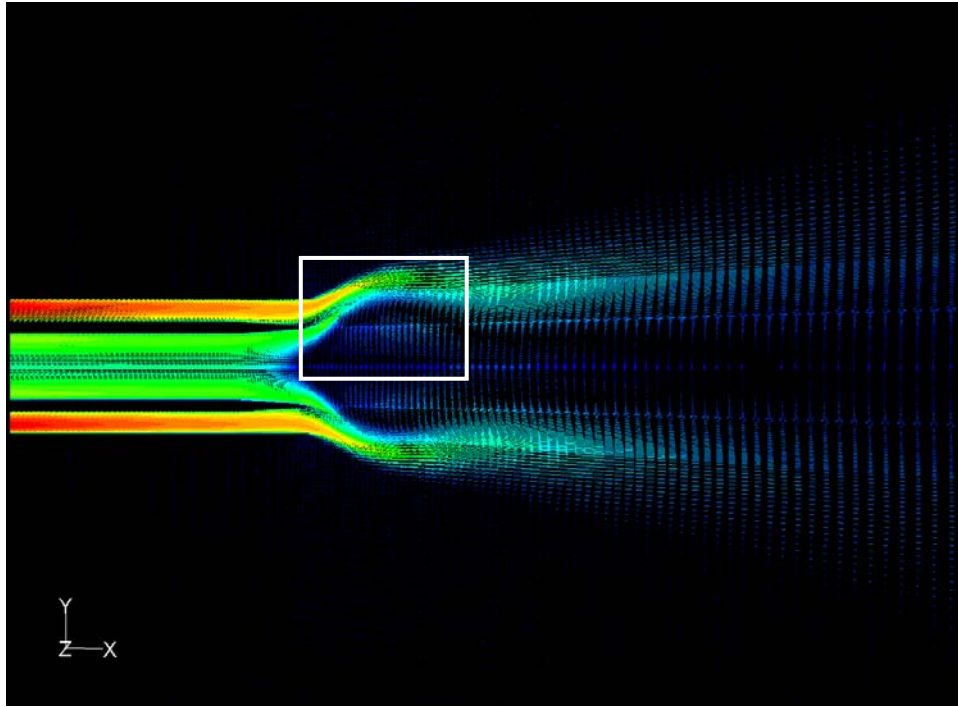
Figure 5.84 MODEL #03: Axial velocity vector profile of CTRZ
(@ z-normal plane)
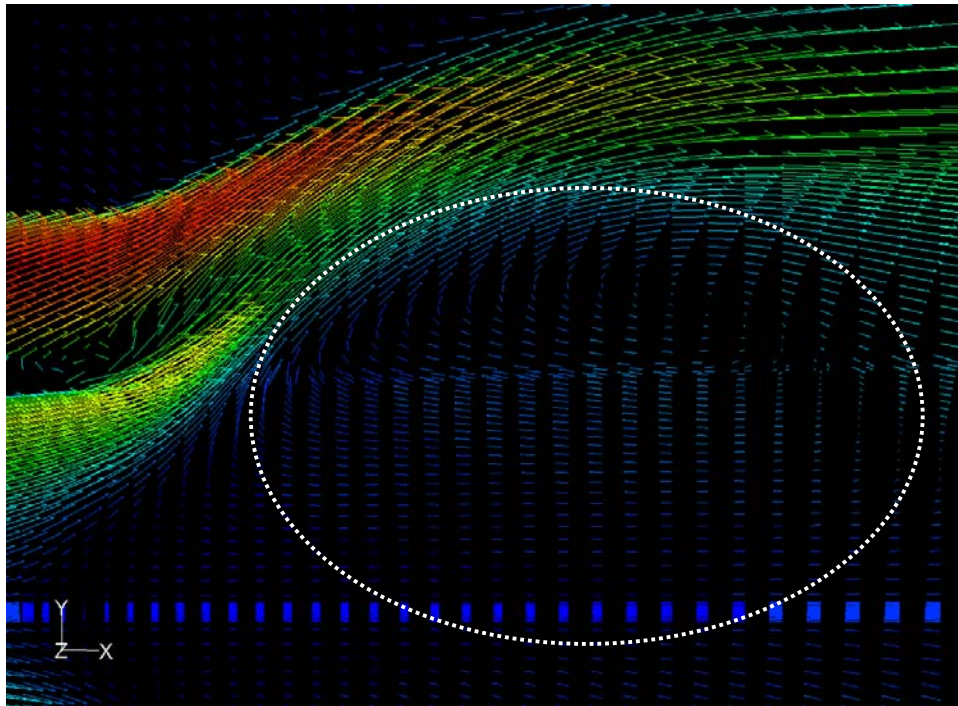
Figure 5.85 MODEL #03: Detailed view of CTRZ in Figure 5.84
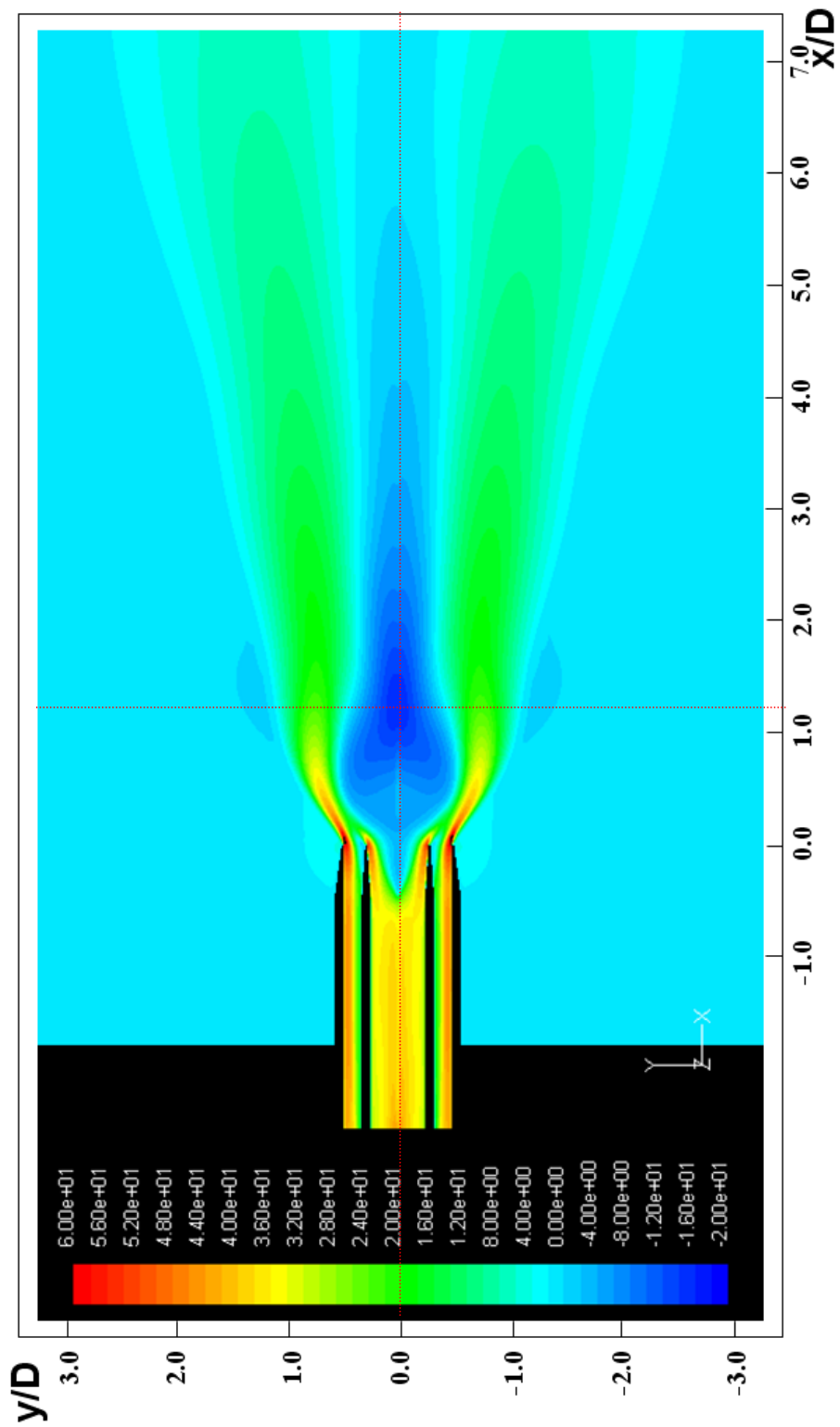
Figure 5.86 MODEL #04: Contour of axial velocity (@ z-normal plane)
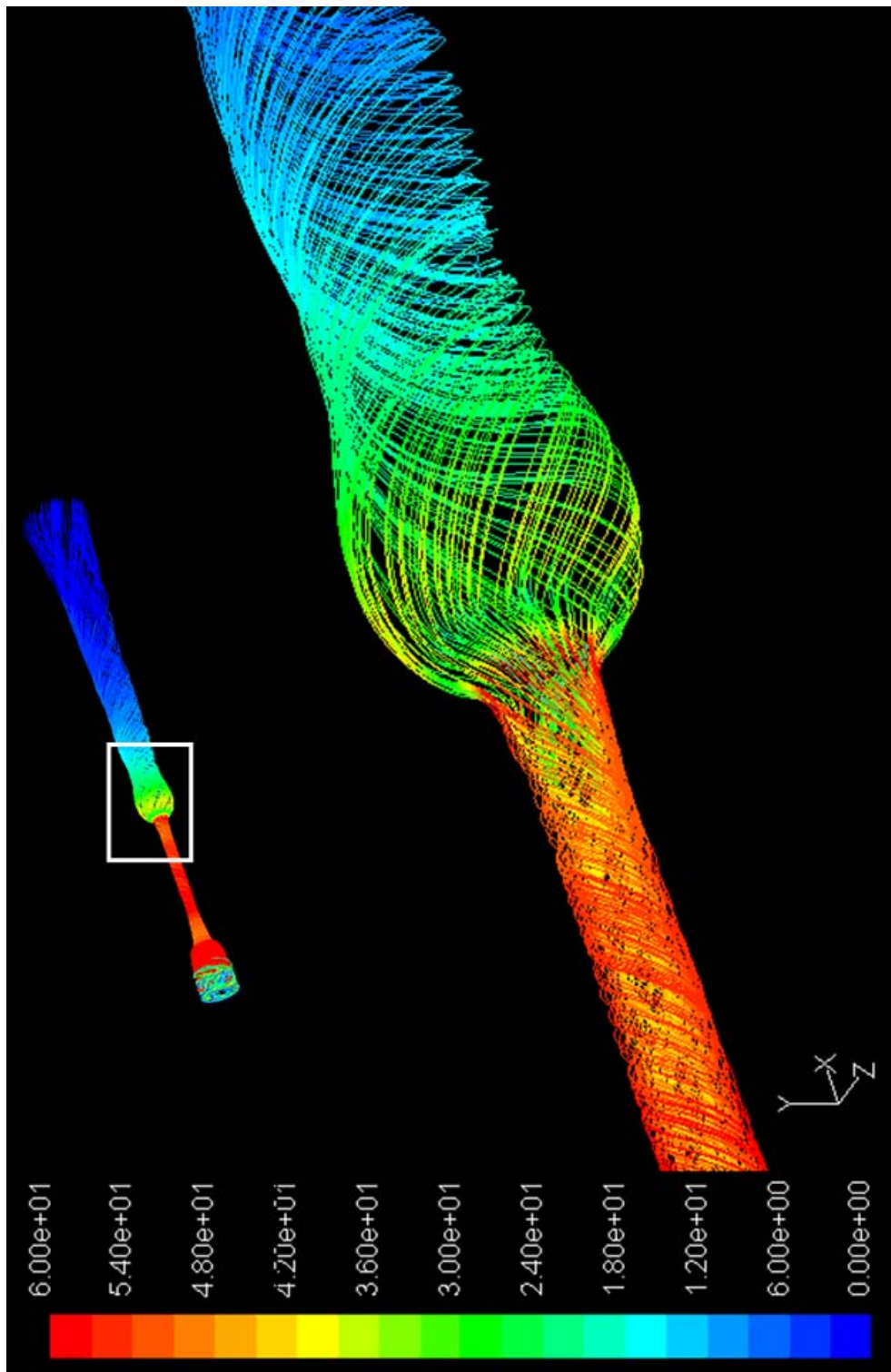
Figure 5.87 MODEL #04: Detailed path-line view around nozzle exit region (inner jet)

5.2.3. Velocity Distributions in Y- and Z-normal Planes

To explore the overall velocity distribution in the axial direction, the axial velocity component contours are plotted for various modes at z-normal (i.e., vertical) plane. A total of four negative helicity (h=-1, -2, -3, and -4) results is presented from the nozzle exit (i.e., x/D=0) to 'x/D=7'. Figures 5.88 through 5.91 show that all the cases have irregular patterns compared with the baseline (MODEL #03). Also, most of the cases show the increased jet boundary angle compared to the baseline's angle, except MODEL #09. The one helically-lobed case shows a highly distorted profile, and this shape has resulted from the combined influence of flow spinning and an eccentric helical perturbation (Figure 5.88). With the increasing number of lobes, the radial stretching effects of the jet boundary are intensified, but reverse effects are presented in the 'h=-4' case (MODEL #09, Figure 5.91). To avoid the possible biased view caused by asymmetric flow distribution, horizontal (i.e., y-normal) views are added in Figures 5.92 through 5.97. The further detailed velocity profile analyses, with some numeric values, will be presented in the next section, '5.2.4 Wave Propagation into Far Fields'.
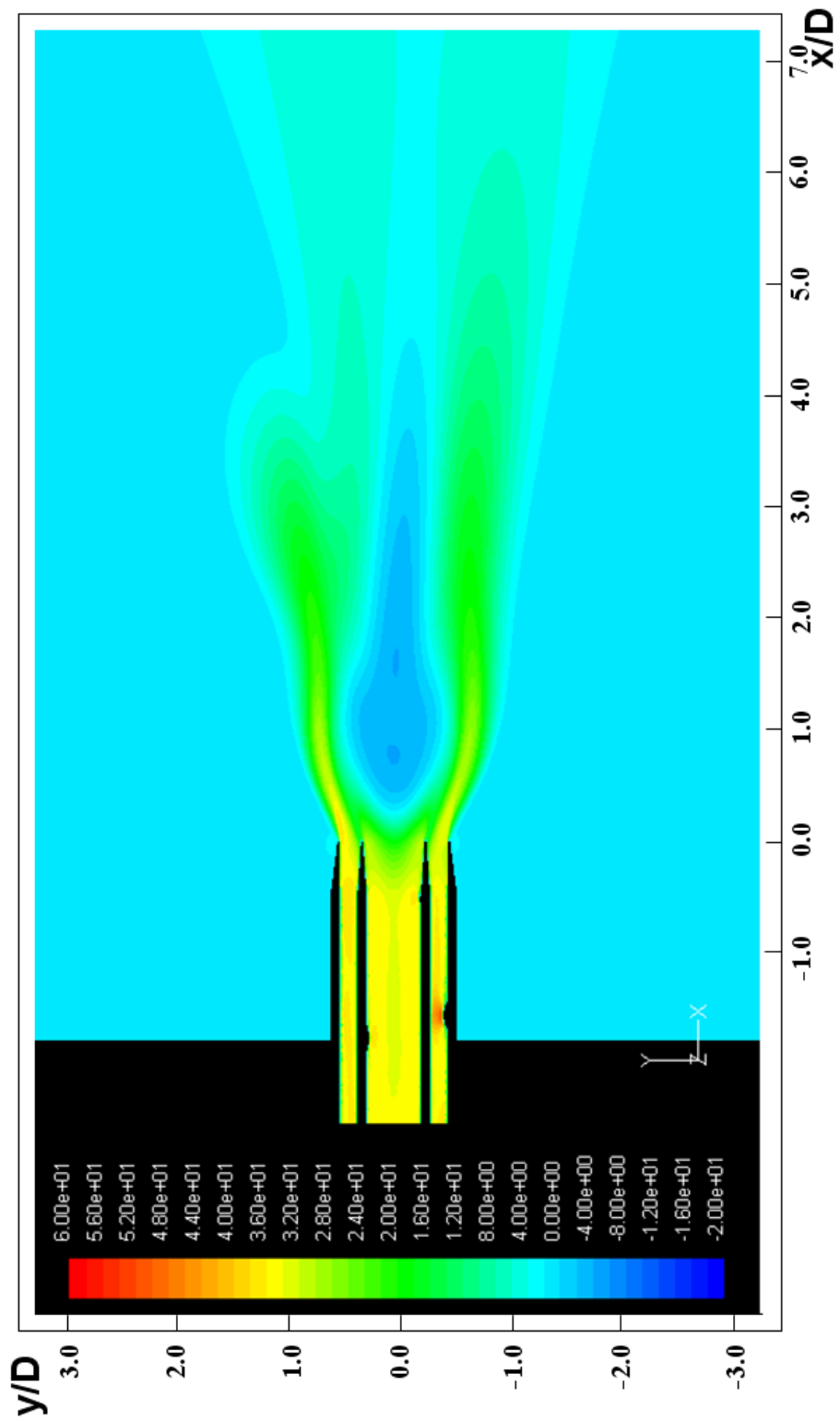
Figure 5.88 MODEL #05 (h=-1): Contour of axial velocity (@ z-normal plane)
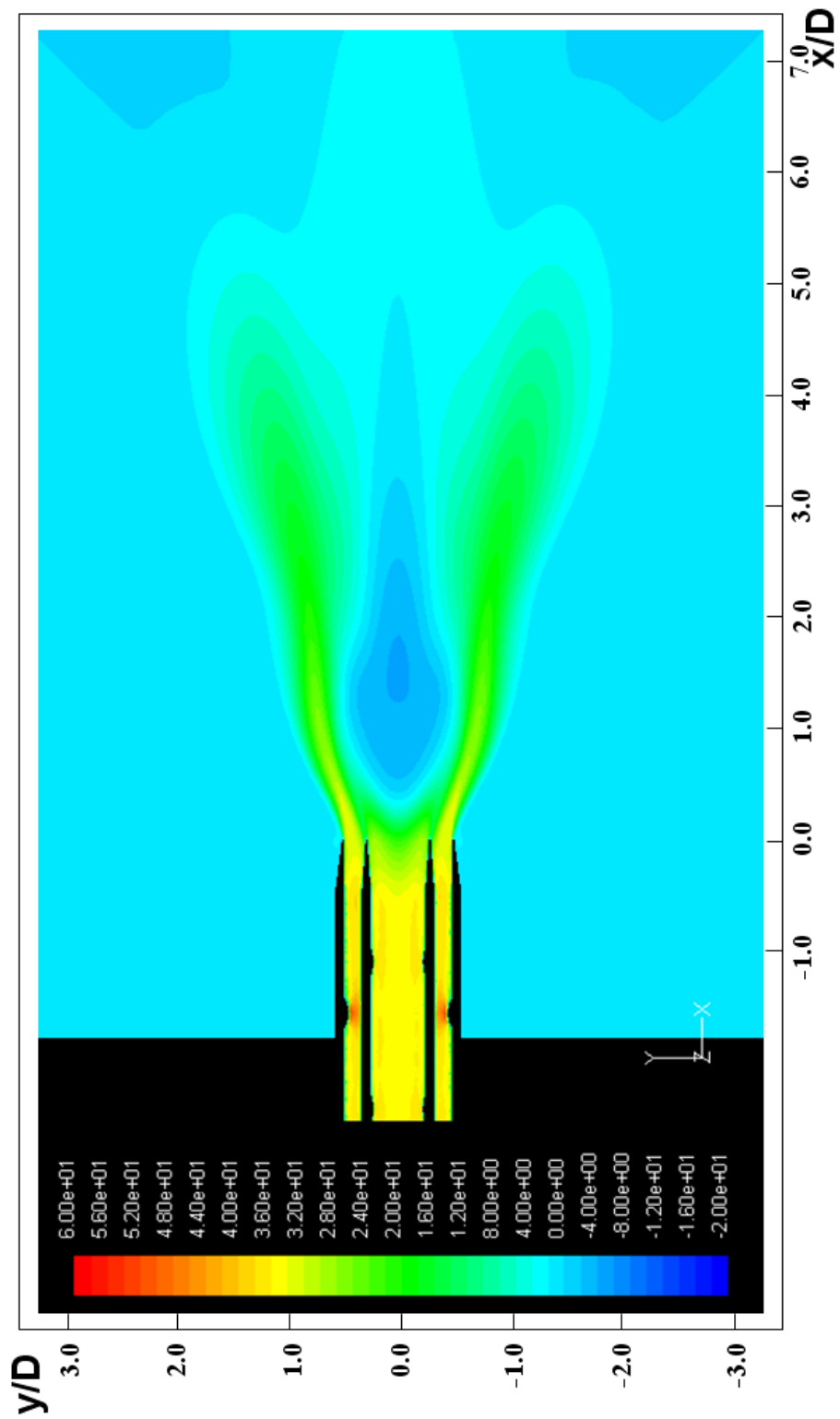
Figure 5.89 MODEL #06 (h=-2): Contour of axial velocity (@ z-normal plane)
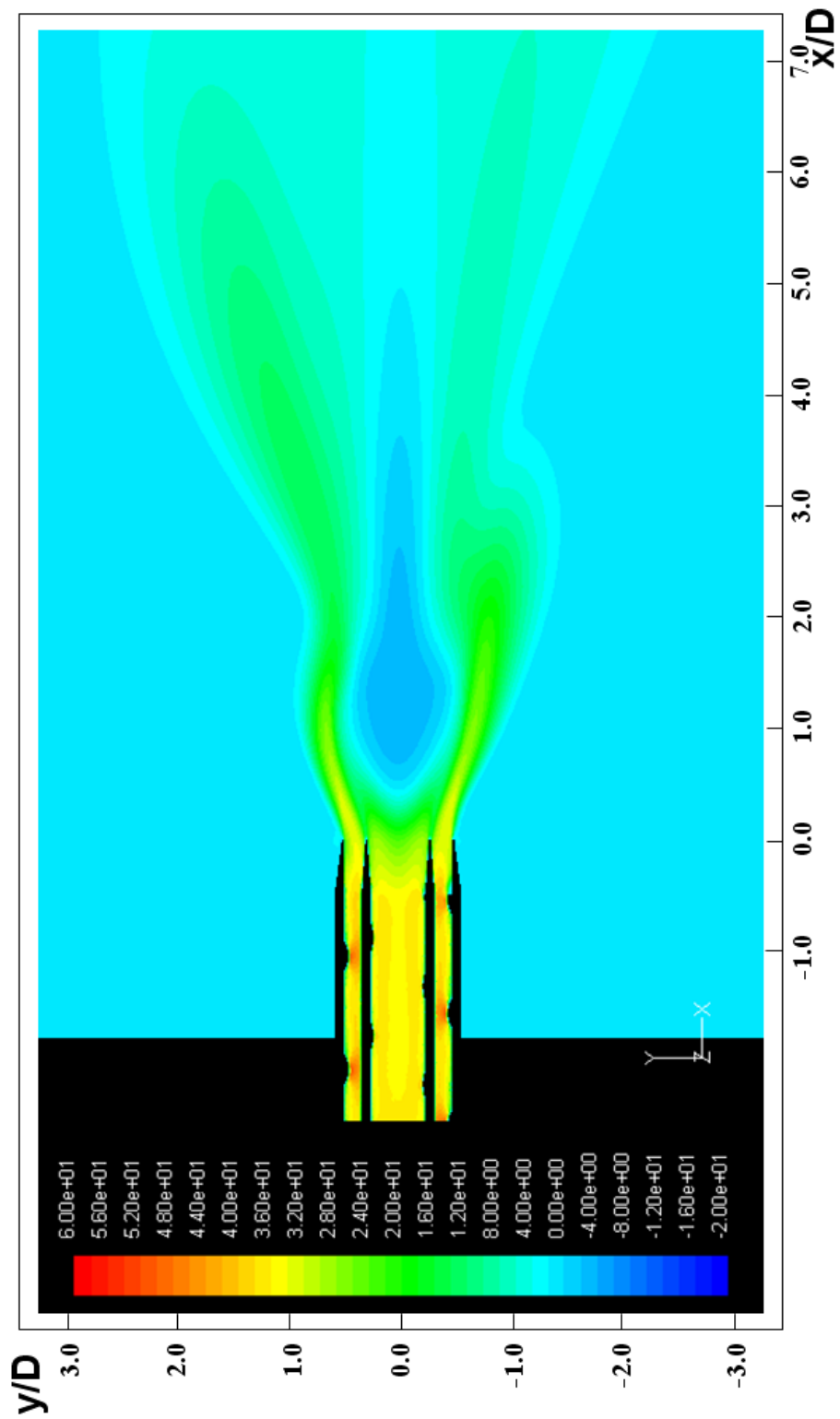
Figure 5.90 MODEL #08 (h=-3): Contour of axial velocity (@ z-normal plane)

Figure 5.91 MODEL #09 (h=-4): Contour of axial velocity (@ z-normal plane)
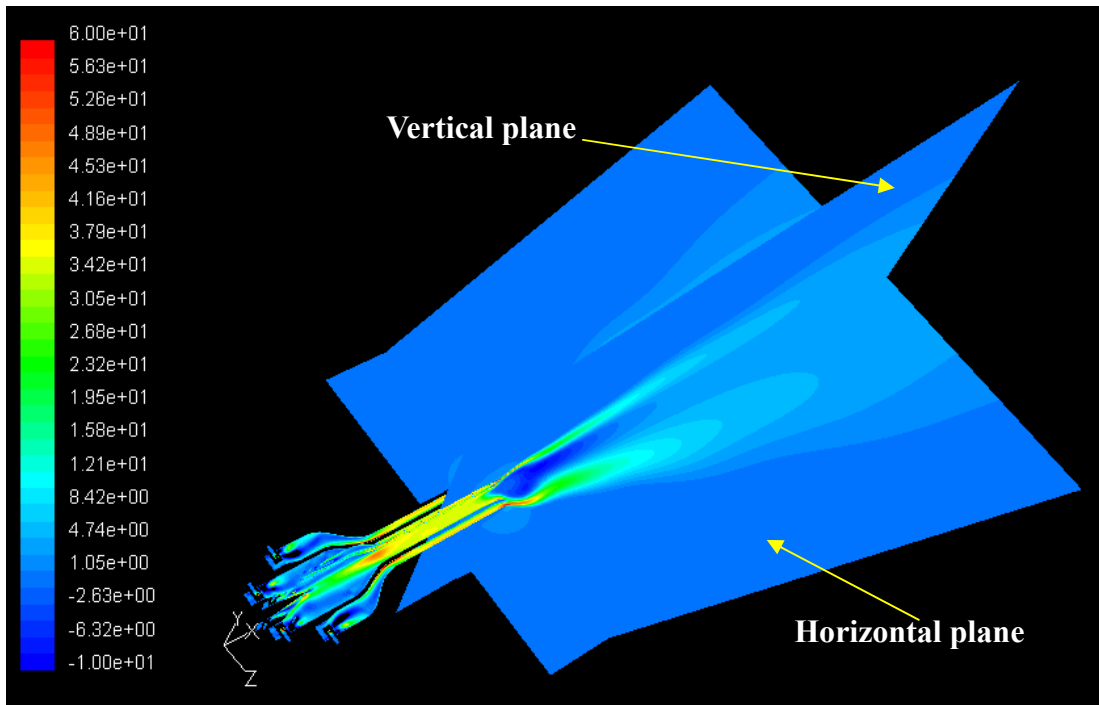
Figure 5.92 MODEL #03: Contour of axial velocity (m/s) in vertical (z-normal) and horizontal (y-normal) planes
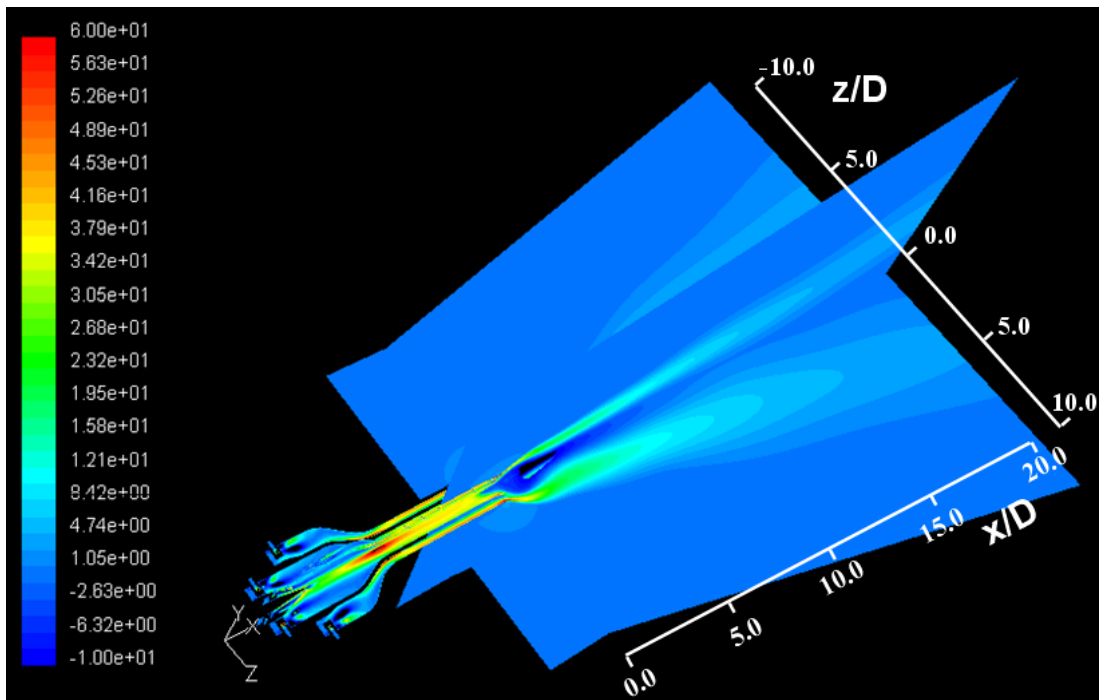
Figure 5.93 MODEL #04: Contour of axial velocity (m/s) in vertical (z-normal) and horizontal (y-normal) planes
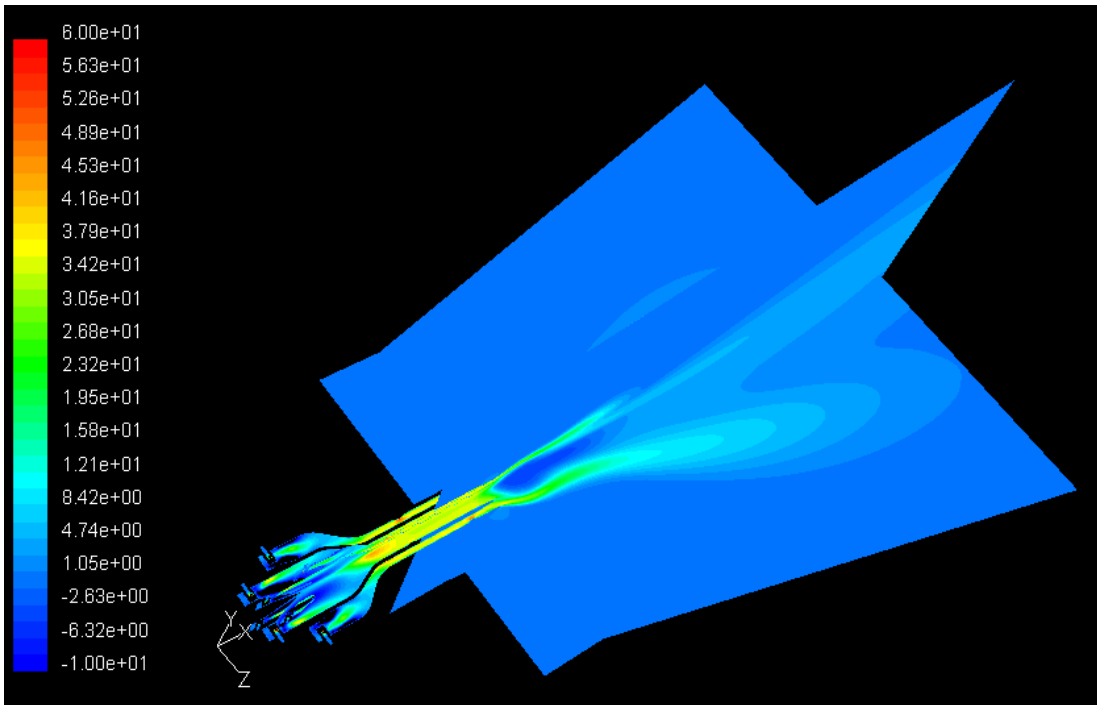
Figure 5.94 MODEL #05 (h=-1): Contour of axial velocity (m/s) in vertical (z-normal) and horizontal (y-normal) planes
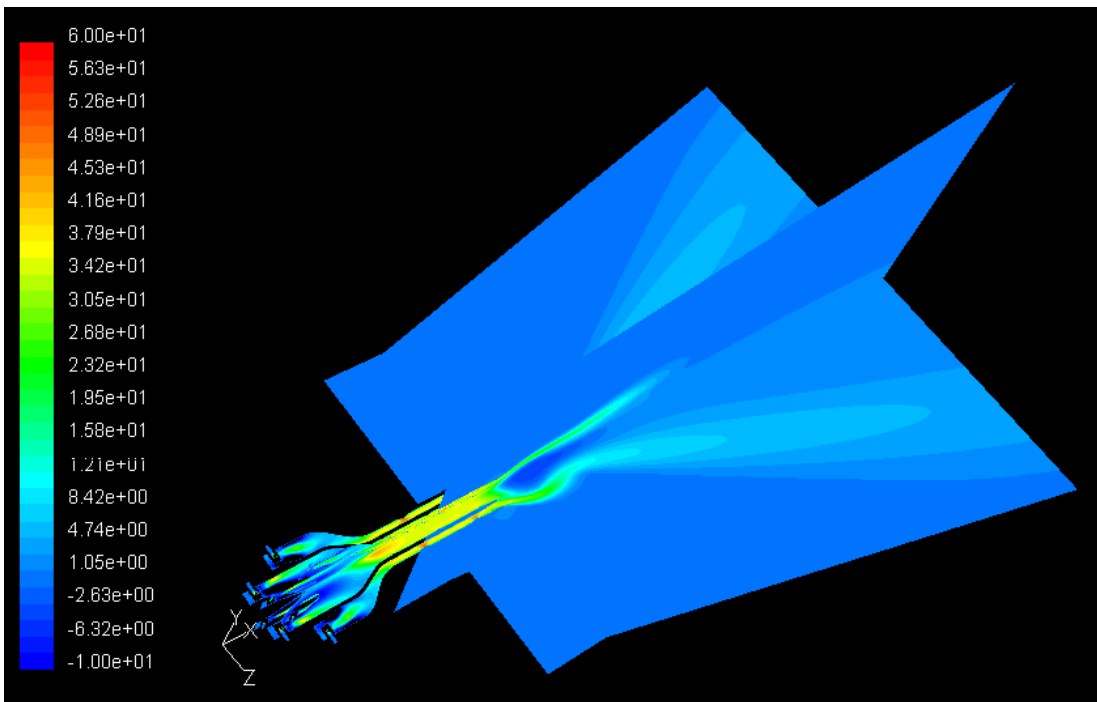
Figure 5.95 MODEL #06 (h=-2): Contour of axial velocity (m/s) in vertical (z-normal) and horizontal (y-normal) planes
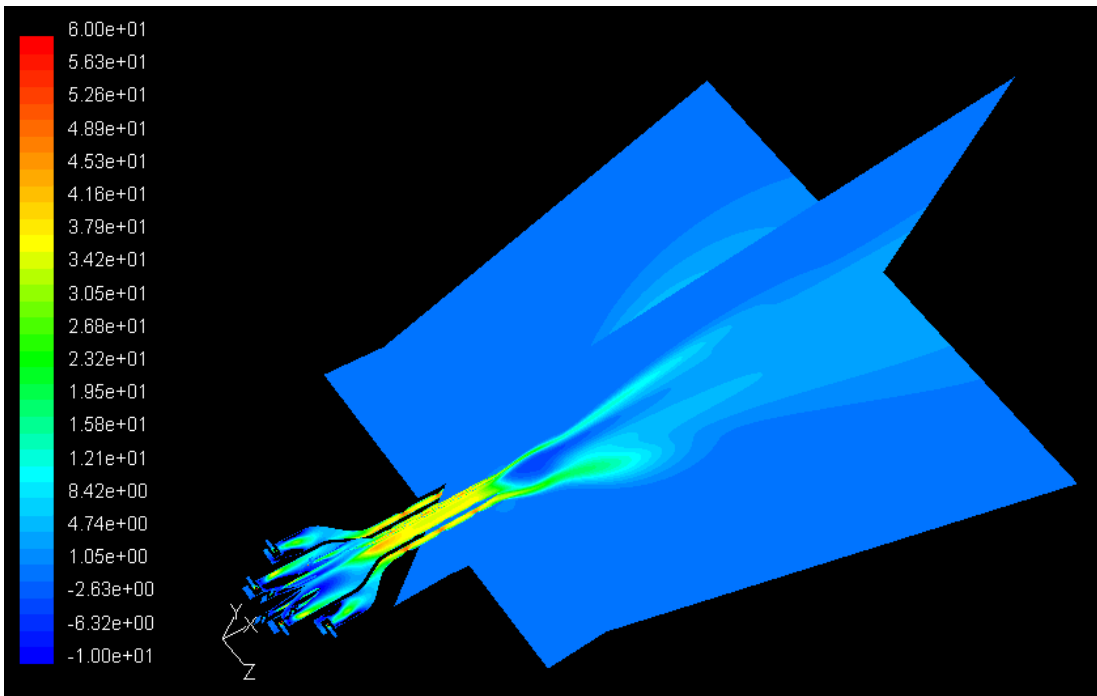
Figure 5.96 MODEL #08 (h=-3): Contour of axial velocity (m/s) in vertical (z-normal) and horizontal (y-normal) planes
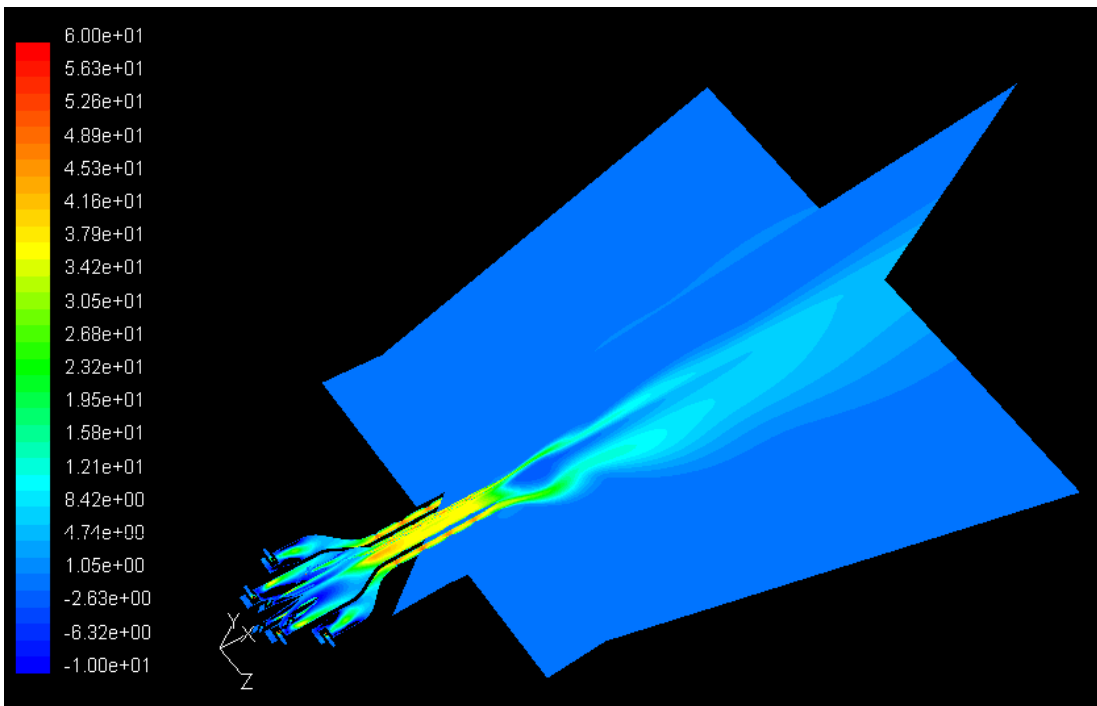
Figure 5.97 MODEL #09 (h=-4): Contour of axial velocity (m/s) in vertical (z-normal) and horizontal (y-normal) planes

5.2.4. Wave Propagation into Far Fields

The detailed u-velocity magnitude contours are generated on the various axial stations which are perpendicular to the x-axis from the nozzle exit to downstream (Figures 5.98 to 5.109). The effects of excitation on the velocity are seen instantly via the contour levels, and especially the transformed jet periphery shape of the axial velocity field corresponds to the number of lobes. Considering the jet boundary, the maximum distance of each simulation is compared to one another at the 'x/D=6' station. The baseline (MODEL #03) shows that the maximum distance from the center (i.e., y/D=z/D=0) to the '1.2m/s' contour line is approximately 4 (=r/D, Figure 5.99(d)). The other cases are as follows; 'r/D=4.4' for 'h=-1', 'r/D=4.9' for 'h=-2', 'r/D=4.3' for 'h=-3', and 'r/D=3.4' for 'h=-4' (ref. Figures 5.103(d), 5.105(d), 5.107(d), and 5.109(d)). Corresponding to the z-normal plane results, with an increasing number of lobes, the radial stretching effects of the jet boundary are fortified up to 'h=-3' compared to the baseline. On the other hand, the effects vanish, and are even quenched in the 'h=-4' case (MODEL #09). In this analysis, the second negative helicity (h=-2) shows the maximum spreading effect, and the length of

maximum distance from center is raised by approximately 23% compared to the

baseline.
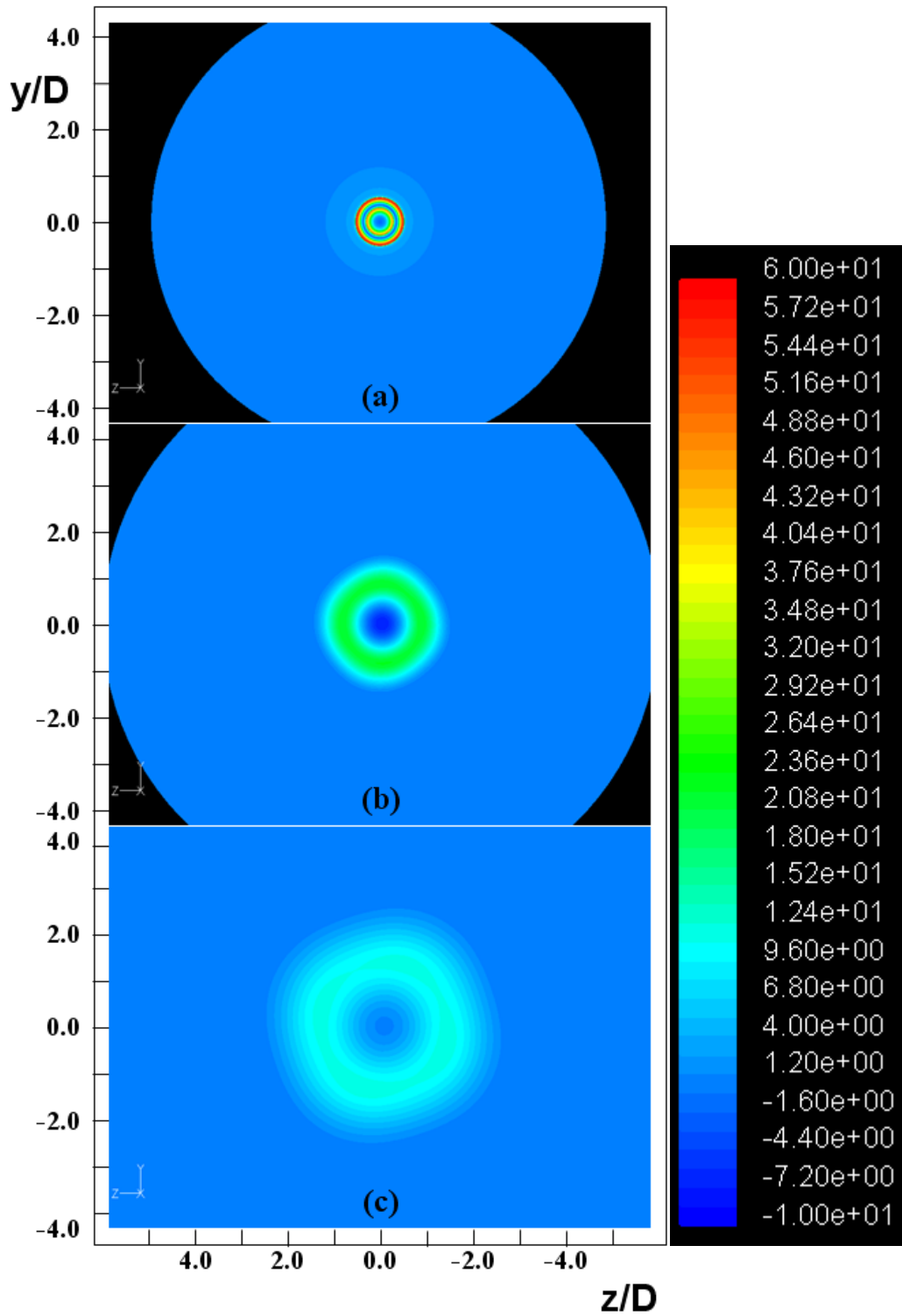
Figure 5.98 MODEL #03: Contour of axial velocity (m/s) at various stations (a) x/D=0 (b) x/D=2 (c) x/D=4
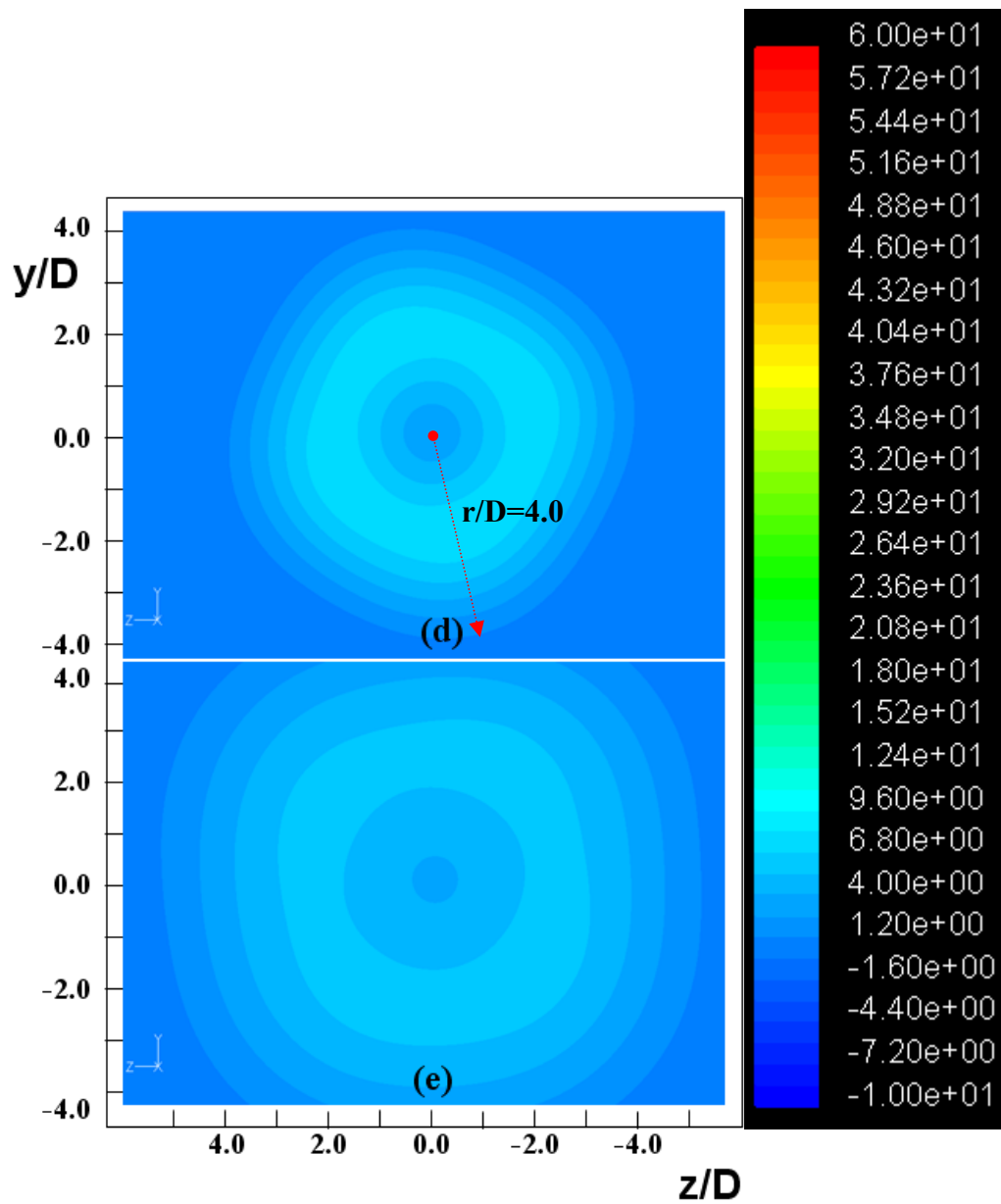
Figure 5.99 MODEL #03: Contour of axial velocity (m/s) at various stations (d) x/D=6 (e) x/D=8
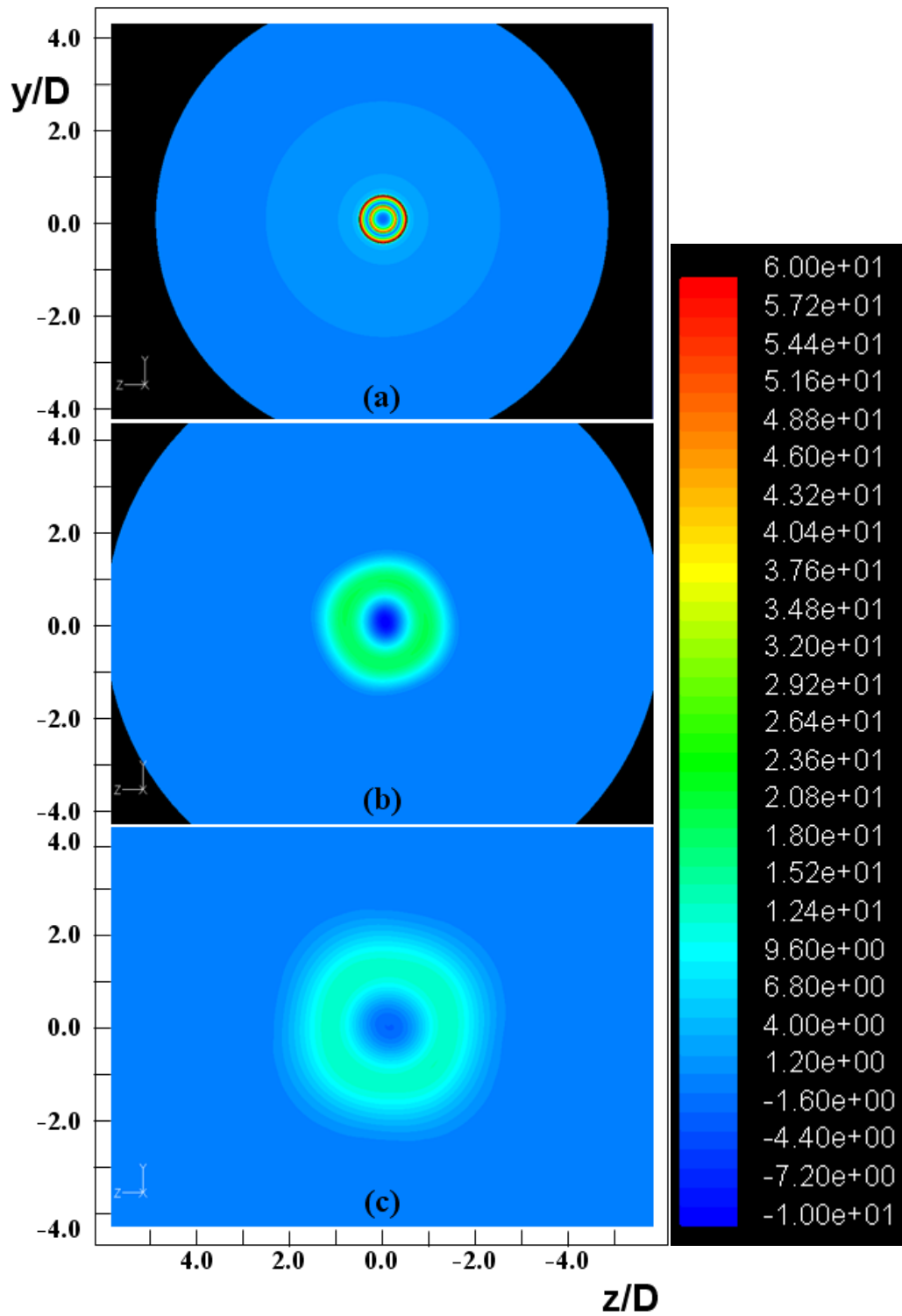
Figure 5.100 MODEL #04: Contour of axial velocity (m/s) at various stations
(a) x/D=0 (b) x/D=2 (c) x/D=4

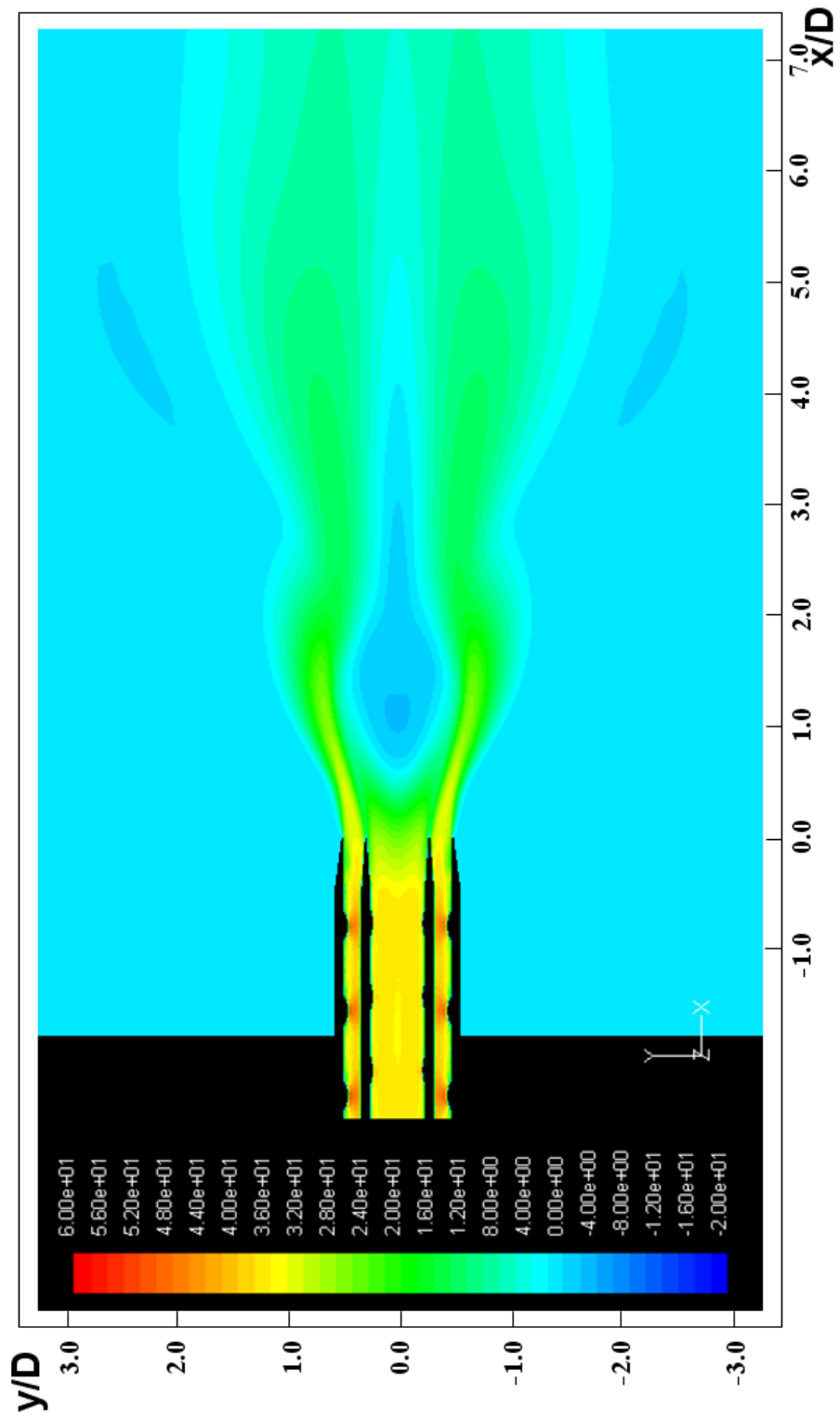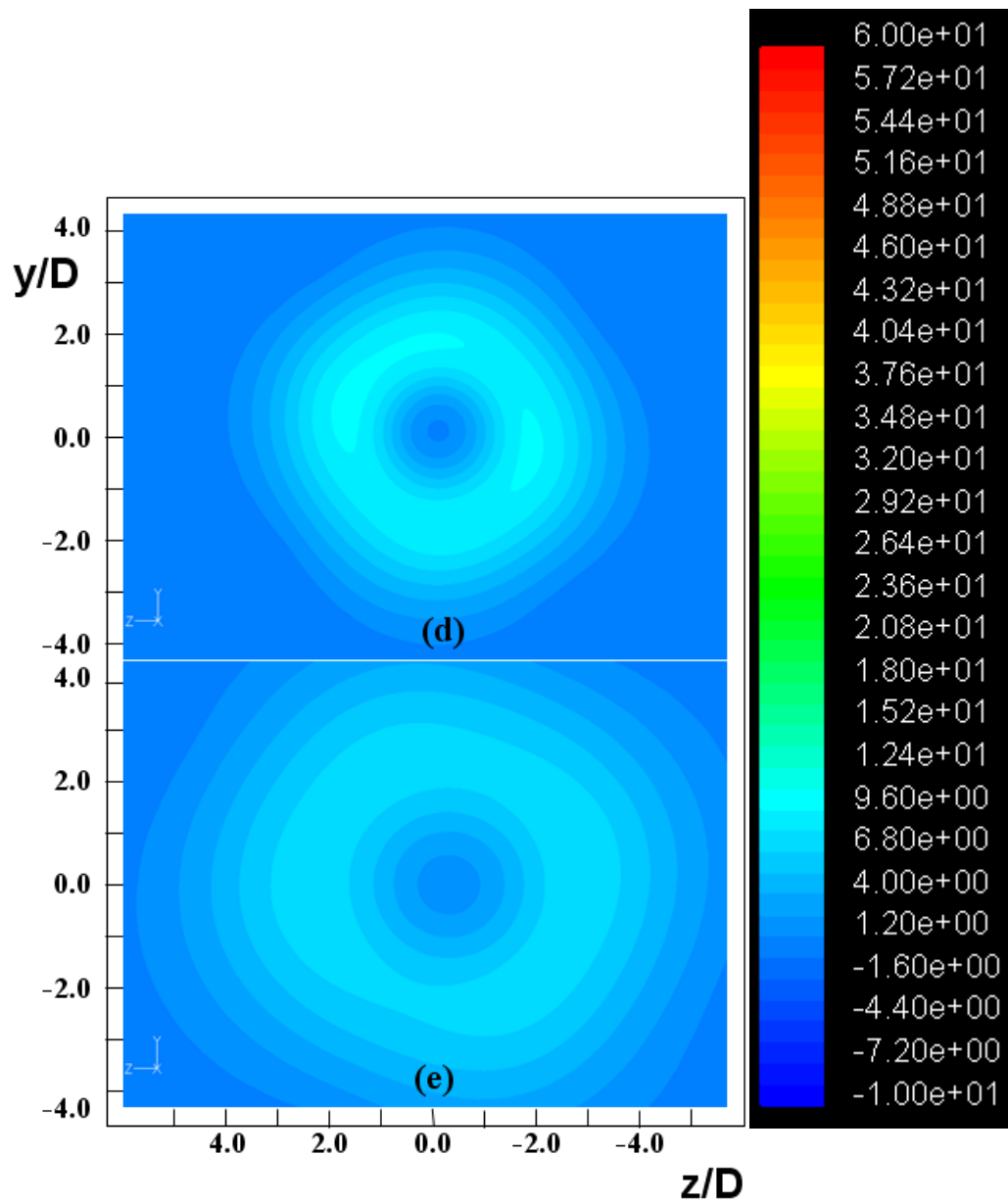**Figure 5.101 MODEL #04: Contour of axial velocity (m/s) at various stations (d) x/D=6 (e) x/D=8**
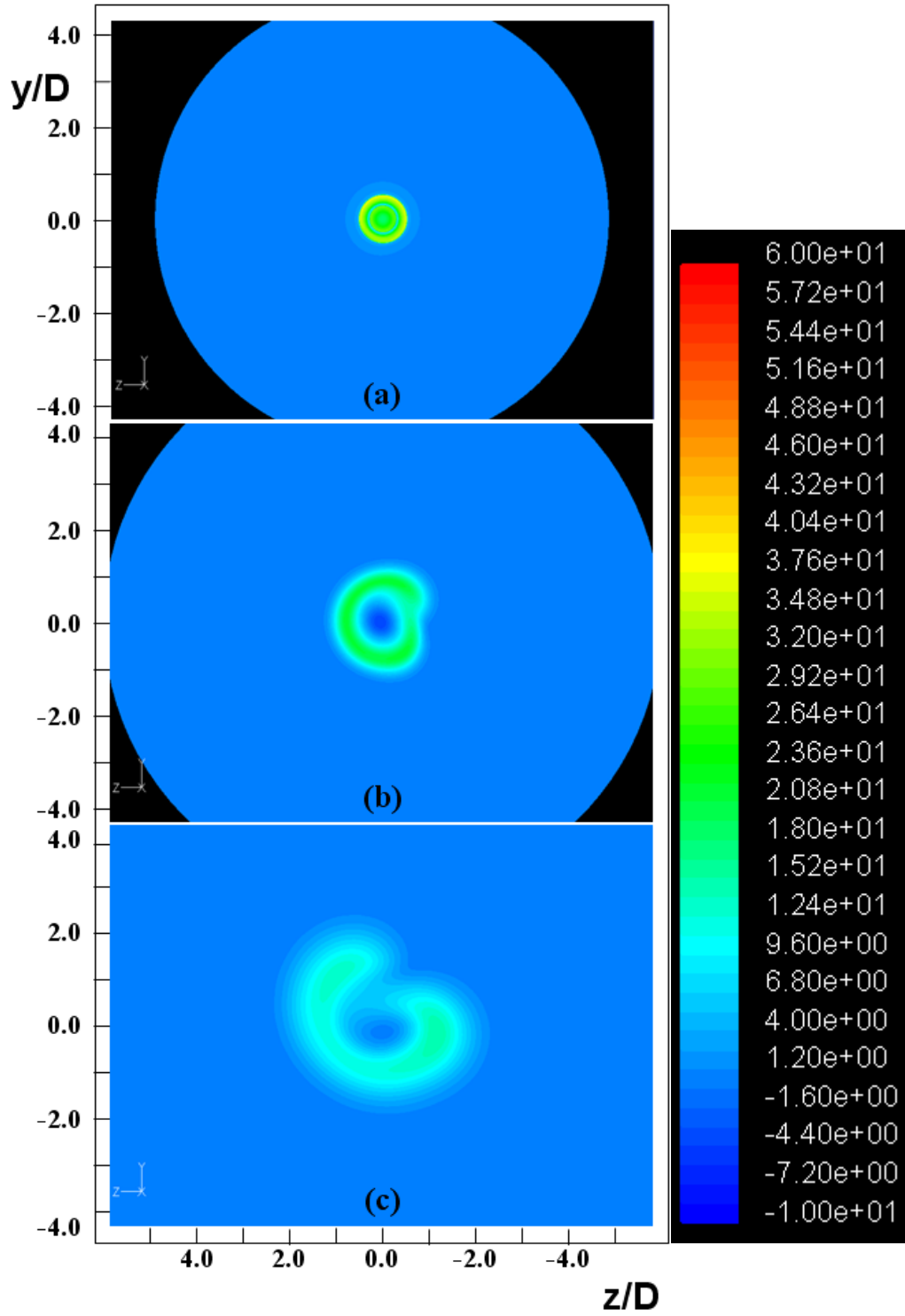
Figure 5.102 MODEL #05 (h=-1): Contour of axial velocity (m/s) at various stations (a) x/D=0 (b) x/D=2 (c) x/D=4
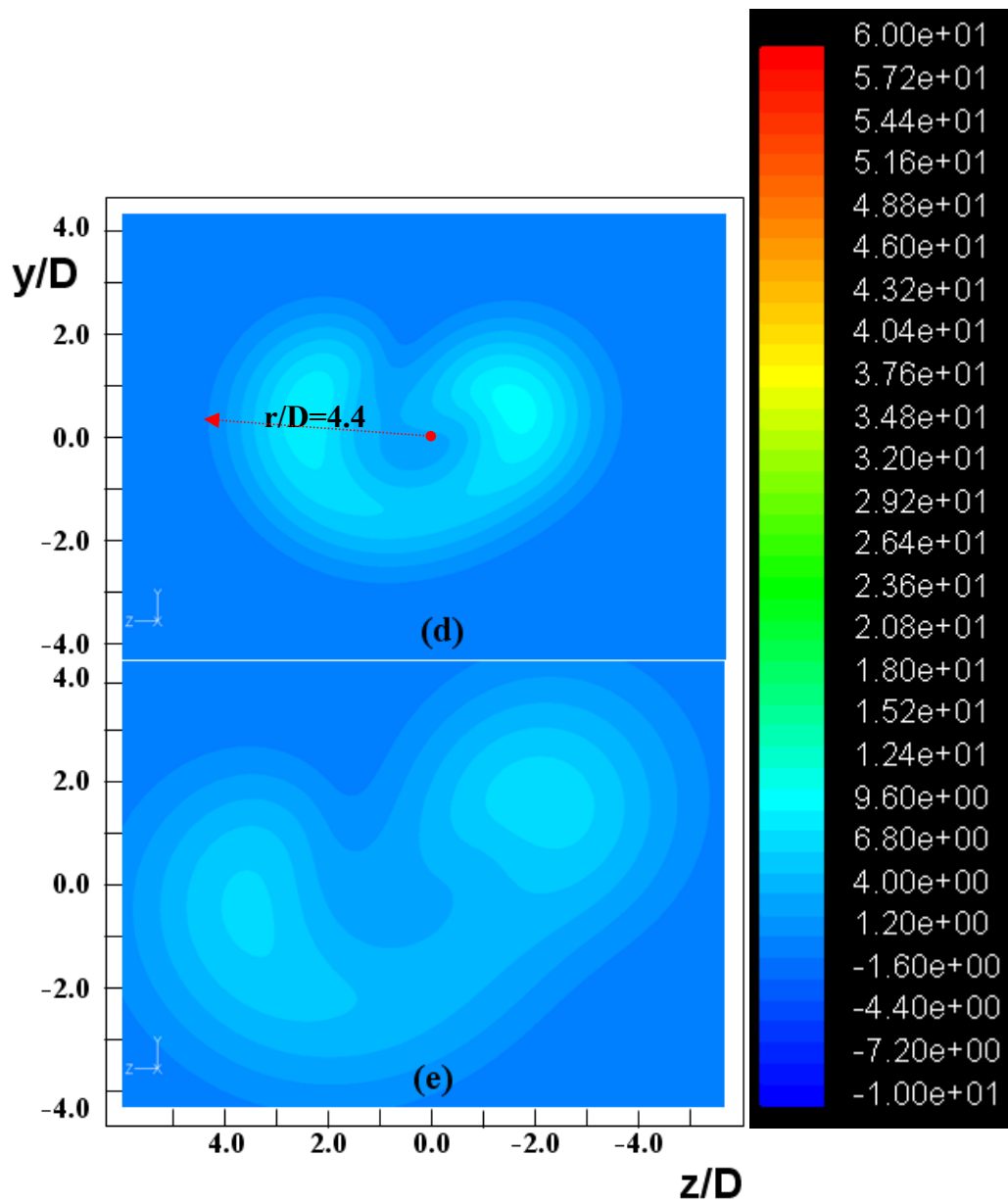
Figure 5.103 MODEL #05 (h=-1): Contour of axial velocity (m/s) at various stations (d) x/D=6 (e) x/D=8
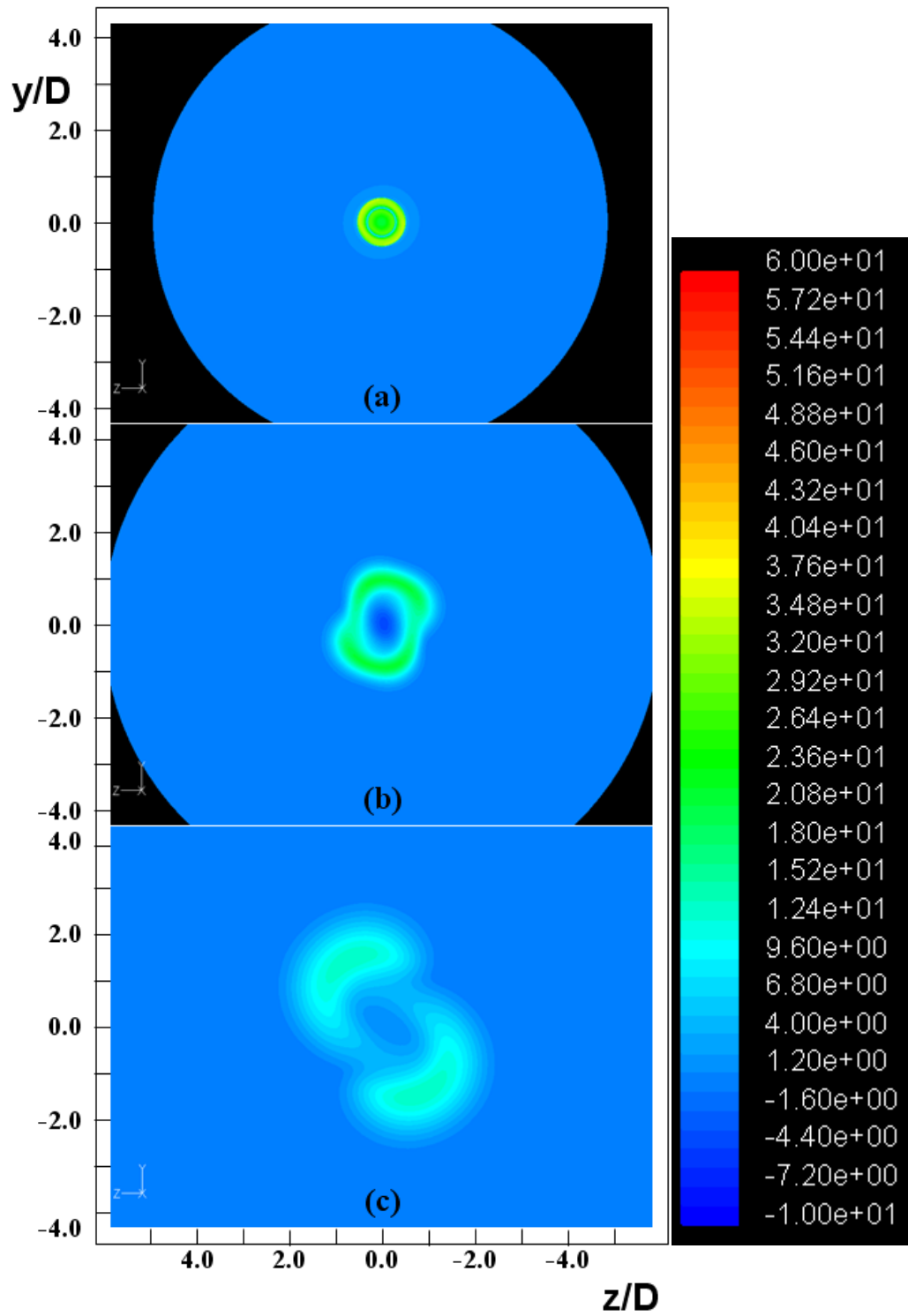
Figure 5.104 MODEL #06 (h=-2): Contour of axial velocity (m/s) at various stations (a) x/D=0 (b) x/D=2 (c) x/D=4
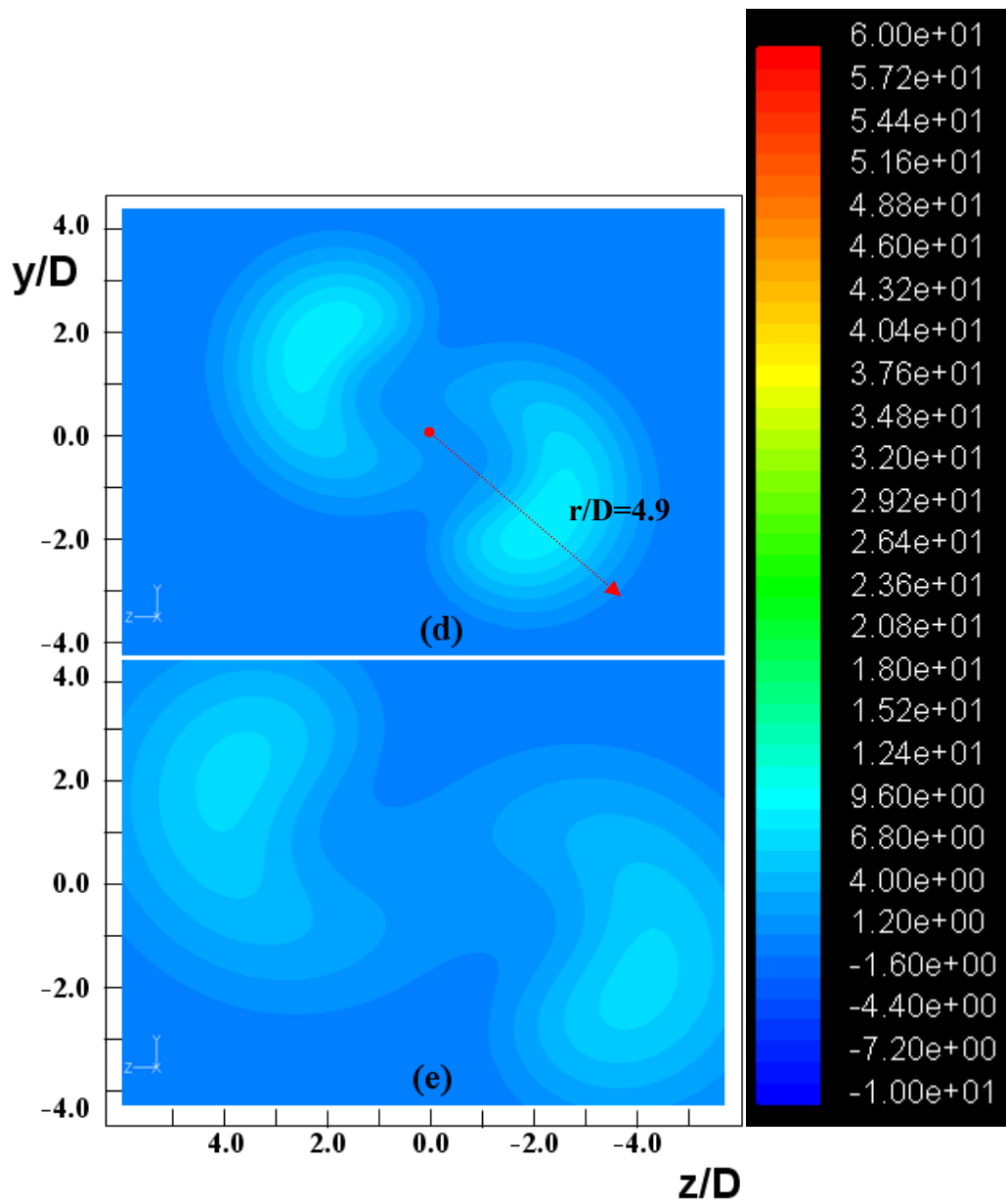
Figure 5.105 MODEL #06 (h=-2): Contour of axial velocity (m/s) at various stations (d) x/D=6 (e) x/D=8
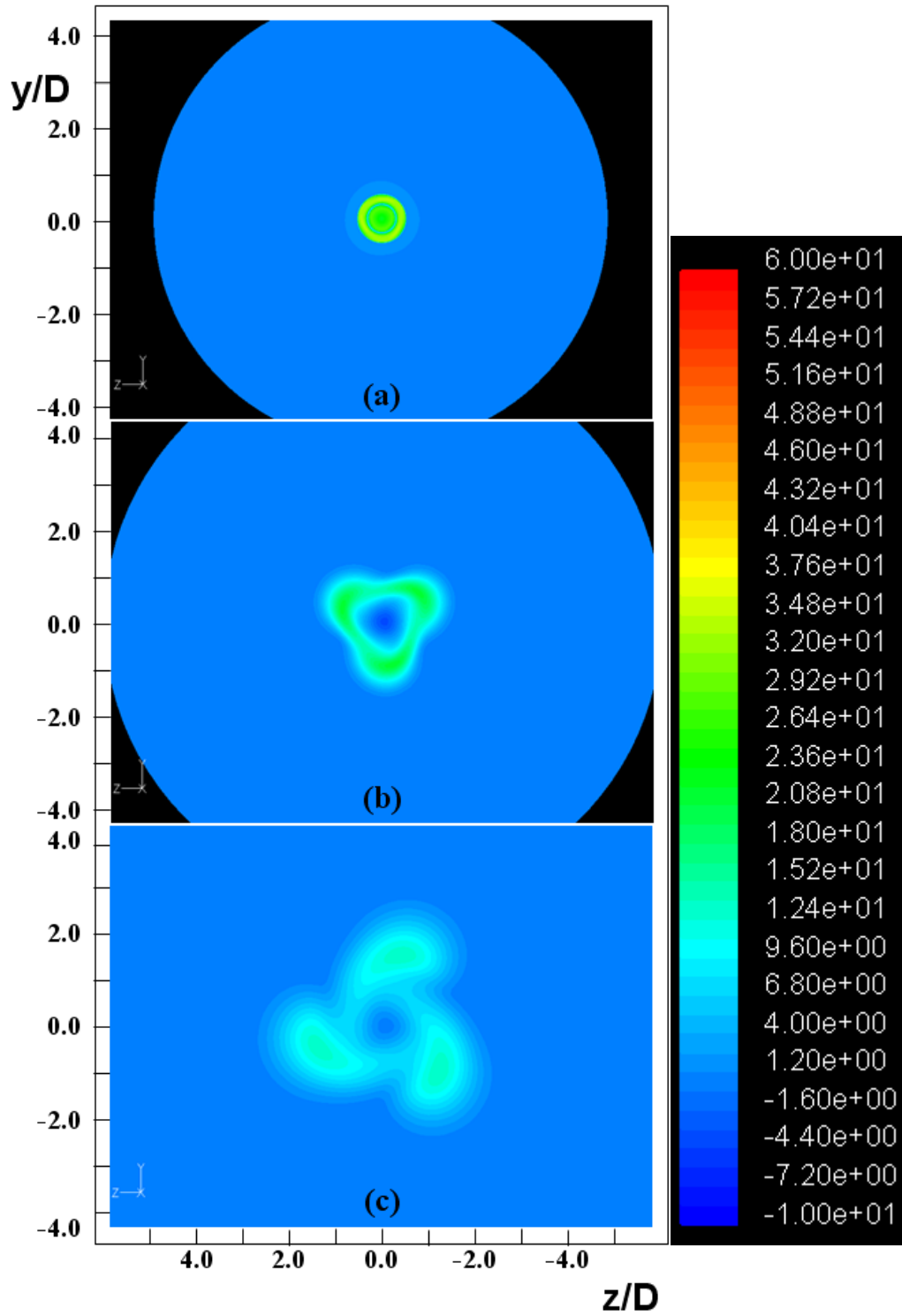
Figure 5.106 MODEL #08 (h=-3): Contour of axial velocity (m/s) at various stations (a) x/D=0 (b) x/D=2 (c) x/D=4
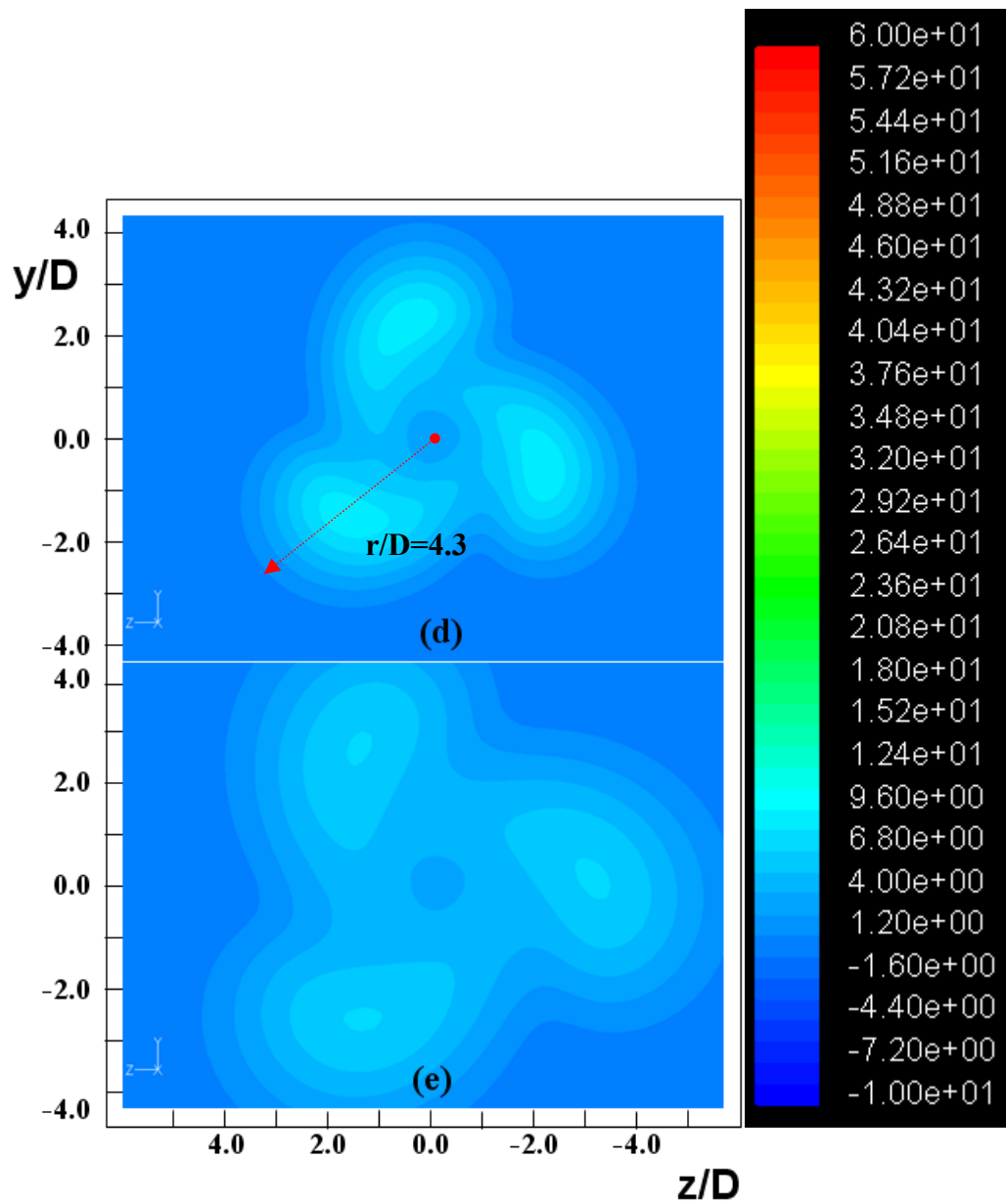
Figure 5.107 MODEL #08 (h=-3): Contour of axial velocity (m/s) at various stations (d) x/D=6 (e) x/D=8
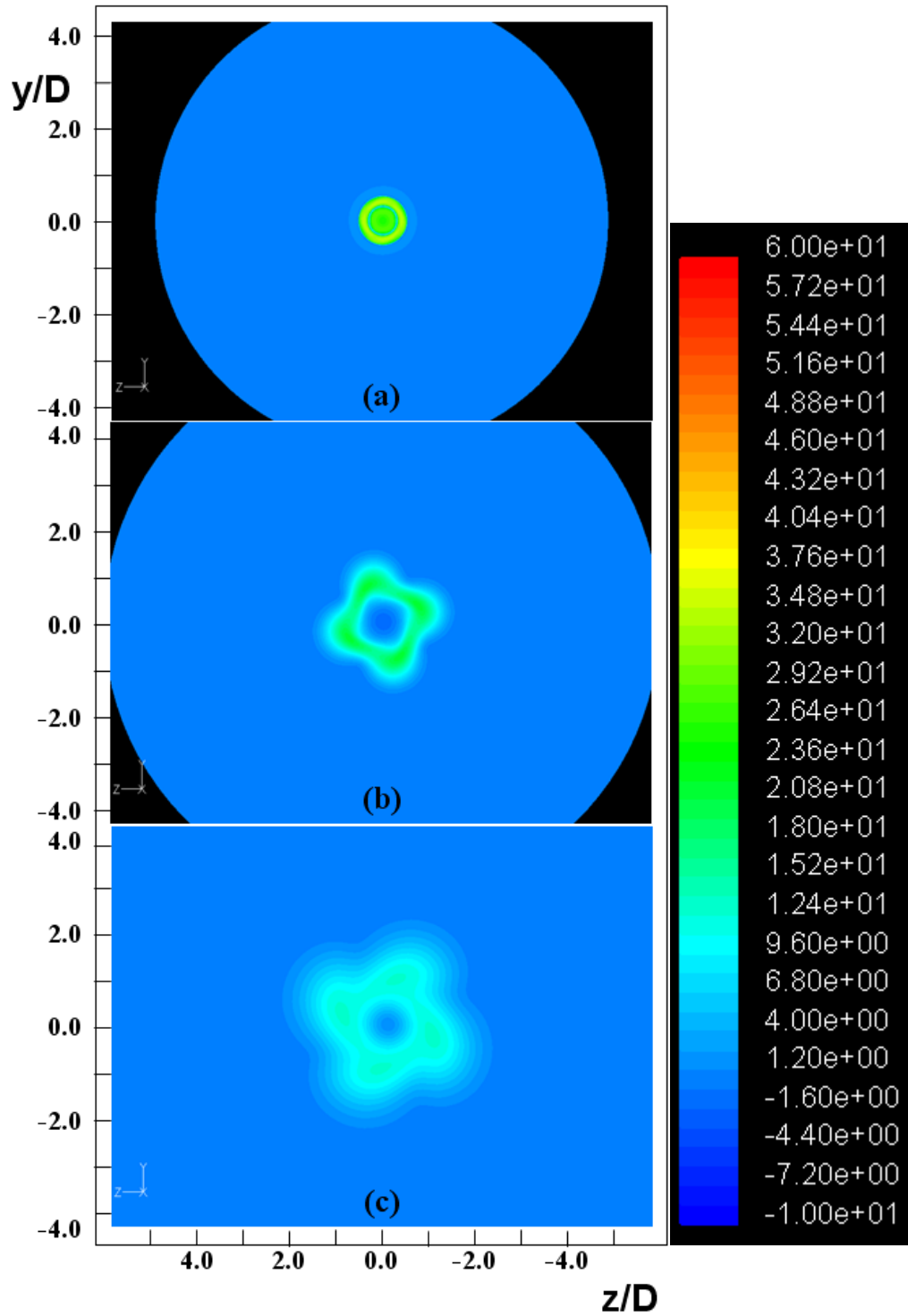
Figure 5.108 MODEL #09 (h=-4): Contour of axial velocity (m/s) at various stations (a) x/D=0 (b) x/D=2 (c) x/D=4
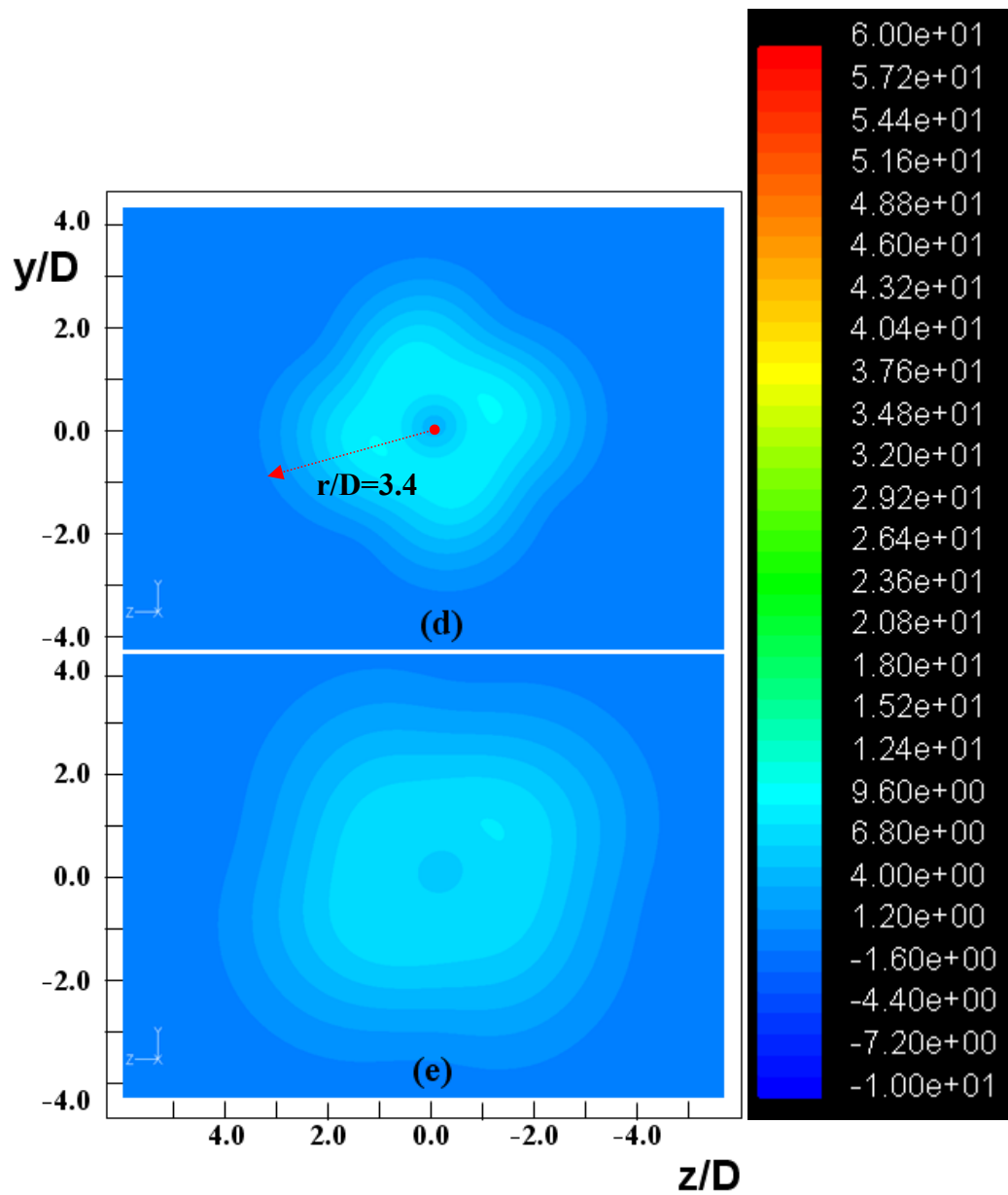
Figure 5.109 MODEL #09 (h=-4): Contour of axial velocity (m/s) at various stations (d) x/D=6 (e) x/D=8

5.2.5. Trace of Particles

To acquire a better understanding from flow motion and mixing phenomena in a cubic effect, the path-line plots of injected particles from swirl generators are illustrated up to x/D=20. The presented plots (Figures 5.110 through 5.124) are categorized in two parts, according to the locations from which the particles are released (i.e., outlet of outer- or inner-swirl injectors). From this approach, two kinds of mixing phenomena are observed. One is between the inner- and outer-swirl flow, and the other one is between the outer-swirl flow and free stream.

Once the swirl effects are implemented (MODEL #03, Figures 5.111 and 5.112), the spiral behavior is observed in both inner and outer jets. Even though the swirl effects are applied, the particles themselves do not spread out in a radial direction in both jets. With the one-lobe perturbed case (h=-1, Figure 5.116), only the outer-swirl flow spreads out compared to the near exit region, as it moves towards the axial direction. The most remarkable effects (i.e., mixing) are shown in 'h=-2' in both the inner and outer jets (Figures 5.117 and 5.118). In this case, flow expands more widely in a radial direction than in any other cases, and a relatively small

amount of particles stays at the core. Furthermore, due to the effective angular momentum exchange between the jets and their surroundings (i.e., ambient air), the 'h=-2' case shows that rotational energy dissipates simultaneously. These are noticeable shear control effects distinguished from the baseline characteristics. This analysis reveals the mixing enhancement between the outer-swirl flow and environment, and shows the maximum diffusion angle, too. This result also implies that the mixing enhancement effects exist between outer- and inner-swirl flows, which are not present in their counterparts.

On the contrary, the 'h=-3' case shows the reduced effects in both jets compared to the two-lobed condition (Figures 5.119 and 5.120). If the helicity is raised up to 'h=-4', the jet expansion angle is even reduced compared to the baseline as the particles traverse in the axial direction (Figures 5.121 and 5.122). As a result, the preferable helicity for mixing enhancement is regarded as 'h=-2' in this analysis, and the effects, however, are decreased when 'h=-4' is applied. To avoid the reverse effects (i.e., less effective than the baseline), finding a preferred mode that can produce maximum mixing effects should be considered.

To investigate the environmental flow behavior around the jet exit, Figures

5.123 and 5.124 are illustrated. Particles that are numerically released from the linear line at 'x/D=1, y/D=0' travel to the downstream area, influenced by the jet's main stream. In the baseline model, the trace instantly shows the existence of strong entrainment effects at the near exit, and the particles accelerated gradually as they moved down to the far fields with a spinning motion (Figure 5.123).

On the other hand, when the 'h=-2' mode is applied, the entrained particles travel into the free stream with maximum dispersion, and, simultaneously, the angular motion almost vanishes instead (Figure 5.123). These noticeable phenomena reveal that the second negative helicity contributes to the flow entrainment and the wide penetration and fast mixing into ambient air.
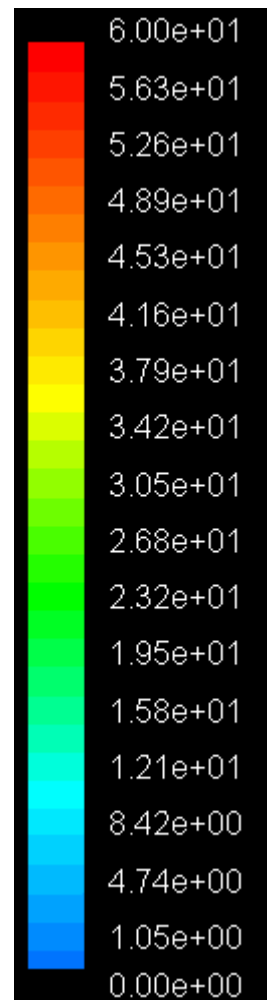
**Figure 5.110 Legend for Figures 5.111 through 5.122
(colored by velocity magnitude, m/s)**
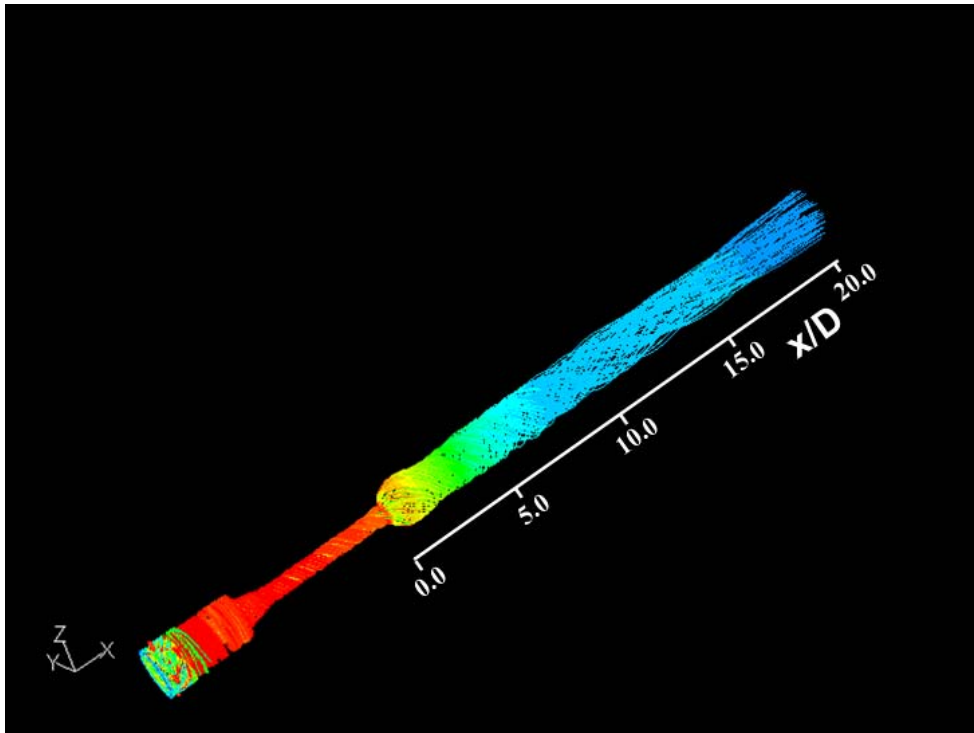
Figure 5.111 MODEL #03: Trace of particles from swirl injectors (inner)
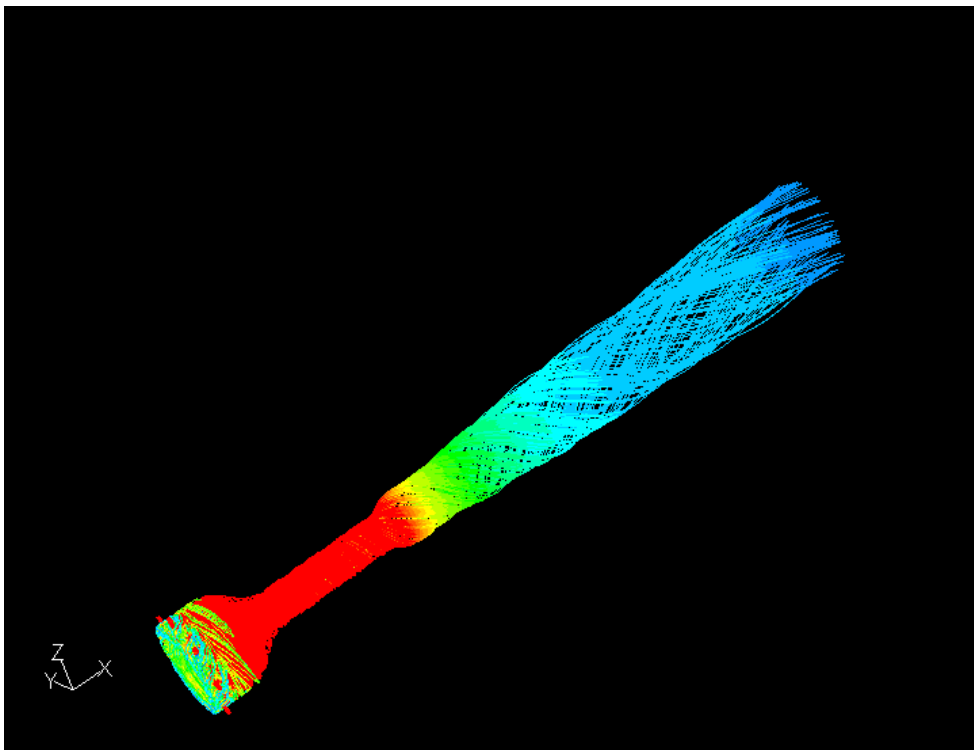
Figure 5.112 MODEL #03: Trace of particles from swirl injectors (outer)
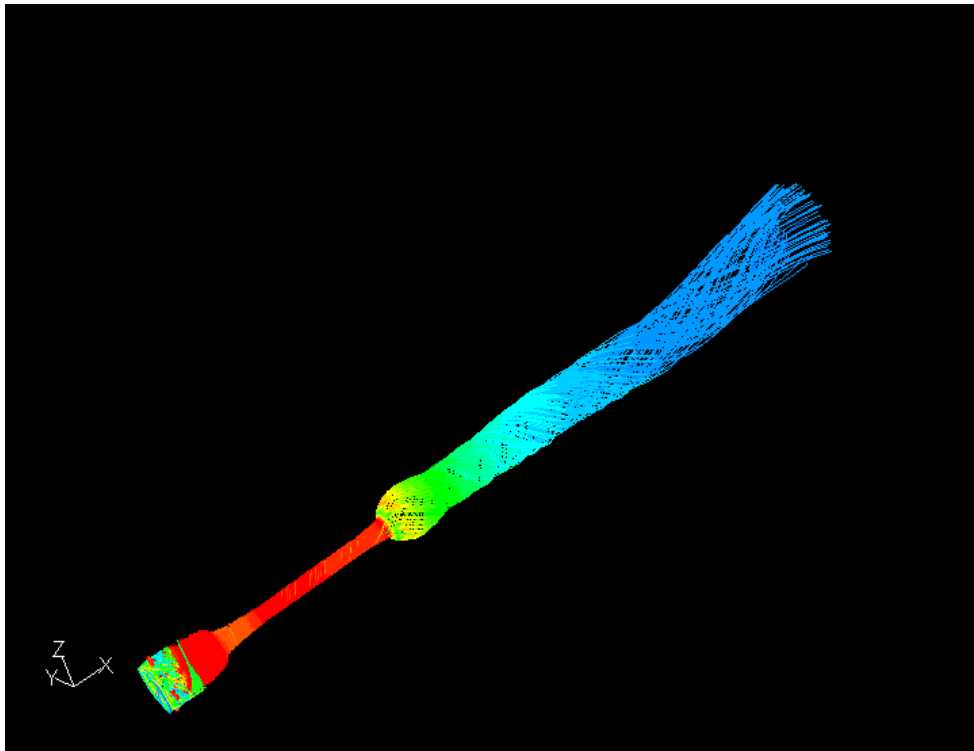
Figure 5.113 MODEL #04: Trace of particles from swirl injectors (inner)
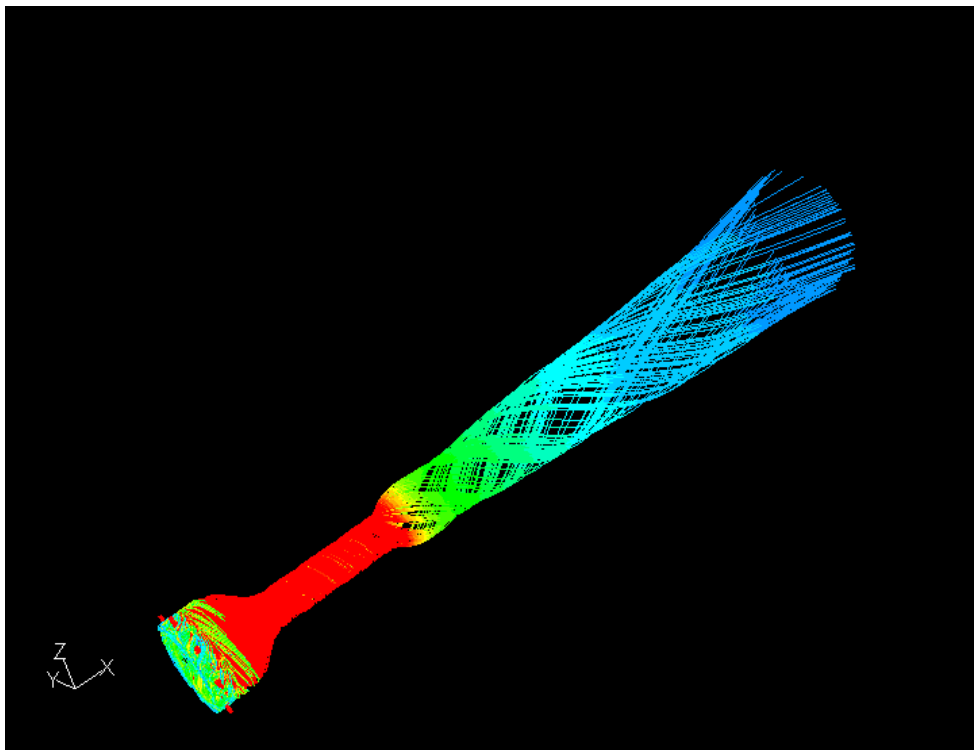
Figure 5.114 MODEL #04: Trace of particles from swirl injectors (outer)

232
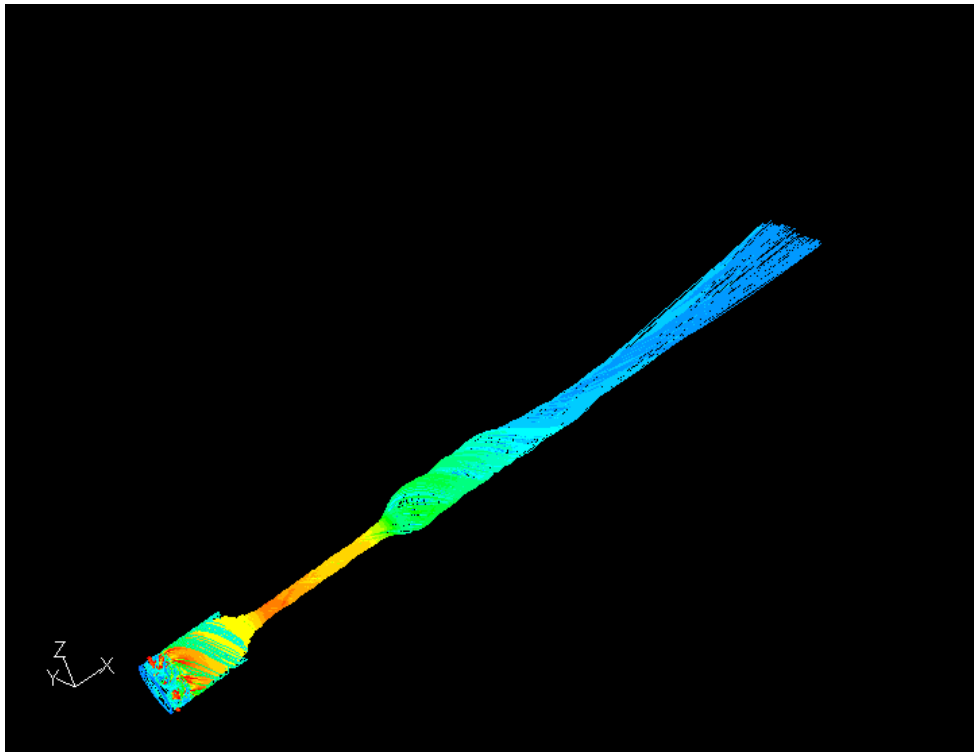
Figure 5.115 MODEL #05: Trace of particles from swirl injectors (inner)
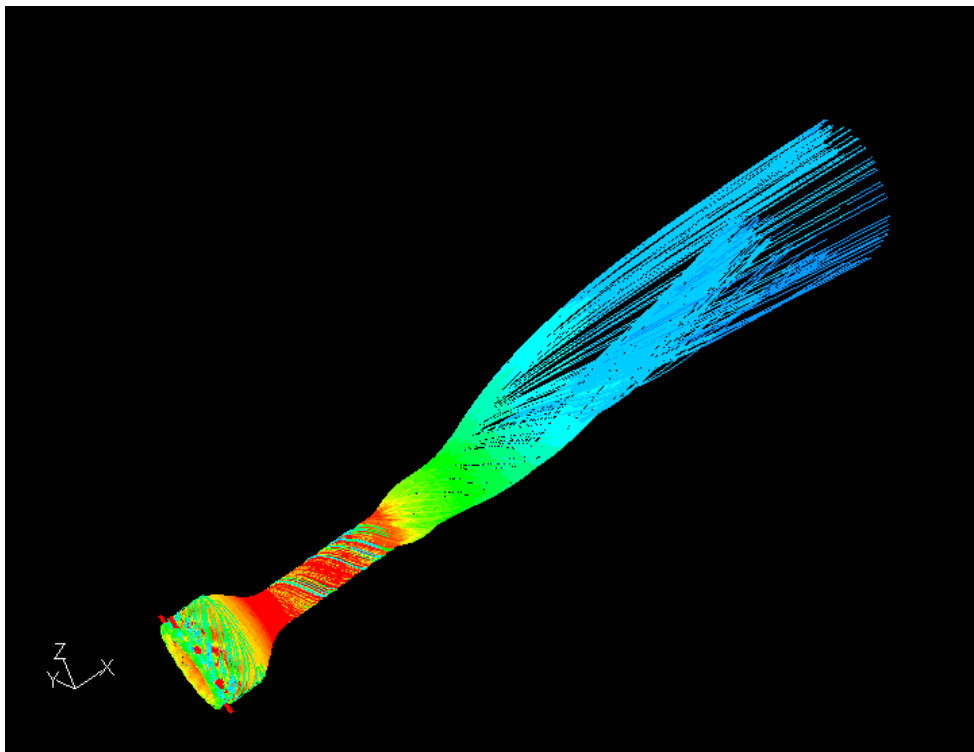
Figure 5.116 MODEL #05: Trace of particles from swirl injectors (outer)
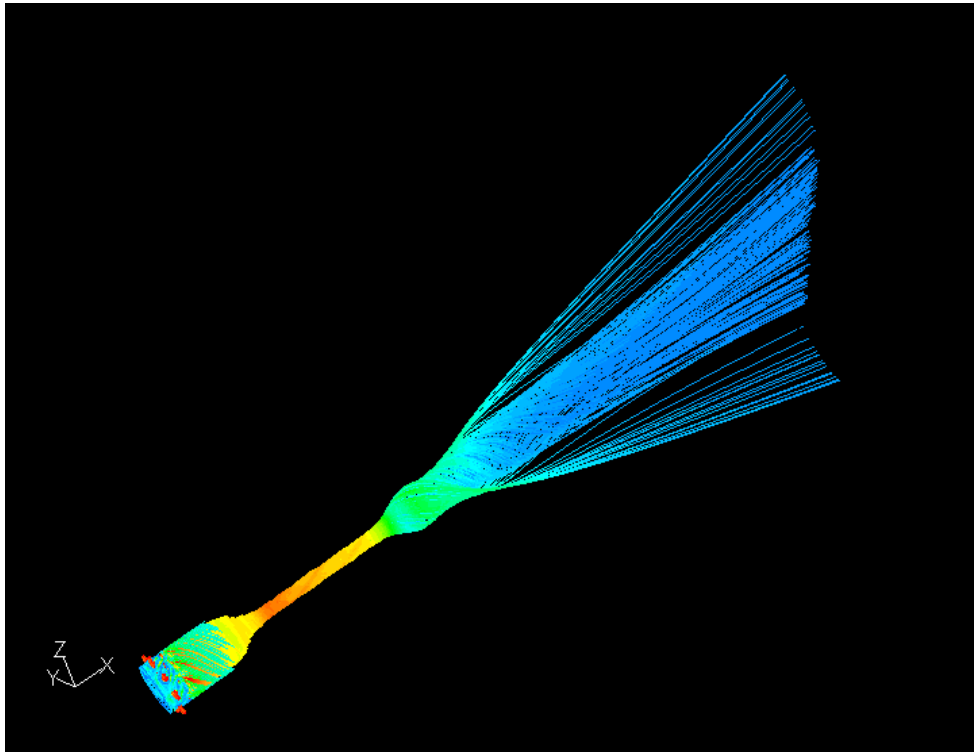
Figure 5.117 MODEL #06: Trace of particles from swirl injectors (inner)
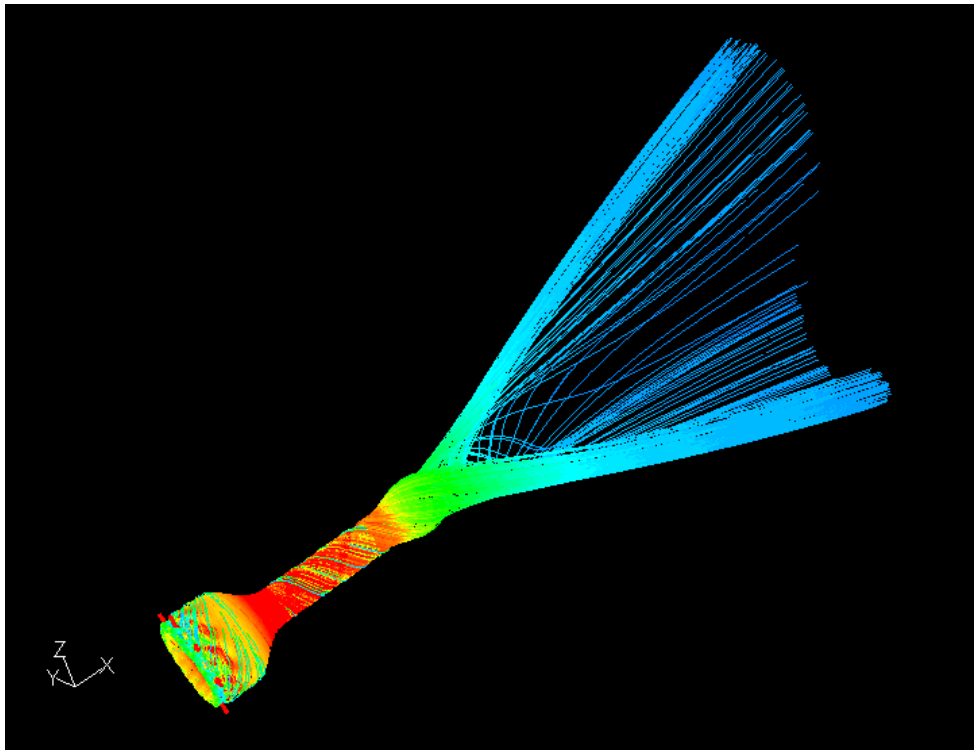
Figure 5.118 MODEL #06: Trace of particles from swirl injectors (outer)
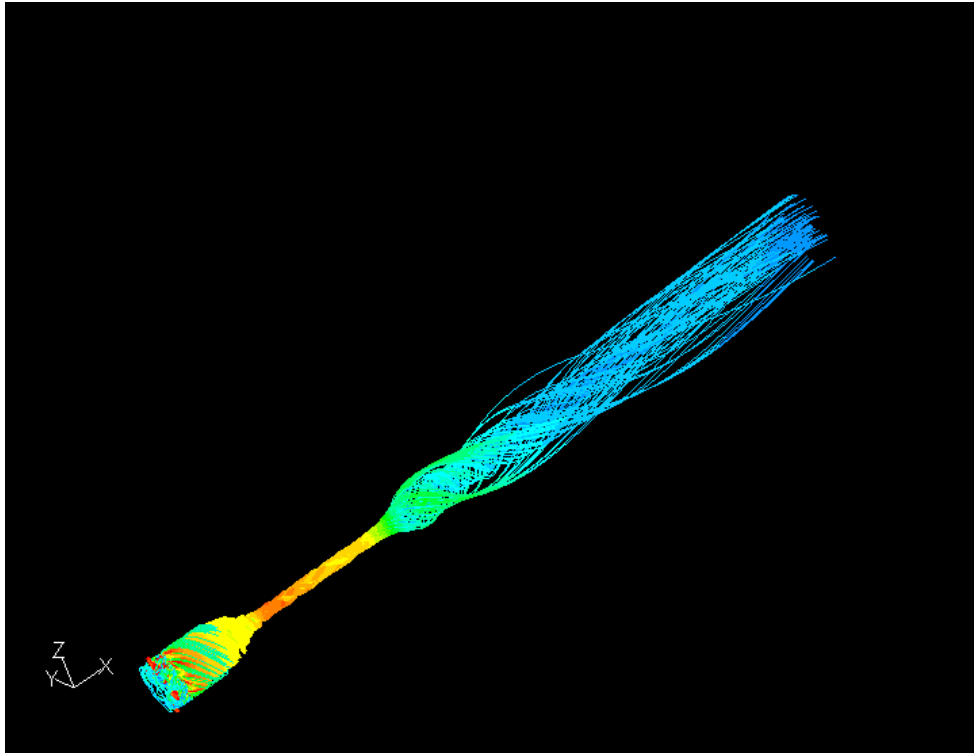
Figure 5.119 MODEL #08: Trace of particles from swirl injectors (inner)
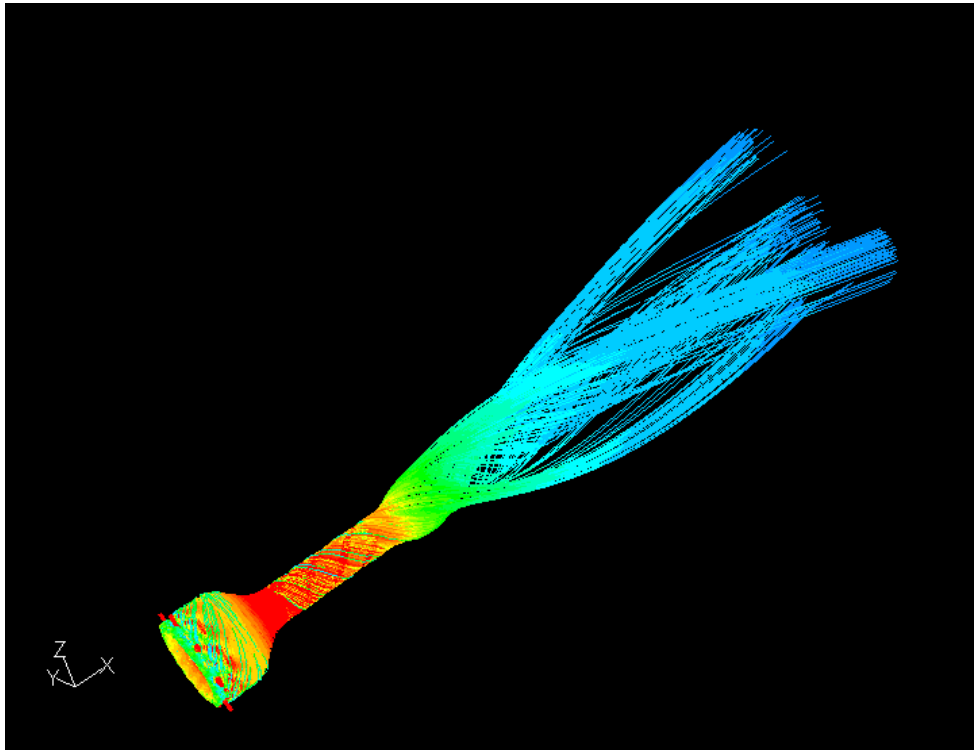
Figure 5.120 MODEL #08: Trace of particles from swirl injectors (outer)
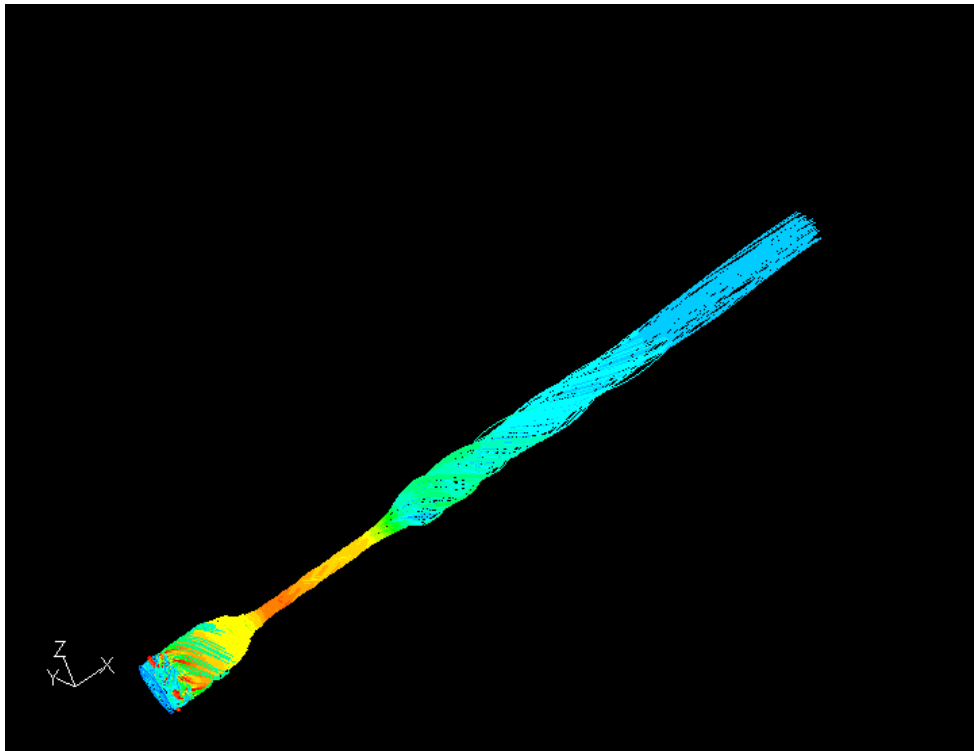
Figure 5.121 MODEL #09: Trace of particles from swirl injectors (inner)
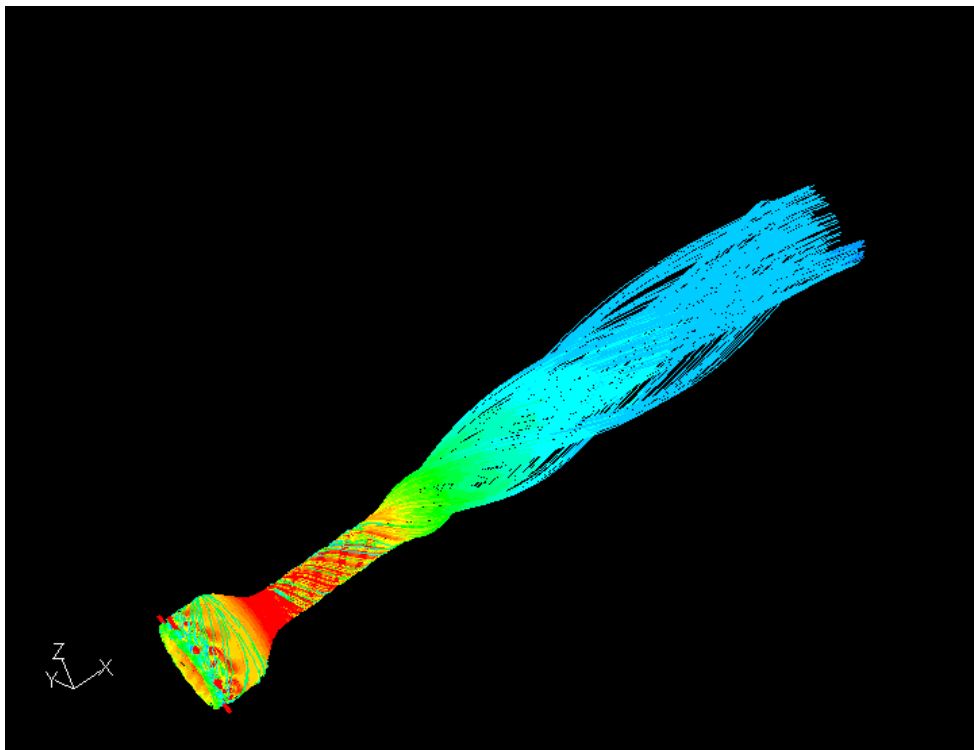
Figure 5.122 MODEL #09: Trace of particles from swirl injectors (outer)

236
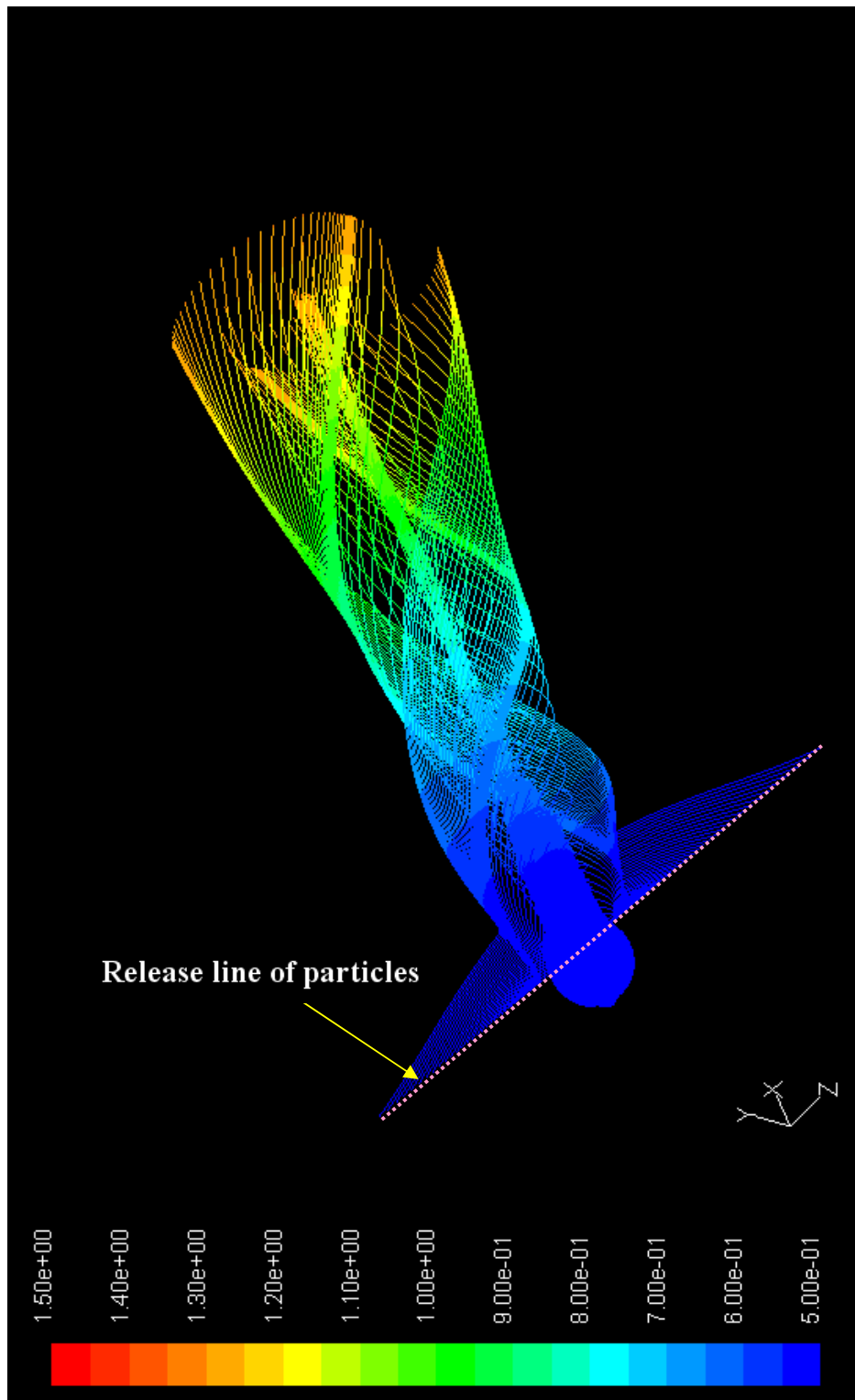
**Figure 5.123 MODEL #03: Particle trace from the line at x/D=1, y/D=0
(colored by velocity magnitude, m/s)**
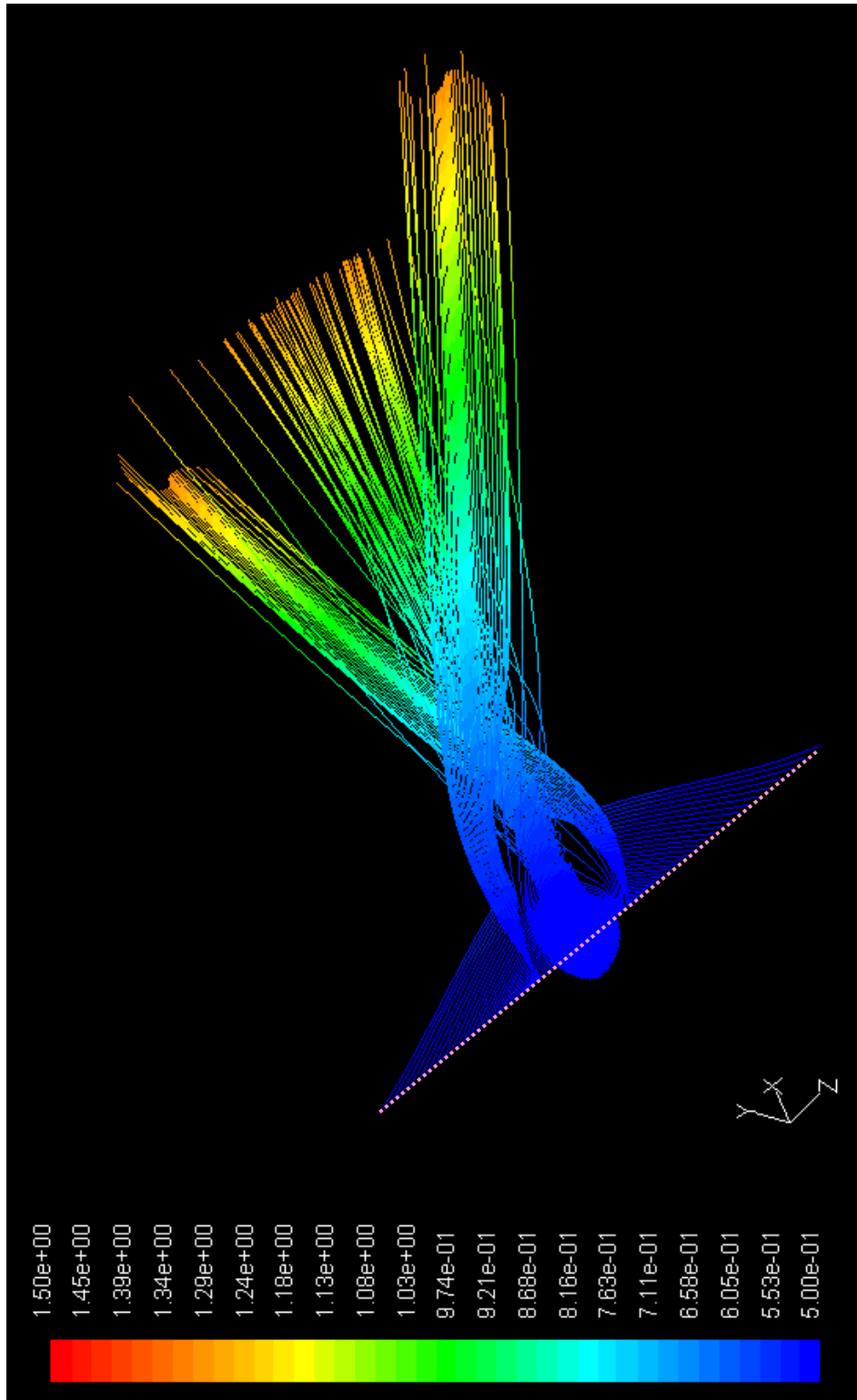
**Figure 5.124 MODEL #06: Particle trace from the line at x/D=1, y/D=0
(colored by velocity magnitude, m/s)**

5.2.6. Excitation Effects on Thermal Jets

In this section, the excitation effects on hot gas (i.e., T_o= 400K at the nozzle

exit) flows are investigated. To solve the thermal jet problem, energy equation is

considered for pressure based solver. In addition, to consider the density variation of

fluid (i.e., air) based on the gas temperature, the ideal gas option is applied.

In the comparison with the unexcited jet (MODEL #02), the radial distance

of MODEL #07 from the core (i.e., x/D=10, y/D=z/D=0) to the static temperature

contour boundary of 302.5K is augmented from 'r/D=2.07' (Figure 5.125) to

'r/D=4.31' (Figure 5.127, 108% up). At the same time, the two-lobed excited swirl

presents the fast reduction in temperature along the jet core centerline. The

temperature at (x/D, y/D, z/D) = (5, 0, 0), for instance, is reduced from 395K (Figure

5.125) to 345K (Figure 5.127) by shear controlled effects. To acquire the information

of density distribution in each jet, Figures 5.126 and 5.128 are supplemented.

Generally jet plume temperature reduction is favorable to several practical

applications such as, cutting down on the infra-red (IR) signature, reduction of wing

surface heating in both over or under the wing engine installations. As can be seen

from Figures 5.125 and 5.127, the shear excitation with helical disturbance provides

the remarkable effects on heat diffusion in radial direction as well as temperature

reduction along the jet centerline.
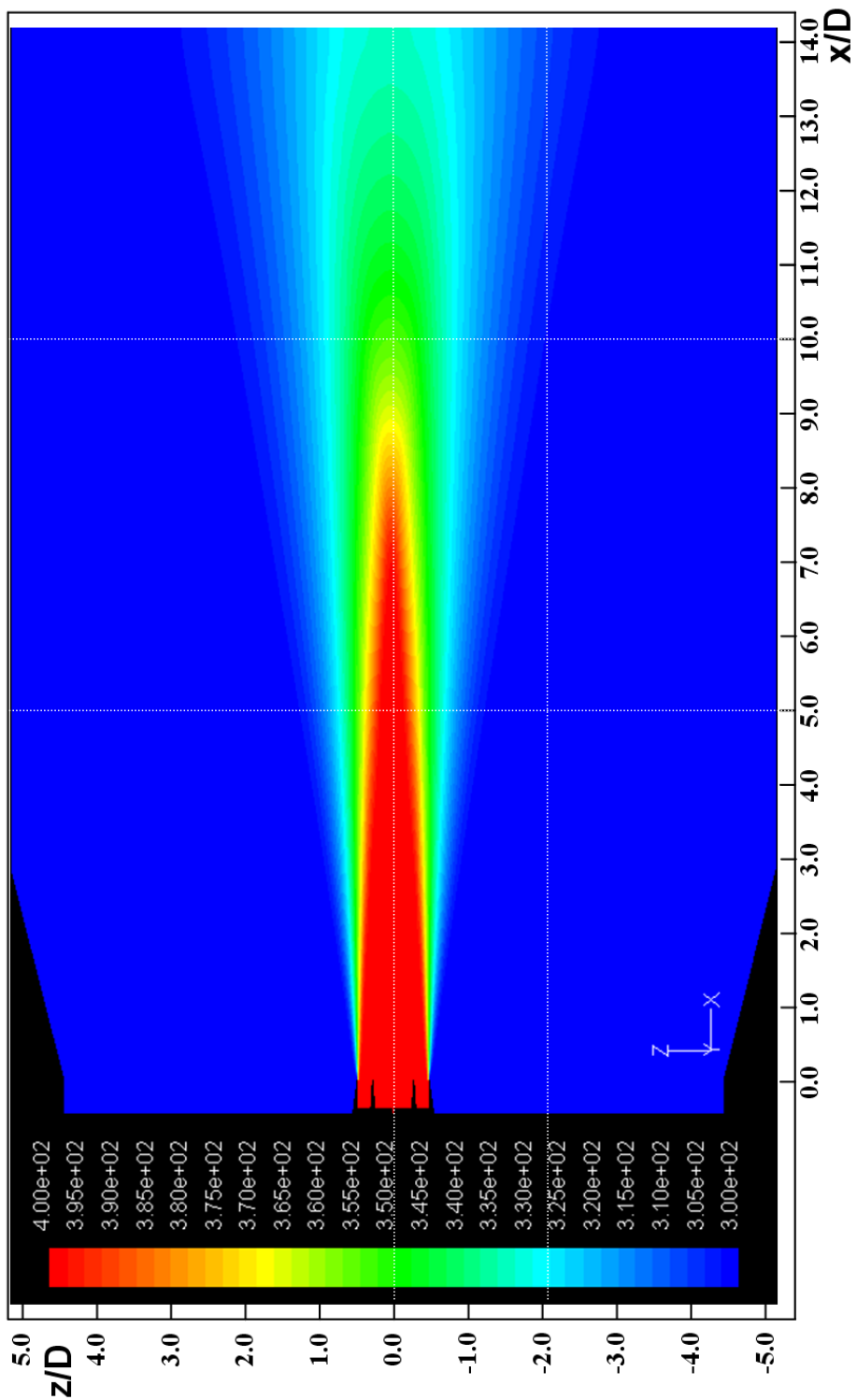
Figure 5.125 MODEL #02: Static temperature (K) distribution (@ z-normal plane) of hot gas (T_o=400K at x/D=0)
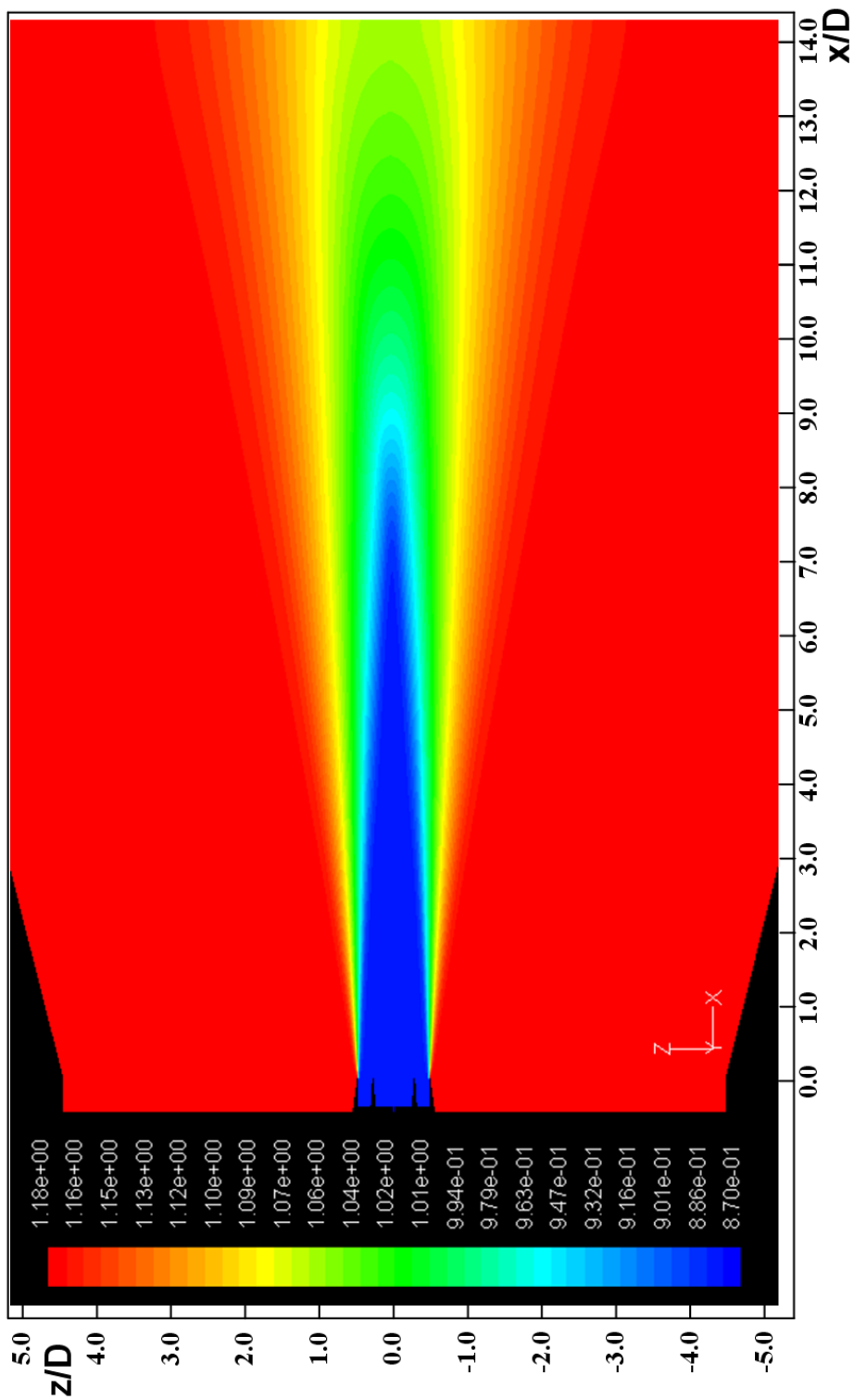
Figure 5.126 MODEL #02: Density (kg/m^3) distribution (@ z-normal plane) of hot gas (T$_o$=400K at x/D=0)
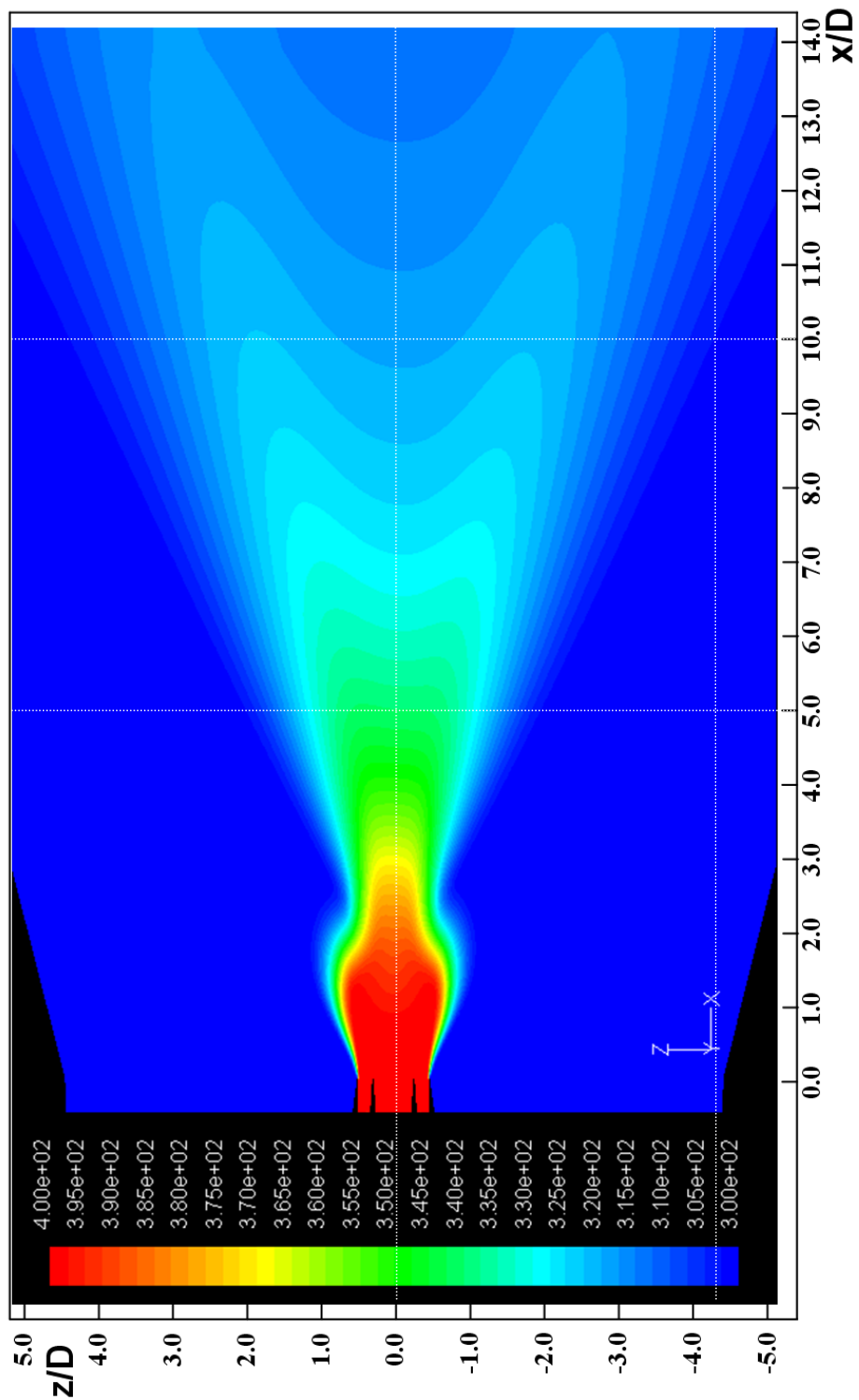
Figure 5.127 MODEL #07: Static temperature (K) distribution (@ z-normal plane) of hot gas (T_o=400K at x/D=0)
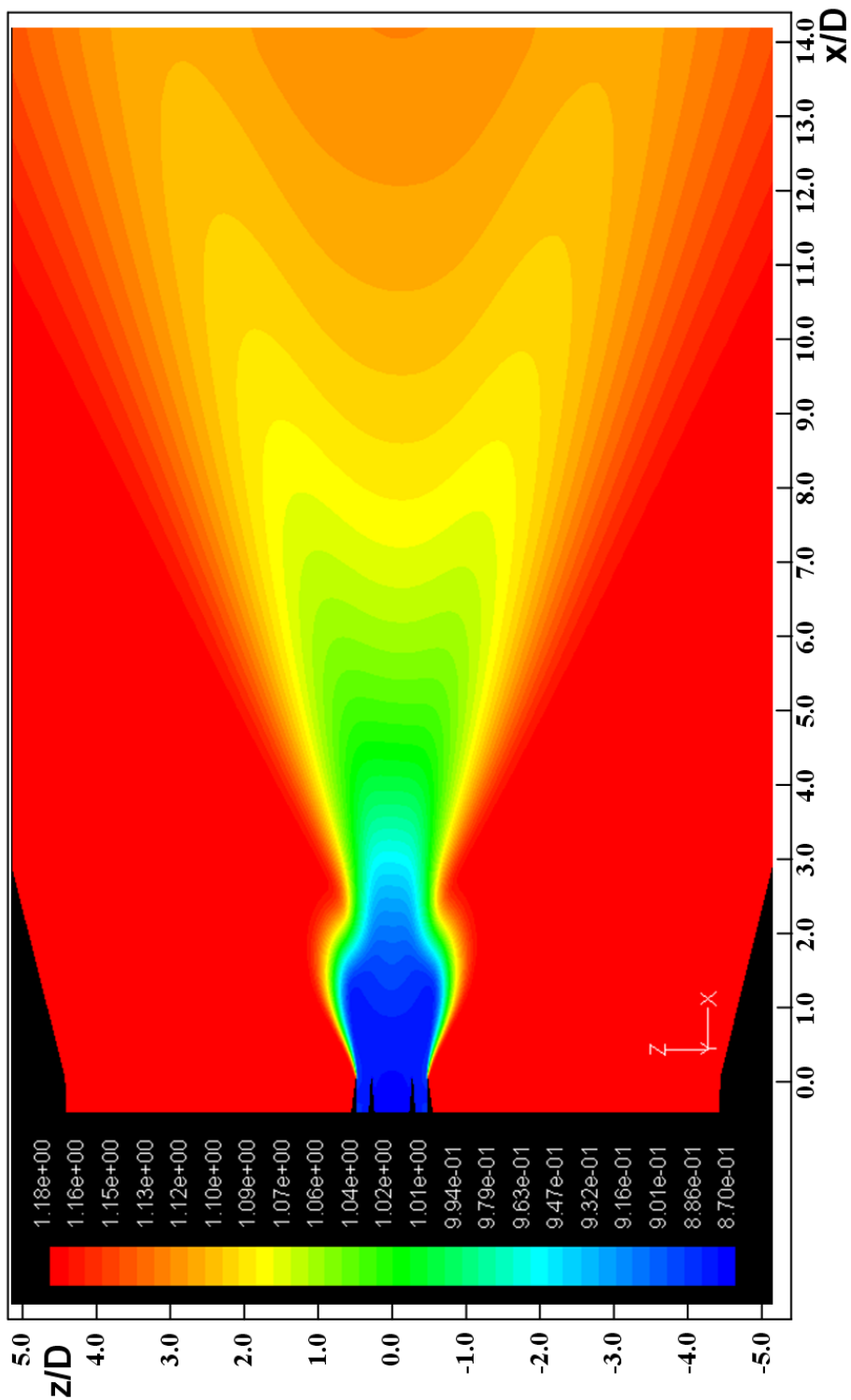
Figure 5.128 MODEL #07: Density (kg/m^3) distribution (@ z-normal plane) of hot gas (T$_o$=400K at x/D=0)

5.3. Comparisons with Analytical Stability Analysis

In this section, the results are compared with the analytical results of Wu[4][39]. In his investigation, the third helical mode in the direction of the shear layer rotation (i.e., m=+3) was the least amplified instability wave, while the third helical mode against the direction of shear layer rotation (i.e., m=-3) was the most amplified one, among the seven modes (i.e., m=0, ±1, ±2, ±3) investigated.

The present investigation, however, reveals several different results. The plain wave excitation which is experimentally investigated shows no remarkable regular pattern compared to the helical perturbation cases. On the other hand, the second negative helical (i.e., h=-2) excitation is found to be the most effective method by numerical simulation for the fast dispersion around the shear layer, diminishing wake effect at the vortex core, and outer flow entrainment and mixing enhancement. Overall, the excitation at negative helicities resulted in more mixing enhancement compared to plain wave cases.

Even though the results of this investigation do not exactly agree with Wu's, the general fact that negative helical modes are more effective than the positive ones

in the application of instability wave agrees very well. It should be considered in the light of Wu's theoretical results being based on the stability analysis of swirling jets with top-hat initial axial velocity distributions. In our case, the axial profiles were double-humped and far away from the top-hat approximation.

6. CONCLUDING REMARKS

A novel mechanical device for shear excitation of swirling jets is designed, built, and tested for plain wave perturbation. In addition, the numerical analysis is performed to simulate the helical excitation effects. In this study, the fact[40-42] that the initial disturbance on the axisymmetric jet exit affects the development of the large-scale vortical structure, which is in the near exit area, is confirmed for swirling jets.

6.1. Summary of Results

Experimental Study

- The experimental facility including the intensity controllable swirl generators and plain wave excitation devices, which are uniquely designed is fabricated and tested.

- Overall behavior of plain jet and its swirl input effects are compared and presented (especially the existence of 'central toroidal recirculation zone, CTRZ'). The radii of peaks and the jet boundary are stretched out in a radial direction. At the same time, the depth of the vortex core is reduced to compensate for the peak's velocity reduction.

- Implementation effects of straight-lobed perturbation are displayed and analyzed. The contour shape of the axial velocity field is transformed from the baseline, and corresponds to the number of lobes. When the 'm=2' of the counter-swirl is applied, the inward velocity is extremely fortified, and it helps CTRZ to dominate the vortex core region. In addition, the result shows

248

that the turbulence fluctuations are quenched by shear control.

- In the analysis of velocity gradient effects, the increased velocity of the outer-swirl prevails over the inner's augmentation. The augmented outer velocity affects the entire region of investigation, especially at the center core. The raised velocity of the outer-swirl not only fortifies the peak velocities, but also deepens the depth of the vortex core simultaneously.

- The decreased outer kinematic viscosity effects indicate a similar pattern to the increased outer velocity case. This can be explained as the augmented Reynolds number, either by density or velocity, stimulates the flows in the similar pattern.

- In the wave propagation analysis, the 'm=3' case is effective in stretching the wave into a radial direction. Turbulent intensity results show the excited cases have stabilized quickly, and this reveals that the turbulent mixing is completed in a relatively short distance and time.

Numerical Analysis

- Computational domain and grids including helical perturbation are generated and simulated for numerical analysis.

- Unique phenomena of a high degree of swirl, CTRZ and a double-hump profile, are illustrated, and the detailed views are presented.

- The appropriateness of several turbulent models is examined and compared. The calculation with the 'Realizable k-ε' model simulates the unique swirl characteristics most accurately for this study.

- The cause of the similarity between co- and counter-swirl phenomena is revealed by the particle trace analysis.

- In the helical exciting wave investigation, the second negative helicity (i.e., h=-2) case shows the maximum dispersion effects. At the same time, it diminishes the wake effects at the vortex core.

- The most noticeable effects from the particle trace result are shown in the 'h=-2' case. Fluid particles are expanded in a radial direction more widely than any other cases, and a relatively small amount of particles stays at the core.

- Also, the 'h=-2' case simultaneously presents the fast decay of angular behavior, and this is remarkably distinguished from the baseline. This reveals the mixing enhancement between the outer-swirl flow and environment, and outer- and inner-swirl flows, which are not present in their counterparts.

- The excited swirl jet presents the fast reduction in temperature along the jet core centerline and the wide dispersion in radial direction at the same time.

6.2. Conclusions

In general, axisymmetric swirling jets are unstable in the near field ($x/D < 3$) to all the excitation modes examined experimentally and numerically. It is shown that the overall response of the swirling jet to excitation is not only dependent on the wave mode number, but also strongly on its sign; meaning the spiral direction of the convex lobes with respect to the swirl rotation. This confirms the previous theoretical results. Excitation at both plain and helical perturbation affects the flow property distributions in the vortex core and the shear layer at the jet periphery simultaneously.

Also, negative helical wave excitation is considered as the effective way of mixing enhancement for swirling jets compared to the straight-lobe perturbation. These results agree with the theoretical calculations of other researchers.

In addition, the decreased jet plume temperature which is resulted from mixing enhancement is applicable to cut down on the infra-red (IR) signature, to reduce wing surface heating in both over or under the wing engine installations, as well as in vertical takeoff and landing aircraft, to avoid ground erosion and hot gas ingestion.

Consequently, the knowledge gained from this research could benefit the advanced designs for combustors, quiet jet engines, and other technological applications, depend on the identification of strategies for effectively modifying the spreading rate of shear layers formed at the exit of a jet. The preferred mode is negative two by helical excitation (i.e., h=-2) in the present work.

REFERENCES

1. Lim, D. W.; Redekopp, L. G. "Absolute instability conditions for variable density, swirling jet flows" European journal of mechanics. B, Fluids, v.17 no.2, 1998, pp.165-185

2. Loiseleux, T.; Chomaz, J. M.; Huerre, P. "Effect of swirl on jets and wakes: linear instability of the Rankine vortex with axial flow" Physics of fluids, v.10 no.5, 1998, pp.1120-1134

3. Rayleigh, J. W. S. "On the Dynamics of Revolving Fluids" Proceedings of Royal Society, A93, 1916, p.148

4. Wu, C. "Hydrodynamic Stability Analysis of Swirling Jets" Ph.D. Dissertation, University of Kansas, 1992

5. Farokhi, S.; Taghavi, R.; Rice, E. J. "Effect of Initial Swirl Distribution on the Evolution of Turbulent Jet" AIAA Journal, v.27, no.6, June 1989, pp.700-706

6. Gupta, A. K.; Lilley, D. G.; and Syred, N. "Swirl Flows" Abacus Press, Tunbridge Wells, England, 1984

7. Chigier, N. A.; Cherivinsky, A. "Experimental Investigation of Swirling Vortex Motion in Jets" Transactions of the ASME, Journal of Applied Mechanics, June 1967, pp.443-451

8. Raman, G.; Rice, E. J. "Sub-harmonic and Fundamental High Amplitude Excitation of an Axisymmetric Jet" AIAA Paper 89-0993, March 1989

9. H., J. S.; W., J. C.; S., Y. J.; T., L. H. "Correlation of Swirl Number for a Radial-Type Swirl Generator" Experimental thermal and fluid science: ETF science, v.12 no.4, 1996, pp. 444-451

10. Ivanic, T.; Foucault, E.; Pecheux, J. "Dynamics of swirling jet flows" Experiments in fluids, v.35 no.4, 2003, pp.317 – 324

11. Garcia-Villalba, M.; Frohlich, J. "LES of a free annular swirling jet - Dependence of coherent structures on a pilot jet and the level of swirl" The International journal of heat and fluid flow, v.27 no.5, 2006, pp.911-923

12. Panda, J.; McLaughlin, D. K. "Experiments on the instabilities of a swirling jet" Physics of fluids, v.6 no.1, 1994, p.263

13. Howard, L. N.; Gupta, A. S. "On Hydrodynamic and Hydro-magnetic Stability of Swirling Flows" Journal of Fluid Mechanics, v.14, 1962, pp.463-476

14. Lalas, D. P. "The Richardson Criterion for Compressible Swirling Flow" Journal of Fluid Mechanics, v.32, pp. 693-704, 1968

15. Michalke, A. "On Spatially Growing Disturbances in an Inviscid Shear Layer" Journal of Fluid Mechanics, v.23, Pt.3, Nov. 1965, pp.521-524

16. Freymuth, P. "On Transition in a Separated Laminated Boundary Layer" Journal of Fluid Mechanics, v.25, Pt.4, Aug. 1966

17. Michalke, A. "Instability of a Compressible circular Free Jet with Consideration of the Influence of the Jet Boundary Layer Thickness" NASA TM-75190, 1977

18. Bechert, D.; Pfizenmaier, E. "On Wavelike Perturbations in a Free Jet Traveling Faster than the Mean Flow in the Jet" Journal of Fluid Mechanics, v.72, Pt.3, Nov. 25, 1975, pp.341-351

19. Volchkov, E. P.; Lebedev, V. P.; Terekhov, V. I.; Shishkin, N. E. "An experimental study of the flow stabilization in a channel with a swirled periphery jet" International journal of heat and mass transfer, v.43 no.3, 2000, pp.375-386

20. Cooper, A. J.; Peake, N. "The stability of a slowly diverging swirling jet" Journal

of fluid mechanics, v.473, 2002, pp.389-411

21. Farokhi, S.; Taghavi, R.; Rice, E. J. "Controlled Excitation of a Cold Turbulent Swirling Free Jets" Transactions of the ASME Journal Vibration, Acoustics, Stress, and Reliability in Design, v.110 no.2, 1988, pp.234-237

22. Farokhi, S.; Taghavi, R.; Rice, E. J. "Large-Amplitude Acoustic Excitation of Swirling Turbulent Jets" AIAA paper 89-0970

23. Crow, S. C.; Champagne, F. H. "Orderly Structure in Jet Turbulence" Journal of Fluid Mechanics, v.48, Pt.3, Aug.16, 1971, pp.547-591

24. Raman, G.; Rice, E. J.; Zaman, K. B. M. Q. "Initial Turbulence Effects on Jet Excitability" AIAA Paper 87-2725, October, 1987.

25. Sun, D. J.; Hu, G. H.; Gao, Z.; Yin, X. Y. "Stability and temporal evolution of a swirling jet with centrifugally unstable azimuthal velocity" Physics of fluids, v.14 no.11, 2002, pp.4081-4084

26. Merkle, K.; Haessler, H.; Buchner, H.; Zarzalis, N. "Effect of co- and counter-swirl on the isothermal flow- and mixture-field of an air-blast atomizer nozzle" The International journal of heat and fluid flow, v.24 no.4, 2003, pp.529-537

27. Huang, R. F.; Tsai, F. C. "Flow field characteristics of swirling double concentric jets" Experimental thermal and fluid science: ETF science, v.25 no.3/4, 2001, pp.151-161

28. Chigier, N. A.; Beer, J. M. "Velocity and Static Pressure Distributions in Swirling Air Jets Issuing from Annular and Divergent Nozzles" Transactions of the ASME, Journal of Basic Engineering, December 1964, pp.788-796

29. Pratte, B. D.; Keffer, J. F. "The Swirling Turbulent Jet" Transactions of the ASME, Journal of Basic Engineering. v.93, December 1972, pp. 639-748

30. Chigier, N. A.; Cherivinsky, A. "Experimental and Theoretical Study of Turbulent Swirling Jets Issuing from a Round Orifice" Israel Journal of Technology v.4 no.1-2, 1966, pp.44-54

31. Kusek, S. M.; Corke T. C.; Reisenthel, P. "Seeding of Helical Modes in the Initial Region of an Axisymmetric Jet" Experiments in Fluids, v.10, 1990 pp. 116-124

32. Hilgers, A.; Boersma, B. J. "Optimization of turbulent jet mixing" Fluid dynamics research, v.29 no.6, 2001, pp.345-368

33. Gallaire, F.; Rott, S.; Chomaz, J. M. "Experimental study of a free and forced swirling jet" Physics of fluids, v.16 no.8, 2004, pp.2907-2917

34. Frank, M. White "Fluid Mechanics" Second Edition, McGraw-Hill, Singapore, 1987

35. M. Raffel; C. Willert; J. Kompenhans "Particle Image Velocimetry", Springer, Germany, 1998

36. Dantec Dynamics Co. Ltd. "Educational Material for 3D PIV" 2006

37. FLUENT Inc. "FLUENT 6 User's Guide" 2001

38. FLUENT Inc. "Fluent Software Training Material, Advanced Turbulence" 2005

39. Wu, C., Farokhi, S.; Taghavi, R. "On Spatial Instability of a Swirling Jet-Theory and Experiment" AIAA Paper 91-1771

40. Ho, C. M.; Huerre, P. "Perturbed Free Shear Layers" Ann. Rev. Fluid Mech. v.16, 1984, pp. 365-424.

41. Thomas, F. O. "Structures of Mixing Layers and Jets" Appl. Mech. Rev., v.44 no.3, 1991, pp. 119-153.

42. Mankbdi, R. R. "Dynamics and Control of Coherent Structure in Turbulent Jets" Appl. Mech. Rev., v.45 no.6, 1992, pp. 219-247.